Constraining cycles of deformation at submarine plate boundaries using cabled ocean bottom seismometers

Zoe Krauss

A dissertation

submitted in partial fulfillment of the

requirements for the degree of

Doctor of Philosophy

University of Washington

2024

Reading Committee:

William S.D. Wilcock, Chair

Marine A. Denolle

Kenneth C. Creager

Program Authorized to Offer Degree:

School of Oceanography

©Copyright 2024

Zoe Krauss

University of Washington

Abstract

Constraining cycles of deformation at submarine plate boundaries using cabled ocean bottom seismometers

Zoe Krauss

Chair of the Supervisory Committee:
William S. D. Wilcock
School of Oceanography

The processes that reorganize the Earth's crust occur primarily beneath our oceans, where it is difficult to make observations. Much of our knowledge of deformation at mid-ocean ridges and subduction zones is therefore limited to large events that can be recorded on land, including dike emplacements and moderate to large earthquakes. Although these large deformation events are thought to relieve most of the strain built up by plate motions, some fault slip can occur in the interim. Close seafloor observation of seismic signals at mid-ocean ridges and subduction zones between large events is needed to properly constrain how fault slip varies across frictional conditions and to address hazards associated with offshore faults. In this dissertation, I leverage novel cabled ocean bottom seismometer (OBS) datasets, which provide the first long-term (> 10 year) time series of seafloor seismic activity, to constrain deformational behavior between large events at submarine plate boundaries. In Chapter 2, I combine cabled OBS data from the Endeavour segment of the Juan de Fuca ridge with past autonomous OBS datasets to create an earthquake catalog that tracks how activity evolves between dike emplacements in relation to regional tectonics, magmatism, and hydrothermal fluid circulation. In Chapter 3, I show how just one cabled OBS can be used to constrain earthquake rates at the Endeavour segment, which allows the earthquake catalog to be extended by five years and supports that seismicity rates

remain relatively low for most of the spreading cycle. In Chapter 4, I investigate multiplet earthquakes, groups of earthquakes with highly similar waveforms, at the Endeavour segment. I show that they represent a range of fault slip types, including fluid-induced earthquake swarms and repeating earthquakes, which provide the first direct evidence for aseismic slip at a mid-ocean ridge. Finally, in Chapter 5, I develop a new approach to search for tectonic tremor, a signal associated with slow fault slip, on individual OBSs. Application of this approach to cabled seismometers in the Cascadia subduction zone finds potential tectonic tremor signals that suggest localized shallow slow slip may occur near the deformation front.

Table of Contents

Acknowledgements

This dissertation is a culmination of many years of painstaking, all-encompassing, and overall beautiful work with many collaborators. To those who shared their love of the scientific process and the questions of geophysics, thank you for inspiring me every single day. It would be impossible to name all those who contributed to this work. I thank my committee, my fellow graduate students, the Oceanography community, and my bonus community in the Earth Sciences department, whose support and camaraderie kept me going. Above all, I thank my advisor, William Wilcock, whose intrepid guidance pushed me to be a better scientist and taught me lessons I will carry with me for my entire career.

And to my friends, family, and my husband, Otis, whose support through this endeavor kept me grounded and buoyed me towards the finish line. I love you all.

To my grandfathers, whose combined examples made this undertaking seem feasible and maybe, even, a good idea.

To George Krauss, a pillar of scholarship, hard work, curiosity, and unbridled love for the natural world. I know you will read the whole thing. I hope that it makes you proud.

And to Howard Gleason, a pillar of persistence, tenacity, and confidence. You probably would have thought this was all crazy, and then read the whole thing anyway. I think you would have loved it. I know it would have made you proud.

Chapter 1: Introduction and Organization of the Dissertation

Across the majority of Earth's surface, the crust moves uniformly following the large-scale organization of tectonic plates at a speed unnoticeable by humans. At the boundaries of these plates, however, stresses are concentrated and the resulting crustal strain is relieved rapidly during episodic large deformational events. At subduction zones, strain is built up on the scale of decades to centuries as the oceanic lithosphere dives into Earth's mantle; this strain is relieved during very large earthquakes (M_W 8-9+) (Satake & Atwater, 2007). At mid-ocean ridges, the release of extensional strain coincides with the formation of new oceanic crust during periodic volcanic events, where magma is injected into vertical planar fractures to form new crust (Delaney et al., 1998).

Although large deformational events are thought to relieve most of the strain built up by plate motions, some fault slip can occur in the interim. Scientific advances over the last several decades have shown that fault slip can occur not only as fast earthquakes, but also as slow slip, a form of fault motion where the fault slips stably without generating shaking in events that can last from days to years (Beroza & Ide, 2011; Bürgmann, 2018; Peng & Gomberg, 2010; Rubinstein et al., 2010). The exact fault conditions required to initiate slow slip are an ongoing area of study. In subduction zones, shallow slow slip is thought to be promoted by various factors that increase fluid pressures, including the amount and composition of subducting sediment, changes in the geometry of subduction, permeability of the overlying and underlying plates, and seamounts on the subducting plate (e.g. Barker et al., 2018; Han et al., 2017; Métois et al., 2012; Shillington et al., 2015). More observations that tie slow slip to fault conditions on both large and small scales are needed to fully characterize the underlying conditions needed to initiate slow slip. At mid-ocean ridges, it has long been recognized that a significant portion of

plate motions are accommodated aseismically (e.g. Cowie et al., 1993; Olive & Escartín, 2016), but there has never been direct observation of slow slip or aseismic creep between large-strain events. Which types of faults at mid-ocean ridges experience slow slip and how much slow slip occurs between seafloor spreading events is an ongoing question.

The amount and type of deformation that occurs between periodic large events can also help to anticipate the events themselves. At subduction zones, the fault portions that undergo slow slip are not generally expected to rupture in great earthquakes, such that defining the extent of where slow slip occurs can define the maximum size of expected earthquake hazard (Dixon et al., 2014; Radiguet et al., 2012). Slow slip events have also been pointed to as triggers of large subduction zone earthquakes (Kato et al., 2012; Meng et al., 2015), suggesting that they could be used as a precursory warning signal of heightened large earthquake hazard. At mid-ocean ridges, which are typically more volcanic environments, exponentially increasing seismicity levels can indicate where a fault segment is approaching failure, allowing the planning of scientific response to ensure observation of various phenomena (Chadwick et al., 2022; Tolstoy et al., 2006; Weekly et al., 2013).

Because signals of fault slip between large deformational events are typically small, they require close-range observation. This is particularly challenging in the oceans, where it is prohibitively expensive to deploy seismometers and batteries typically limit autonomous instrument deployment to ~1 year. Observations of small, localized slip at mid-ocean ridges and the offshore portions of subduction zones are therefore relatively poor in comparison to on land. Cabled seafloor observatories, where scientific instrumentation is connected to and powered from land, newly allow for both long-term and real-time observation of submarine plate boundaries. In the Pacific Northwest, both the Cascadia subduction zone and the Juan de Fuca

mid-ocean spreading ridge are now instrumented by cabled observatories: the Ocean Networks Canada NEPTUNE cabled observatory came online in 2011 (Heesemann et al., 2014), and the Ocean Observatories Initiative (OOI) Regional Cabled Array came online in 2015 (Smith et al., 2018). However, the node-based design of cabled observatories means that they can support only sparse networks of stand-alone or few instruments with a small footprint (< 10 km) around widely spaced nodes. Pioneering techniques are needed to overcome the limitations of these small networks to make broad observations of submarine plate boundaries.

This dissertation works to fill knowledge gaps of deformational patterns at submarine plate boundaries by developing new techniques to observe seismic signals with limited cabled ocean bottom seismometer (OBS) networks. A common theme of Chapters 2-5 is developing more flexible and robust techniques that allow the observation of small seismic signals with small OBS networks amidst oceanic noise. This facilitates the characterization of interseismic deformational patterns at a resolution and duration that was not previously possible for both mid-ocean ridges and subduction zones. With better observations of small seismic signals, we can better infer underlying fault conditions at small scales and tie local processes to larger tectonic patterns.

In Chapter 2, I compile OBS data for the Endeavour segment of the Juan de Fuca mid-ocean spreading ridge to create an earthquake catalog that spans multiple decades and the period before, during, and after a large extensional event, which includes new analysis of 5 years of cabled data. I show that, despite a small OBS network footprint, earthquake locations are robust on the segment scale when 3-dimensional seismic velocity models are used. I use the earthquake catalog to show that stress evolves heterogeneously along the segment depending on which portion last released strain. I identify characteristics of earthquake rates and spatial patterns prior

to the last large deformational event to predict that the central portion of the Endeavour segment will be the first to undergo a subsequent large event, likely within the next five years. The earthquake catalog also suggests that the intersecting faulting patterns created by regional tectonics directly affects fluid circulation, leading to the surprising longevity of the localized hydrothermal vent fields. The contents of this chapter are published in *The Journal of Geophysical Research: Solid Earth* under the title "A Long-Term Earthquake Catalog for the Endeavour Segment: Constraints on the Extensional Cycle and Evidence for Hydrothermal Venting Supported by Propagating Rifts" (Krauss et al., 2023).

In Chapter 3, I explore the feasibility of using a single cabled OBS to observe seismicity at the Endeavour segment. I show how single-station location is theoretically possible in the marine setting if *P* wave first motion polarization, *S* waves, and the *P* wave water column reflections are used, but I show that earthquake azimuth calculation is prevented at a mid-ocean ridge setting if localized scattering is high, which occurs in the Endeavour axial valley. Although a single OBS at the Endeavour segment cannot provide full earthquake locations, I show that it can be used to effectively approximate overall earthquake rates and distances. I use the single-station network to add five additional years of data coverage to the earthquake catalog from Chapter 2. The expanded catalog shows that earthquake rates remain relatively low for over a decade following a rupture event in 2005. This work is currently under review at *Seismological Research Letters*.

Manual inspection of earthquake detections from Chapters 2 and 3 reveals that many earthquakes at the Endeavour segment occur as multiplets, which are sets of earthquakes with highly similar *P* and *S* waveforms. This implies repeated slip of a fault patch or near-contemporaneous slip on nearby fault patches (Nadeau et al., 1995; Rubin et al., 1999). The

interevent times and distances of earthquake multiplets can be used to distinguish styles of deformation: multiplets that are identified as repeating earthquakes indicate slow slip events or aseismic creep and can be used to estimate aseismic slip rates (Uchida, 2019). Alternatively, multiplets that occur within earthquake swarms can represent varying transient processes depending on their migration characteristics, such as aftershock sequences (Kimura et al., 2006; Schaff et al., 1998; Templeton et al., 2008) and/or fluid diffusion (Mesimeri & Karakostas, 2018). In Chapter 4, I investigate these multiplet earthquakes to explore whether they can be used to observe slow slip and fluid-induced deformation. I identify a repeating earthquake family that provides the first direct evidence of aseismic slip at a mid-ocean ridge, and I show that swarms of multiplets refelct both internal and external driving mechanisms. Investigation of these multiplets suggests they could be useful tools to identify deformational styles at mid-ocean ridges. This work is being prepared for publication in a peer reviewed journal.

In Chapter 5, I move to the Cascadia subduction zone to develop a flexible, marine-specific method to look for evidence of slow slip. Land-based observations suggest that the shallow plate interface near 44.5°N in Cascadia, where seamounts have been subducted, may only be partially locked (Li et al., 2018; Schmalzle et al., 2014; Trehu et al., 2015). However, seafloor observations of slow slip signals are needed to test this hypothesis. Serendipitously, the OOI cabled observatory has supported two buried broadband seismometers near 44.5°N in Cascadia since 2015. To search for tectonic tremor signals, a proxy for slow slip, I investigate the relationship between seismic noise and environmental factors at these sites and develop a technique to isolate tremor-like signals amongst marine-specific noise. I apply this single-station approach to the OOI OBS to show that there is no evidence of widespread slow slip in shallow Cascadia as has been seen at other subduction zones. However, I find potential signals of

tectonic tremor recorded at only one site near the deformation front. This suggests that small-scale tectonic tremor may occur at very shallow depths in Cascadia. This tectonic tremor detection technique could be applied elsewhere to limited OBS datasets to improve coverage of slow slip detection and potentially identify additional smaller-scale patches of slow slip. This work is being prepared for publication in *Seismica*.

In Chapter 6, I summarize the implications of the new observations of mid-ocean ridge and subduction zone deformation made using cabled OBS networks in Chapters 2-5. I also discuss how this work will help prepare the broader community to maximize discovery as extended observations of submarine plate boundaries are planned.

Chapter 2: A long-term earthquake catalog for the Endeavour segment: constraints on the extensional cycle and evidence for hydrothermal venting supported by propagating rifts

Zoe Krauss[1], William S.D. Wilcock[1], Martin Heesemann[2], Angela Schlesinger[2], Jacob Kukovica[2], Joseph J. Farrugia[2]

[1]School of Oceanography, University of Washington, Seattle, Washington, USA
[2]Ocean Networks Canada, University of Victoria, British Columbia, Canada

2.0 Abstract

We use ocean bottom seismometer data from the Endeavour segment of the Juan de Fuca ridge to construct a long-term earthquake catalog for an intermediate spreading rate mid-ocean ridge. We present > 50,000 new earthquake locations for 2016-2021 from the Ocean Networks Canada NEPTUNE cabled observatory and relocate earthquakes from two autonomous networks in 1995 and 2003-2006. The catalog comprises > 85,000 earthquakes located using three-dimensional segment-scale P- and S-wave velocity models from a prior tomography experiment. Despite the small footprints of networks near the segment center, locations show good agreement with geologic features at segment ends. The improved locations show that the northern Endeavour segment ruptured southwards from 48.3°N to 48.05°N during two diking events in early 2005, possibly accompanied by diking on the West Valley propagator. Persistent off-axis seismicity near the segment center appears to be related to the West Valley and Cobb propagating rifts which we infer extend ~10 km closer to the Endeavour segment center than is apparent in bathymetry. We suggest that the proximity of the propagators to the Endeavour vent fields contributes to the localization, vigor and longevity of the fields by focusing permeability through ongoing fracturing and by limiting extrusive magmatism through degassing of the axial magma lens. Increasing rates of seismicity beneath the vent fields beginning in late 2018 and a deepening of earthquakes in 2020 indicate that the central portion of the segment may be entering the later stages of the eruptive cycle.

2.1 Introduction

To study the global mid-ocean ridge (MOR) system is to study the creation of Earth's oceanic lithosphere. Extension from seafloor spreading is accommodated in two ways: during episodic diking events, magma is injected into and cools within ridge-parallel dikes that may or sometimes feed eruptions (Delaney et al., 1998), and both during and between discrete spreading events, extension is also accommodated by faulting (e.g., Buck et al., 2005). The relative contributions from volcanic and tectonic processes at MORs vary widely both spatially (e.g., Karson et al., 1987) and temporally (e.g., Kappel & Ryan, 1986), depending on spreading rate, magma supply, and the effects of hydrothermal cooling on rheology (Behn & Ito, 2008; Chen & Morgan, 1990). The periodicity of diking events means that MOR activity is intrinsically cyclical. Detailed observations not only of discrete seafloor spreading events, but also of the time in-between them, are therefore essential to fully understanding how volcanism and tectonism interact at a MOR segment to produce the oceanic lithosphere.

Volcanic seafloor spreading events were first observed using hydroacoustic records of earthquake swarms (Dziak et al., 2011, 2012a), with T-phases constraining the location and timing of dike injection (Bohnenstiehl et al., 2004; Dziak et al., 1995; Dziak & Fox, 1999b). Volcanic extensional events have since been identified on ridges across the full range of spreading rates, including the Gakkel Ridge (Tolstoy et al., 2001), Mid-Atlantic Ridge (Dziak et al., 2004), Gorda Ridge (Fox & Dziak, 1998), Juan de Fuca Ridge (Dziak et al., 1995; Dziak & Fox, 1999b) and East Pacific Rise (EPR) (Dziak et al., 2009). Hydroacoustic observations on spreading ridges have also illuminated relationships between static and dynamic stresses and seismicity triggering (Bohnenstiehl et al., 2004), thermal structure and along-axis earthquake distribution (Smith et al., 2002), and detachment faults, crustal cooling and extension accommodation (Escartín et al., 2008).

Hydroacoustic arrays provide extensive spatial coverage but have detection thresholds of M_L > ~2.5 and so do not capture the smaller microearthquakes that dominate MOR seismicity (Dziak et al., 2011, 2012a). Local ocean bottom seismometer (OBS) networks offer much lower detection thresholds, decreased epicentral uncertainties, and depth constraints, albeit over a limited area. OBS observations on the EPR have detailed both vertical and horizontal earthquake migration on the scale of hours and captured discrete lava extrusions during an extensional event while also constraining three years of precursory activity as increasing daily seismicity rates (Tan et al., 2016; Tolstoy et al., 2006). In contrast, hydroacoustic observations of the same event recorded only the largest earthquakes, revealed no evidence of earthquake migration, and constrained only the general eruption location (Dziak et al., 2009).

OBS observations on scales of a few to tens of kilometers have also proven particularly useful in constraining hydrothermal processes. Microearthquake depths at slow spreading ridges show that hydrothermal cooling penetrates the mantle (Toomey et al., 1985) and heat extraction can occur along detachment faults (deMartin et al., 2007). Beneath hydrothermal vent fields, enhanced microseismicity at mid-crustal depths has been linked to thermal contraction in the heat uptake zone (Golden et al., 2003; Sohn et al., 2004; Wilcock et al., 2002) and mechanical cracking from crustal magma chamber recharge (Waldhauser & Tolstoy, 2011; Wilcock et al., 2009). Because fracturing within the heat uptake zone thins the thermal boundary layer overlying crustal magma chambers, correlations between seismicity rates and heat flux (Arnoux et al., 2017; Kellogg, 2011) and transient swarms and increased venting temperature (Sohn et al., 1998b) have been identified. Observations of shallow seismicity have also informed the pathway of fluids within a hydrothermal system and their relation to tectonic structures (Tolstoy et al., 2008).

Autonomous OBS deployments are typically limited by battery capacity and clock capability to ~1 year which makes observations of diking events difficult and effectively precludes observations that span a full extensional cycle. Even at fast-spreading segments (~10 cm yr^{-1} spreading rate), extensional events are only expected every 10 years when a dike width of 1 meter is assumed (Liu & Buck, 2020; Qin & Buck, 2008). However, in the last decade, two cabled observatories have been installed on the Juan de Fuca ridge, an intermediate-rate spreading center (Heesemann et al., 2014; Smith et al., 2018). The 25-year design lifetime of these observatories (Barnes et al., 2008) now permits seismic observations on a timescale comparable to an extensional cycle. Real-time monitoring of seafloor activity (Wilcock et al., 2016) and extended OBS deployments are now a reality.

In this study, we take advantage of these new cabled capabilities and analyze seismic data from the Ocean Networks Canada NEPTUNE OBS network to obtain four years of earthquake locations for the Endeavour segment of the Juan de Fuca ridge. We combine these new observations with improved locations of earthquakes from past OBS experiments to present an earthquake catalog that spans two decades. We use this long-term catalog to investigate the interaction of volcanic, tectonic, and hydrothermal processes on the Endeavour segment before, during, and after an extensional sequence.

2.2 Endeavour segment Background

The 90-km long Endeavour segment is an intermediate-rate spreading ridge (52 mm yr^{-1} full spreading rate; DeMets et al., 2010) near the northern end of the Juan de Fuca Ridge (Figure 1). The segment sits precariously between two propagating ridges which form two left-stepping overlapping spreading centers (OSCs) at its northern and southern ends, the West Valley OSC and Cobb OSC, respectively (Figure 1a). The Endeavour is one of the best-studied ridge

segments on the global network, well-known for supporting a long-lived and particularly vigorous hydrothermal venting system (Kelley et al., 2012). The Endeavour vent fields are unique in their uniform spacing, with five major vent fields spaced 2-3 km apart on the central 15 km of the segment with additional diffuse venting sites.

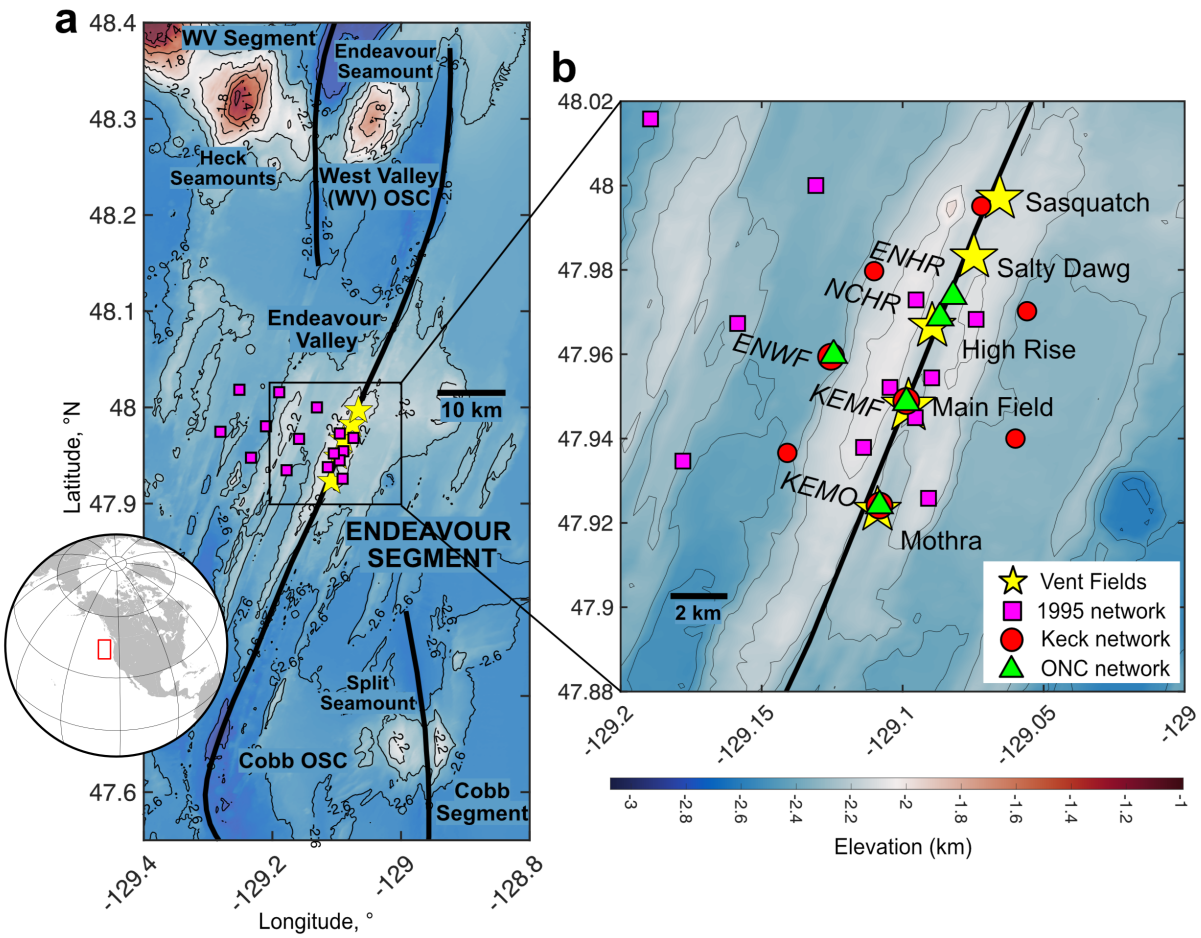

Figure 1. Map of **(a)** Endeavour Segment with global inset and **(b)** central vent field region, with bathymetry shown by color scale and contours at 200 m intervals in (a) and 100 m intervals in (b). Locations of stations in the 1995 and Keck network are shown with magenta squares and red circles, respectively. ONC network stations are shown with green triangles and annotated with the station name in italicized text in (b). The names of the five main vent fields, shown with yellow stars, are annotated with regular text in (b). Plate boundaries are overlain with black lines. The Cobb segment is alternatively referred to as the Northern Symmetric segment. The colormaps used in this figure and the remainder of this paper come from the cmocean package of Thyng et al. (2016).

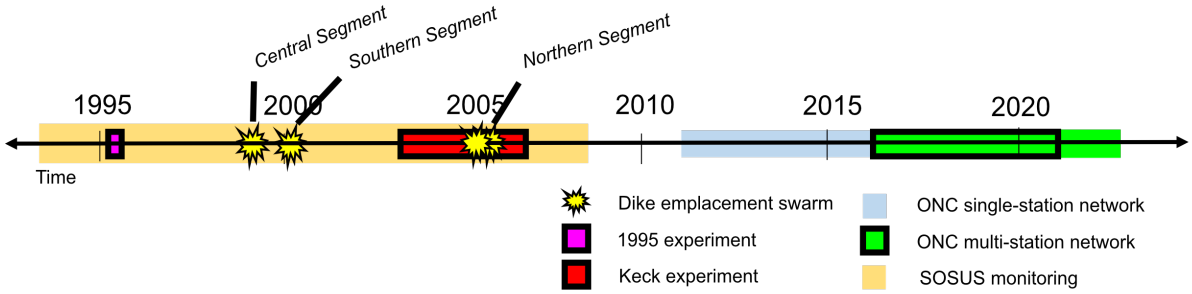

Figure 2. Timeline of seismic monitoring of the Endeavour segment and the 1999-2005 extensional sequence. Periods of data availability are colored by network and those analyzed in this study are outlined in black. Times of earthquake swarms associated with diking events are denoted by yellow stars and annotated to indicate which portion of the segment underwent extension.

The high-temperature vents are supported by a mid-crustal axial magma lens (AML) (Carbotte et al., 2021; Van Ark et al., 2007), with ongoing replenishment maintaining a thin conductive boundary layer atop the AML (Wilcock et al., 2009). Low-velocity anomalies, which suggest higher permeability due to cracking, underlie the most powerful black smoker fields (Arnoux et al., 2017): the Main Endeavour and High Rise fields (Figure 1b) (Delaney et al., 1992). These high-temperature vents are surprisingly long-lived, with the Main Endeavour field dating to at least 2300 years (Jamieson et al., 2013), and display a consistent record of vigorous activity throughout their lifetime (Jamieson et al., 2014). The longevity of the vents is made possible in part by a paradoxical low level of extrusive volcanism over the past ~4000 years, which has prevented the vents from being paved over (Clague et al., 2014, 2020).

Melt distribution at the Endeavour segment is complex, varying on- and off-axis and with depth. At crustal depths, melt is focused along the ridge axis, with a well-imaged AML 2.1-3.3 km below the seafloor at the segment's center (Carbotte et al., 2021; Van Ark et al., 2007). The Endeavour AML is segmented, as is the axis of the central portion of the segment itself (Le Saout et al., 2019), but underlies all five major vent fields. The AML runs in total ~20 km along-

axis at varying depth (Carbotte et al., 2008; Van Ark et al., 2007) with additional sub-AML mid-crustal stacked sills beneath the major vent fields (Carbotte et al., 2021). At mantle depths, the distribution of melt is much broader and traces the strike between the ridge propagator tips, such that melt pools within the OSCs and in a ~10-km-wide swath striking north-south underneath the Endeavour segment (Arnoux et al., 2019). This skew between the mantle and crustal magmatic distributions appears to be correlated with hydrothermal venting: observations from both the EPR and the Endeavour segment show that locations of the most vigorous black-smokers coincide with where mantle and crustal melt distributions are vertically aligned (Arnoux et al., 2019; Toomey et al., 2007).

The most recent segment-scale extensional event on the Endeavour segment occurred as a series of non-eruptive dike emplacements during 1999-2005 (Figure 2). The first event, observed as a microearthquake swarm in June 1999 by the SOSUS regional hydroacoustic array (Dziak et al., 2011), began in the central portion of the segment (~48 °N) and migrated steadily southward to ~47.7 °N (Bohnenstiehl et al., 2004). Epicentral migration and duration, volumetric strain observations from nearby borehole pressure sensors (Davis et al., 2001), and transient increases in magmatic gases within the vent fields (Lilley et al., 2003; Seewald et al., 2003; Seyfried Jr et al., 2003) all suggest dike emplacement originating from the AML (Carbotte et al., 2021) and propagating to the south (Bohnenstiehl et al., 2004). A subsequent notable swarm observed in January 2000, near the southernmost extent of the 1999 migratory sequence at ~47.7 °N, was interpreted by Bohnenstiehl et al. (2004) as a statically triggered response to extension associated with the 1999 dike.

Heightened rates of seismicity continued until a final dike emplacement sequence began in January 2005. The sequence was observed by the Keck OBS network, a compact 8-station

network surrounding the vent fields (Figure 1b), allowing for the detection of much smaller earthquakes and higher-resolution locations over three years. The 2005 sequence began in the northern WV OSC region (Figure 1a) and consisted of a pair of north-south migrating earthquake swarms in January and February which were inferred to followed roughly the same path (Hooft et al., 2010; Weekly et al., 2013). The swarms have been interpreted as an intrusion of magma on the northern ridge, with both the January and February 2005 events also involving activity on the opposing limb of the WV OSC. Despite the 5-year delay between the 2000 and 2005 events, they are thought to be connected, with static triggering, viscoelastic rebound, and possibly the slow diffusion of pressure perturbations between magma bodies accounting for the delay between swarms (Weekly et al., 2013).

No evidence of extrusive magmatism has been associated with the 1999-2005 sequence, and it is thus interpreted as a 6-year segment-scale intrusive magmatic event (Weekly et al., 2013; Hooft et al., 2010). After the 2005 swarms, the background rate of microseismicity dropped in most parts of the segment to approximately ~15% of the previous value (Weekly et al., 2013). This drop as well as the migratory paths of the 1999-2005 diking sequences are taken as evidence of the release of extensional stress along the entire ridge segment, marking the end of an extensional cycle.

2.3 Data

The earthquake catalog presented in this study is comprised of observations from three separate OBS deployments (Figures 1 and 2): the 1995 microearthquake experiment (Wilcock et al., 2002), the 2003-2006 Keck experiment (Weekly et al., 2013), and the Ocean Networks Canada (ONC) NEPTUNE multi-station network. Travel-time picks, earthquake locations, and seismic moments are obtained from previous analyses of the 1995 and 2003-2006 experiments

(Weekly et al., 2013; Wilcock et al., 2002). The 1995 dataset provides a snapshot of seismicity prior to the 1999-2005 extensional sequence, and the Keck dataset captures activity at the end of the sequence and immediately afterwards. We expand the earthquake catalog into a multi-decadal dataset with new earthquake locations and magnitudes calculated using data from the ONC Endeavour network from July 1 2016 to February 28 2021. Segment-scale 3-dimensional (3-D) P- and S-wave seismic velocity models derived from a tomography experiment (Arnoux et al., 2019; Kim et al., 2019) are used to locate all earthquakes.

2.3.1 1995 Microearthquake Experiment

The first dataset in our catalog comes from a 55-day microearthquake experiment in 1995 (Wilcock et al., 2002) (see Text S1 for details). Fifteen three-channel OBS were deployed (Figure 1a). A total of 1750 earthquakes were originally located using Hypoinverse (Klein, 2002) with a 1-D velocity model based on a refraction experiment (Cudrak & Clowes, 1993). The experiment design, including the triggering settings, was configured to record and analyze earthquakes within and near the network: nearly all earthquakes were located within 10 km of the network. The picking error for the 437 best recorded earthquakes (≥ 8 picks with epicenters within 3 km of the network) was found to be 0.028 s following the expression of Sohn et al. (1998a):

$$\sigma^2 = \frac{\sum_{i=1}^{n}\sum_{j=1}^{m_i} w_{i,j}^2 \Delta \mathrm{t}_{i,j}^2}{\sum_{i=1}^{n}(m_i - p)}, \quad (1)$$

where w is the weight of each individual arrival time pick, Δt the travel time residual, p the number of free parameters (4 for free-depth, 3 for fixed-depth), n the number of earthquakes, m

the number of arrival time picks used in the location of the event, and *i* and *j* the indices of the earthquake and arrival times, respectively. Earthquake moments were calculated using the displacement spectra following Toomey et al. (1988) and Tréhu & Solomon (1983).

2.3.2 2003-2006 Keck Experiment

The second dataset in the catalog comes from the 8-OBS Keck network that recorded data from August 2003 to October 2006 (Weekly et al., 2013) (see Text S1 for details). Seven short-period three component seismometers (Stakes et al., 1998) and one broadband three component seismometer (Romanowicz et al., 2006; Stakes et al., 2002) were deployed in a 10 km aperture network in the central vent field region (Figure 1b).

There are two catalogs with manual picks available for the Keck network deployment (Hooft et al., 2010; Wilcock et al., 2009), but neither cover the entire duration of the experiment. Therefore, we primarily use the automatically picked catalog of Weekly et al. (2013) which extends over the entire deployment. We use the manually picked catalog of Wilcock et al. (2009), which spans only the first year of the Keck deployment and focuses on the vent field region, solely for earthquake depth comparisons to inform our interpretations.

The catalog of Weekly et al. (2013) contains 36,564 earthquakes located using Hypoinverse and a 1-D layered velocity model similar to the 1995 experiment. Following Equation 1, the overall picking error was found to be 0.095 s. Earthquake moments were calculated with the same approach used for the 1995 experiment.

2.3.3 Ocean Networks Canada NEPTUNE Network

The Ocean Networks Canada (ONC) NEPTUNE cabled observatory became operational at the Endeavour Segment in early 2011. The observatory has provided continuous real-time data

for over a decade, with an expected design lifetime of 25 years (Barnes et al., 2008). The ONC Endeavour seismic network covers the central vent field region (Figure 1b) and has undergone substantial instrument changes throughout its operation (summarized in Figure 3 and Table S1). There are additional small data gaps due to cable observatory outages and data diversion by the US and Canadian navies.

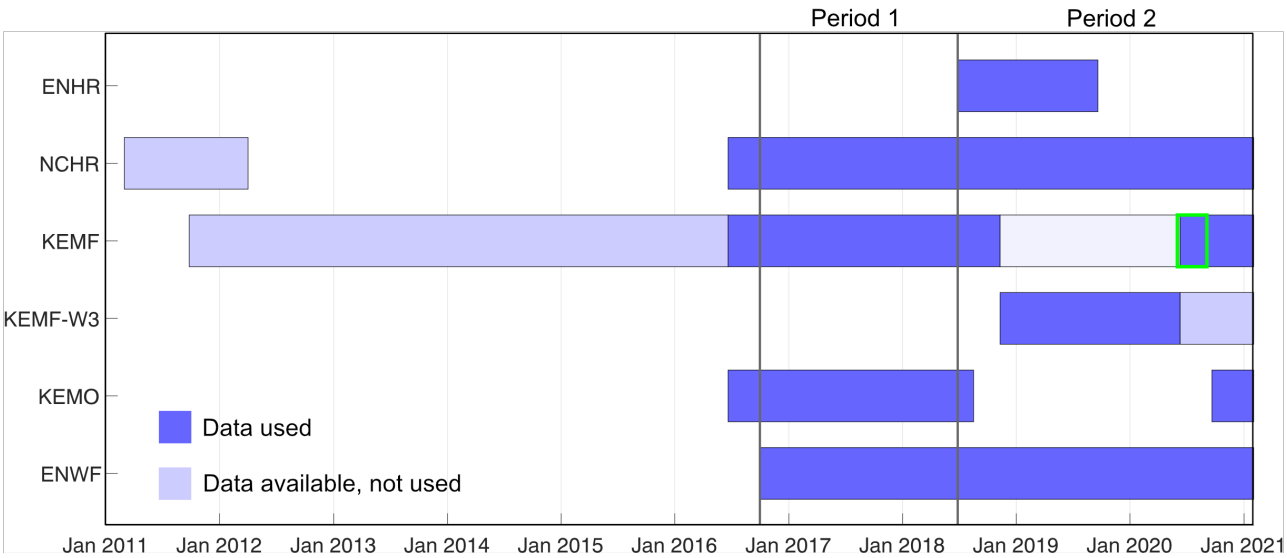

Figure 3. Summary of instrument data availability and use for the ONC network up to the end of the study period. The time periods for which data are available for each of the 6 stations are shown using blue bars, with darker shading given to the data used in our catalog. The sensor type and deployment style for each station code is listed in Table S1. The endpoints of the two network periods, designated as Period 1 when four stations were reliably available and Period 2, where the network underwent frequent changes, are shown with black vertical lines in the bar chart. All instruments are seismometers apart from KEMF-W3, which is an accelerometer. The green rectangle on the KEMF bar represents the period from June-September 2020 when another broadband seismometer, location code B1, was briefly operational at the KEMF site. We do not use this instrument in our catalog because it is duplicative of the short-period seismometer at the same site.

We divide the data into two time periods based on network operation. In June 2016 the network was expanded from a single-station (KEMF) to a four-station network with a station spacing of 2 km (Figures 1a and 3; see instrument details in Table S1). The first period

encompasses the time when the four-station network was continuously operating, September 2016 to June 2018.

Period 2, June 2018 to February 2021, contains much more station variability, at times with only three stations in operation (Figure 3). An autonomous broadband seismometer was deployed from June 2018 to September 2019 at a location (ENHR) slightly north of the NCHR site. The short-period seismometer at the Mothra site (KEMO) failed in December 2018 and was replaced with a broadband instrument in September 2020. Software-associated noise on the KEMF short period seismometer observed from November 2018 to June 2020 necessitates the temporary use of the quietest and most vertically oriented of the three accelerometers in operation at the KEMF site (KEMF-W3) to maintain the minimum three stations needed for location.

2.3.4 Velocity Models

The 3-D velocity models used in earthquake relocation were derived from the 2009 Endeavour tomography (ETOMO) seismic experiment (Arnoux et al., 2017, 2019; Kim et al., 2019; Soule et al., 2016; VanderBeek et al., 2016; Weekly et al., 2014). Using a nested grid geometry centered on the ridge axis, 68 OBS and ~5,500 air gun shots from the R/V *Marcus G. Langseth* provided data for detailed tomographic inversions on a 90-km-by-50-km portion of the ridge (Figure 4).

Two separate velocity models from the ETOMO experiment are used in this study. The P-wave velocity model (Arnoux et al., 2019) was developed from an inversion of *Pg*, *PmP* and *Pn* travel times, yielding both isotropic slowness and anisotropy values up to 11 km depth. The S-wave model, the first segment-scale 3-D shear velocity model produced for a mid-ocean ridge, comes from a joint P- and S-wave inversion (Kim et al., 2019). Both models fit the *Pg* arrivals in

the tomography dataset to 0.011 s, and the Kim et al. (2019) model fits *Sg* arrivals to 0.038 s. Preference was given to the P-wave model of Arnoux et al. (2019) over that of Kim et al. (2019) since it constrains velocities over a broader region with higher resolution. The chosen P- and S-wave models both have a node spacing of 0.2 km and are similar enough that their concurrent use maintains realistic V_P/V_S ratios (see Text S2).

To ensure spatial coverage at segment ends, we extrapolated the velocity models to a 120 x 90 x 10 km^3 volume using a weighted algorithm that transitions smoothly to a depth-averaged 1-D profile at the grid edges (see Text S3). Horizontal sections of the 3-D velocity models at 3 km depth can be seen in Figure 4. The velocity structure of the central segment is highly heterogenous, with mid-crustal velocities ~10% lower on the central Endeavour axis than 10 km off-axis, and velocities in the center of the OSCs up to ~15% lower than the segment center. Travel time grids were derived from the slowness models by solving the forward problem for each station using the same shortest path algorithm used for the tomographic studies (Moser, 1991).

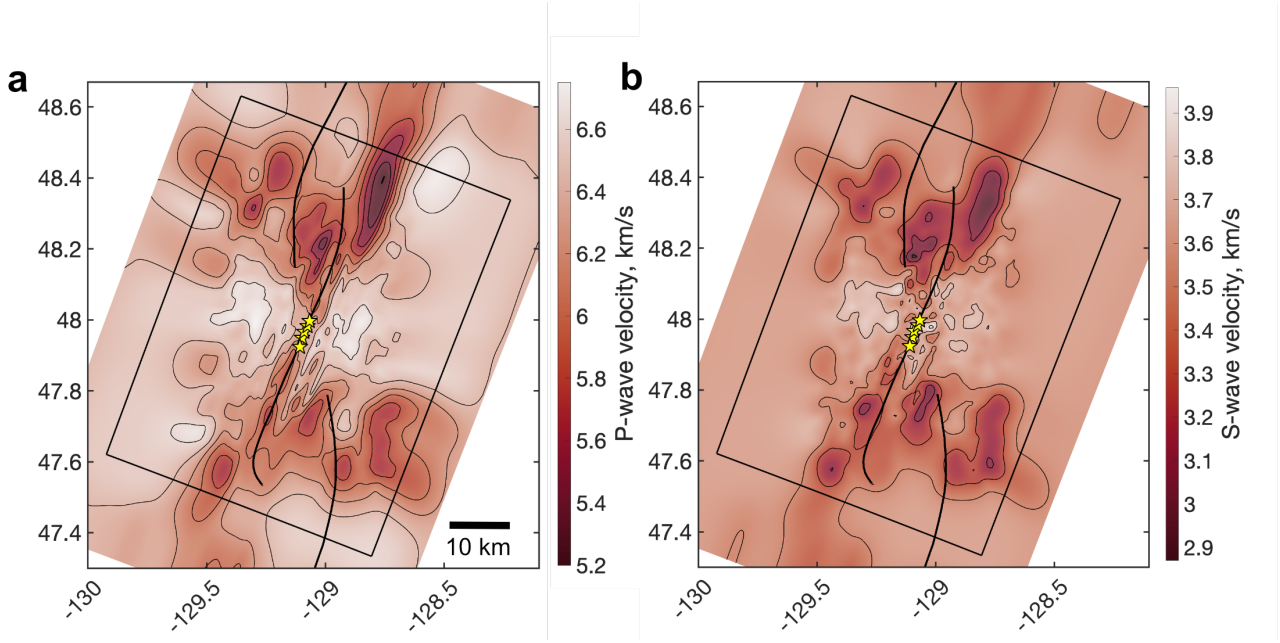

Figure 4. Map-view sections at 3 km depth, the depth at which earthquakes outside of networks are fixed, of the 3-D **(a)** P-wave (Arnoux et al., 2019) and **(b)** S-wave (Kim et al., 2019) velocity models used in earthquake relocation, shaded by seismic velocity in km s^{-1} with contours at 0.2 km s^{-1} intervals. The models have been extrapolated beyond their edges, marked with a black box, and have a node spacing of 0.2 km in all directions. The main tectonic boundaries are shown with bolded black lines and locations of the five main vent fields are shown as yellow stars.

2.4 Methods

2.4.1 ONC Earthquake Catalog

Time series data from the ONC cabled network is processed for the multi-station period of 2016-2021 using a suite of algorithms developed in MATLAB originally for use on Axial Seamount (Wilcock et al., 2016) and adapted for use on the Endeavour Segment (see Text S4 for details). Events are identified using a short-term long-term RMS triggering algorithm, P- and S-wave arrivals are identified using an iterative approach, and picks are refined with kurtosis (Baillard et al., 2014). Pick weights (the reciprocal of relative uncertainties) are assigned based on signal to noise and S picks are downweighted by 0.5. Events with a minimum of four phase arrivals are located using Hypoinverse (Klein, 2002) as in the earlier catalogs.

2.4.2 Earthquake Relocation with NonLinLoc

The NonLinLoc software (Lomax et al., 2000, 2009) is used to locate earthquakes using P- and S-wave arrival times from the 1995, Keck and ONC networks. The genetic grid search algorithm that NonLinLoc employs, OctTree, allows us to efficiently utilize the fine-scale resolution of our travel-time grids. OctTree approximates a global grid search by automating a nested grid search, starting with a coarse grid and iteratively splitting the grid cells with highest probability until converging on a predetermined final grid spacing (see chosen parameters in Table S2). A posterior probability density function for the best fit location is then calculated

using the method of Tarantola & Valette (1982). NonLinLoc estimates 1-σ horizontal location uncertainties by calculating a confidence ellipsoid from the covariance matrix of the probability density function. Scatter samples of the posterior probability density cloud are saved to use in the visualization of 3-D location uncertainties.

Since NonLinLoc performs a full grid search, earthquake depth cannot be held constant. Therefore, for fixed depth locations, we slice the travel time grid to contain only a 10 m horizontal band centered on the desired depth (see Table S2). For events with free depths, we calculate 1-σ vertical location uncertainties by projecting the confidence ellipsoid onto the vertical axis.

To solve the inverse problem, NonLinLoc defines pick weights as a combination of Gaussian arrival time pick uncertainties and travel-time grid uncertainties. However, we follow the approach used by Hypoinverse and set the travel-time grid uncertainties to zero, effectively wrapping all uncertainties into the picking error. We take pick uncertainties to be a baseline uncertainty, that of a fully weighted arrival, divided by the output pick weight from the initial Hypoinverse locations. Picks with lower Hypoinverse weights are therefore assigned greater uncertainties. For the relocations, we use the baseline uncertainty value from the original locations: 0.03 s for the 1995 catalog (Wilcock et al., 2002) and 0.05 s for the Keck catalog (Weekly et al., 2013). For the ONC catalog, we derive the uncertainty estimate from the data itself by using the picking error of the earthquakes with at least eight arrivals (Equation 1).

Due to the relatively small footprint of the networks, our catalog includes both free- and fixed-depth earthquake relocations. We consider earthquake depth to be poorly constrained when the epicenter obtained with a free depth is further than a fixed distance (equal to the fixed depth) from all stations with both a P- and S-wave pick. For both the 1995 and Keck network datasets,

all earthquakes with poorly constrained depths are fixed to a depth of 3 km (Weekly et al., 2013; Wilcock et al., 2002) since off-axis earthquakes are located at mid-crustal depths and all fixed-depth earthquakes for these datasets are located outside of the vent field region. However, for the ONC network dataset, the smaller footprint of the network leads to a considerable number of earthquakes with poorly constrained depths within the vent field region. In this region earthquakes are shallower because they are mostly concentrated above the AML at ~2 km depth (Wilcock et al., 2009). Therefore, we fix depths for ONC earthquakes to 2 km when they are within 2 km of one of the vent fields, and to 3 km elsewhere.

2.4.3 Earthquake Moment Calculation

We follow earlier studies of MOR earthquakes (Toomey et al., 1988; Tréhu & Solomon, 1983; Weekly et al., 2013) to calculate seismic moments for the ONC catalog, but refine the values of several corrective physical parameters (see Text S5 for details of our approach). Each earthquake has multiple moment estimates, one for each recorded arrival. Since site effects can lead to systematic differences in amplitudes, taking the moment of an earthquake to simply be an average of all arrivals can create offsets in moment calculations when earthquakes are recorded on different sets of stations. We account for these effects by applying corrections to each arrival based on its recording station and phase (see Text S6), which results in individual moment estimates being multiplied by factors ranging from 0.6 to 1.6 (Table S4). After site effect corrections, the final moment of an earthquake is taken as the median of all corrected P- and S-moments for that event.

Moment magnitudes (M_W) are calculated using the relation of Hanks & Kanamori (1979) (see Text S5). The distribution of earthquake magnitudes can be used to calculate the magnitude at which the catalog is complete (M_c) for a given spatial region and time period, and thus obtain

the b-value of the distribution. To calculate the b-value, we follow the method of Wiemer & Wyss (2002), which fits the magnitude distribution with an exponential function for a range of M_c. The M_c and its corresponding b-value are chosen as the minimum M_c at which the distribution matches the exponential with residuals below 15%. The uncertainty of the b-value is then calculated following Shi & Bolt (1982).

2.5 Results

The complete catalog of earthquakes consists of 1750 earthquakes relocated from the 1995 microearthquake experiment, 36,564 earthquakes relocated from the Keck experiment, and 50,428 earthquakes newly located with the ONC network. We present the results from each of these experiments chronologically; however, since the 1995 and Keck catalogs have already been analyzed, we primarily present our relocations of those catalogs in relation to our new results from the ONC network. We describe earthquake distributions in the framework of five main regions of activity as revealed by the ONC network (Figure 5a,f). The vent field (VF) region describes earthquakes occurring roughly on-axis in the vicinity of the five major venting sites, extending 2 km to either side of the main spreading axis and 2 km beyond the northern and southernmost major vent fields. The East Flank (EF) region is defined as an 8-km-wide box directly east of the VF region with the same axis-parallel extent. The southwest Endeavour Valley (SWEV) region is an 9 km x 9 km area directly west and 6 km north of the VF region. The West Valley (WV) and Cobb OSC regions refer to the areas of the segment ends where most seismicity occurs (Figure 5a).

2.5.1 1995 Experiment

Relocations from the 1995 microearthquake experiment yield mostly small epicentral changes with a median of 0.5 km and only nine events moving > 10 km (Wilcock et al., 2002)

(Figure S7). The picking error for the best-fit earthquakes, 0.028 s, matches that reported by Wilcock et al. (2002). The median maximum horizontal errors for earthquakes located within and outside of the network are 0.45 km and 0.55 km, respectively. Within the VF region, earthquake epicentral patterns are similar to 2016-2021, with most earthquakes clustering between the Main and Salty Dawg fields (Figure 5f). The median depth of earthquakes within the vent fields, 1.9 km, is markedly deeper than the overall median of 0.99 km in 2016-2021 (Figure 6).

To enable comparison of seismicity rates between catalogs, in sections 5.1 and 5.2 we only present moment release rates summed from earthquakes larger than a common magnitude of completeness within each region (see Table S6) and subdivide the WV and Cobb OSC regions into sub-regions that separate the two limbs (dotted lines in Figure 5a).

The majority of the moment release in the VF region (90% when considering only earthquakes > M_c) is accomplished by a 4-day swarm sequence in late June 1995 that may have been associated with the emplacement of a dikelet (Crone et al., 2010; Wilcock et al., 2002). Including the swarm, the adjusted moment release rate in the VF region in 1995 is 1.8 times that observed in late 2020. However, removal of the swarm contribution shows a much lower background seismicity rate of 1.7 times that seen in 2016 and only 0.3 times that of late 2020 (Figure 7a, Table 1).

Within the EF region, earthquakes are primarily located in a ridge-normal pattern adjacent to Main and High Rise fields (Figure 5f), notably in the same pattern observed in 2016-2021 (Figure 5j). The moment release rate in the EF region (Figure 7b), 6 x 10^{20} dyne-cm yr^{-1}, is over twice that observed in 2016-2021 (Table 1). In the SWEV region, there are several small earthquake clusters but they do not encompass the full areal extent of seismicity seen in 2016-

2021 (Figure 5j). The adjusted rate of moment release in the SWEV, 1.4 x 10^{20} dyne-cm yr^{-1}, is only 0.3 times the rate seen in 2016-2021 (Table 1). However, since the moment release in the SWEV in 2016-2021 is largely accomplished by swarms, it is possible that the 1995 observed rate is lower and the spatial extent more limited due to the short observation period.

The 1995 experiment detected only a few earthquakes in the WV OSC region and none in the Cobb OSC. This is likely due to the earthquake triggering algorithm. However, the 1995 network detected more earthquakes on the southern Endeavour segment (Figure 5a) within 20-30 km of the segment center than in 2016-2021 (Figure 5e). Very few of these earthquakes are larger than the Keck catalog M_c so their contribution to moment release is not listed in Table 1. However, if we instead correct for the larger M_c in this region for the 2016-2021 catalog (Table 2), we find that in 1995, the moment release rate on the southern Endeavour ridge is 1.5 times larger than in 2016-2021 despite the network having little sensitivity to the end of the segment. The same approach applied to the northern Endeavour segment shows that moment release rates are roughly the same in 1995 and 2016-2021.

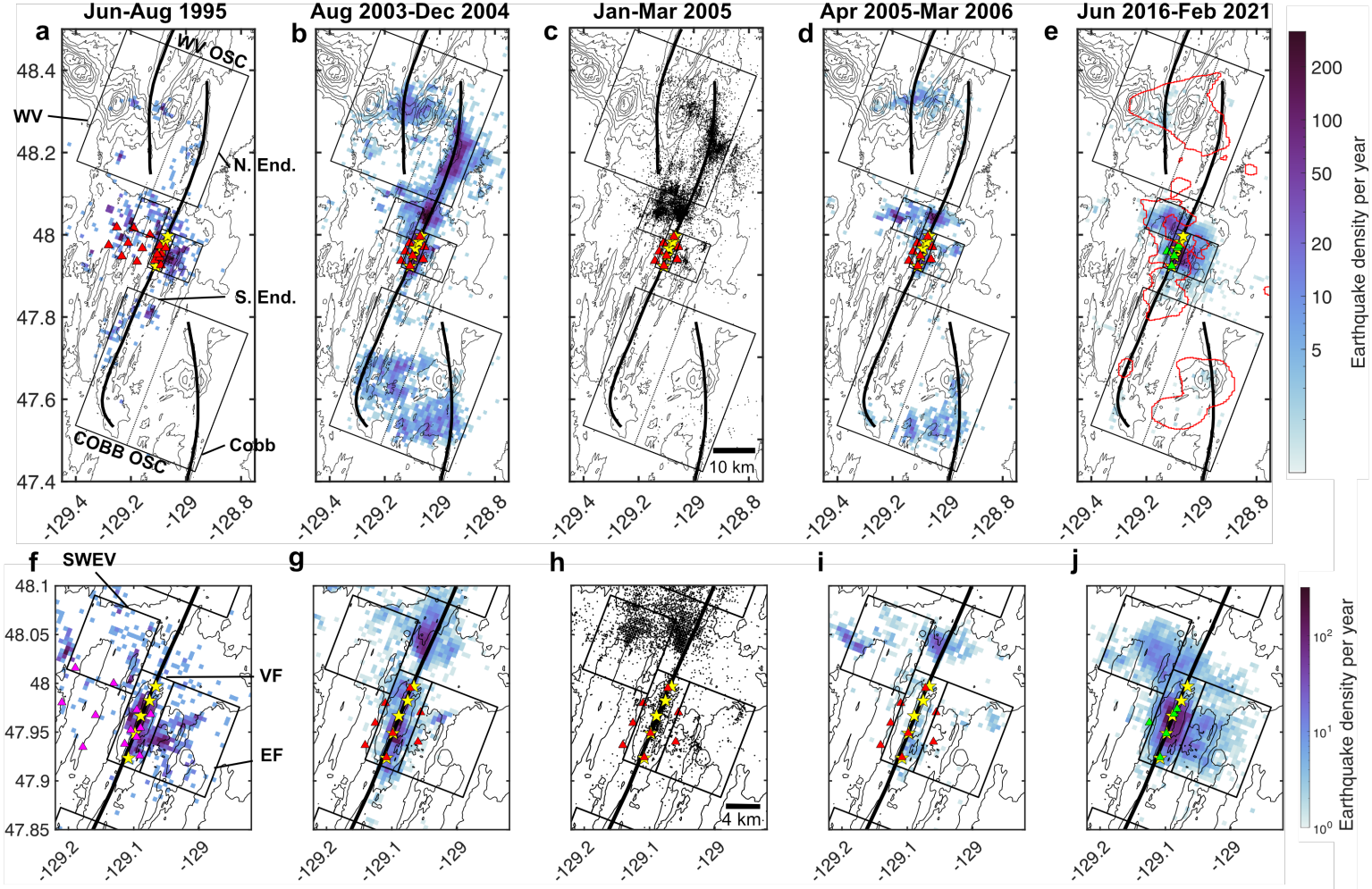
Jun-Aug 1995
Aug 2003-Dec 2004
Jan-Mar 2005
Apr 2005-Mar 2006
Jun 2016-Feb 2021
a
b
c
d
e
WV OSC
WV
N. End.
S. End.
COBB OSC
Cobb
10 km
200
100
50
20
10
5
Earthquake density per year
f
g
h
i
j
SWEV
VF
EF
4 km
10^2
10^1
10^0
Earthquake density per year

1

Figure 5. Seismicity patterns for different time periods on two different spatial scales, scaled to represent 1 year of seismicity and corrected for M_c as in Table 1, shown as spatial density both on the segment scale (top row, **a,b,d,e**) with bin sizes of 1 km x 1 km and on the vent scale (bottom row, **f,g,i,j**) with bin sizes of 0.5 x 0.5 km. Time periods shown with earthquake density in log scale are **(a,f)** June-August 1995, **(b,g)** August 2003-December 2004, **(d,i)** April 2005-August 2006, **(e,j)** June 2016-February 2021. The period of January-March 2005, during which two large swarms occurred, is shown in **(c,h)** with earthquakes as a scatter plot instead. Each subplot is overlain with the network for that time period and boxes denoting the main regions of activity described in the text. Symbols follow Figure 1. Red contour in (e) represents 1% mantle melt content at 7.8 km depth from Arnoux et al. (2019). The names of the segment-end regions are given in (a); note that the OSC region boxes are split in order to compare moment release rates between catalogs, with WV for West Valley segment, N End. for North Endeavour segment, Cobb for Cobb segment, and S End. for South Endeavour segment. The names of the central segment regions are given in (f), including Vent Fields (VF), East Flank (EF), and Southwest Endeavour Valley (SWEV). Equivalent maps plotted with moment release can be found as Figure S8 and S9.

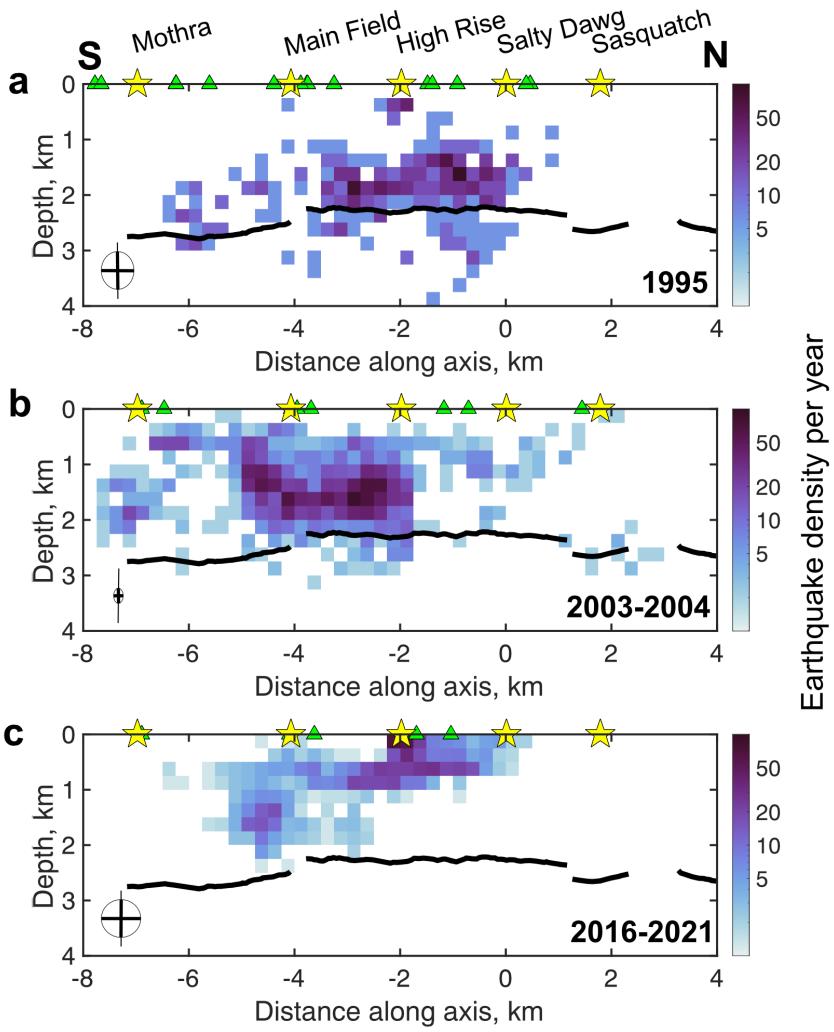

Figure 6. Along-axis cross-sections of earthquake densities for earthquakes with well-constrained depths located within 2 km of the Endeavour segment axis in the vent field region, scaled to represent one year of seismicity. Earthquakes with maximum vertical uncertainties < 0.5 km are shown for **(a)** the 1995 catalog, **(b)** the manually picked 2003-2004 catalog (Wilcock et al., 2009) and **(c)** the 2016-2021 ONC catalog. Cross-sections show spatial density of earthquakes with bin sizes of 0.25 x 0.25 x 4 km^3 with the long axis centered on and perpendicular to the spreading axis. Depth of the AML reflector is shown with a black line (Carbotte et al., 2021). The median horizontal and vertical uncertainties for the earthquakes plotted are shown as ellipses in the bottom left corner of each subfigure, with thin black vertical lines atop the ellipse denoting the maximum vertical uncertainty. Symbols follow Figure 1, with vent field names annotated.

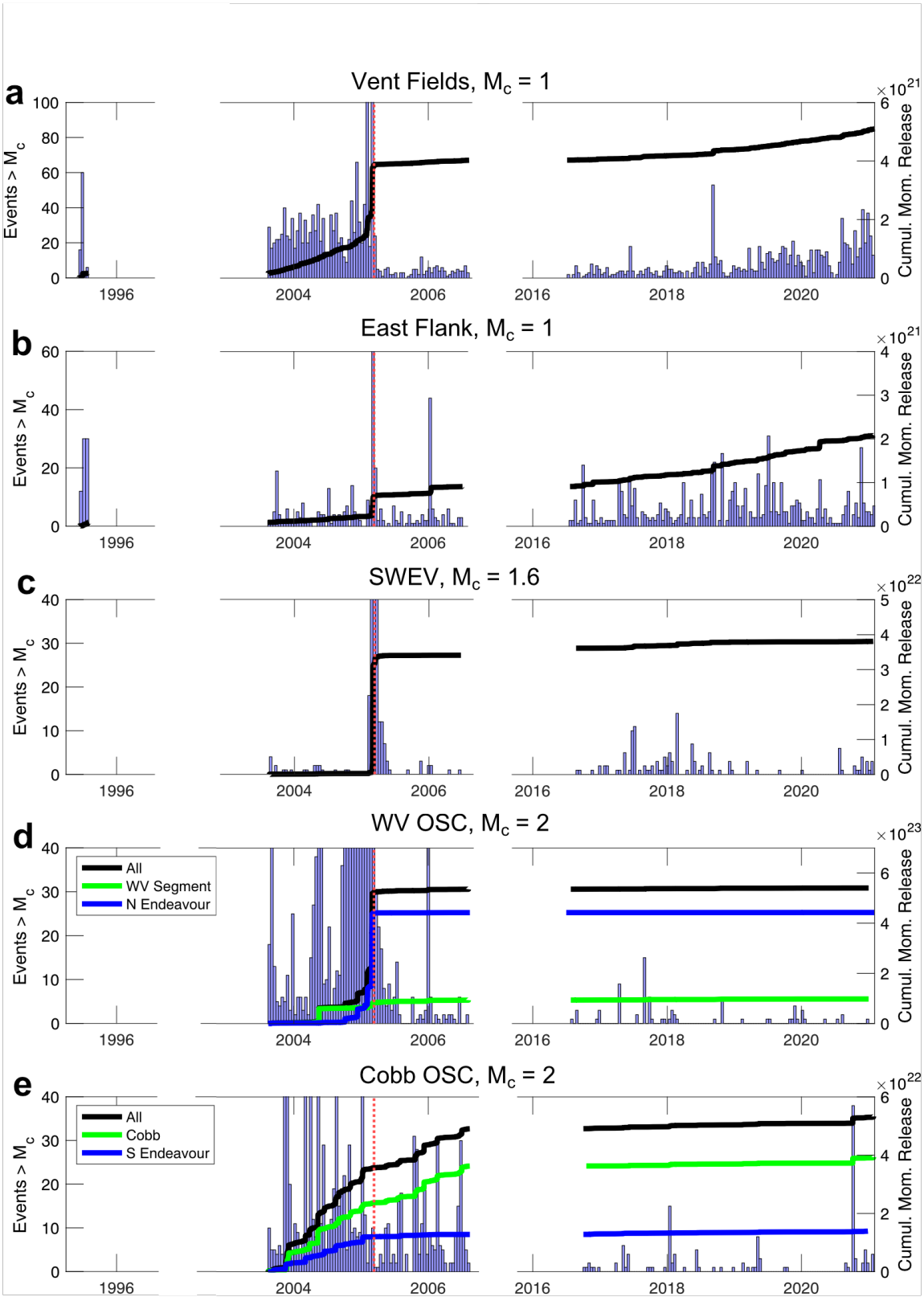
a
Vent Fields, M_c = 1
Events > M_c
Cumul. Mom. Release
$\times 10^{21}$
b
East Flank, M_c = 1
Events > M_c
Cumul. Mom. Release
$\times 10^{21}$
c
SWEV, M_c = 1.6
Events > M_c
Cumul. Mom. Release
$\times 10^{22}$
d
WV OSC, M_c = 2
All
WV Segment
N Endeavour
Events > M_c
Cumul. Mom. Release
$\times 10^{23}$
e
Cobb OSC, M_c = 2
All
Cobb
S Endeavour
Events > M_c
Cumul. Mom. Release
$\times 10^{22}$
1996
2004
2006
2016
2018
2020

Figure 7. Comparison of earthquake counts and cumulative moment release between the 1995 experiment, Keck experiment (2003-2006) and ONC network (2016-2021) datasets, shown for each spatial region defined in Figure 5. Counts for earthquakes with magnitudes > M_c are shown as a blue histogram with a bin size of 14 days, with the M_c taken as the largest M_c of the individual experiments. Total cumulative moment release, also corrected for M_c, is overlain in black. In **(d)** and **(e),** the regions are split (Figure 5a) to show moment release rates for each OSC limb separately. The red vertical dashed line marks one week after the end date of the 1999-2005 spreading sequence, March 5 2005. Note the breaks in time on the x-axis, and the changing y-axis limits between each subplot. The y-axis limits for the histograms clip the 2005 swarms to improve the visibility elsewhere.

Table 1

Regional Moment Release Rates

	VF, $M_c = 1$ (10^{20} dyne-cm/yr)	EF, $M_c = 1$ (10^{20} dyne-cm/yr)	SWEV, $M_c = 1.6$ (10^{20} dyne-cm/yr)	WV segment, $M_c = 2$ (10^{20} dyne-cm/yr)	North Endeavour segment, $M_c = 2$ (10^{20} dyne-cm/yr)	Cobb segment, $M_c = 2$ (10^{20} dyne-cm/yr)	South Endeavour segment, $M_c = 2$ (10^{20} dyne-cm/yr)
1995	9.2[1]	6	1.4	34	N/A (none above M_c)	N/A (none above M_c)	4.3
Pre-swarm 08/13/2003-12/15/2004	8.4	1	1.7	08/13/2003-10/01/2004: 530	08/13/2003-10/01/2004: 53	150	75
				10/10/2004-12/15/2004: 230	10/10/2004-12/15/2004: 360		
Post-swarm 04/01/2005-08/15/2006	1	1.5	0.7[2]	67	6.6	91	5.5
2016-2021	08/2016-09/2018: 1	2.5	4.4	9.4	0.94	6.9	2.5
	09/2018-08/2020: 3						
	08/2020-02/2021: 5						

Note. Each moment release rate given has been corrected for the magnitude of completeness (M_c) common to the region, as specified in each column title (see Table S6). Region boundaries are shown in Figure 5. Some time periods are described with more granularity to properly illustrate trends.

[1]If the contribution from the June 1995 swarm is removed (90% of moment release), the VF background moment release rate is 1.7 x 10^{20} dyne-cm/year.

[2]Moment release for the SWEV region for the two months following the final swarm (04/01/2005-06/01/2005), is higher, at 2.7 x 10^{20} dyne-cm/year.

2.5.2 2003-2006 Keck Experiment

Relocations from the Keck experiment lead to a distinct improvement in the alignment of locations to geologic features at segment ends (Figure 8). Though Weekly et al. (2013) report an earthquake distribution spread from 10 km west of the WV OSC to 10 km east of the northern Endeavour axis (Figure 8a), our relocations are primarily located between the overlapping ridges, on the WV segment between seamounts, and on the northern Endeavour segment (Figure 8b). The relocations in the Cobb OSC also show tighter clustering within the overlapping portion of the OSC. On both segment ends earthquakes are brought ~5 km closer to the network (Figure 8).

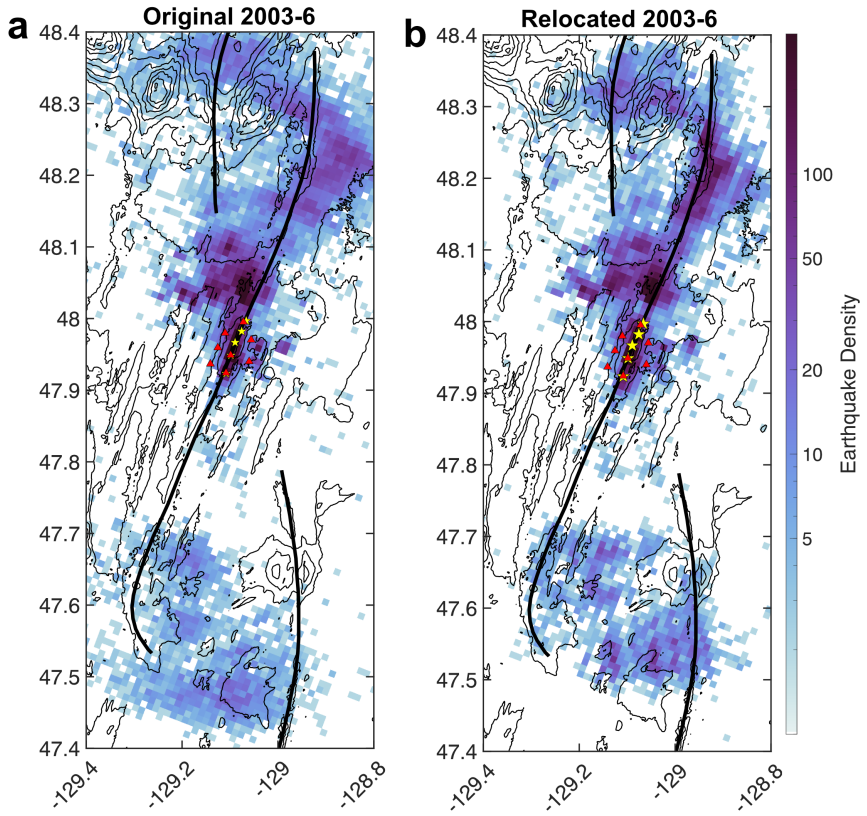

Figure 8. Comparison of locations for the Keck experiment showing (a) the original locations of Weekly et al. (2013) and (b) the relocations made in this study shown as spatial density with bin sizes of 1 km^2. All other symbols follow Figure 1.

Using Equation 1, we find that the picking error for the relocated Keck catalog is 0.068 s, a significant improvement from the 0.095 s picking error in the original catalog (Weekly et al., 2013). The median maximum horizontal uncertainty for the Keck catalog is 1.4 km for events within the network, increasing to 2-3 km for events at the segment ends. We describe seismicity before, during and after the 2005 swarms separately.

2.5.2.1. Pre-swarms, August 2003-December 2004

At the start of observation in 2003, adjusted moment release rates in the VF are some of the highest observed in the catalog, ~8 times larger than those observed in 2016 (Table 1). In contrast, in the other central regions, moment release rates are similar (SWEV region) or 6 times lower (EF region) than seen in 1995 (Table 1). None of the central segment regions display a significantly increasing rate of moment release in the year preceding the 2005 swarms (Figure 7).

The spatial distribution of epicenters in the VF region before the 2005 swarms is similar to 1995 and 2016-2020, with the highest earthquake density coincident with Main and High Rise fields, except there are relatively fewer earthquakes to the north of High Rise field and more earthquakes to the south of Main field (Figures 5 and 6). Earthquake depths obtained by relocating the manually picked catalog of Wilcock et al. (2009) (median vertical uncertainty of 0.14 km) (Figure 6b) have a median value of 1.5 km, slightly shallower than in 1995 but considerably deeper than the overall median value of 0.99 km in 2016-2021. The areal extent of epicenters in the EF and SWEV is greatly diminished compared to other times, with seismicity in the SWEV limited to a small northwestern cluster that is also apparent at other times (Figure 5).

Notably, at the start of observation in 2003, the adjusted moment release rate on the northern Endeavour segment is nearly two orders of magnitude higher than seen in 2016-2021. This rate then increases by nearly another order of magnitude after a swarm occurs on the northern Endeavour segment and SWEV in October 2004 (Weekly et al., 2013) (Table 1, Figure

7d). Moment release rates are also high for the WV segment (Table 1, Figure 7d), but do not increase following the October 2004 swarm. Moment release rates in the Cobb OSC during 2003-2005 are the highest observed in the catalog (Table 1, Figure 7e), with epicenters distributed uniformly between and on the OSC limbs. However, in contrast to the northern Endeavour segment, on-axis earthquakes on the southern segment do not extend from the segment end to the VF region, but instead are only present south of ~47.7°N (Figure 5b).

2.5.2.2. Swarms on the Northern Endeavour, January-March 2005

The first swarm in the 2005 sequence, as reported by Weekly et al. (2013), begins on January 31. The swarm initiates on the northern Endeavour segment at ~48.3°N, where our relocations show the locus of seismicity atop the ridge axis (Figure 9b) as opposed to 5 km west as reported by Weekly et al. (2013) (Figure 9a). We do not resolve a clear southeastern migration across the ridge axis as described by Weekly et al. (2013) but instead see a southern migration from 48.3 to 48.2°N along the Endeavour axis and ~5 km east, with epicenters systematically relocating ~5 km further south (Figure 9, Figure S10a). The most intense seismicity overall travels ~10 km south over 3 days. Our relocations also reveal an additional pattern: a significant number of earthquakes locate in a northeast-southwest distribution across the OSC at ~48.2°N (marked as a dotted line in Figure 9b). After the OSC-crossing seismicity appears, relocations show a southward migration on the WV segment from February 5-12 like Weekly et al. (2013), culminating in a cluster of earthquakes in the SWEV region at 48.1°N.

The second, larger swarm, as reported by Hooft et al. (2010) and Weekly et al. (2013), begins on February 22. As suggested by Hooft et al. (2010) and newly resolved in our relocations, the swarm begins under the Endeavour seamount (Figure 1) at 48.3°N (Figure 9d) in contrast to Weekly et al. (2013) who show the swarm beginning in West Valley (Figure 9c). On February 27, earthquakes extend in a southwest direction across the OSC from the Endeavour

segment at ~48.2°N (Figure 9d) following the same trend seen for the January swarm. However, for this swarm we can clearly discern that they migrate southwest at a speed of ~3.3 km hr^{-1} (Figure S11). The February swarm then continues to propagate south separately along both the Endeavour segment and the WV propagator. Our relocations on the Endeavour segment are consistent with Weekly et al. (2013) who observed 20 km of migration at ~0.25 km hr^{-1}, but we more clearly locate the epicenters on the Endeavour axis. On the WV propagator, migration relocations are also consistent with Weekly et al. (2013) showing a rapid 20-25 km migration at the speed of 2 km hr^{-1} (Figure S10b).

The southward migrations on both the Endeavour segment and the WV segment merge and end at ~48.05°N on March 3, consistent with previous analyses (Hooft et al., 2010; Weekly et al., 2013). On March 1, heightened activity begins in the VF region, ~5 km south of the terminus of the swarm. However, as for previous analyses, we resolve no migration of earthquakes between the northern swarms and the VF region. The Cobb OSC is the only region that does not show a step in cumulative moment release during the 2005 swarms (Figure 7e).

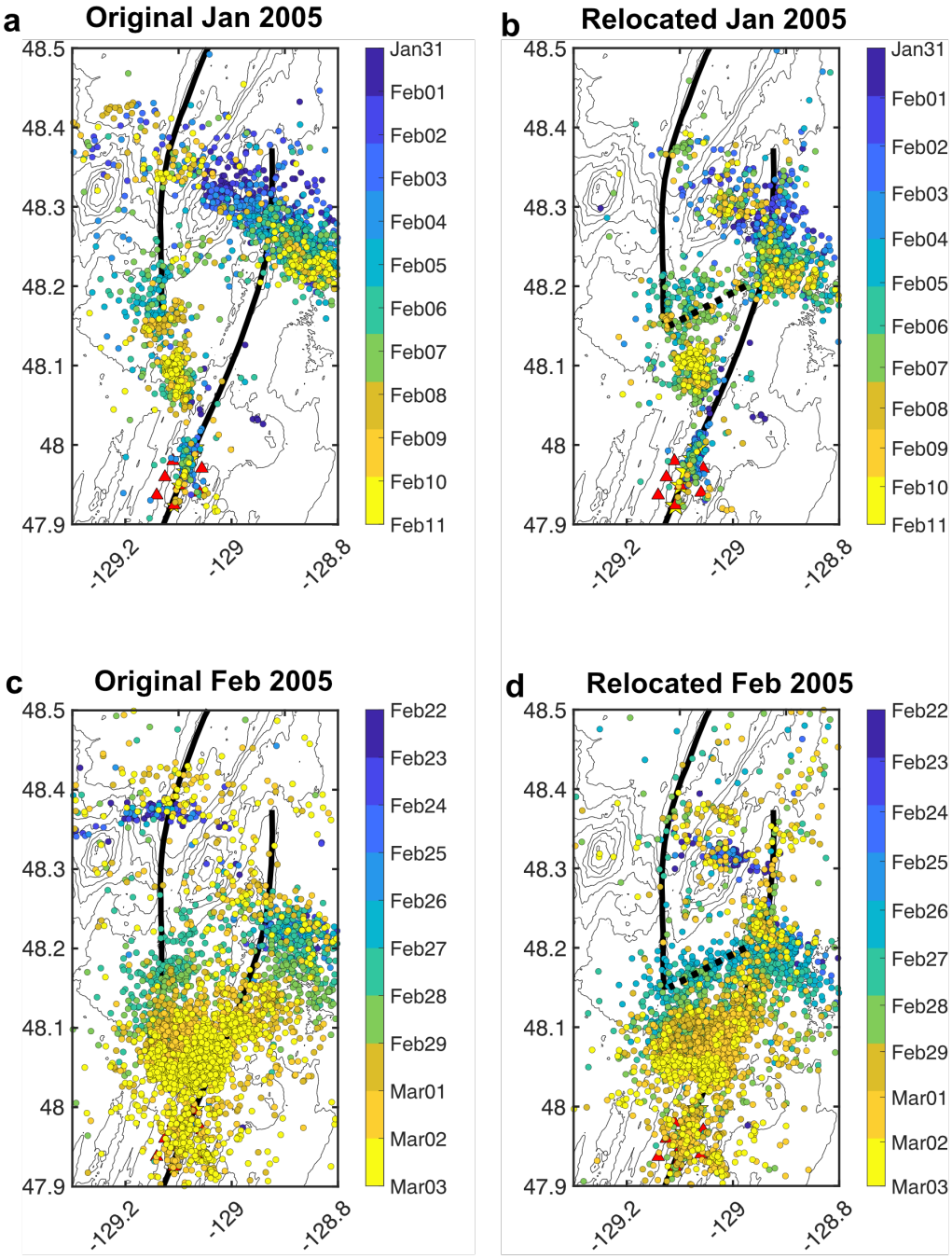

Figure 9. Earthquakes associated with the January 2005 swarm compared between (a) the original locations of Weekly et al. (2013) and (b) the relocations made in this study, shown as scatter plots colored by the day of the year in 2005. The same is shown for the February 2005 swarm with (c) the original locations and (d) the relocations made in this study. The location of the OSC-crossing seismicity observed in both swarms is marked with a thick dashed black line in (b) and (d). All other symbols follow Figure 1.

2.5.2.3. Post-swarms, April 2005-August 2006

As reported by Weekly et al. (2013), following the final 2005 diking sequence, seismicity decreases dramatically (Figures 5d and 7). The moment release rate on the northern Endeavour segment drops two orders of magnitude and the WV segment and VF region moment release rates drop one order of magnitude (Table 1). Following the swarms, almost no earthquakes locate on the northern Endeavour segment and epicenters in the WV segment region are largely confined to the Heck Seamounts (Figure 5d). Both of these patterns persist in 2016-2021 (Figure 5e).

Activity rates in the SWEV remain similar to pre-swarm levels for the two months immediately following the swarms. The distribution of epicenters within the SWEV is markedly different than seen later in 2016-2021 (Figure 5i, 5j), with a paucity of epicenters in the center of the region. Moment release rates in the SWEV decrease by a factor of 2.4 relative to pre-swarm levels beginning in June 2005. An additional on-axis cluster of epicenters due east of the defined SWEV region, also observed in 2003-2005 but not at other times, remains active following the swarms (Figure 5i).

The Cobb OSC is not associated with the 2005 earthquake swarm sequence, but the southern Endeavour segment appears to respond to the event, with an order of magnitude decrease in moment release rate (Table 1) and the northernmost extent of seismicity moving south from ~47.7° to 47.6°N (Figures 5b,d). In contrast, seismicity is largely unaffected on the Cobb segment and the EF region.

Though activity decreased overall following the 2005 swarms, in many regions the adjusted moment release rate is the same (VF) or even lower (WV segment, northern Endeavour segment, Cobb segment, southern Endeavour segment) 11 years later in 2016 (Table 1). The only regions that show increased activity between 2006 and 2016 are the off-axis central regions,

where moment release increases by a factor of 1.7 and 6.3 in the EF and SWEV regions, respectively.

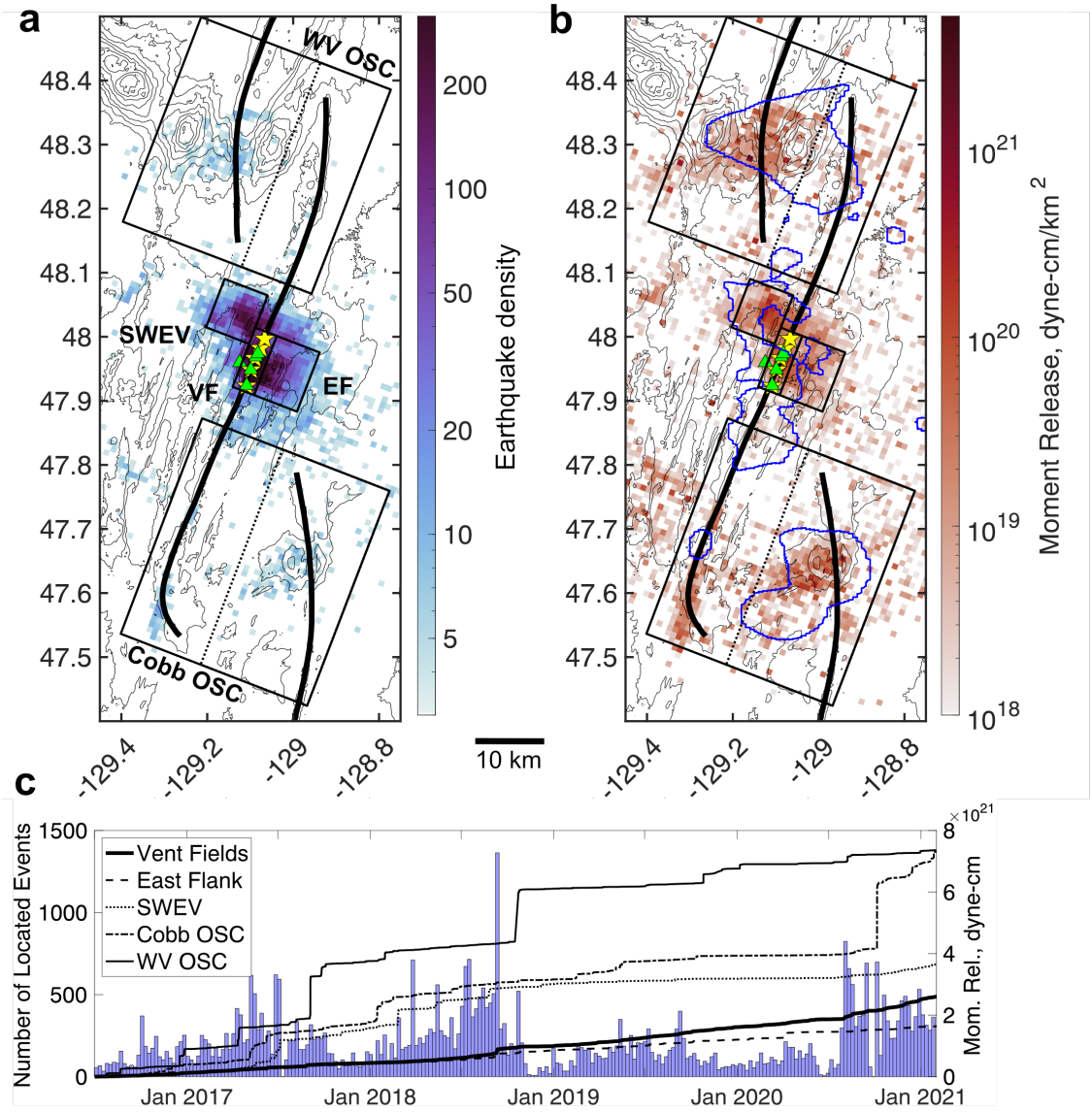

Figure 10. Summary of the spatial and temporal distribution of the ONC catalog. **(a)** Map showing spatial density of earthquake counts in 1 km^2 bins, shaded on a logarithmic scale. Black boxes delineate the five main regions of activity as in Figure 5. Dotted lines delineate how the WV and Cobb OSC regions are split when comparing moment release rates between catalogs. All other symbols follow Figure 1. **(b)** As for (a) but showing the cumulative moment release density, totaled for each bin. Blue contour represents 1% melt content at 7.8 km depth from Arnoux et al. (2019). **(c)** Histogram of number of earthquakes for the entire study site for the 2016-2021 period shown in blue with a bin size of one week, overlain by cumulative moment release in black lines for each of the 5 regions delineated in (a) and (b), with no corrections applied for magnitude of completeness.

Table 2

Magnitudes of Completeness (M_c) and b-Values

	Median maximum horizontal error	Period 1: Sep 2016-Jun 2018		Period 2: Jun 2018-Feb 2021	
		M_c	b-value	M_c	b-value
Vent Fields[1]	0.64 km (vertical, 0.74 km)	0.21	1.59± 0.02	0.52	1.82 ± 0.02
East Flank	1.16 km	0.45	1.52 ± 0.03	0.63	1.39 ± 0.03
SWEV	0.95 km	0.55	1.12± 0.02	0.55	1.20 ± 0.02
WV OSC	6 km	1.16	1.24 ± 0.04	1.07	0.97 ± 0.04
Cobb OSC[2]	5.4 km	1.15	1.23 ± 0.04	1.07	0.93 ± 0.03

[1]For the Vent Field region for Period 2, and the [2]Cobb OSC region for both periods, the residual fit for the linear function when calculating M_c was raised to 30% to yield an M_c that visually matched the shape of the distribution.

2.5.3 ONC Endeavour Network

Detection levels across the time period of the ONC network vary due to network changes (Figure 3, Table S1) and seasonal noise variation. The rate of located earthquakes typically decreases in the winter, from November to February (Figure 10c), due to increased noise from fin whales and possibly winter storms. To account for network changes, we assess the b-values and M_c of each region for Periods 1 and 2 separately (Figure 3, Table 2).

The baseline input uncertainty of a fully weighted arrival, taken to be the picking error calculated from Equation 1 using only the 3,873 earthquakes that had at least eight recorded arrivals, is 0.030 s. The standard deviation of S-wave residual travel times is ~4 times larger than P-waves (Figure S16c); to account for this, we downweighted S-waves by a factor of 0.25. Using Equation 1, we find that the picking error for all earthquakes in the ONC catalog is 0.041 s. Maximum horizontal location uncertainties increase with distance from the network (Figure S4) and are presented for each region in Table 2.

2.5.3.1 Earthquakes in the Segment Center

Within the VF region, there are 26,562 earthquakes, although they account for only 12% of the total moment release (Figure 10c). This region has the highest b-values (> 1.5) (Table 2 and Figure 11). The moment release rate is relatively constant until September 2018, when it roughly doubles following a swarm of ~350 earthquakes near the High Rise vent field (V1 in Figures 11d and S6a). The swarm exhibits no mainshock-aftershock sequence and occurs simultaneously with a swarm in the East Flank region. In August 2020, the rate again roughly doubles but without any discernable swarm activity.

Of the earthquakes located within the VF region, 52% and 18% of those with maximum horizontal error < 0.5 km (9,011 earthquakes) are located within 1 km of High Rise and Main Field, respectively. Earthquakes with constrained depths, 19,852 in total, mainly cluster at shallow depths < 2 km, with the shallowest earthquakes beneath the High Rise field (Figure 6c). The increase in moment release rate in August 2020 is associated with an overall deepening of earthquakes: the median earthquake depth increases from 0.80 km to 1.16 km. These changes do not coincide with changes in network geometry (Figure S5).

In the EF region, there are 5,865 earthquakes, accounting for 7% of the total moment release (Figure 11d). Unlike the VF region, the moment release rate remains relatively constant. However, there are two large spikes: one in September 2018 (E1) associated with a swarm of ~300 earthquakes with no clear mainshock-aftershock sequence (Figures 11d and S6a), and one step in April 2020 attributed to one M_w 2.7 earthquake (Figure 11d). Swarm E1 occurs parallel to and at the same time as swarm V1, but E1 is located ~2 km off-axis and earthquakes show no migration between the swarm loci (Figure S6a). The b-value of the EF region is slightly lower than the VF region but still > 1 (1.39-1.52) (Table 2). Most earthquakes in the EF region are

located at the latitude of High Rise and Main Field in a region that extends 5-6 km off axis. Some moment release also occurs directly north of the EF region (Figure 11a).

The SWEV region contains 5,031 earthquakes. The cumulative moment release within the SWEV is the highest of the central regions (Figure 11d), accounting for 16% of the total moment release. Most spikes in cumulative moment release are due to earthquake swarms without clear mainshock-aftershock sequences, the largest of which occur in June 2017 (S1), July 2017 (S2) and February 2018 (S3) (Figure 11d, Figure S6a). The small spike in moment release in August 2018 is due to two earthquakes, M_w=2.6 and M_w=2.7, and occurs only 15 days prior to the swarm seen in both the VF and EF regions. However, earthquake locations show no migration between the locations of the earthquakes in the SWEV and the locations of swarms V1 and E1. The b-value within the SWEV region is smaller than both the VF and EF regions (1.12-1.20) (Table 2). The epicenter distribution within the SWEV is notably roughly aligned with the strike of the WV propagating tip (Figure 10).

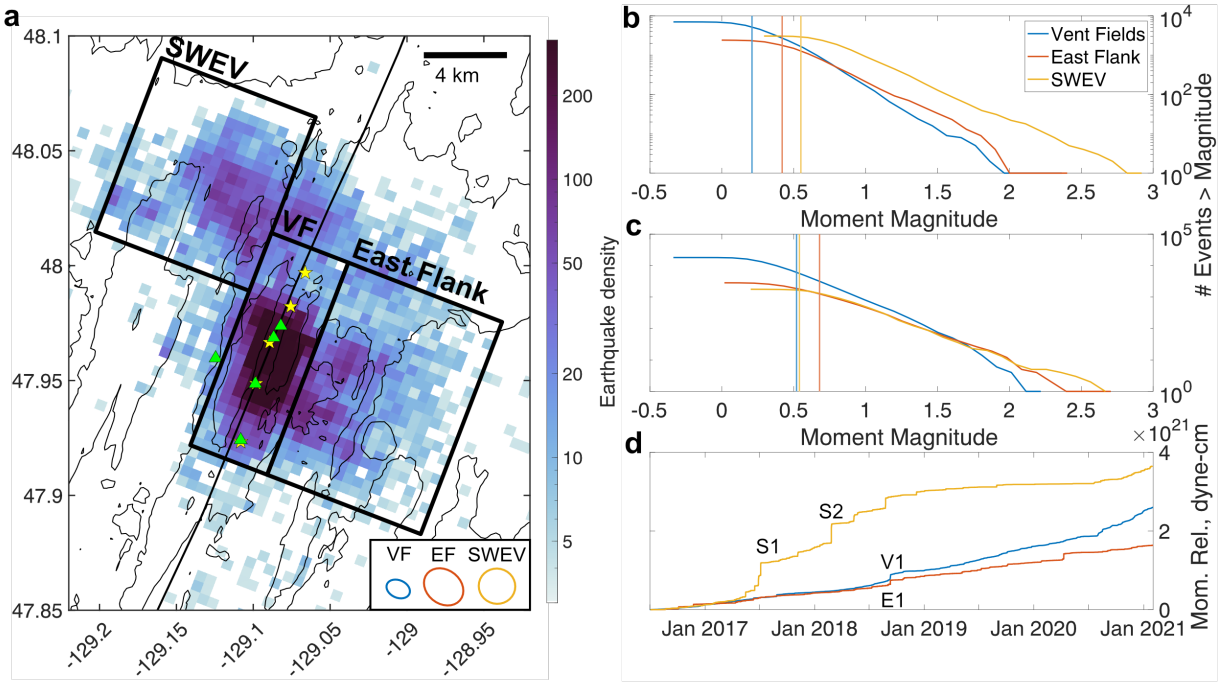

Figure 11. Detailed spatial patterns and magnitude distributions for the ONC catalog in the central Endeavour segment regions. **(a)** Map showing spatial density of earthquake counts in 0.5 km x 0.5 km bins, shaded on a logarithmic scale. Median 1-σ epicentral uncertainty ellipses are shown for each region. Symbols follow Figure 10. **(b)** Earthquake magnitude distributions during Period 1 with M_c overlain as a vertical line. **(c)** Same as (b), but for Period 2. **(d)** Cumulative moment release, not corrected for M_c, with swarms of interest annotated. Locations of labeled swarms are shown in Figure S6.

2.5.3.2 Earthquakes in the OSCs

Nearly half of the 1,617 earthquakes in the WV OSC region are clustered on the WV segment between the easternmost Heck and Endeavour seamounts (Figure 12a). There are 292 earthquakes within 4 km of the northern Endeavour segment axis. Few earthquakes occur inside the OSC or near the bathymetric definition of the West Valley propagator tip.

Moment release within the WV OSC region accounts for 33% of the total, with a b-value near 1 (1.07-1.16) (Table 2 and Figure 12). Much of the moment release occurs in earthquake swarms (Figure 12d), with the swarms in April 2017 (WV2) and August 2020 (WV4) both occurring in horizontal bands running roughly east-west (Figure S6b). Only the swarms in December 2016 (WV1) and October 2018 (WV3) have a clear mainshock-aftershock sequence: the first earthquake accounts for > 85% of the moment release of each swarm, with mainshock magnitudes of 2.9 and 3.4, respectively (Figures 12d and S6b). All other swarms occur with no clear mainshock or discernable spatial pattern.

Like the WV OSC, few earthquakes are located inside the Cobb OSC or near the bathymetric definition of the Cobb segment tip (Figure 12b). Overall moment release in the Cobb OSC accounts for 32% percent of the total, with b-values similar to the WV OSC (1.07-1.15) (Table 2 and Figure 12). Of the 2,212 earthquakes located in the Cobb OSC region, 652 are within 4 km of the southern Endeavour segment spreading axis. These earthquakes occur mainly at uniform rates in a segment-end cluster throughout 2016-2021, with only one swarm in May 2017 (C1) (Figures 12d and S6c). As for the WV OSC, many of the earthquakes are coincident

with a volcanic feature and are on the axis of the opposing limb, as seen in a cluster of 496 earthquakes near Split Seamount (Figure 1). These earthquakes occur primarily during two swarms without mainshocks in January 2018 (C2) and October 2020 (C3) (Figures 12d and S6c).

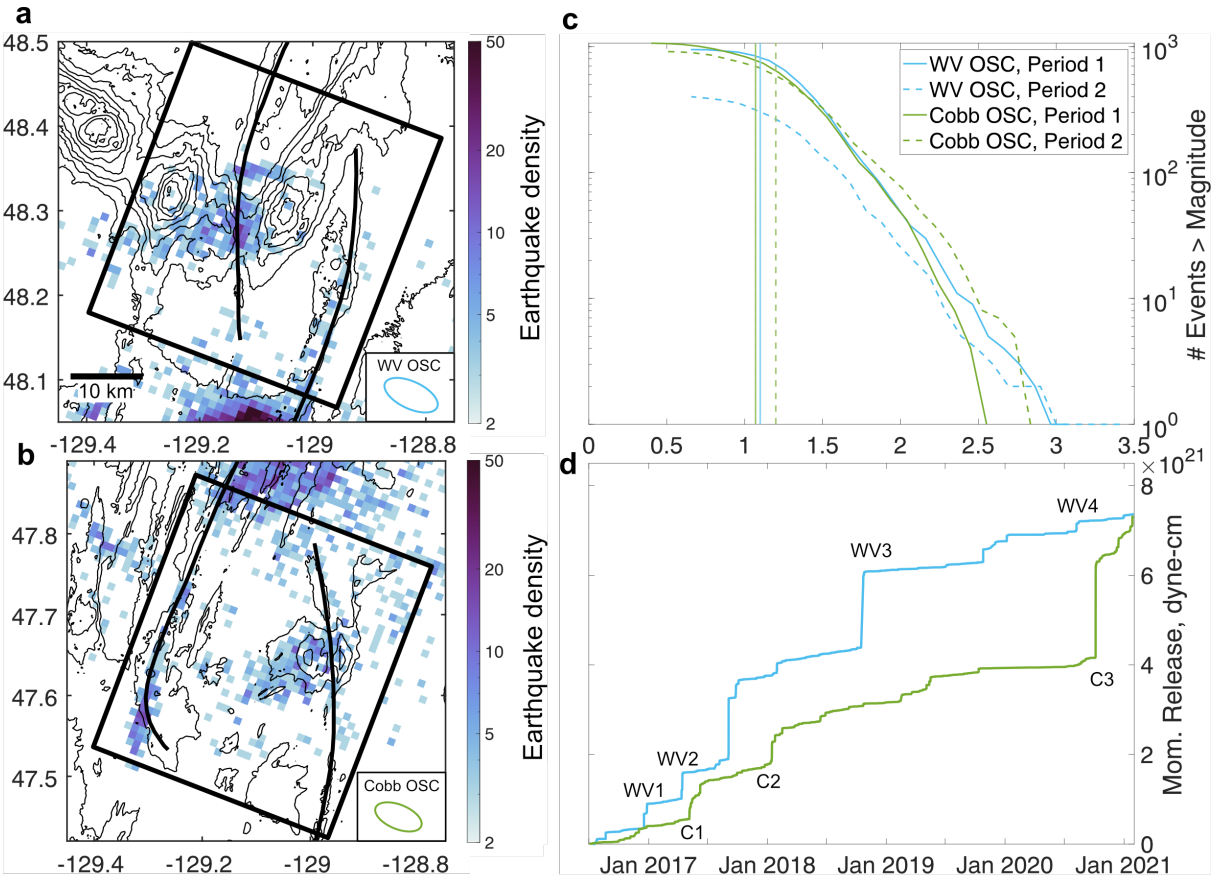

Figure 12. Detailed spatial patterns and magnitude distributions for the ONC catalog in the OSC regions. **(a)** Map of the WV OSC region showing spatial density of earthquake counts in 1 km^2 bins, shaded on a logarithmic scale. The extent of the defined region is shown with a black box. The ellipse shows the median 1-σ epicentral uncertainty. All symbols follow Figure 1. **(b)** Same as (a) but for the Cobb OSC region. **(c)** Earthquake magnitude distributions for Period 1 in solid lines and for Period 2 in dashed lines. M_c for the corresponding period and regions are shown with vertical lines. **(d)** Cumulative moment release, not corrected for M_c, with swarms of interest annotated. Locations of labelled swarms are shown in Figure S6.

2.6 Discussion

2.6.1 Strengths and Limitations of the Catalog

Our study demonstrates the value of 3-D seismic velocity models for locating earthquakes in submarine settings. On oceanic spreading centers, OBS networks are often deployed with small footprints so that the station spacing is appropriate for studying shallow volcanic and hydrothermal systems (e.g. Crawford et al., 2013; deMartin et al., 2007; Kelley et al., 2014; Tolstoy et al., 2008; Wilcock et al., 2009). This means that on the segment scale most epicenters lie well outside the network. We show that 3-D velocity models reduce bias for these epicenters, most clearly by the marked improvement in the Keck catalog epicenters, with a ~5-10 km decrease in the epicentral spread across ridge axes and the relocation of many off-axis earthquakes to within the OSCs (Figure 8). These changes coincide with the largest differences between the 3-D velocity models used in this study and the 1-D models used previously: epicenters at the segment ends move systematically closer to the network than calculated with the 1-D velocity model (Text S7, Figure S12) while earthquakes within 10 km of the network show little change from the 1-D locations (Figure S7).

For some earthquakes located far outside the ONC network with a suboptimal combination of stations, our nonlinear location method yields large or bimodal 3-D probability distributions (Figure S14) as is predicted for poorly constrained locations (Tarantola & Valette, 1982). As noted by Latorre et al. (2016), NonLinLoc's Gaussian uncertainty estimates do not hold as error approximation when probability distributions are not ellipsoidal. To understand whether this effect impacts our uncertainties, we compare median uncertainties derived from the NonLinLoc probability distributions to those derived from the scatter of earthquake swarms for the ONC network. Assuming that a swarm occurs in one location, the uncertainties should match

if they are well approximated by NonLinLoc. We find that they do match in most regions, but for both the EF and Cobb OSC regions, there are many locations with bimodal or long-tailed probability distributions (Figure S14a) and uncertainties appear to be overestimated by up to 50% (Table S5, Figure S6). This is likely due to the lack of a seismometer on the eastern flank which creates a particularly poor network geometry for sources in these regions. We also find that the orientations of uncertainty ellipses in both OSC regions differ between NonLinLoc and the swarms. This can be attributed to the bimodality or long-tails of some probability distributions, where the orientation of the main probability cloud matches well to the swarm, but the presence of a secondary probability cluster or a long tail skews the orientation of the calculated uncertainty (Figure S14a,b,d).

Analysis of picking error suggests that the ONC catalog could be improved by strengthening the ability of the location method to identify and eliminate outlier picks (see Text S8). Future work could pursue this by exploring an alternative form of the likelihood function formulated specifically to manage outliers, the Equal Differential Time function, offered by NonLinLoc (Font et al., 2004). Additionally, increasing the aperture of the ONC network would decrease the epicentral uncertainty outside the network.

2.6.2 The Influence of Propagating Ridge Tips

The strong alignment between seismicity in the SWEV and EF regions and the tips of the opposing OSC limbs (Figure 5, Figure 10) shows that both the West Valley and Cobb ridge segments extend past where they are apparent in the multibeam bathymetry to within several kilometers of the Endeavour axis (Figure 13a). The progression of these tips towards the Endeavour segment is consistent with known propagation patterns. The West Valley segment formed within the last 200,000 years when spreading jumped from Middle Valley and has been

propagating south since (Karsten et al., 1986). The Cobb offset has a long history of alternating directions of propagation, with the latest episode of northward propagation starting 50,000-100,000 years ago (Johnson et al., 1983). The Cobb tip is presently advancing at 0.4-0.9 km/kyr (Shoberg et al., 1991). Geochemical evidence shows that, on similar time scales, the composition of lavas at the ends of the Endeavour Segment have become distinct from those near the segment center, consistent with the changing conditions expected for a failing rift (Karsten et al., 1990).

The connection between the WV propagator and the SWEV region is confirmed by the January and February 2005 earthquake swarms. During both swarms, earthquakes extend past the bathymetric tip of the WV propagator (Figure 9) and during the February swarm earthquakes migrated down the propagator at 2 km hr^{-1} (Figure S10b). Our relocations are consistent with previous studies which interpret the 2005 swarms as a propagation event of the WV segment to a latitude of 48.05°N (Hooft et al., 2010; Weekly et al., 2013) (Figure 9). This is the location of the SWEV seismicity cluster observed throughout our catalog (Figure 5).

The tip of the WV propagator defined by the bathymetry at 48.15°N has undergone significant extension, consistent with a propagator limb that stretches further south. Profiles of 100-m resolution bathymetry (Kelley, 2015) (Figure S17) show a rift that is 2.5-3 km wide and 30-50 m deep, indicating a cross-sectional area of subsidence of ~0.075-0.15 km^2. Assuming a balanced cross-section such that the area of subsidence is equal to the free space created above intruded dikes and a depth to the top of the dikes of 500 m (the average off-axis layer 2A thickness from Van Ark et al., 2007), a cumulative 150-300 m width of intruded dikes is required. For spreading on the WV limb of 26 mm yr^{-1}, half of the full spreading rate (Demets et al., 2010), extension at 48.15°N must have been occurring for at least 6,000-12,000 years, consistent with a propagating tip that is now much further south.

Although our earthquake catalog does not include a swarm that migrates along the Cobb propagator, the bathymetry similarly suggests that seismicity in the EF region is focused by the tip of the Cobb propagator. The tip of the Cobb propagator defined by the bathymetry at 47.78°N is characterized by a ~2-km-wide and 50-m-deep rift (Figure S17) which requires 200 m of extension or 7,000 years assuming a spreading rate of 26 mm yr^{-1}. Based on the propagation speed of Shoberg et al. (1991) this would place the tip 3-6 km further north. Given that the spreading rate near the tip of a propagator is likely much less than half the full spreading rate, it is quite feasible that the propagator has advanced >10 km to the southern limit of seismicity in the EF region near 47.9°N (Figure 13).

Attributing the seismicity in the SWEV and EF to the WV and Cobb propagator tips (Figure 13), respectively, is consistent with the stress field expected from the propagating ridges. Modeling results show that the maximum extensional stress of an opening fracture is ahead of its propagating tip (Scholz et al., 1993; Sun & Jin, 2012). When ridge segments overlap, this remains true; stress maxima are concentrated at both overlapping tips (Pollard & Aydin, 1984). We note that the deformation caused by the active tips of the propagating ridges in the SWEV and EF regions may be more consolidated and focused than our catalog shows because of unconstrained depths. When a hypocenter is in reality deeper or shallower than 3 km, fixing the depth will lead to an epicenter located further from and closer to the network, respectively, resulting in a wider spread of locations than is real.

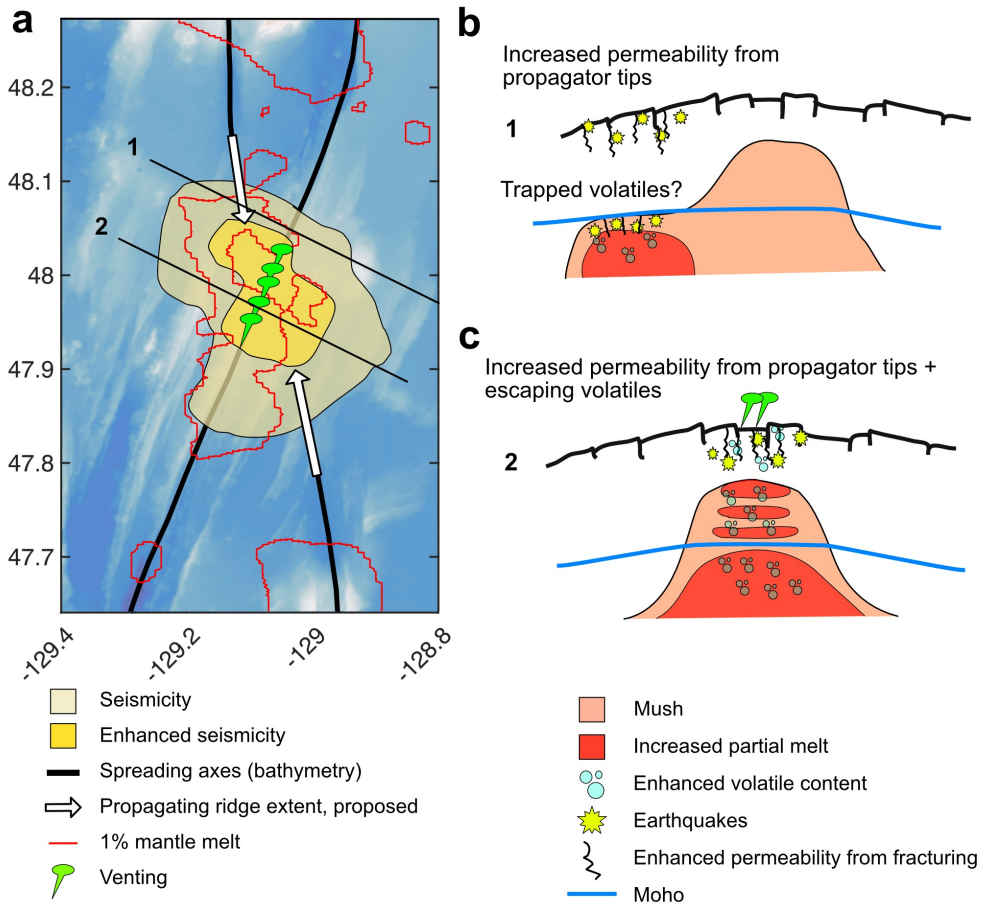

Figure 13. Schematic diagrams illustrating the influence of the propagating rift tips and mantle melt distribution on the observed seismicity. **(a)** Map illustrating how the observed extent of seismicity and hydrothermal venting locations spatially relate to the extent of mantle melt (Arnoux et al.'s (2019) 1% mantle melt contour) and the location of the propagating spreading ridges. Two cross-sections through (a) demonstrate how seismicity is promoted both (b) off-axis of the main spreading ridge and (c) on-axis. **(b)** In regions where seismicity is observed off-axis, both the East Flank and the Southwest Endeavour Valley, shallow earthquakes may be promoted by fracturing from the propagating rift tips. Deeper earthquakes may also be promoted by off-gassing of the increased mantle melt, perhaps through over pressurization and the creation of fluid flow pathways. **(c)** In regions on-axis where seismicity is observed, hydrothermal venting is supported both by a permeability structure focused by the propagating rift tips and by a mid-crustal magma lens, leading to intense microseismicity. The cartoons in (b) and (c) follow those made by Toomey et al. (2007) and Arnoux et al. (2019).

2.6.3 The Influence of Mantle Melt

There is a strong coincidence between our observed spatial patterns of seismicity and the distribution of mantle melt just below the Moho (Arnoux et al., 2019; VanderBeek et al., 2016),

particularly in the off-axis EF and SWEV regions (Figure 5e, Figure 10b, Figure 13a, Figure S9d). In the magma plumbing model of Toomey et al. (2007), the alignment of mantle melt with the spreading axis leads to volatile-rich melts within the crust that support vigorous volcanic and hydrothermal systems (Figure 13c). When mantle melt is instead supplied off axis, volatiles are lost from the magma as it migrates to the spreading axis and the ridge is thus less volcanically and hydrothermally active (Arnoux et al., 2019; VanderBeek et al., 2016). Therefore, in the off-axis regions of the SWEV and EF, volatile degassing may work to weaken the crust and promote seismicity, in addition to deformation from the propagating rifts (Figure 13b).

In various locations globally, CO_2 exsolution is well correlated with increased seismicity: substantial tectonic degassing of deep carbon is observed at rift zones and other highly fractured areas where the upward movement of fluids deep in the crust is facilitated by extension (e.g., Hunt et al., 2017; Lee et al., 2016). Whether the CO_2 exsolution promotes seismicity or vice versa is unclear, with both processes likely possible and also intertwined in a feedback mechanism (Tamburello et al., 2018). In central Italy, these two processes have been observed simultaneously: seismically quiescent springs with high CO_2 flux, where high-angle faulting networks allow CO_2 to escape at the surface, are adjacent to an active seismicity band with lower CO_2 flux, where thrust faults in the active seismicity band are interpreted to trap CO_2 and lead to overpressures (Chiodini et al., 2004, 2020) and therefore seismicity (Miller et al., 2004).

We assess the feasibility of two processes of CO_2 exsolution at the base of the crust in the off-axis regions where mantle melt is imaged: (1) complete volatile exsolution from the solidification of melt that underplates the crust and (2) exsolution from oversaturated melts that occurs between when they reach the base of the crust and when they rise into the crust at the spreading center. Lithostatic pressure at the base of the crust in the EF and SWEV regions is 250 MPa (7 km of 3300 kg m^{-3} oceanic crust with 2 km of 1030 kg m^{-3} water) (Arnoux et al., 2019).

The saturation value of CO_2 at this pressure is ~1500 ppm for tholeiitic melt (Holloway, 1998). Analyses of mid-ocean ridge basalt glasses show that the global mean concentration of CO_2 in primary melt lies in the range of 1700-2600 ppm (Michael & Graham, 2015). This range is consistent with the analysis of LeVoyer et al. (2019) of glass samples from the Endeavour segment specifically (Clague et al., 2009; Karsten, 1988): 1931 ppm but with up to 1100 ppm deviation between samples. Therefore, assuming the global range of mean concentrations (1) oversaturated melt solidifying at the base of the crust would release 1700-2600 ppm CO_2, and (2) melt re-equilibrating before entering the crust would release 200-1100 ppm CO_2. For process (1), a reasonable estimate of the maximum thickness of underplated material is 1 km (Nedimović et al., 2005) and taking a spreading rate of 52 mm yr^{-1} and a melt density of 2750 kg m^{-3} (LeVoyer et al. 2019), underplating will exsolve 240-370 t yr^{-1} CO_2 on each kilometer of ridge axis. For process (2), using a crustal thickness at the ridge axis of 6.7 km (Arnoux et al., 2019), oversaturated melt will exsolve 190-1050 t yr^{-1} km^{-1} CO_2.

Assuming CO_2 is released over a region that is 8 km wide across axis (i.e., the width of the seismically active regions in the EF and SWEV), combining the ranges of processes (1) and (2) gives a minimum CO_2 flux of 24 t km^{-2} yr^{-1} (low mantle CO_2 concentrations and no underplating) and a maximum of 180 t km^{-2} yr^{-1} (high mantle CO_2 concentrations and underplating). These endmember estimates are comparable to measured fluxes in regions where seismicity and CO_2 degassing are well correlated: ~250 t km^{-2} yr^{-1} in central Italy (Chiodini et al., 2004), ~118 t km^{-2} yr^{-1} at the Eastern Ethiopian rift (Hunt et al., 2017), and ~53 t km^{-2} yr^{-1} in the Himalayas (Becker et al., 2008). We therefore speculate that it may be feasible that mantle melt supplied in the off-axis areas beneath the EF and SWEV regions exsolves sufficient CO_2 to induce seismicity through over pressurization, upward fluid flow that weakens the crust, or the creation of pathways for hydrothermal fluid circulation from above (Figure 13b).

2.6.4 Links Between Propagating Rifts and Hydrothermal Venting

The arrival of the propagating rift tips to within several kilometers of the segment center provides an explanation for the unique characteristics of hydrothermal venting at the Endeavour segment. The maintenance of vigorous hydrothermal circulation requires both a sustained source of heat and frequent fracturing to create permeable pathways as fast as they are clogged by mineral precipitation (Curewitz & Karson, 1997). On MORs, these conditions are accomplished under two endmember regimes, largely governed by spreading rate (Wilcock & Delaney, 1996). At fast-spreading ridges with a mid-crustal magma lens, magma replenishment on timescales of ≤ 10 years (Liu & Lowell, 2009; Lowell & Germanovich, 1994) and fracturing associated with frequent eruptions (Wilcock et al., 2009; Wilcock & Delaney, 1996) maintain high-temperature hydrothermal circulation through permeable crust, separated from the heat source by a thin conductive boundary layer (Wilcock & Delaney, 1996). Because each eruption reorganizes the permeability, this results in small, ephemeral vents that have temporarily high outputs but change location frequently or are paved over by eruptive activity before reaching significant age (Cowen et al., 2007; White et al., 2002).

In contrast, at slow- and ultra-slow-spreading ridges, which have limited magma supply, established faults can support long-lived venting with minimal threat of disruption from magma extrusion (e.g., Canales et al., 2007; deMartin et al., 2007; Yu et al., 2018; Zhao et al., 2012). Olive & Crone (2018) show that in areas undergoing infrequent but regular magma injection, the necessary replenishment period of magma needed to maintain hydrothermal fields can be stretched to ~10 kyr if tectonic fracturing promotes downward migration of a cracking front during the cooling period, as originally proposed by Lister (1974). Alternatively, large long-lived vent structures may simply be inactive on the scales of thousands of years and grow only during short bursts of magma emplacement at depth (Humphris & Cann, 2000). Thus, under the regime

of slow-spreading ridges, hydrothermal vents are much older and larger, and persist for longer in one fixed place at overall lower rates of activity (e.g., Fouquet, 1997; Hannington et al., 2011).

The Endeavour segment vent fields do not subscribe to either of these regimes. They are paradoxical in that they are long-lived despite being supported by a steady-state mid-crustal magma lens (Van Ark et al., 2007; Wilcock et al., 2009). High temperatures and stable venting have been observed at the vents for over two decades (Butterfield et al., 1994; Seyfried Jr et al., 2003), and ^{226}Ra dating of sulfides from the Endeavour vent fields shows that they are all at least 500 years old, with Main Field likely older than 2000 years (Jamieson et al., 2013). Further, a consistent spread of ages suggests that the central vent fields have been active throughout their lifetimes without hiatuses (Jamieson et al., 2013) at rates higher than those on slow-spreading ridges (Jamieson et al., 2014). This duration of sustained high-temperature activity is significantly longer than observed at the EPR (170 years; Lalou et al., 1985).

The history of sulfide structures within the Endeavour axial valley, all of which are less than 3000 years old, suggests that this venting style has developed within the last several thousand years. Although Clague et al. (2014, 2020) argue that the axial valley is at most 4300 years old, the cumulative tectonic extension across the valley of 430 m (Jamieson et al., 2013) requires a much older age of at least ~8000 years. Axial valley formation was followed by a tectonic phase of sparse magmatism from 4300-2300 years ago (Clague et al., 2014), after which a hydrothermal phase began. Clague et al. (2014) argue that this phase is a result of renewed magmatism coinciding with fluid circulation that exploits permeability created during the tectonic phase. We think this explanation unlikely because hydrothermal circulation would clog preexisting permeability on much shorter timescales (Wilcock & Delaney, 1996). Instead, we argue that the arrival of the propagating rift tips near the segment center has provided a time-independent source of ongoing fracturing that enhances permeability (Figure 13c). We note that

our catalog suggests that the Cobb propagator is more influential than the WV propagator, since WV seismicity lies mostly to the north of the vent fields while EF seismicity lies directly east of the two most active vent fields (Main Field and High Rise; Figure 5f, 5i, Figure S8a, S8d) and merges with the seismicity observed on axis.

The inference that the rift tips focus the vent fields on a segment scale is consistent with smaller scale studies of hydrothermal springs that show they are most likely to be located in regions of heightened permeability from intersecting fracture tips (Curewitz & Karson, 1997). Although there is some evidence for small (meter scale) coincidence between conjugate faulting structures and vent locations (Delaney et al., 1992), these patterns are not observed at all vent sites and there is no evidence for kilometer scale cross-axis faulting structures in the bathymetry as might be expected if the rift tips were propagating into the central segment (Clague et al., 2014). This may mean that the impact of the rift tips is too recent to be observed at the surface, as we have shown to be true in the SWEV and EF regions. However, the pervasive shallow earthquakes within the vent fields throughout our catalog (Figure 6) point to a contribution from tectonism. Focal mechanisms in 2003 showed normal and thrust faulting mechanisms on faults striking primarily parallel to the ridge axis that were consistent with AML inflation, but focal mechanisms in 1995 showed considerable scatter and included slip on faults striking oblique to the ridge axis (Wilcock et al., 2002, 2009) that may be indicative of the influence of the propagating tips.

Furthermore, the enhanced permeability created by the propagators may explain the paradox of the Endeavour segment: an AML that does not erupt sufficiently to pave over the hydrothermal vents. We suggest that the fracturing from the propagating rift tips provides pathways that enable the AML to degas into the hydrothermal systems so that magma injected into dikes does not have a density low enough to erupt. The estimated heat flux for the entirety of

the active Endeavour hydrothermal fields is ~800 MW with a mean temperature of ~300°C (Kellogg, 2011). The concentration of CO_2 within the vent fluids for periods not impacted by dike emplacements is on the order of 15-20 mmol/kg, with 80% of the output believed to be sourced from melt (Love et al., 2017; Proskurowski et al., 2004). Taking a change in enthalpy of 1600 kJ kg^{-1} between 0 and 350 °C at 220 bars for a 3.2 wt.% NaCl solution (Anderko & Pitzer, 1993), we estimate that the vent fields emit 10,000-14,000 tons of melt-derived CO_2 per year. This is quite similar to the mantle CO_2 flux of 16,600 t yr^{-1} obtained by multiplying the estimate of Le Voyer et al. (2019) of 1.66 t yr^{-1} for each meter of the ridge by the 10 km length of ridge axis that hosts hydrothermal venting. Therefore, we propose that most of the CO_2 within the AML is degassed through hydrothermal venting such that during magmatic extensional events, extrusive volcanism is discouraged (Wallace & Anderson Jr, 2000) (Figure 13). The lack of CO_2 within the melt prevents the building of the pressure gradient needed to extrude above the seafloor (Buck et al., 1997).

2.6.5 Reinterpretation of the 2005 Swarms

The January 2005 swarm was first analyzed by Weekly et al. (2013), who observed activity beginning west of Endeavour seamount on January 31 and then enigmatically migrating eastward across the northern Endeavour segment (Figure 9a). In contrast, our relocations show the swarm begins on January 31 atop the Endeavour segment axis and earthquakes then migrate southward primarily on the Endeavour axis over 3 days from ~48.35°N-48.2°N, although a considerable amount locate east of the axis (Figure 9b). Weekly et al. (2013) then observed seismicity jumping to the WV segment and migrating southward (Figure 9a). Based on this pattern and the positive sign of borehole pressure perturbations in Middle Valley and the Endeavour east flank, they concluded that the sequence was dominated by magmatic intrusion on

the WV segment, propagating into the SWEV (Figure 9a). We observe largely the same pattern of southward earthquake migration on the WV segment (Figure S10), but we also observe earthquakes extending across the OSC at ~48.2°N on February 5 before seismicity begins further south on the WV segment (Figure 9b).

We infer that the January 2005 swarm includes two magmatic intrusions, with dike emplacement on the Endeavour segment from 48.3°N to 48.2°N preceding the dike emplacement on the WV segment interpreted by Weekly et al. (2013). Our relocated epicenters suggest that the Endeavour dike initiated near the northern limit of a crustal low velocity zone near where the northern Endeavour ridge is underlain by the mantle low velocity zone that extends across the WV OSC (Arnoux et al., 2019). The Endeavour and WV intrusions appear to be linked by earthquakes that span the OSC at ~48.2°N, the latitude at which intrusion on the northern Endeavour segment appears to stop. Although the positive borehole pressure perturbation at ODP site 857 in Middle Valley was previously interpreted as evidence that the majority of extension occurred on the WV segment (Weekly et al., 2013), our relocations of the Endeavour segment intrusion to further north negate this. The geometric pattern of modeled pressure anomalies from a dike would predict a borehole pressure perturbation as measured at Middle Valley as negative when the dike occurs south of 48.2°N, but positive when the dike occurs further north (Davis et al., 2001). Thus, a dike intruded at 48.3-48.2°N would yield the observed positive pressure perturbation.

For the February 2005 swarm, both prior studies agree that the dominant process was a southward magmatic intrusion on the northern Endeavour segment from 48.2°N to 48°N which triggered a response in the SWEV (Hooft et al., 2010; Weekly et al., 2013). Weekly et al. (2013) speculate that the magma source could have been Endeavour seamount, although their locations show the swarm beginning on the WV segment (Figure 9c). Both Hooft et al. (2010) and Weekly

et al. (2013) observe that seismicity jumped to the WV segment on February 27 and then migrated south into the SWEV. The largest earthquakes in the sequence, which have right-lateral strike-slip focal mechanisms, occur in the SWEV following this migration. Hooft et al. (2010) suggest these are a result of reactivated ridge-parallel faults triggered by the intrusion on the northern Endeavour. Hooft et al. (2010) point out that although high b-values and migrating seismicity suggest dike intrusion on the WV segment into the SWEV, borehole pressure records are inconsistent with that process. Weekly et al. (2013) argue instead that the borehole pressure records simply require that an intrusion on the northern Endeavour has a larger effect on pressures than one on the WV propagator.

Our relocations show that the February swarm began beneath the Endeavour seamount, consistent with the interpretation that the magma for the dike was ultimately sourced from the mantle melt anomaly beneath the OSC (Arnoux et al., 2019). However, if magma migrated down the Endeavour axis from the starting point of the January intrusion at 48.3°N, it was largely aseismic until it reached 48.2°N, the stopping point of the January 2005 intrusion. Alternatively, magma for the February intrusion could have been sourced from a small mid-crustal magma lens at ~48.2°N as suggested by a potential reflector (Carbotte et al., 2021). We observe seismicity propagating south to ~48.05°N at a similar speed to that resolved by Weekly et al. (2013), ~0.25 km hr^{-1} (Figure S10), primarily on-axis but with some epicenters at higher latitudes to the east (Figure 9d). As Arnoux et al. (2019) note, the crustal low velocity zone is offset to the east near 48.2°N which may explain why some epicenters are offset east for both the January and February swarms. We newly find that seismicity on the WV segment does not begin until there is a migration of seismicity across the OSC at the same stopping latitude of 48.2°N at a speed of 3.3 km hr^{-1} (Figure S11, Figure 9d).

We interpret that the January and February 2005 swarms progressively ruptured the northern Endeavour segment via magmatic intrusion from 48.3°-48°N, ~10 km further north than cited by Weekly et al. (2010). Since the dikes initiated at different latitudes we infer they were sourced from distinct crustal magma bodies, with the northern intrusion most likely statically triggering the southern intrusion (Bohnenstiehl et al., 2004). The activity on the northern Endeavour segment triggered activity on the WV segment during both swarms, with our relocations suggesting that the process of strain transfer is focused along a WSW trend that extends from the Endeavour axis at 48.2°N. This latitude marking the boundary between the two intrusions on the Endeavour is roughly coincident with an along-axis minimum in mantle melt (Arnoux et al., 2019) and a potential mid-crustal axial magma lens on the Endeavour segment (Carbotte et al., 2021).

Both Hooft et al. (2010) and Weekly et al. (2013) speculate that the intrusion on the WV propagator could be sourced from within the OSC although tomographic imaging suggests that the highest mantle melt concentration in the WV OSC is located north of the seismicity (Arnoux et al., 2019). Although our reinterpretation of the January swarm no longer requires an intrusion on the WV propagator to explain the borehole pressure anomalies, the southward migration of seismicity along the WV propagator observed in both swarms (Weekly et al., 2013) is strongly suggestive of propagating dikes. If two separate dikes did propagate along the same path, a month apart, it could be simply explained by the limited size of the crustal magma body and the need for more than one diking event to relieve the extensional stress (Buck et al., 2006). Indeed, the observation of large earthquakes in the SWEV near the end of the February swarm suggests that stresses in the area were not fully relieved by any magmatic extension.

At Axial Seamount, the occurrence of eruptions at a predictable level of inflation (Nooner & Chadwick Jr, 2016) and finite element stress models (Cabaniss et al., 2020) suggest that

eruptions are triggered at a threshold magma pressure. A contrasting view is that spreading events are triggered by extensional stress levels, an inference supported by a 35-km near-concurrent rupture of 9°50'N on the East Pacific Rise (Tan et al., 2016). The 2005 event was likely triggered by extensional stresses reaching a critical level on a timescale of months, as suggested by the precursory increasing seismicity along the segment from 48.05-48.3°N in a region that does not have an extensive continuous AML reflector (Carbotte et al., 2021; Van Ark et al., 2007).

The inference that extensional stress levels play an important role at the Endeavour segment has interesting implications for the response of the southern segment to the 2005 extensional event: after the February 2005 swarm, seismicity ceased on the southern Endeavour segment south of 47.7° except for the very southern tip (Figure 5d, Figure S9c). Weekly et al. (2013) proposed that this could be due to reduced magmatic pressures following the February 2005 swarm if the magmatic system is well-connected along the entire segment. Although there is a crustal low velocity zone extending from 48.2°N to 47.7°N (Arnoux et al., 2019), Carbotte et al. (2021) do not show evidence of a continuous axial magma lens. It is also not obvious why decreased magmatic pressure would be sustained long term. Thus, the view that extensional stress levels are a primary trigger suggests instead that the cessation of seismicity was linked to an extensional event on the southern portion of the segment that was entirely aseismic.

2.6.6 Evolution of Stresses During the Extensional Cycle and the Next Diking Event

The temporal patterns of seismicity at oceanic spreading centers are clearly influenced by the evolution of stresses over the extensional cycle (Dziak et al., 2012a; Dziak & Fox, 1999a; Tan et al., 2016; Tolstoy et al., 2006) but at the Endeavour segment they are complicated by the geometry of the OSCs. An example of this is seen in the EF region, where the moment release

rate in 2003-2005 is only a sixth of that seen in 1995 (Table 1) and the spatial extent of seismicity is much less than in both 1995 and 2016-2021 (Figure 5, Figure S7). This suggests that extension on the Endeavour axis from 47.7-47.9°N in 1999-2000 decreased stress on the Cobb propagator tip. The moment release rate in the EF has since increased, consistent with stress rebuilding, but rates in 2016-2021 have only reached half those seen in 1995 (Table 1), suggesting that the Cobb propagator is not yet approaching failure.

It is more difficult to interpret how stress evolves on the WV propagator because the spatial distribution of seismicity in the SWEV region changes between the earlier deployments and 2016-2021 (Figure 5). Prior to the 2005 sequence, seismicity in the SWEV is mostly limited to the northeast corner of our bounding box in a cluster that appears to be associated with extensional stresses on the Endeavour ridge (Figure 5g). Following the dike intrusion swarms, the distribution shifts to a region just south of the inferred dike and more seismicity appears on the western edge of the SWEV (Figure 5i). Both this spatial shift and a 2-month increase in moment release rates after the intrusion suggest a brief static stress change from dike emplacement (Bohnenstiehl et al., 2004). Moment release rates then decrease by a factor of 3 in April 2005, suggesting that overall, extension on the northern Endeavour lowered extensional strain on the WV propagator. In 2016, stress appears to have rebuilt on the WV propagator, with a larger spatial distribution of seismicity in the SWEV (Figure 5j) and an increase in moment release rate by a factor of 6 relative to 2006 (Table 1).

The 2005 diking events led to a 70% reduction in moment release rates in WV where most of the seismicity is near the Heck Seamounts and a 40% reduction on the Cobb segment where most of seismicity is around Split Seamount (Table 1). However, the moment release rates were still high relative to other regions following the diking event and, rather than increasing in 2016-2021, as might be expected from accumulating extensional stress, the moment release rates

are about an order of magnitude lower (Table 1). Further, both regions show a large drop in b-value from > 1.5 in 2005 (Weekly et al., 2013) to near-unity in 2016 (Table 2). We thereby infer that stresses must have been relieved on these segments by diking events between 2006 and 2016. Indeed, the earthquake catalog obtained from land networks shows that several migrating swarms occurred on both segments during this time period (Figure S18). The strain relief from these events will presumably delay the next extensional events on the northern and southern Endeavour and explains the low rates of seismicity in these regions in 2016-2021. A static stress change from extension on the WV segment north of the propagator tip may also account for the higher seismicity rates observed in the SWEV.

We predict that the VF region will be the first portion of the Endeavour to experience a diking event in the next spreading sequence and that this may occur within a few years. In the VF region, seismicity levels were the highest observed in the catalog during 2 months in 1995 (Table 1), four years before the 1999 diking event. Seismicity levels were similarly high in 2003-2004, with seismicity linked to inflation of the AML (Wilcock et al., 2009). Seismicity then dropped nearly an order of magnitude following the 2005 diking events. At the onset of the 2016-2021 observation period, moment release rates in the VF region were the same as after the 2005 diking events. But, by February 2021, they had risen 5-fold, to half the rates seen before the diking events. Interestingly, the last increase in moment release rates in the VF region in August 2020 (Table 1) is accompanied by a pronounced and sudden deepening of earthquakes that is not related to changes in network geometry (Figure S5). The depth distribution of earthquakes after August 2020 is similar to that seen in 1995 and 2003-2004. This is suggestive of an episode of magma chamber inflation that could potentially be precursory to diking.

An important question is whether real time observations of precursory seismic signals made using the cabled observatory at the Endeavour segment could provide enough warning and

accuracy to enable either the placement of additional autonomous sensors or a rapid response cruise that is more timely and comprehensive than prior efforts (Cowen et al., 2004; Dziak et al., 2006). Clear precursory activity preceding the January 2005 swarm was observed in the form of a swarm followed by exponentially increasing moment release in the regions of imminent rupture for only ~3 months prior (Figure 7) (Weekly et al., 2013), which may be sufficient if equipment is ready for response. Observations preceding rupture from Axial Seamount (Dziak et al., 2012b; Dziak & Fox, 1999a; Wilcock et al., 2016) and the EPR (Tolstoy et al., 2006) show that seismicity builds up over several years, and as the system moves to failure, rates may increase exponentially (Chadwick Jr et al., 2022; Kilburn, 2012). While our catalog is insufficient to detect exponential trends over such timescales for the 1999-2005 extensional sequences, it is, as discussed above, consistent with increased levels of seismicity over several years. Given the increasing rates of seismicity in the VF region (Figure 11d), it is clearly important to monitor seismicity going forward and consider how the community might respond to an imminent diking event.

2.7 Conclusions

We have constructed the first multi-decadal earthquake catalog for an intermediate-rate spreading ridge, spanning three OBS experiments from 1995-2021, for the Endeavour segment of the Juan de Fuca ridge. We show that high-resolution 3-D velocity models derived from marine active seismic experiments (Arnoux et al., 2019; Kim et al., 2019) enable accurate epicenter location on the segment scale despite small, non-optimal seismometer networks. This is particularly important because cabled observatories can only support small aperture networks. This location capability and the ~25-year lifespan of cabled networks together represent a significant step in the ability to make meaningful long-term observations of earthquakes on ocean spreading centers.

The findings of this study can be summarized as follows:

1. Consistent off-axis seismicity in the central Endeavour segment throughout the catalog reveals that the physical tips of both the West Valley segment to the north and the Cobb segment to the south extend ~10 km closer to the center of the Endeavour segment than seen in multibeam bathymetry.
2. Off-axis seismicity is strongly coincident with mantle melt distribution (Arnoux et al., 2019), which may promote seismicity in these areas through fracturing processes related to the degassing of CO_2.
3. The proximity of the rift tips to the Endeavour vent fields may help maintain the longevity of highly localized and vigorous venting through time-independent fracturing and a focused stress field. The strength and consistency of the resulting venting may also limit extrusive volcanism by degassing CO_2 from the axial magma chamber.
4. The January and February 2005 earthquake swarms together ruptured the northern Endeavour segment from 48.3°-48.05°N in two diking events. Dikes may have also been emplaced along the WV propagator during one or both swarms.
5. Seismicity rates reflect a pattern of evolving extensional stresses complicated by overlapping spreading limbs, showing decreases on an overlapping limb when extensional strain is relieved by diking on the opposing limb.
6. The center of the Endeavour segment is likely within a later stage of its extensional cycle and may experience a diking event within the next few years.

Our results show that there is extensive off-axis activity near the center of the Endeavour segment in the EF and SWEV regions. Our understanding of this seismicity and its relationship to the ridge propagators, mantle melt, and hydrothermal venting would clearly be enhanced by temporarily expanding the cabled network with autonomous OBSs in these regions to constrain

focal depths and mechanisms. Since only a small fraction of the extensional strain during diking events is relieved seismically, the interpretation of complex events like the 2005 swarm sequence would also be enhanced by additional seafloor geodetic data beyond volumetric strain measurements in regional boreholes.

2.8 Acknowledgements

We acknowledge Ocean Networks Canada for the operation of the NEPTUNE cabled array. We thank Emilie Hooft, Deb Kelley, Eunyoung Kim, Marvin Lilley, and Doug Toomey for helpful discussion. The data analysis was supported by NSF under grant OCE-1833419 and through a National Defense and Science and Engineering Graduate Fellowship to ZK.

Chapter 3: a single-station earthquake catalog for the Endeavour segment of the Juan de Fuca ridge (2011-2016): challenges and implications for the spreading cycle

Zoe Krauss[1], Christian Baillard[1], William S. D. Wilcock[1], Martin Heesemann[2], Angela Schlesinger[2], Jacob Kukovica[2]

[1]School of Oceanography, University of Washington, Seattle, Washington, USA
[2]Ocean Networks Canada, University of Victoria, British Columbia, Canada

3.0 Abstract

The Endeavour segment of the Juan de Fuca Ridge oceanic spreading center has been intermittently monitored by ocean bottom seismometer (OBS) networks for three decades. The available long-term earthquake record is influenced by magmatic, tectonic and hydrothermal processes surrounding a sequence of dike emplacements from 1999-2005. Background seismicity decreased at the end of this sequence and was low a decade later in 2016 when multi-station monitoring began with the Ocean Networks Canada NEPTUNE cabled observatory. Due to a gap in the catalog, it is unknown whether the rates were consistently low from 2006-2016. We expand the catalog to include 2011-2016 using a single OBS on the NEPTUNE cabled observatory. We perform single-station earthquake detection and attempt earthquake localization using *P* wave polarization and *P*, *S* and P_W differential arrival times. We assess the accuracy of these techniques by comparison to traditional network methods in 2016-2017. We find that distances between the earthquake and station are estimated well using a single station, but for most stations, *P* waves display a strongly preferred polarization direction that is independent of earthquake source azimuth. This is only observed for stations within the highly fractured axial graben. We propose that this effect is intrinsic to the mid-ocean ridge environment and is a result of shallow fracture-induced scattering very near the OBS. Although this prevents us from calculating full earthquake locations, we present earthquake counts for the 2011-2016 period in comparison to the multi-station catalog that begins in 2016. We show that seismicity rates

remain consistently low both in the segment center and segment ends for 2011-2016. Our results provide further evidence that the 1999-2005 dike emplacements relieved most of the extensional strain on the segment.

3.1 Introduction & Motivation

Short range earthquake observations are necessary to properly observe seismicity at small magnitudes. Unfortunately, it is not atypical in a marine setting to have sparse ocean bottom seismometer (OBS) networks comprising only one or two stations, or unideal network geometries such that small earthquakes are only recorded on 1-2 stations. Nevertheless, the value of sparse seafloor observations has been shown time and again: even one OBS can significantly expand the capability of onshore networks to detect small earthquakes (D'Alessandro et al., 2013; Monna et al., 2014; Sgroi et al., 2007; Tréhu et al., 2018) and improve earthquake locations and source mechanism constraints (Frontera et al., 2010; Romanowicz et al., 2006; Sgroi et al., 2021).

If only one seismometer records earthquakes, single-station localization techniques can still allow tectonic characterization in the absence of a larger network (Frohlich & Pulliam, 1999). With three components of particle motion, one can extract the polarization direction of the incoming *P* wave (Jurkevics, 1988; Park et al., 1987; Roberts et al., 1989); in the absence of significant scattering near the receiver, the horizontal polarization should point away from the epicenter. With earthquake azimuth calculated, an epicenter can be constrained with a single seismometer by calculating distance through differential *S* and *P* wave arrival times. Pioneering authors showed three-component-based localization methods to be effective by comparing solutions to network locations for local earthquakes (Alessandrini et al., 1994), regional earthquakes (Magotra et al., 1989), and explosions (Kim & Gao, 1997; Ruud et al., 1988). Polarization methods have also been valuable in extending the reach of limited networks using

stand-alone stations (Agius & Galea, 2011; Gómez-Arredondo et al., 2016) and show potential in constraining rupture propagation in near-real time (Bayer et al., 2012).

Single-station techniques have also been successfully applied to OBS. Offshore Palermo, D'Alessandro et al. (2013) were able to detect earthquakes unseen by land-based networks down to M_L -0.5 and determine epicenters and hypocentral depths via polarization methods and emergence angle of the *P* wave. Similar results were reported by Sgroi et al. (2007) for a subset of earthquakes recorded by an OBS offshore Sicily. Both studies calculated single-station locations that agree well with known tectonic patterns. At the Southwest Indian Ridge, Liu et al. (2019) calculated well-clustered hypocenters for both volcano-tectonic earthquakes and regional earthquakes using single-station polarization methods.

At the Endeavour segment of the Juan de Fuca mid-ocean spreading ridge, there are five years of seismic data suitable for single-station analysis. The dataset comes from an OBS on the Ocean Networks Canada NEPTUNE cabled observatory, which provides real-time streaming data from and long-term power to seafloor instruments (Heesemann et al., 2014). The observatory came online in 2011 and supported a maximum of two OBS at once until 2016 (Figure 1a). Seismic data from the multi-station network installed in 2016 has been analyzed to produce an earthquake catalog that continues through 2021 (Krauss et al., 2023) and beyond (Krauss & Wilcock, 2021). The single-station sites remain instrumented following the installation of the multi-station network in 2016, providing an opportunity to verify single-station methods against the multi-station catalog.

The Endeavour segment is a 90-km portion of the intermediate-rate Juan de Fuca Ridge ocean spreading center. An axial graben ranges in width from 0.4-1 km, increasing from south to north (Clague et al., 2014, 2020). Along the central 10-km of the segment, there are five main high-temperature hydrothermal vent sites within the graben (Kelley et al., 2012). The Endeavour

segment is capped at both ends by left-stepping overlapping spreading centers (OSCs) that are propagating towards the segment center (Figure 1b). Complex plate boundary reorganization in the region (Dziak, 2006; Johnson et al., 1983; Karsten et al., 1986; Shoberg et al., 1991), hydrothermal circulation, and seafloor extension all lead to extensive small-magnitude seismicity on the segment. Earthquakes at the Endeavour segment have been characterized using networks of OBS for three decades, starting in 1995 and continuing into the foreseeable future with a near-real-time catalog from the NEPTUNE cabled network (Krauss et al., 2023; Weekly et al., 2013; Wilcock et al., 2002).

The Endeavour segment is expected to undergo extensional rupture episodes in the form of dike emplacements ("spreading" events) every ~20 years (Krauss et al., 2023). The last extensional episode occurred as a series of spreading events from 1999-2005 (Weekly et al., 2013), with seismicity increasing prior to dike emplacements, and dying off nearly completely afterwards. Krauss et al. (2023) showed that seismicity rates remained low in 2016, comparable to rates seen in 2005 immediately following rupture, and then began to increase in the following years. Whether these low rates persisted during 2011-2016 is unclear without analysis of the single-station period. Krauss et al. (2023) also suggested that the opposing limbs of the overlapping ridge segments on either end of the Endeavour may have undergone further spreading events between 2006-2016; even with one station, we would expect to record such an event if it occurred.

Using a single station to make earthquake observations can introduce higher uncertainty in earthquake locations due to a lack of multiple observations and unstable azimuth calculations when signal to noise ratios (SNR) are low (Agius & Galea, 2011; Sgroi et al., 2007). However, one station can still constrain earthquake rates and the locations of seismically active areas. Earthquake patterns within vent fields are often correlated to changes in hydrothermal venting

character, and are therefore useful to document (Arnoux et al., 2017; Kellogg, 2011; Sohn et al., 1998b). In this study, we take advantage of the single OBS at the Endeavour segment for 2011 to 2016 and apply single-station earthquake detection and localization techniques. The value of this work is twofold: it (1) informs technical methods of single-station localization on mid-ocean ridges, and (2) augments our understanding of inter-rupture seismicity patterns by completing the analysis of available seismic observation at the Endeavour segment.

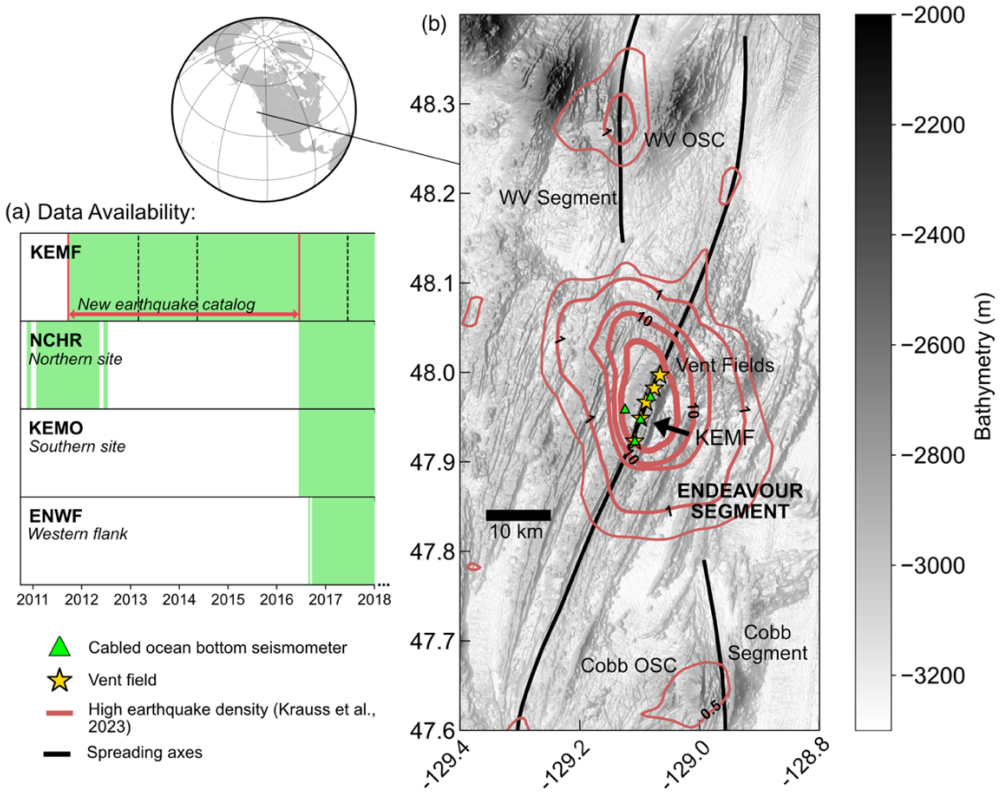

Figure 1. Summary of study site and data availability. **(a)** Timeline showing when data is available (green) for the four main ocean bottom seismometer sites on the NEPTUNE cabled observatory operating before 2018. Times when the KEMF site underwent an instrument change are marked with dashed black vertical lines. The period for which we present new earthquake information is bounded by solid pink vertical lines and labeled with an arrow. **(b)** Map of the Endeavour segment with the inset showing its global location. Bathymetry is shown in gray scale with the main features annotated. WV stands for West Valley. Spreading axes are shown with black lines, vent fields with gold stars, and seismic stations with green triangles. The station in place from 2011-2016, KEMF, is annotated. The distribution of seismicity for 2016-2021 (Krauss et al., 2023) is shown using pink contours, with the contours representing 0.5, 1, 5, 10, and 25 earthquakes per km^2, in order of increasing thickness.

3.2 Data

3.2.1 ONC Cabled Network

The first OBS on the Endeavour segment node of the Ocean Networks Canada NEPTUNE cabled observatory (Heesemann et al., 2014) came online at the High Rise site (station code NCHR) in November 2010. Until June 2016, a maximum of two short period OBS were functioning at one time, either at High Rise or the Main Field site (KEMF), with only a brief overlap period from September 2011-May 2012 (Figure 1a). The KEMF site provides five years of continuous single-station observations that then continued as part of the multi-station network from June 2016. The KEMF site underwent instrumentation changes in March 2013 and May 2014 (Figure 1a). For validation of our single-station detection rates and localization method, we compare our single-station detections and locations to the multi-station detections and locations of Krauss et al. (2023) for October 2016-June 2017, a period when four stations were in operation without instrument changes.

3.2.2 Velocity models

For earthquake localization, we use 3-dimensional velocity models for both *P* and *S* waves generated from a marine active seismic experiment (Arnoux et al., 2019b; Kim et al., 2019b). The velocity models extend over a volume of 60 x 90 x 9 km^3 with a grid spacing of 0.2 km.

3.3 Methods

3.3.1 Automatic earthquake detection, phase picking, and moment calculation

Three-component seismic time series data are processed for a single station using detection algorithms developed for use on Axial Seamount (Wilcock et al., 2016) and then adapted for the Endeavour segment. As detailed in Krauss et al. (2023), impulsive signals are

identified using a short-term long-term RMS (Root-Mean-Square) triggering algorithm, associated across the three components on a single seismometer, and then classified as earthquakes, whale calls, or noise based on their frequency content and similarity across channels. For events flagged as earthquakes, *P* and *S* wave arrival times are picked using an iterative approach (Krauss et al., 2023) and then refined using Kurtosis (Baillard et al., 2014).

3.3.2 Single-station earthquake ranging and localization

Full earthquake localization with a single seismometer is, in principle, possible in the marine setting via the approach depicted in Figure 2. The back-azimuth to the earthquake can be determined using the particle motions of the *P* wave. The horizontal range and depth of the earthquake can then be obtained via the relative arrival times of *P*, *S* and P_W (the sea-surface reflection of the *P* wave). This was the initial objective of our single station analysis. However, we were unable to calculate reliable back-azimuths for the earthquakes (Section 4.1). Since the modeling of P_W requires accurate knowledge of the water depth at the locations where P_W crosses the seafloor, we were therefore unable to use P_W to constrain earthquake depths. Instead, we determined horizontal ranges to earthquakes by assuming the earthquake depths and modeling the *S* - *P* arrival times. We describe this simplified approach here and discuss the use of P_W arrivals in Text S1.

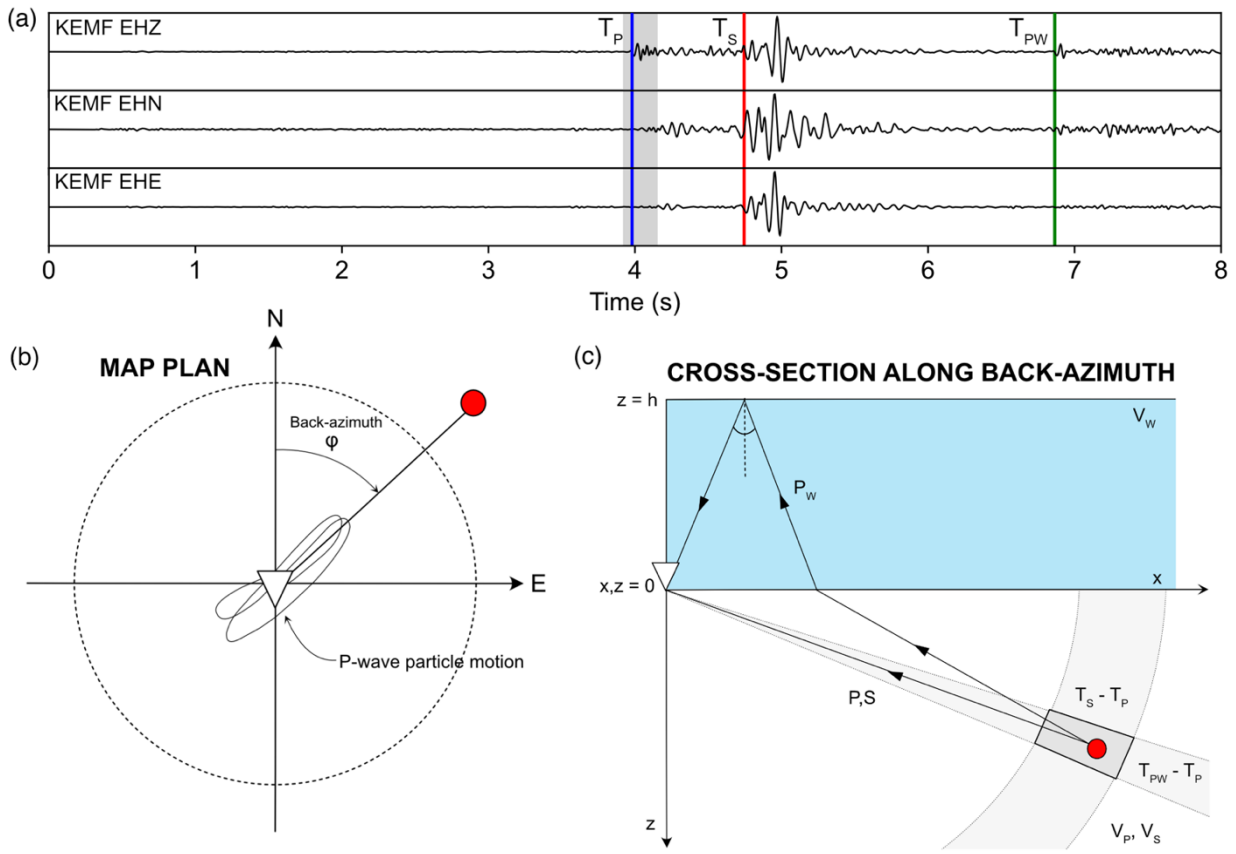

Figure 2. Illustration of attempted single-station localization method. **(a)** Filtered waveform of a local microearthquake with high signal to noise, with arrival times T, of P, S, and P_W arrivals annotated and marked by blue, red, and green vertical lines, respectively. The window used to measure P wave polarity, 0.05 s before and 0.12 s after the arrival, is shown in gray. **(b)** Plan view showing how P wave particle motion calculated using the gray window in (a) relates to the azimuth of the earthquake source. In (b-c), the inverted white triangle represents the seismometer and the red circle represents the earthquake source. **(c)** Cross-section along the azimuth in (b) showing how relative arrival times of the P, S, and P_W waves could be used to calculate an earthquake location. The seafloor is at z = 0. The blue region between z = 0 and z = h is the water column which has a P wave velocity of V_W, and the bottom portion below z = 0 is the crust where P and S wave velocities (V_P, V_S) are from a 3-D velocity model.

First, the three-component seismogram was retrieved for a window extending from 4 s before the *P* wave pick to 4 s after the *S* wave pick. The horizontal components of the seismogram were rotated to N and E using the known OBS orientation and then detrended, tapered using a Hann window with a maximum percentage of 0.05, and bandpass filtered between 8-35 Hz. The instrument responses were then removed and the seismogram was converted to displacement.

We attempted to estimate earthquake azimuth by calculating the principal component of the *P* wave first motion (Figure 2a-b). Since the *P* wave is a rectilinear wave, its particle motion is polarized along the vertical plane connecting the source and the receiver. Therefore, its principal component should point down along the source azimuth of the earthquake. We applied the method of Jurkevics (1988), which takes the eigen decomposition of the covariance matrix of the three-component time series, to a short window cut 0.05 s before and 0.12 s after the *P* wave arrival. This window length, along with the filtered frequency band of 8-35 Hz, was chosen to maximize the rectilinearity of the waveforms (Text S2). Rectilinearity is a measure between 0 and 1 calculated using the eigenvalues of the covariance matrix. Pure body waves have a rectilinearity equal to 1. Azimuths with rectilinearity < 0.5 are discarded. Azimuthal error is defined as the product of 360 degrees and the difference between the rectilinearity and 1, such that the higher the rectilinearity, the smaller the azimuthal error.

As detailed in further sections, we found that our calculated azimuths were inconsistent with expected earthquake locations. We therefore proceeded to fix earthquake depths and simply estimate the horizontal range of earthquakes. To do so in a way that was largely independent of earthquake azimuth, we generated depth-averaged versions of the 3-D *P* and *S* velocity models (Arnoux et al., 2019b; Kim et al., 2019b). We then created travel-time grids for these depth-averaged models using NonLinLoc's Grid2Time software (Lomax et al., 2009), which solves the forward problem using a finite-difference method (Podvin & Lecomte, 1991) and assumes a flat seafloor. An *S* - *P* differenced travel-time grid was then calculated, and ranges were obtained by matching the observed *S* - *P* time to the predicted *S* - *P* time for a fixed earthquake depth: 2 km depth for earthquakes < 2 km from the station (within the vicinity of the vent fields), or 3 km depth for earthquakes further away, following Krauss et al. (2023).

Using the estimated range, *P* and *S* wave moments for each earthquake are calculated using the method described in Krauss et al. (2023). Moment magnitude is then computed for each earthquake using the mean of *P* and *S* wave moments following Hanks & Kanamori (1979).

3.4 Results

3.4.1 Single-station earthquake method validation

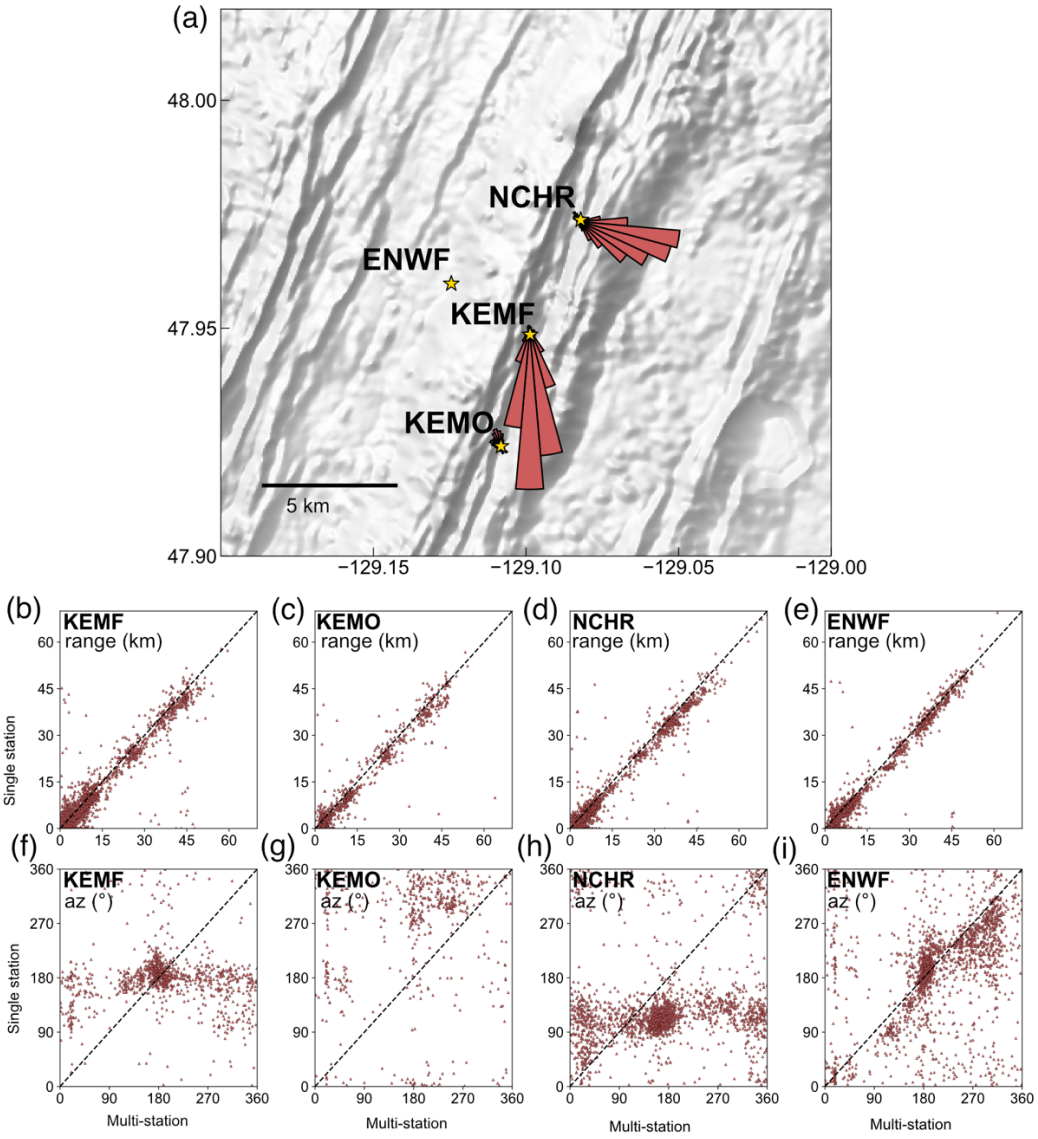

Figure 3. Results of single-station localization for all four available stations for October 2016-December 2018 compared to multi-station localization. For each station, results are only shown if the multi-station location had both a P and S pick on that station. **(a)** Map showing station locations and single-station azimuths as a rose plot for the three stations that show a near constant polarization direction. The rose plot radii are scaled such that the maximum radius corresponds to 950 observations. The rose plot for KEMO is small because the station recorded comparatively few arrivals. **(b-e)** Scatter plots comparing earthquake ranges calculated by the single-station method to multi-station locations for earthquakes detected from October 2016 to December 2018. The dashed line shows ranges that match (slope of 1). **(f-i)** Scatter plots comparing earthquake azimuths (as degrees clockwise from north) calculated by the single-station method to multi-station locations. Results are shown for events with a P-wave SNR ≥ 3 and rectilinearity ≥ 0.85. The dashed line shows azimuths that match (slope of 1).

To evaluate the efficacy of single-station localization, we applied our simplified technique of earthquake azimuth and range calculation to all four available OBS time series for October 1, 2016 to January 1, 2018, the time period that underwent the fewest instrumentation changes (Figure 1). We then compared our single-station azimuths and ranges to those calculated by the traditional multi-station methods of Krauss et al. (2023) (Figure 3). We only present comparisons between multi-station earthquake detections and single-station earthquake detections that have both *P* and *S* arrivals on the same station that agree within 0.5 s.

For three of four stations, earthquake azimuths calculated using *P* polarization show a preferred direction that is inconsistent with the corresponding multi-station locations despite high rectilinearities (> 0.85) (Figure 3). For KEMF (3563 compared arrivals), 75% of *P* arrivals yield an azimuth within 20° of the median of 182° (Figures 3a and 3f). *P* arrivals display a different preferred polarization on NCHR (3448 compared arrivals), with 58% yielding an azimuth within 20° of the median of 117°. For KEMO, the polarization preference is weaker, with only 21% of arrivals within 20° of the median azimuth of 295°; but, there are fewer multi-station locations with both a *P* and *S* pick (1135 arrivals). In contrast, *P* arrivals to ENWF yield earthquake azimuths that are broadly consistent with multi-station locations (Figure 3i).

Ranges calculated using a single station are consistent with corresponding multi-station locations. The median absolute difference between range calculated using a single station and that calculated with the multi-station network is 1.60 km for KEMF, 1.75 km for NCHR, 1.85 km for KEMO, and 1.51 km for ENWF. Single-station ranges appear to slightly underestimate multi-station ranges for all stations, with KEMF single-station ranges on average 1.26 km lower than the corresponding multi-station range. This systematic difference is consistent with that expected from the variation in travel-time grids used between the single-station and multi-station

locations (see Text S3). Uncertainties in ranges, calculated using bootstrapping, do not increase with range and have a median of 1.7 km and maximum of 3.3 km for the KEMF station; we note that these uncertainties do not account for errors that would accumulate with range due to errors in the velocity model.

For all stations, there are some earthquakes at ranges < 10 km that are incorrectly given 0 km range by the single-station localization algorithm (Figure 4c). This is likely a result of fixing the depth. Although we fix earthquake depths to 2 km for earthquakes within 2 km of the station and 3 km for further earthquakes, we know from the multi-station catalog that many of the small earthquakes within 2 km of KEMF are shallower (23% have depths < 1 km) (Krauss et al., 2023). When the fixed depth is too deep, the predicted *S*-*P* time is too large, and the earthquake location moves closer to the station to compensate. This leads to some 0 km ranges. In contrast, for multi-station localizations, when the fixed depth is too deep, the final location balances travel-time misfits between phase picks on all stations, rather than placing earthquakes beneath KEMF.

3.4.2 Seismicity from 2011-2016

The lack of azimuth constraints on NHCR and KEMF means that we are unable to obtain earthquake localizations for 2011-2016. However, we can still calculate earthquake detection counts and ranges. Manual examination of the automatic detections on NCHR for November 2010-May 2012 shows that the instrument is often plagued by high frequency noise that is either falsely identified as earthquakes or obscures *P* wave arrivals (Figure S5a-c). There are times when the algorithm properly detects earthquakes (Figure S5d), but there is no straightforward way to automatically discriminate these from noise. The NCHR-only catalog for 2011-2012 is dominated by misdetections; of the earthquakes in the NCHR catalog during times that overlap

KEMF (Figure 1a), only 4% had a *P* pick within 5 s of a *P* pick on KEMF. For this reason, we only report single-station results for KEMF.

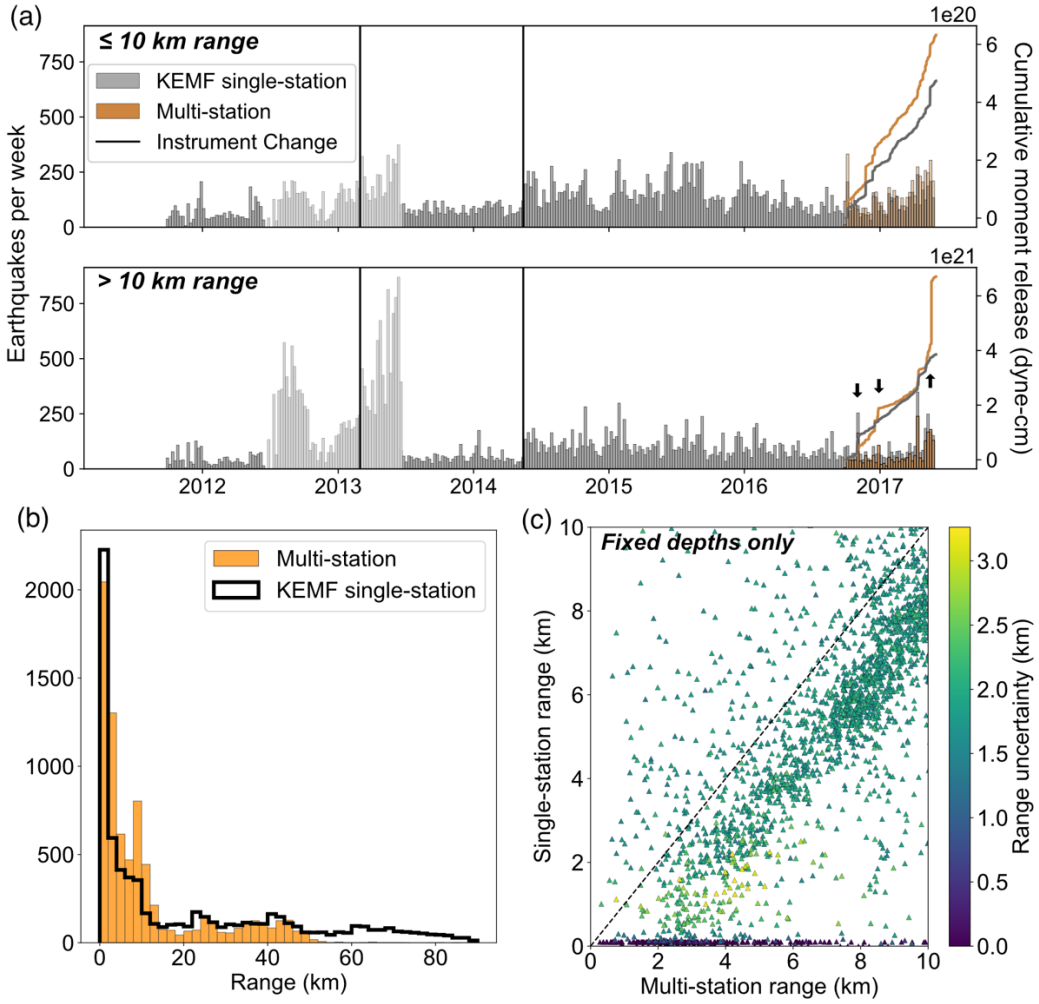

Figure 4. Results of single-station detection using KEMF, compared to the 2016-2017 period of overlap with the multi-station network. **(a)** Histogram showing earthquake counts in 2-week bins with ranges from KEMF < 10 km for single station detections (gray) and the unadjusted multi-station catalog (orange). The cumulative moment release is overlain for the overlap period. Black vertical lines in 2013 and 2014 indicate times when the instrument at the KEMF site was switched out. Lighter shading for the KEMF detections indicates the interval when earthquake detection was corrupted by noise. **(b)** Same as (a) but for earthquakes with ranges from KEMF > 10 km. Black arrows mark discrepancies in the moment release noted in the text. **(c)** Histogram comparing the distribution of source-to-station ranges for all earthquakes detected during the 2016-2017 overlap period by the multi-station network (orange) and KEMF (overlain in black), with bin sizes of 2 km. **(d)** Comparison between multi- and single-station ranges for earthquakes < 10 km from the station. This is a zoomed-in version of Figure 3b, except scatter points are colored by range uncertainty and only earthquakes whose depths were fixed in the multi-station catalog are shown. The dashed line has a slope of 1.

3.4.2.1 Comparison of 2016-2017 overlap period

To understand the confidence with which we can interpret single-station detections, we compare the earthquake catalogs calculated using KEMF and the multi-station network for October 2016 to June 2017; after this timeframe, the LED lights on the KEMF station were accidentally left on, which created pulsating noise that lead to many spurious detections. These could not be removed without arrival time context from other stations. We present earthquakes at ranges < 10 km and ranges > 10 km separately, since there appears to be a change in the sensitivity of the single-station detections near this threshold (Figure S6). This threshold also roughly partitions the seismicity on the segment between the vent field region and the OSCs (Figure 1).

Within 10 km of KEMF, the multi-station catalog includes 5181 earthquakes during the overlap period (Figure 4a) and the KEMF catalog includes 3959 earthquakes (Figure 4a). We do not expect the KEMF catalog to include all earthquakes in the multi-station catalog, only the ones with both a *P* and *S* pick on the KEMF station, and more specifically, a clear *P* arrival. Therefore, for comparison, we create an adjusted multi-station catalog with only earthquakes that have both a *P* and *S* pick on KEMF and require that the *P* pick have a location weight > 0.4. There are 2887 earthquakes in this "adjusted" multi-station catalog. Counting events as the same if they have an origin time within 1 s, the KEMF catalog includes 70% of the earthquakes in the adjusted multi-station catalog (Figure 5a-b).

Only 51% of the earthquakes in the KEMF catalog have origin times, calculated using the estimated travel-time of the *P* wave, matched within 1 s to origin times of earthquakes in the adjusted multi-station catalog. This is not a result of mispicked arrivals because the proportion does not increase significantly if origin times are matched to only within 5 s. Most of the "new" unmatched earthquakes have ranges < 1 km (Figure 5e), which suggests they are small

earthquakes very near KEMF that were not included in the multi-station catalog due to a lack of clear arrivals on neighboring stations.

The cumulative moment release within 10 km of KEMF for the KEMF catalog is 25% less than the unadjusted multi-station catalog, but increases in moment release occur at the same times (Figure 4a). For individual matched earthquakes, the calculated moment is slightly larger in the KEMF catalog; the median ratio of multi-station to KEMF moments is 0.88 (Figure S6).

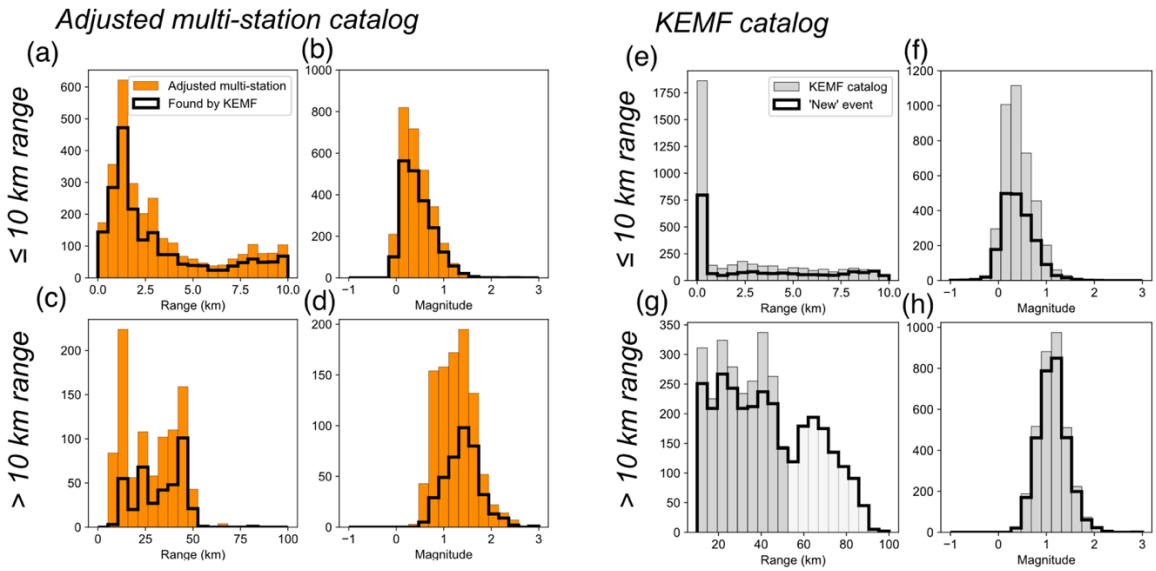

Figure 5. Comparison of earthquake characteristics between the adjusted multi-station and single-station KEMF catalogs. The upper row of subplots shows earthquakes ≤ 10 km from the station and the bottom row shows earthquakes > 10 km. **(a-d)** Comparison between all earthquakes in the adjusted multi-station catalog and those that are also found by the KEMF catalog for 2016-2017, showing range distribution (a, c) and magnitude distribution (b, d). (**e-h**) Earthquakes in the KEMF catalog overlain by earthquakes that are "new" (not in the adjusted multi-station catalog based on origin times within 1 s). The range distribution is shown in (e, g) and magnitude distribution is shown in (f, h). In (g), earthquakes > 50 km are shown with lighter shading because they are not included in the final earthquake count (see Section 5.2).

At ranges > 10 km from KEMF, the multi-station catalog includes 2275 earthquakes in the overlap period (Figure 4b) while the KEMF catalog contains 3430 (Figure 4b). The adjusted multi-station catalog (only events with a *P* weight > 0.4 on KEMF) includes 954 earthquakes. The KEMF catalog includes only 41% of earthquakes in the adjusted multi-station catalog (Figure 5c, 5d) and tends to include those with higher magnitudes (Figure 5d). The KEMF

catalog may miss many of these lower-magnitude earthquakes because events further from the network tend to have arrivals that are less clear (low SNR or emergent character) and so are more often missed or mispicked (Figure S7). Matched earthquakes account for only 11% of the KEMF catalog (Figure 5g, 5h). Of the new events, 37% have ranges > 50 km (Figure 5g). In the multi-station catalog, earthquakes are generally not located this far away because the localization algorithm effectively limits the maximum *S-P* time. From inspecting a sample of these distant events in the KEMF catalog, at least 50% are either true earthquakes that have falsely large S-P times due to incorrect *P* picks, or occasionally, instrument noise (Figure S7).

The total moment release for the KEMF catalog is 42% less than the unadjusted multi-station catalog total moment release. The cumulative moment release rates match until May 19, 2017, when a magnitude 3.5 earthquake ~82 km from the network was anomalously captured by the multi-station catalog but not the KEMF catalog (Figure 4b). There are also discrepancies on November 2, 2016, from a swarm located ~30 km west of the center of the segment, and from December 17-27, 2016, from a swarm located ~40 km north of the network on the West Valley segment (Figure 4b). For individual matched earthquakes at ranges > 10 km, the KEMF catalog has slightly smaller moments than the multi-station catalog; the median ratio of multi-station to KEMF moments is 1.2 (Figure S6).

3.4.2.2 Detections from 2011-2016

For the 5 years preceding the multi-station network, September 2011 to June 2016, the KEMF catalog includes 69,776 earthquakes. Two apparent changes in earthquake rates, in March 2013 and May 2014, are contemporaneous with changes in the deployed instrument and thus presumably artifacts of detection sensitivity (Figure 4a, 4b). In June 2012, the rate of earthquakes increases markedly and then decreases in June 2013. During this interval, the catalog includes

many more earthquakes at > 50 km range (Figure S8). Examination of earthquake records from this interval reveals many misdetections on an instrumental noise source that repeats every ~3 hours (Figure S9). This noise is associated with a subsea junction box near the instrument which failed in June 2012 and was then disconnected in June 2013. The timing of the noise was not consistent enough to allow automated removal of these misdetections. We therefore exclude June 2012-June 2013 from our interpretation.

3.5 Discussion

3.5.1 Implications of the observed azimuthal bias

The preferred polarization directions we see for the ridge-axis stations (Figure 3) are independent of earthquake magnitudes, ranges, and source azimuths. It is unlikely that these preferred polarizations are a result of methodological choices. Polarization characteristics change with frequency, such that the same seismic waveform filtered with different frequency bands may show different polarization strength or direction due to different noise sources such as anthropogenic sources or microseisms (Koper & Hawley, 2010). However, we carefully iterated on the choice of our frequency band (8-35 Hz) to maximize rectilinearity (Text S2). Varying this frequency band reduced overall rectilinearity, but still yielded the same preferred polarizations. Another contribution to misdiagnosed polarization could be mistakenly including the coda of the *P* wave, which tends to have random polarization (Menke et al., 1990). We chose the length of our polarization window (0.05-0.12 s around the *P* arrival) to ensure maximum rectilinearity values. The polarizations shown in Figure 3 are all for *P* waves with rectilinearities > 0.85, indicating we are capturing only the truly polarized arrival. Perhaps the strongest indication that the source of the preferred polarizations is not methodological is that our technique works for station ENWF (Figure 3), the only station not within the axial graben and the only station buried

in thin sediments. We therefore suggest that the preferred polarizations are site-dependent and related to deployments on bare rock in the central ridge axial graben.

Site-specific preferred ground motion direction was investigated by Bonamassa et al. (1991), Bonamassa & Vidale (1991) and Vidale et al. (1991) following the 1989 Loma Prieta earthquake. They observed that seismometers as close as 25 m displayed significantly different preferred directions of S-wave ground motion, regardless of earthquake source azimuths or focal mechanisms. Bonamassa & Vidale (1991) suggested that amplified motion of scattered waves in one preferred direction effectively overrode motion in the orthogonal direction. Xu et al. (1996) used polarization estimates from explosions near the same sites to show that the site-specific preferred direction effect is also seen with *P* waves. They present simple models suggesting this observation is a result of scattering from shallow-dipping velocity heterogeneities near the station.

In some locations, the direction and strength of preferred ground motion appears to be influenced by local scattering from proximal fracture zones. Preferred orientation directions are commonly at a high angle or orthogonal to the strike of the fault zone (Di Giulio et al., 2009; Pischiutta et al., 2012; Rigano et al., 2008). Near the Hayward fault, Pischiutta et al. (2012) observed preferred directionality of ground motion only on stations very close to the fault zone; this effect disappears at a distance of only 200 m from the fault damage zone. At Mt. Etna, Di Giulio et al. (2009) similarly observed directional resonance only for stations near a highly-deformed rift. Pischiutta et al. (2012) attribute the preferred directions to the anisotropic reduction of the Young's modulus normal to the damaged zone; as the angle from the orientation of cracks increases, compliance of the substrate increases, which leads to amplified motion in the fault-orthogonal direction.

We infer that the preferred ground motion directions on stations NCHR, KEMF, and KEMO, which are all located within the region of highest fracturing in the axial graben, arise from local scattering. The only site that does not display a preferred polarization direction (ENWF) is located ~2 km west of the axial graben (Figure 3). However, the preferred motion directions for on-axis stations are not clearly related to the dominant fracture orientation within the axial graben. High-resolution bathymetry shows predominantly ridge-parallel cracks at all sites (Clague et al., 2020), but our observed directions of preferred polarization are not consistently ridge-parallel (Figure 3). Preferred polarizations also change significantly between the NCHR, KEMF and KEMO sites. This suggests that the subsurface structures that cause scattered waves to have a preferred direction are extremely localized, rather than the fissures that define the axial valley on the scale of 10s of meters. This could include, for example, fractures or boundaries between pillow lavas within meters of the instrument. At this small scale, the scattering mechanism could be equivalently viewed as the rocking of a block of crust.

The observation that the off-axis station does not exhibit preferred polarization supports that complex subsurface fracturing begins to heal significantly within several kilometers of the axial walls (Figure 3). This is consistent with *P* wave anisotropy observed at the ridge: the strength of anisotropy, interpreted to represent the dominance of unfilled cracks, drops off significantly at 5 km off-axis and diminishes by > 50% between 5-10 km off-axis (Weekly et al., 2014). Further, the deployment of the instrument in (or on) a few meters of sediment may lead to a more homogenous subsurface near the instrument, diminishing the preferred polarization effect.

Observations from other sites near mid-ocean ridges and seafloor volcanic features show that preferred ground motion directions are commonly observed. Bohidar (2023) attempted to orient short period OBS at various volcanic sites using *P* wave polarization for local earthquakes.

Despite varying earthquake locations, they often observed a near-constant calculated azimuth. This appears to be correlated with stations at highly fractured sites. For several experiments, a preferred azimuth is seen on only some stations within a network: at Mayotte, only stations closest to the main volcanic ridge demonstrated a preferred azimuth; at Rainbow hydrothermal field, the sole station which did not show a preferred azimuth was in a deeper site further from fracturing associated with active venting; and at Axial Seamount, stations near the caldera walls showed preferred polarizations but a station in the central, less fractured caldera did not. In their study, it is unclear how much the preferred polarization directions varied between nearby sites because most station orientations are unknown.

Preferred polarizations may also have biased the earthquake locations obtained by Liu et al. (2019) using a single broadband OBS at the Southwest Indian Ridge. The earthquake locations, which were made using *P* wave polarization, have a consistent azimuth with respect to the station (see their Figure 8). Their polarized *P* wave arrivals have high rectilinearities and their resulting earthquake locations show good clustering, but the locations do not agree with those obtained from earlier multi-station network deployments (Schlindwein & Schmid, 2016; Schmid & Schlindwein, 2016). The relatively small and tight distribution of earthquakes that Liu et al. (2019) observed in comparison to the much broader distribution seen by the previous studies suggests that they may be seeing a similar preferred polarization effect.

3.5.2 Extending the earthquake time series for the Endeavour segment

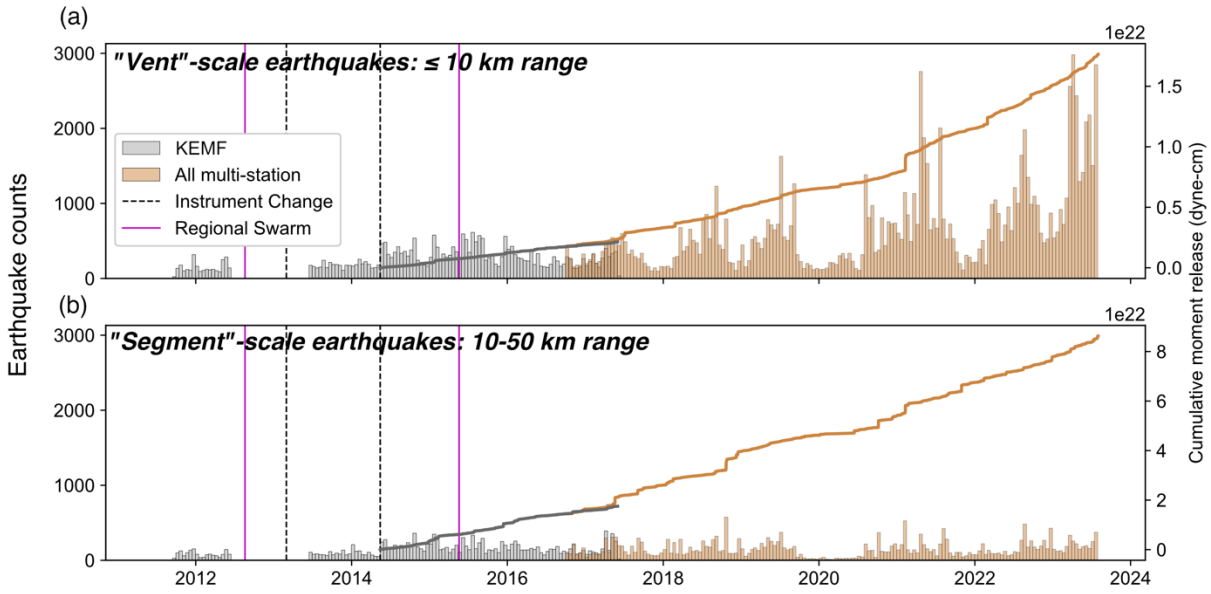

Figure 6. Time series of earthquake counts and moment release for 2011 to 2023 for **(a)** earthquakes within 10 km of the KEMF station and **(b)** earthquakes with ranges 10-50 km. For the multi-station catalog as shown, we do not apply the station-specific corrections for network changes from Krauss et al. 2023, and we update their catalog to show earthquake rates up to August 2023. Earthquake counts are shown as a histogram with bin sizes of 2 weeks. Instrument changes during the single-station period are shown using vertical dashed gray lines and the regional swarms cited as potential segment-end spreading events by Krauss et al. (2023) are marked using vertical magenta lines. Decreases in detections during winter months are due to increased noise from fin whale calls.

We extend the time series of multi-station earthquake counts and moment release for the Endeavour segment by five years to include 2011 to 2016 (Figure 6). For comparison to the multi-station catalog, we present these results separately for vent-scale earthquakes < 10 km range from KEMF (Figure 6a) and segment-scale earthquakes between 10 and 50 km range (Figure 6b). We exclude earthquakes further than 50 km because they are usually not captured by the multi-station catalog and in the KEMF catalog, many of these appear to be spurious picks (Figure 5g). We also exclude earthquakes between June 2012 to June 2013 that are impacted by instrumental noise (Figures S8 and S9). Following comparison to the multi-station catalog, we correct the moment release rates in the KEMF catalog by factors of 0.88 and 1.2 for earthquakes closer and further than 10 km from KEMF, respectively (see Section 4.2.1). During the overlap

period in October 2016 to June 2017, “vent”-scale earthquake detection numbers are slightly underestimated by the KEMF catalog but are roughly comparable, with 5181 found in the multi-station catalog and 3959 found in the KEMF catalog (Figure 6a). For earthquakes further than 10 km from KEMF, the KEMF catalog instead slightly overestimates earthquake counts, but they are also roughly comparable, with 2275 in the multi-station catalog and 3430 in the KEMF catalog (Figure 6b). Reduced detections during winter months (Figure 6) are due to increased noise from fin whale calls (Krauss et al., 2023).

Krauss et al. (2023) suggested that the opposing limbs of the OSCs (Figure 1) may have undergone further spreading events between 2006 to 2016 and pointed to several large earthquakes and swarms detected via land-based networks as candidates for such events. However, there is no indication that the candidate events during our observation period were associated with spreading events on the opposing limbs of the OSCs (see magenta lines in Figure 6). We would expect to see a clear uptick in earthquakes > 10 km from the station leading up to and during an event of that type, with a decrease in background seismicity levels afterward. Rather, seismicity appears at a relatively low rate consistent with the multi-station rates seen in 2016. We also visually inspected the excluded data for the late 2012 regional swarm to confirm that no anomalous activity occurred (Figure 6). If the opposing limbs did undergo further spreading events post 2006, then, it likely occurred prior to 2011.

The extended time series of Endeavour segment seismicity shows that low rates of seismicity have continued at the segment ends for at least 12 years (Figure 6b), with vent-scale seismicity rates near the segment center remaining relatively low until a significant uptick started in ~2018 (Figure 6a). The seismicity rates remain overall low from 2011-2016 in our observations, which leaves the prediction of Krauss et al. (2023), that the central portion of the segment will be the first to undergo a repeated extensional dike intrusion event, unchanged. This

also supports the interpretation that the 2005 rupture of the Endeavour segment largely relieved extensional stresses along the entirety of the main segment (Krauss et al., 2023). Our extended vent-scale seismicity time series suggests that earthquake rates pick up exponentially rather than linearly in relation to increasing extension (Figure 6a), similarly to trends seen at Axial Seamount (Chadwick et al., 2022) and as expected for a system responding to increased stress levels (Kilburn, 2012).

3.6 Conclusions

Using only one OBS, we have extended the available time series of earthquake rates for the Endeavour segment by five years to include 2011 to 2016 (Figure 6). We attempted to perform single-station localization for this period using *P* wave polarizations to constrain earthquake azimuth, differential *P* and *S* wave arrival times to constrain earthquake range, and differential *P* and P_W wave arrival times to constrain earthquake depth. Unfortunately, comparison of azimuth estimates to multi-station locations show that for most stations, *P* waves are polarized in a single preferred direction that is independent of earthquake source azimuth. This preferred polarization is only observed for stations within the highly fractured axial graben. The orientation of the polarization varies widely between stations only ~2 km apart and does not correlate with fracture patterns observable in high-resolution bathymetry. Since similar phenomena have also been observed at other mid-ocean ridge sites, we propose that this effect is inherent to the mid-ocean ridge setting and is a result of near-surface scattering from highly fractured material. We observed that *P* wave polarizations agree with multi-station locations for a station outside of the axial graben, suggesting that this scattering diminishes within ~2 km of the ridge axis at the Endeavour segment.

The lack of azimuth constraints, and thus bathymetry along the source-receiver path, prevents the incorporation of P_W relative arrival times into the solutions. Although we are unable

to obtain full earthquake locations for 2011 to 2016, we present earthquake counts, ranges and moment release rates in comparison to the multi-station catalog (Figure 6), including the overlapping period between single- and multi-station catalogs in 2016 and 2017. We find that single-station earthquake detection occasionally mispicks earthquake arrivals due to a lack of relative timing information from other stations. Despite this, single-station earthquake detection approximates earthquake counts, earthquake ranges, and moment release rates quite well when compared to the multi-station catalog. For earthquakes both near the segment center (< 10 km from the station) and near the segment ends (10 - 50 km), seismicity rates remain low with no changes during 2011 to 2016 (Figure 6). This provides further support that the 1999 to 2005 extensional dike emplacement events relieved most of the extension along the segment, and only after ~20 years did stresses rebuild to the point that seismicity rates were significantly enhanced.

3.7 Acknowledgements

The data analysis was supported by the NSF under Grant OCE-1833419 and through a National Defense and Science and Engineering Graduate Fellowship to ZK.

Chapter 4: Repeating earthquakes and earthquake swarms at the Endeavour segment: direct evidence for aseismic slip at a mid-ocean ridge

Zoe Krauss[1], William S.D. Wilcock[1]

[1]School of Oceanography, University of Washington, Seattle, Washington, USA

4.0 Abstract

We explore the potential of multiplet earthquakes to constrain deformational patterns at the Endeavour Segment of the Juan de Fuca ridge. Earthquake families with highly similar waveforms, termed multiplets, can represent wide-ranging processes including aseismic creep, fluid diffusion, and transient slow-slip events. However, multiplets have never been characterized in a mid-ocean ridge setting. We leverage an existing microearthquake catalog for the Endeavour segment to cluster earthquakes into families with high waveform cross correlations for 2017. We find that more than 25% of earthquakes occur as multiplets. Multiplets appear to include both continuous families, where similar earthquakes occur quasiperiodically over a long time period, and burst-like families, where all similar earthquakes occur within a short time period. These endmember behaviors appear to be evenly distributed throughout all areas of elevated seismicity at the central Endeavour segment. We investigate one continuous multiplet family in detail to show that it includes a true repeating earthquake sequence with a ~1 month recurrence interval. If this repeater sequence represents aseismic slip on a normal fault near the axial valley, its slip rates indicate that 4-27% the half spreading rate is accomodated aseismically. We also investigate two burst-like families in detail and show that they represent earthquake swarms with distinct different driving mechanisms. The largest swarm displays migration behavior consistent with a fluid-induced earthquake swarm. The other swarm example is much shorter in duration with no migration, instead suggesting an internal driving mechanism similar to an aftershock sequence. This pilot study of multiplets at the Endeavour segment

suggests they are widespread and represent multiple modes of deformation, such that they could effectively be used to track varied activity including slow slip and fluid-induced seismicity at mid-ocean ridges.

4.1 Introduction

Earthquake multiplets are sets of earthquakes with very similar waveforms that are inferred to represent repeated rupture of the same or very close fault patches (Uchida & Bürgmann, 2019). This phenomenon has been widely observed in various tectonic settings, including continental strike slip systems (Nadeau et al., 1994; Templeton et al., 2008), oceanic transform faults (Hayward & Bostock, 2017; Materna et al., 2018), subduction zones (Igarashi et al., 2003; Uchida et al., 2003), rift systems (Duverger et al., 2018), and volcanoes (Hotovec-Ellis et al., 2015; Thelen et al., 2011). Multiplet earthquakes are generally split into two groups: burst-like, which occur over a short interval with variable interevent times, and continuous, which occur over a longer duration with larger and more uniform interevent times.

Continuous multiplet families typically indicate repeating earthquakes, which are repeated ruptures of an identical fault patch. True repeating earthquakes have high waveform cross correlation coefficients, typically greater than 0.9, and are validated by demonstrating that their source area is smaller than their interevent distance (Gao et al., 2021; Waldhauser & Ellsworth, 2002). When repeating earthquakes extend over long time periods with consistent recurrence intervals, they are thought to result from stable aseismic creep or long-term slow slip; a “stuck” heterogeneity within an aseismically slipping fault is continually loaded, and ruptures periodically as a repeating earthquake (e.g., Vidale et al., 1994). The areas of stuck patches and their corresponding slip amounts can be inferred from the source properties of the repeating earthquakes. Long-term, continuous families of repeating earthquakes have therefore been used to estimate rates of aseismic creep (Chen et al., 2007; Materna et al., 2018; Nadeau & Johnson,

1998) and variations in fault coupling in space and time (Igarashi et al., 2003; Nadeau & McEvilly, 1999; Uchida et al., 2016).

In contrast, burst-type multiplets are associated with more transient processes and are often recognized within earthquake swarms. Earthquake multiplets within swarms do not necessarily have overlapping source patches, and instead, their spatiotemporal migration characteristics can be used to discern their driving mechanism. Fluid-induced earthquake swarms migrate following a diffusive process, so that their onset and cessation (termed the back-front) times can be fit by the square root of distance from the first event (Shapiro, 2015). In contrast, slow slip-induced earthquake swarms show faster and more linear migration (e.g., Roland & McGuire, 2009). Multiplet earthquake migration speeds can also be used to distinguish between magmatic and tectonic drivers for earthquake swarms (e.g., Massin et al., 2013). Burst-type, short-lived families of repeating earthquakes can also indicate transient loading processes associated with volcanic settings, such as stick-slip events surrounding magma extrusion and degassing (Thelen et al., 2011) or resonance of magmatic chambers (Battaglia et al., 2003).

Many of the processes thought to generate multiplet earthquakes are expected at a mid-ocean ridge setting. The release of accumulated plate motions and the formation of new oceanic crust at fast and intermediate-spreading mid-ocean ridges occurs cyclically, with large-strain magmatic and tectonic events recurring on decadal scales (Delaney et al., 1998). During these events, earthquakes occur in swarms that mark the injection of magmatic dikes along a ridge axis. Shorter, smaller swarms, not necessarily associated with diking, are also common. Abundant microseismicity and earthquake swarms are seen at steeply dipping detachment faults at the slow-spreading Mid-Atlantic ridge (Parnell-Turner et al., 2017, 2020). An early experiment at the Endeavour segment, an intermediate-rate spreading ridge, also identified several earthquake swarms with varying migration speeds, suggesting the influence of fluids on fault failure

(Wilcock et al., 2002). Some of these non-diking earthquake swarms have been associated with hydrothermal vent fluid temperature transients (Crone et al., 2010; Sohn et al., 1998b). Earthquakes with highly similar waveforms have also long been noted at mid-ocean ridges; for instance, at the Mid-Atlantic ridge, Toomey et al. (1988) observed 11 microearthquakes with similar waveforms (cross correlation > 0.8) occurring in less than 24 hours.

It is inferred that a significant portion of faulting at mid-ocean ridges is accommodated aseismically, but a lack of seafloor geodesy has prevented direct observation of this behavior. At the fast-spreading East Pacific Rise (EPR), Cowie et al. (1993) compared seismicity rates to estimates of fault slip from sonar and bathymetry data to estimate a 1% seismic coupling rate, which describes the percentage of faulting accomplished via earthquakes. The high geothermal gradient, perhaps also enhanced by hydrothermal fluid circulation, is thought to prevent deformation from occurring in the brittle stick-slip domain. At the slow-spreading Mid-Atlantic ridge, Olive & Escartín (2016) compared coupling for two endmember forms of faulting, and found slightly higher but still low seismic coupling rates: 10-30% coupling on ridge-parallel abyssal hills and 40-60% coupling on large-offset detachment faults. At the intermediate-spreading southern Juan de Fuca ridge, Ito & Behn (2008) show that faulting accounts for < 20% of overall spreading rates, with the rest of spreading accomplished magmatically. How much of this faulting occurs aseismically, however, is less clear. If multiplet earthquakes at mid-ocean ridges show direct evidence of aseismic slip in the form of repeating earthquakes, they could be used to better constrain seismic coupling, and if long-term data are available, changes in seismic coupling over time.

An opportunity to investigate mid-ocean ridge multiplet earthquakes in detail arises at the Endeavour segment of the Juan de Fuca Ridge, where seismicity has been monitored since 2016 with a small ocean bottom seismometer (OBS) network on the Ocean Networks Canada

NEPTUNE cabled observatory (Barnes et al., 2008; Heesemann et al., 2014; Figure 1). The Endeavour segment is marked by five high-temperature hydrothermal venting sites along the central 10 km of the axial valley, underlain by an axial magma lens (Carbotte et al., 2021; Kelley et al., 2012; Van Ark et al., 2007). A long-term microearthquake catalog for the Endeavour segment shows that seismicity is concentrated within the vent fields, but also occurs off-axis, likely due to the influence of the overlapping ridge segments that bound the Endeavour on either end (Krauss et al., 2023; Figure 1). During 2016-2018, seismicity rates are relatively low, but begin to pick up in 2018 following increasing strain since the last diking event in 2005 (Hooft et al., 2010; Weekly et al., 2013).

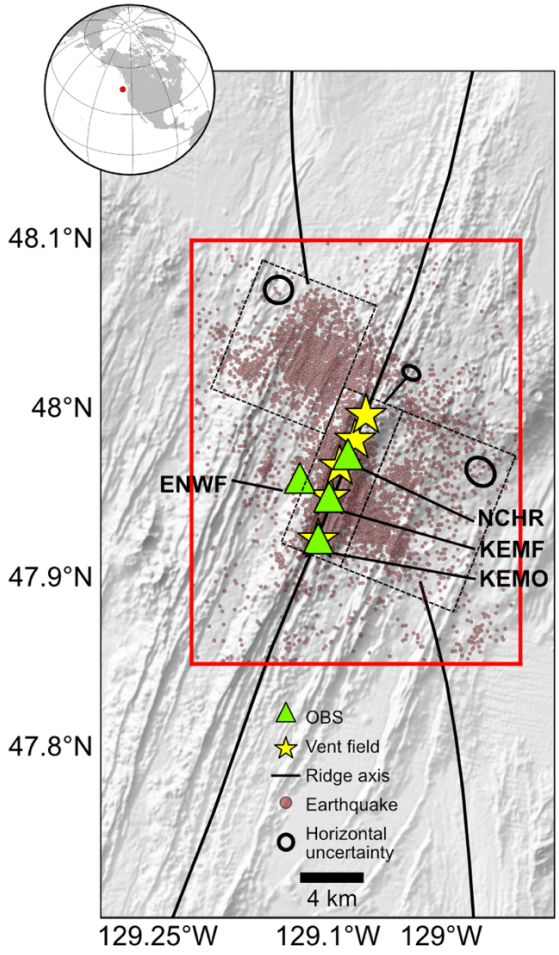

Figure 1. Bathymetry map of Endeavour segment study area shown using hillshade to emphasize structure. Seafloor depths range from 2,100 to 2,750 m. Main tectonic boundaries, including the

overlapping propagating ridge tips from Krauss et al. (2023), are shown in thick black lines. Epicenters for 2016-2021 from the Krauss et al. (2023) catalog are shown with pink circles, with corresponding horizontal uncertainty ellipses shown for the three main areas delineated with black dashed lines. The region in which earthquakes used in this study is shown with a red box. The four OBSs in the 2017 NEPTUNE cabled network are shown with green triangles and annotated with their station codes. The five main vent fields are shown with yellow stars, and the inset shows the general global location of the study area.

Visual inspection of the microearthquake catalog constructed from the 2016-2021 NEPTUNE OBS data indicates abundant multiplet activity with nearly identical earthquake waveforms at times arriving within seconds of each other (Krauss et al., 2023). Because the existing catalog only highlights closely spaced multiplets, it is unknown whether this activity is spatially widespread and whether some multiplets are continuous-type. To explore how multiplet earthquakes could inform mid-ocean ridge deformation, we perform earthquake clustering via waveform cross correlation for the Endeavour segment for 2017. We find many multiplet earthquake families both on- and off-axis, and we detail endmember examples of burst- and continuous-type families to investigate the range of potential driving mechanisms.

4.2 Data

We use ocean bottom seismometer (OBS) waveform data from the Ocean Networks Canada NEPTUNE cabled observatory (Heesemann et al., 2014) and the earthquake catalog constructed from this data for 2016-2021 (Krauss et al., 2023). NEPTUNE hosts a small network at the Endeavour segment, with ~2 km station spacing centered on the spreading axis near the hydrothermal vent fields (Figure 1). The maximum number of stations simultaneously operating during this period is four (see Krauss et al. 2023 for network details). The three stations within the axial valley (NCHR, KEMF, and KEMO) are GeoSense BH1 short period seismometers housed in coreholes, and the off-axis station (ENWF) is a buried Guralp CMG-1T broadband seismometer. Krauss et al. (2023) detected earthquakes using automatic phase picking and located earthquakes using NonLinLoc (Lomax et al., 2000) with 3-D *P* and *S* wave velocity

models derived from a marine active seismic experiment. The *P* wave model (Arnoux et al., 2019) and the *S* wave model (Kim et al., 2019) cover the entirety of the Endeavour segment over a 60 x 90 x 9 km^3 volume with 0.2 km grid spacing. We use these same velocity models for our analysis.

We focus on one year only, 2017, when the network geometry is strongest. We also subset the starting catalog to only include the areas of elevated seismicity in the central segment where earthquake locations are better constrained (within ~10 km of the network, limits shown in Figure 1), which leaves 8,364 events. Earthquakes further than 2 km from an OBS have fixed depths, at 2 km when they are in the vicinity of the vent fields and 3 km elsewhere. The limited network geometry means that earthquake location uncertainties can be large; typical uncertainty ellipses for a given region are shown in Figure 1.

4.3 Methods

4.3.1 Earthquake cross correlation

We cross correlate pairs of earthquakes using the Z channel for *P* wave picks and the E channel for *S* wave picks. For each earthquake, raw data is pulled in for 5 seconds before and after the earliest and latest picks. We detrend the raw data, apply a 4^{th} order Butterworth bandpass filter from 8-35 Hz, and trim a window around the pick time: [-0.2,+0.6] s for *P* waves, and [-0.3,+0.6] for *S* waves. We cross correlate waveform pairs, allowing up to 0.5 s of lag and normalizing by dividing by the square root of the autocorrelation of each waveform. For use in earthquake clustering and relocation, we calculate the differential arrival times using the shift of the maximum correlation and save the cross-correlation value, which is the maximum of the normalized cross correlation.

4.3.2 Earthquake clustering and relative relocation

To identify earthquake multiplet families with similar waveforms, we employ GrowClust3D, an open-source Julia package that uses cross-correlation values and differential arrival times to cluster similar earthquakes hierarchically and perform relative relocation with 3-D velocity models (Trugman et al., 2022). For a pair of earthquakes to be clustered together, we require at least 4 out of 8 channel pairs to have cross-correlation values higher than a chosen minimum threshold.

The GrowClust algorithm performs relative relocation of clustered earthquakes through a grid-search approach and chooses the solution that minimizes the L1 norm of the travel time residuals (Shearer et al., 2005; Trugman & Shearer, 2017). The joint clustering and relocation approach of GrowClust3D prevents the computation of formal uncertainties. Instead, non-parametric location uncertainties are estimated from a bootstrap approach that perturbs relative relocations by resampling the input cross-correlation data (Efron & Tibshirani, 1994). Horizontal and vertical uncertainties are derived from the median absolute deviation of the resampled hypocenter distribution. For uncertainty estimates, we employ 1000 iterations of the bootstrap resampling.

4.3.3 Template matching

For a few earthquake clusters of interest, we perform additional analysis. To ensure detection of all multiplet earthquakes belonging to a given cluster, we perform matched-filter detection with a template event. For each earthquake in a cluster, the signal-to-noise ratio (SNR) is calculated for each pick as the ratio of the maximum RMS value of signal and noise windows taken from [-0.1,+0.2] s and [-1,-0.1] s relative to the pick, respectively. The earthquake with the highest median SNR across all picks is chosen as the template. We then manually repick *P* and *S* waves, yielding 8 total picks for the template event.

Matched-filter detection is then performed using EQcorrscan, an open-source Python package (Chamberlain et al., 2017). Using the repicked template event, we build a template from waveform data filtered using a 4th order Butterworth bandpass from 8-35 Hz. For each channel (*P* waves on Z component, *S* waves on E component), the template is 0.8 s long starting 0.1 s before the pick. The template is then used for matched-filter detection for all data in 2017. We require a detection value (the sum of cross-correlation coefficients for all channels) of at least 3 and a 0.75 s minimum gap between detections. We note that these parameters are conservative and at this stage, yield many detections with relatively low cross-correlation values.

4.3.4 Absolute distances between earthquakes

Identifying multiplet earthquakes as true repeating earthquakes requires verification that their interevent spacing is smaller than their source area. Because the poor network geometry at our study site introduces considerable location uncertainties (Figure 1), we estimate minimum absolute distances between earthquakes using subsample differential *S*-*P* arrival (*dSP*) times. We calculate *dSP* times using the same cross correlation method described in Section 3.1, but data are upsampled to 1000 Hz via the Lanczos method (Burger & Burge, 2009) with a 50-sample window width to provide 0.001 s precision. We use lag times to calculate the *dSP* time for each of the four stations for each earthquake, relative to a given event.

The *dSP* time can be related to distance between hypocenters *dx* as:

$$dx = \frac{1}{(\frac{1}{V_S} - \frac{1}{V_P})} dt_{S-P} \quad \text{Eq. 1}$$

where S wave velocity V_S and P wave velocity V_P are taken as the depth-averaged velocities from the 3-D velocity models at 2 km depth: 6.35 km/s for V_P and 3.60 km/s for V_S. A *dSP* time of 0.001 s is therefore equivalent to a minimum absolute hypocentral separation of 8 meters.

4.3.5 Earthquake source parameters

Following Krauss et al. (2023), we first estimate earthquake moments using displacement spectra calculated for a 1 s window around S waves and 0.3 s windows around P waves. Displacement spectra are corrected for attenuation following Toomey et al. (1988) and Tréhu & Solomon (1983), and then moments are calculated following Brune (1970) (see Krauss et al., 2023 for parameter details). Moment magnitudes are then calculated following Hanks & Kanamori (1979).

When using repeating earthquakes to estimate slip rates, stress drops are commonly assumed to vary from 3-10 MPa (Gao et al., 2021). The most widely-used relationship between earthquake moment and earthquake slip for repeating earthquakes infers that stress drop increases with decreasing earthquake moment (Nadeau & Johnson, 1998), which contrasts with observations of typical earthquakes (Abercrombie, 1995). Since most earthquakes at the Endeavour segment have moment magnitudes < 3, we verify appropriate stress drops by exploring corner frequencies of S waves, which we found to be more consistent than P waves. We follow the method of Abercrombie et al. (2017), which estimates the corner frequency of a given earthquake from the spectral ratios between the earthquake and empirical Green's functions (EGFs), taken as nearby similar earthquakes that are at least 1 magnitude unit smaller. In this method, the path, instrument and site effects are removed, leaving only the source properties. Following Abercrombie et al. (2017), we consider EGF candidates within 2 km epicentral distance from the target earthquake and require that candidate EGF waveforms cross

correlate with the target event. Using the EGF spectral ratios, stress drop $\Delta\sigma$ can then be calculated from *S* wave corner frequency f_c assuming the circular rupture model of Eshelby & Peierls (1997):

$$\Delta\sigma = \frac{7M_0}{16}\frac{f_c^3}{k^3V_S^3} \quad \text{Eq. 2}$$

where M_0 is earthquake moment, in N-m, V_S is *S*-wave velocity in m/s, and *k* is taken from Abercrombie et al. (2017) as 0.26. Rupture radius *r* assuming circular rupture can then be calculated as:

$$r = \sqrt[3]{\frac{7M_0}{16\Delta\sigma}} \quad \text{Eq. 3}$$

And, following, earthquake slip *d* can be calculated as:

$$d = \frac{M_0}{\mu\pi r^2} \quad \text{Eq. 4}$$

using a shear modulus μ of 36 GPa, obtained from a V_S of 3.60 km/s and a density of 2800 kg/m^3.

4.3.6 Diffusive triggering fronts

If an earthquake swarm is driven by the diffusion of fluids, earthquake locations can be expected to define a triggering front of the form:

$$R = \sqrt{\pi D t} \qquad \text{Eq. 5}$$

where R is the distance from the initial event, t is the time from the initial event, and D is a hydraulic diffusivity coefficient in m^2/s related to permeability (Shapiro et al., 1997).

4.4 Results

4.4.1 Overall multiplet patterns in starting catalog

To characterize the overall patterns of multiplets at the Endeavour segment for 2017, we begin by clustering earthquakes in the starting catalog. We cross correlate all earthquake pairs within 2 km of each other. Using cross-correlation values and differential arrival times, we group the initial 8,364 events into clusters with GrowClust3D. We require a minimum cross-correlation value of 0.85 across at least 4 channel pairs for this initial clustering.

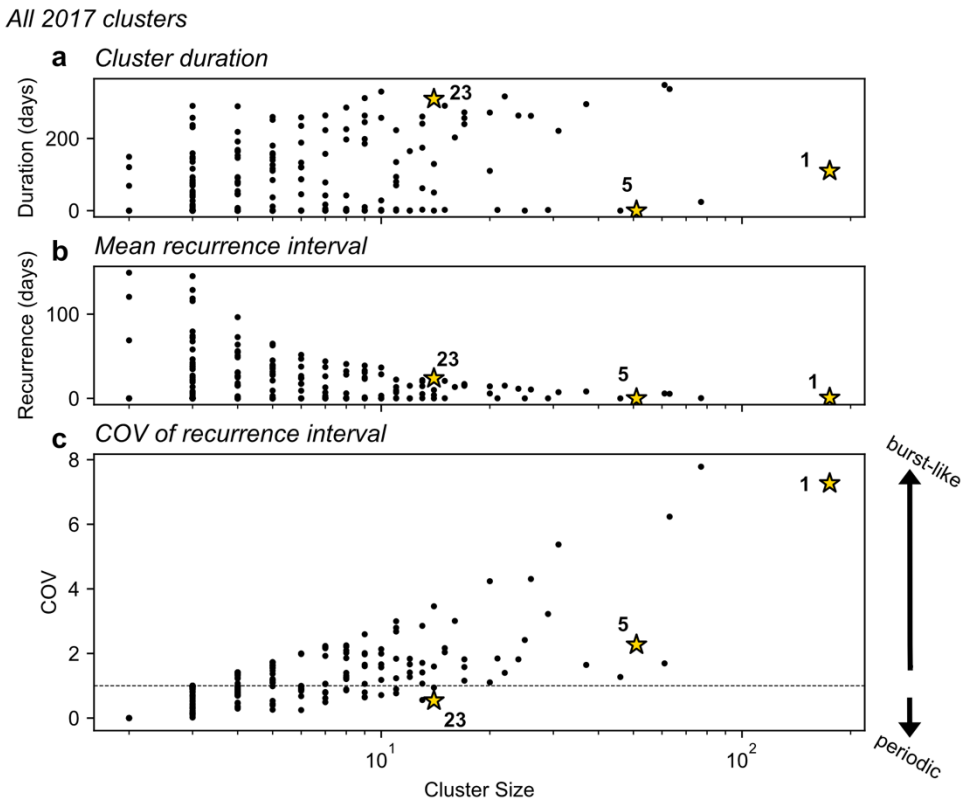

Figure 2. Clustering results from the starting catalog for 2017 showing 219 clusters that contain more than 2 events. **(a)** Cluster size versus cluster duration in days. Note that the x-axis has a logarithmic scale. Here and in the remaining subplots, Clusters 1, 5, and 23, which are analyzed in detail, are marked with yellow stars and annotated. **(b)** Cluster size versus mean recurrence interval of events. **(c)** Coefficient of variation (COV) of recurrence intervals for a given cluster. The horizontal line at COV = 1 denotes that the recurrence has a Poisson distribution; for COV < 1, the recurrence interval is quasiperiodic to periodic, while for COV > 1, multiplets are clustered in time (burst-like) (Kagan & Jackson, 1991).

We find 380 clusters in total, 161 of which contain just two earthquakes (doublets). Of the initial 8,364 events, 2,243 were added to a cluster. Figure 2 summarizes the distribution of cluster characteristics for all clusters with more than two events. The largest cluster, Cluster 1, contains 175 events. Cluster durations, or the time between the first and last event in a cluster, vary from hours to nearly the entire year (Figure 2a). To characterize whether clusters are more burst-like or periodic in time, we calculate the coefficient of variation (COV) of their recurrence intervals (Kagan & Jackson, 1991). COV values of 1 indicate Poisson recurrence, values < 1 indicate periodic behavior, and values > 1 indicate temporal clustering (burst-like). Perfectly

periodic clusters would have a COV of zero. COV values range from 0.02 to 7.78 (Figure 2c). Of the non-doublet clusters, there are 121 continuous-type clusters (COV < 1), containing 528 earthquakes total. The remaining 98 non-doublet clusters are burst-type (COV > 1), containing 1,393 earthquakes total.

There are no strong patterns in the spatial distribution of the COV of recurrence, with both types of clusters distributed throughout the study area. We plot the cluster centroids of all non-doublet clusters, colored by their COV of recurrence, in Figure 3a. We see that clusters are located both near the vent fields and in the off-axis regions of high seismicity, northwest of the vent fields in the Southwest Endeavour Valley and east of the vent fields on the East Flank. We note that these centroids, which were relatively relocated using GrowClust3D, were constructed using automatic phase picks that were not manually verified, such that mispicks and high location uncertainties are possible especially outside of the network (see Figure 1). We do not report earthquake depths, which are not constrained outside of the network.

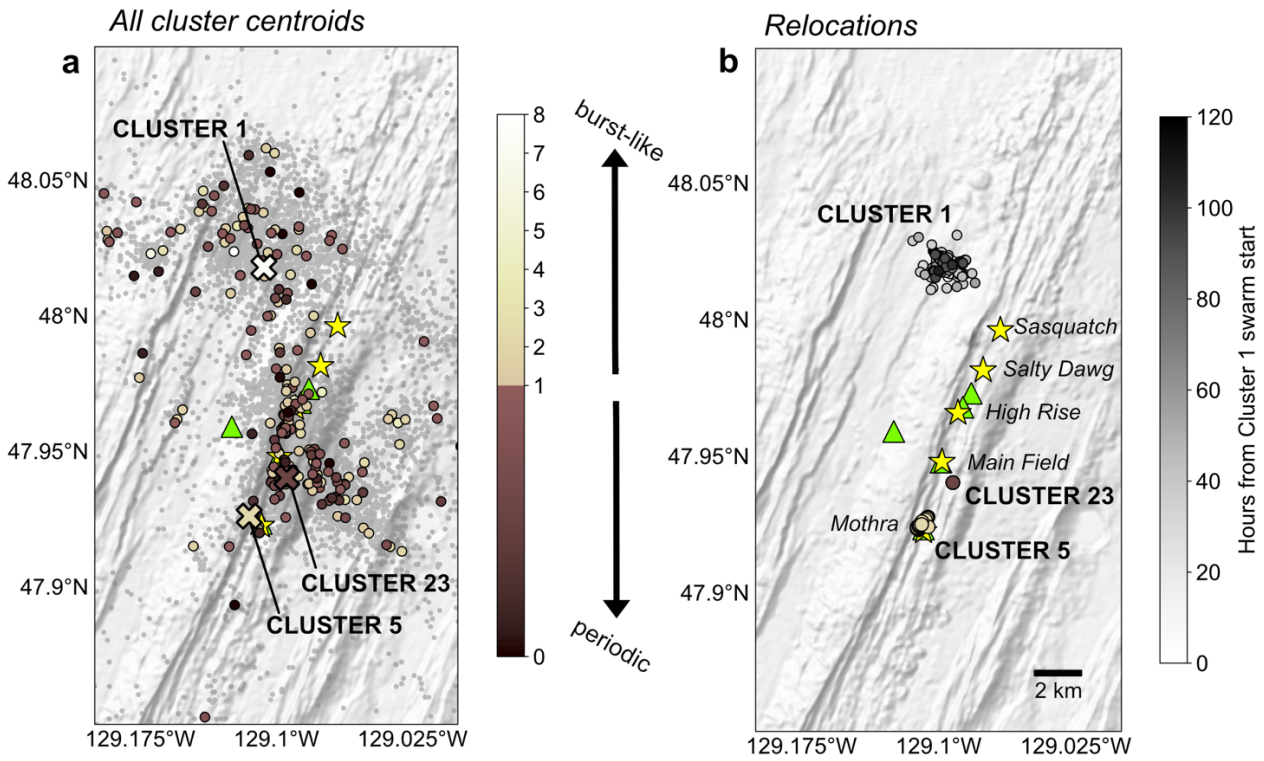

Figure 3. (a) Bathymetry map showing centroids of non-doublet clusters from the starting catalog, relatively relocated using GrowClust3D. Cluster centroids are shown using circles colored by the COV of recurrence interval. The distribution of background seismicity for 2017 is shown using transparent grey dots. Clusters 1, 5 and 23 are annotated and shown using large X-marks colored by their COV of recurrence: 7.27, 2,27, and 0.54, respectively. All other symbols follow Figure 1. **(b)** Bathymetry map showing epicenters of relative relocations of the repicked, template-matched clusters of interest. Cluster 23 shows only the 8 earthquakes identified as repeating. Cluster 1 epicenters are colored by their occurrence as hours from the start of the swarm. Names of the five main hydrothermal vent fields (yellow stars) are annotated using italic text. All other symbols follow Figure 1.

We identify three endmember clusters for further analysis (Figure 3a). To explore whether the periodic-type clusters are repeating earthquake sequences, we investigate Cluster 23. Cluster 23 has 14 events, a duration of 309 days, a mean recurrence interval of 24 days, and a COV of recurrence of 0.54, indicating quasi-periodic recurrence (Figure 2). To explore the potential driving mechanisms of burst-like clusters, we investigate Clusters 1 and 5. Cluster 1 is the largest cluster, with 175 events, a mean recurrence interval of 0.63 days, and a COV of recurrence of 7.27. Cluster 5 is a smaller swarm-like cluster with 51 events, a mean recurrence interval of 66 seconds, and a COV of recurrence of 2.27.

4.4.2 Repeating earthquakes: Cluster 23

We manually repick the highest SNR event from Cluster 23 and use it as a template to perform matched-filter detection on all data from 2017. Because we are specifically investigating whether Cluster 23 represents a repeating earthquake sequence, we need to determine whether the interevent distances of detections are smaller than their rupture radii. To estimate the rupture radius, we explore *S* wave corner frequencies for the two highest SNR repeating earthquakes, which includes the template event and another event with median waveform cross correlation > 0.9. For spectral ratio calculation, we chose candidate Empirical Green's Functions (EGFs) as earthquakes from the starting catalog of Krauss et al. (2023) with moment magnitudes from 0.1-0.8, eight picks, and epicenters within 2 km of the Cluster 23 epicenters. This resulted in 169 candidate EGFs. Given the moment magnitudes of the Cluster 23 events, the method of Abercrombie et al. (2017) suggests that candidate EGF cross-correlation values should be calculated with a low pass filter of 25 Hz. We find that very few of our EGF candidates have cross-correlation values of at least 0.7 if frequencies up to 25 Hz are considered, so we instead only require a cross-correlation value > 0.7 in the 2-10 Hz range. This leaves 11 EGFs for the ENWF station, 2 for NCHR, 40 for KEMO, and 46 for KEMF (Figure 4). Both the cross-correlation values and spectral ratios were calculated using a 0.4 s window around the *S* wave, also following Abercrombie et al. (2017).

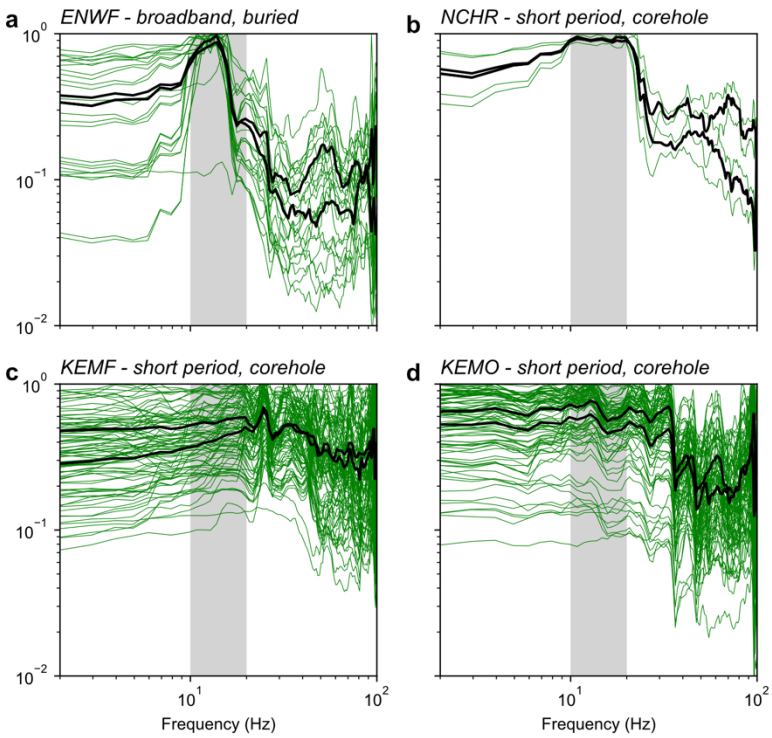

Figure 4. *S* wave spectral ratios for the two earthquakes from the Cluster 23 repeater sequence with the highest SNR, for all four stations: **(a)** ENWF, **(b)** NCHR, **(c)** KEMF, and **(d)** KEMO. Station ENWF is a buried broadband OBS and the other stations are corehole short period OBSs. Spectral ratios from EGFs are shown in green, with the stacked spectral ratios for the two different earthquakes overlain in black. The range of corner frequencies that we use to calculate slip rates, 10-20 Hz, is shown with a grey box.

Figure 4 shows the *S* wave displacement spectral ratios between the two highest SNR Cluster 23 earthquakes and the EGF subset for each of the four stations. We see that the shape of spectral ratios and apparent corner frequency varies considerably between stations. Station ENWF, which is expected to have the highest quality data because it is buried and is the only broadband station, suggests *S* wave corner frequencies between 10-20 Hz (Figure 4a). Contrastingly, the short period corehole instruments NCHR, KEMO, and KEMF suggest higher corner frequencies between 20-40 Hz (Figure 4b-d). We assume a 10-20 Hz range for our calculations due to our higher confidence in the ENWF instrument. We calculate the moments of the two earthquakes and use the 10-20 Hz range in corner frequency to estimate a range of stress drops from 0.3-2.8 MPa (Equation 2). This corresponds to a range in rupture radii from 47-98 m (Equation 3),

suggesting that earthquakes located less than 47 m from the template event can be considered as repeating earthquake candidates.

To avoid the influence of location errors introduced by the small network, we approximate interevent distance using subsample differential S-P times, which represent the minimum absolute distance between events. We note that we would need constraints on uncertainties in all directions to calculate maximum absolute distances. However, because we only calculate the minimum, we conservatively only consider detections that have a maximum differential subsample S-P time of 0.003 s (equivalent to 30 m; Equation 1). We also require high waveform similarity: we only consider detections that have a cross-correlation value greater than 0.9 on at least 4 channels. True repeating earthquakes are also expected to have the same moment release (e.g., Nadeau & Johnson, 1998). We therefore calculate moments and moment magnitudes for all detections, and only consider detections that have a moment magnitude difference of less than 0.3 with the template event.

Our requirements leave eight detections as members of the true repeating earthquake sequence out of 81 initial detections, with a median recurrence interval of 42 days from January 24 to November 10 (Figure 5). We calculate initial locations for these events using NonLinLoc (see Krauss et al., 2023) and relocate them using GrowClust3D (Figure 3b). The relocations are consistent with the original cluster centroid, east of the Main Field hydrothermal system near the eastern axial wall at a depth of 1.5 km (Figure 3). The template event has a moment magnitude of 1.84, with moment magnitudes of all eight events ranging from 1.56-1.86. We assume that this repeating earthquake sequence represents a non-transient stable slip, so we use it to estimate a slip rate. We use the 0.3-2.8 MPa range of stress drops to calculate a range of potential cumulative slip rates of 4.5-20 mm/year (Equation 4, Figure 5e).

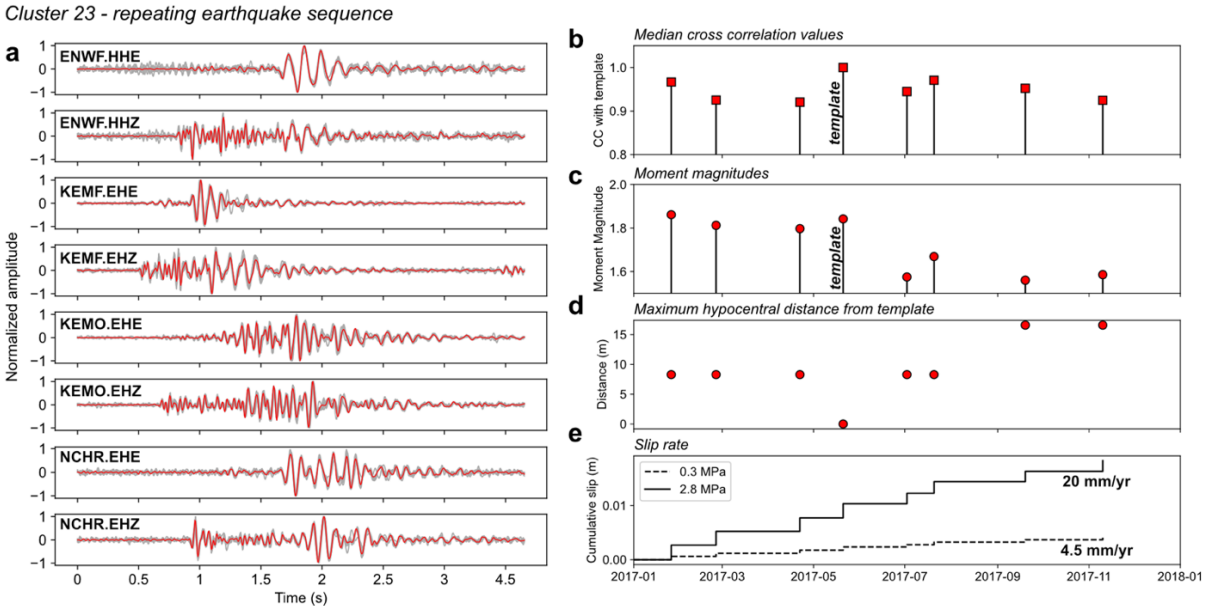

Figure 5. Details for Cluster 23, identified as a repeating earthquake sequence. **(a)** Waveforms for the 8 earthquake identified as repeating events from all channels used, bandpass filtered from 8-35 Hz, normalized by maximum amplitude, and aligned by cross-correlation. The waveform of the template event is overlain in red with the remaining waveforms in grey. **(b)** Stem plot showing median cross-correlation values of the 8 events identified as repeating earthquakes. The template event is annotated. **(c)** As in (b) but showing moment magnitudes. **(d)** Minimum hypocentral distances from the template event, calculated using subsample differential S-P times.. **(e)** Cumulative slip of 8 repeating earthquake events, calculated using two different stress drops. Slip rates from the best fit straight line are annotated.

4.4.2 Burst-like multiplets

4.4.2.1 Cluster 1

We manually repick the highest SNR event from the largest cluster in 2017, Cluster 1, and use it as a template to perform matched-filter detection on all data from 2017. For burst-like multiplet families that occur in the form of earthquake swarms, we do not expect perfectly correlated waveforms as in repeating earthquakes. Instead, we may expect nearby source patches that migrate as the swarm progresses. We therefore apply a less strict filtering scheme than used for Cluster 23: we only consider detections that are relocated by the GrowClust3D algorithm. This requires that an event have at least 4 channels with cross-correlation values > 0.85 with respect to at least one other event in the family. Because the template earthquake is located

outside of the network, we calculate initial locations for all detections using NonLinLoc with a fixed depth of 3 km and relocate them using GrowClust3D (Figure 3b). GrowClust3D relocates 172 events total, which occur during an earthquake swarm that lasts ~100 hours from 22:00 on June 25 to 12:00 on June 30 (Figure 6a-b). The relocations are consistent with the original cluster centroid, ~3 km northwest of the Sasquatch vent field (Figure 3a).

We calculate moments and moment magnitudes and find that the template event has the largest magnitude, 3.41. Moment magnitudes of the remainder of the swarm have a minimum of 1.56 and a median of 1.86; four events have moment magnitudes > 3 (Figure 6a). To get a sense for swarm migration, we estimate absolute hypocentral distance between the first event in the swarm and the following events using the GrowClust3D relocations, which account for the station geometry and the velocity structure. Location uncertainties are large due to earthquakes locating outside the network, but Cluster 1 appears to exhibit clear migration (Figure 6b).

The GrowClust3D relocations suggest a migration of 2 km over the ~100 hour duration of the swarm. Fluid-induced swarms are typically observed to migrate following a triggering front described by a diffusivity value *D* (Shapiro, 2015; Equation 5). The Cluster 1 swarm visually appears to exhibit a triggering front: we overlay several diffusion curves that show reasonable agreement with the swarm migration (Equation 5, Figure 6b). Assuming a fluid diffusion front beginning at the start of the swarm, the observed migration suggests diffusivity values near ~2.5 m^2/s. A back front is not apparent in the data (Figure 6b).

4.4.2.2 Cluster 5

Manual repicking and template matching for Cluster 5 shows that the main swarm occurs over less than 1 hour, starting at 00:45 on May 6. As for Cluster 1, we only consider detections that are relocated by the GrowClust3D algorithm with a cross-correlation requirement of 0.85 on

at least 4 channel pairs. This leaves 70 events in the main swarm (Figure 6c). Relocations of the repicked events show that the swarm is located beneath the Mothra vent field, with the template event at 1.9 km depth (Figure 3b). The largest magnitude event in the swarm is the template event, with moment magnitude 2.6. The smallest event has moment magnitude 1.14, and the median across the swarm is 1.40. Three events in the swarm have moment magnitudes larger than 2 (Figure 6c).

The GrowClust relocations of the Cluster 5 swarm show that nearly all earthquakes occur within 600 meters of the first earthquake in the sequence (Figure 6d). Most earthquakes occur within 30 minutes of the start of the swarm. For visual comparison, we overlay the triggering front corresponding to the diffusivity value suggested by Cluster 1, 2.5 m^2/s (Figure 6d), which clearly does not match the migration of Cluster 5. Extremely high diffusivity values near 50 m^2/s would be needed to create a triggering front that shows agreement with the migration (Figure 6d). There is some evidence of rapid migration at the start of the swarm; overlaying a linear migration front at a speed of 4 km/hour shows some visual agreement (Figure 6d). However, given the location uncertainties, we cannot resolve a clear migration of the Cluster 5 swarm.

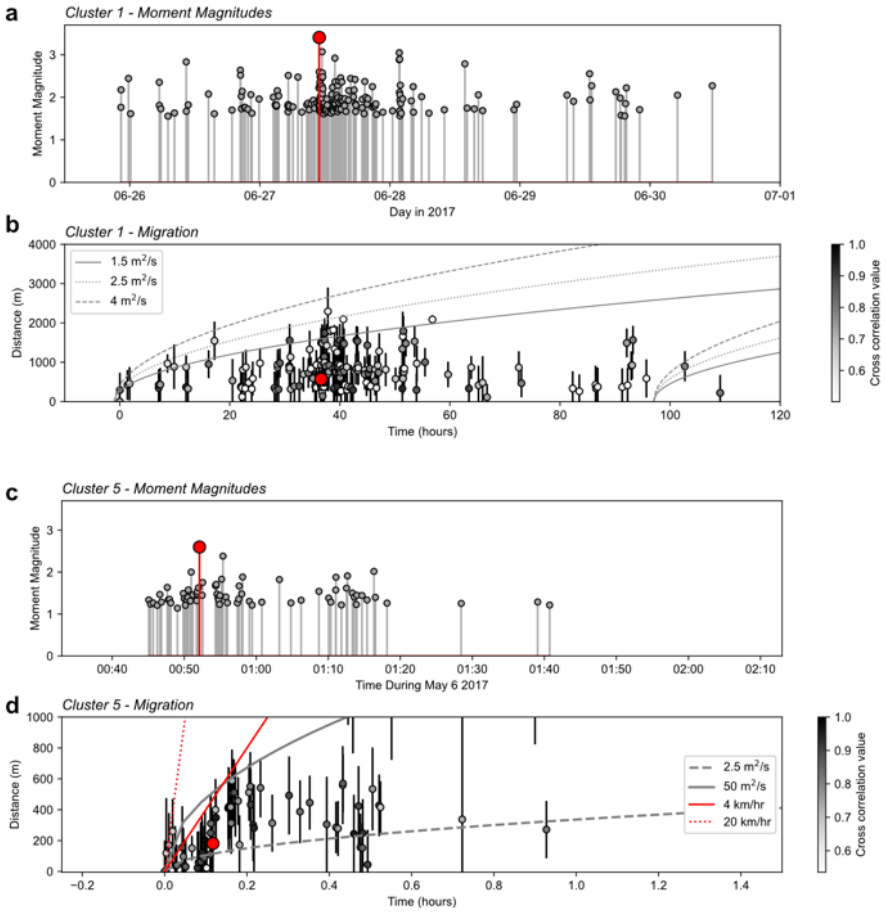

Figure 6. Details for Clusters 1 and 5, examples of burst-type multiplet families. **(a)** Moment magnitude distribution over time shown as a stem plot for the 172 events in the main Cluster 1 swarm. The template event, the largest event in the swarm, is shown with a red marker. (**b)** Migration of the Cluster 1 swarm shown as absolute distance from the first relocated hypocenter over time, as calculated by GrowClust3D. Events are colored by their cross-correlation value with the template, which is shown with a larger red circle. Error bars correspond to the maximum location uncertainty (horizontal or vertical) calculated by GrowClust3D via bootstrapping. For visual assessment, fluid diffusion triggering and back-fronts are overlain for three different diffusivity values (not fit to the data). The triggering front begins at 0 hours and the back-front is placed at 97 hours. **(c)** Same as (a) but for the 70 events in the main Cluster 5 swarm. **(d)** Same as (b) but for the Cluster 5 swarm. Note the different x- and y-axes. The dashed gray line is the same triggering front shown in (b), for a diffusivity of 2.5 m^2/s. The red lines are for linear migration at two different speeds.

4.5 Discussion

4.5.1 - Evidence of aseismic slip

Cluster 23 appears to contain a true repeating earthquake sequence that spans nearly the entire year of 2017 (Figure 5). High waveform cross-correlation values, consistent recurrence intervals, and similar moment magnitudes all indicate repeating rupture, and our calculated *dSP*

times are consistent with overlapping rupture patches (Gao et al., 2021; Nadeau & Johnson, 1998). This behavior is consistent with aseismic creep or a long-term slow slip event (Uchida & Bürgmann, 2019). However, we note that location uncertainties would need to be resolved in all directions to verify that maximum absolute interevent distances are indeed smaller than rupture radii. Different window sizes for waveform cross-correlation should also be explored to ensure that the *P* wave windows do not include any *S* wave signal, which could contaminate the *dSP* time results.

The small network coverage precludes the association of these earthquakes to a specific fault plane. However, their location suggests they could be related to normal faults that form the east side of the axial valley. An experiment with a larger autonomous OBS network in 1995 showed that the axial valley faults dip at 70° (Wilcock et al., 2002). Assuming this dip and a half-spreading rate of ~25 mm/year (DeMets et al., 2010), a fault slip of 73 mm/year would be required to fully accommodate spreading. If the Cluster 23 repeating sequence results from aseismic slip on the fault, the range of slip rate estimates (4-20 mm/year) suggests that 5-27% of the half-spreading rate is accommodated through aseismic fault slip (Figure 5e). For an intermediate-rate ridge, where fault slip is assumed to account for only ~20% of total plate motions (Ito & Behn, 2008), this suggests that most fault slip occurs aseismically. This is consistent with the aseismic contribution suggested by coupling rates at both slow spreading ridges (40-90%, Olive & Escartín, 2016) and fast spreading ridges (~99%, Cowie et al., 1993). Further investigation is needed to resolve the repeating earthquakes to a fault plane and investigate whether they are associated with the axial valley walls.

Our estimates of coupling rates are limited by our ability to constrain corner frequencies. Between the four available stations, we see large variations in apparent corner frequencies (Figure 4). This may be due to recording quality of the different stations: three of the stations,

NCHR, KEMF, and KEMO, are short period instruments in coreholes, while station ENWF is a broadband instrument buried within sediment. Polarization analyses of *P* waves recorded by these same instruments show that the three short period stations exhibit preferred polarization directions independent of earthquake azimuth, suggesting they may be poorly coupled and/or are susceptible to preferred ground motion caused by scattering very near the instruments (Krauss et al., in review). This same effect is not observed at station ENWF, which is the only station located outside of the highly fractured axial graben (Figure 1). Regardless of station recording quality, with a four station network we cannot confidently constrain corner frequencies if we lack azimuthal coverage; if an earthquake source displays even minimal directivity, it can lead to significant differences in corner frequencies at different azimuths (Kaneko & Shearer, 2015).

The identification of repeating earthquakes at the Endeavour segment provides direct evidence for aseismic slip at a mid-ocean ridge and suggests that multiplets could be used as a tool to better constrain fault coupling patterns in space and time. Tracking repeating earthquake families at the Endeavour segment over a longer time period could show whether they start and stop, and therefore represent more transient slow slip events (Nadeau & McEvilly, 2004; Uchida et al., 2016), or whether they occur continuously, consistent with aseismic creep. Changes in recurrence rates or the spatial extent of repeaters throughout a rupture cycle could also track whether slip rates on different portions of the segment increase as the ridge approaches failure.

4.5.2 - Multiple drivers of earthquake swarms

Investigation of two different burst-like multiplet families suggests multiple driving mechanisms for earthquake swarms at the Endeavour segment. Cluster 1, which shows spatiotemporal migration, is generally consistent with a diffusive triggering front (Figure 6b), as expected for fluid-induced earthquake swarms (Shapiro, 2015). A back-front is not obvious, but back-fronts tend to be less clear in both natural and induced earthquake swarms (Shapiro &

Dinske, 2009). The diffusivity values of the triggering fronts that visually agree with the Cluster 1 migration, near ~2.5 m^2/s (Figure 6b), are higher than typically seen at rift-related swarms (0.02-0.25 m^2/s) and in volcanic regions (0.2-0.7 m^2/s) (Chen et al., 2012). However, these diffusivities lie within the range observed globally for hydraulic-fracturing-induced earthquake swarms, 0.1-10 m^2/s (Talwani et al., 2007). The relatively high diffusivity seen for the Cluster 1 swarm may reflect the high permeability associated with the extensional environment near black smoker vents (Lowell & Germanovich, 1994; Wilcock & McNabb, 1996); diffusivity is proportional to the hydraulic permeability of the fault (Shapiro et al., 1997)

The migration rate of the Cluster 1 swarm is much slower than swarms driven by a migrating slow slip event (0.1-1 km/hour), as has been seen at oceanic transform faults (Roland & McGuire, 2009). However, throughout the duration of the Cluster 1 swarm, there are repeater-like earthquakes that occur very near the starting event with high cross-correlation values (Figure 6b). This suggests there may be an ongoing background loading process in addition to a migrating slip front. Recent laboratory studies suggest that fluid-induced swarms are actually comprised of iterative stages, where diffusing fluids create a slowly migrating front of pressure build-up that generates faster aseismic slip fronts once fault heterogeneities are encountered (Danré et al., 2022; Eyre et al., 2019). This is further supported by detailed observations of natural swarms with extensive seismic networks, which resolve multiple stages of migration within a single swarm: slower background migration rates (fluid diffusion) are interspersed with periods of faster migration and more repeaters (aseismic slip) (De Barros et al., 2020; Hatch et al., 2020). Even with relatively poor constraints on earthquake migration, the Cluster 1 swarm hints at multiple phases of migration: around ~35 hours, migration rate appears to increase with the larger earthquakes (Figure 6b). This suggests that improved migration constraints could resolve multiple driving mechanisms within a single swarm.

It is also possible that the Cluster 1 swarm represents a magmatic event such as a dike injection, but we think it is unlikely. If the spatiotemporal migration of Cluster 1 is instead considered to be linear, it suggests a migration speed on the order of ~1 km/day. A similar migration rate of ~1 km/day was observed for an multiplet swarm associated with an injected dike in the Yellowstone caldera (Massin et al., 2013). However, past dike injections at the Endeavour segment, including the June 1999 and March 2005 events, displayed much faster migration rates of 0.25-3.2 km/hour (Johnson et al., 2000; Krauss et al., 2023). Similarly high migration rates from 0.3-3 km/hour are typical for dike propagation elsewhere, including Axial Seamount and Krafla volcano (Einarsson & Brandsdóttir, 1980; Wilcock et al., 2016). Dike injections also tend to display an overall farther migration on the order of ~10 km, including the Yellowstone and previous Endeavour events (Krauss et al., 2023; Massin et al., 2013).

In contrast to the Cluster 1 swarm, the Cluster 5 swarm displays no obvious spatiotemporal migration and is much shorter in duration than the Cluster 1 swarm (< 1 hour versus ~100 hours) (Figure 6). It is possible that there is a rapid linear migration over ~600 m at the beginning of the Cluster 5 swarm, but location uncertainties are large in relation to this distance, and the speed of the potential migration as suggested by visual inspection (~4 km/hr) is much faster than expected for earthquake swarms driven by aseismic slip (Figure 6d). The magnitude of the diffusivity value needed to create a visually fitting triggering front, ~50 m^2/s, is also unrealistic. Both scenarios, either non-migration or very rapid but limited migration, suggest that the Cluster 5 swarm is driven by an internal mechanism rather than an external mechanism such as aseismic slip, fluid diffusion, or magmatic injection (Fischer et al., 2023). Internally driven swarms are a result of the earthquake ruptures themselves, which trigger adjacent ruptures via stress changes and the creation of pore space (Yamashita, 1999). This same process is consistent with aftershock sequences.

4.6 Conclusions and Future Work

Our investigation of the starting earthquake catalog of Krauss et al. (2023) suggests that multiplet earthquakes at the Endeavour segment, which comprise at least 25% of all seismicity, are spatiotemporally widespread and are likely driven by a range of mechanisms including transient fluid diffusion and aseismic creep. We identified a repeating earthquake sequence that provides direct evidence of aseismic slip; slip rates estimated from this sequence indicate that 5-27% of overall plate motion is accommodated aseismically during the period between diking events. Earthquake swarms at the Endeavour segment also appear to include both internally driven (aftershock-like) and externally driven (fluid-induced) swarms. There is evidence that multiplet activity between these endmember behaviors also occurs (Figure 2), suggesting recurring swarms or more short-lived repeating earthquake families. More exhaustive investigation of all multiplet families could potentially identify transient slow slip events and specific fault sections that host recurring slip.

Multiplet earthquake analysis would be greatly enhanced by a larger OBS network with better azimuthal coverage. We have shown that repeating earthquakes offer an alternative way to observe mid-ocean ridge aseismic slip in the absence of seafloor geodesy. However, better estimates of earthquake depths and corner frequencies, which require a larger network, are necessary to resolve fault plane geometries and accurate slip rates of the repeating earthquakes. Improved earthquake locations would also allow better constraints on swarm migration behavior, helping to distinguish between driving mechanisms including fluid diffusion, aseismic slip, internal aftershock sequences, and potentially illuminating multiple mechanisms within a single swarm.

This pilot study suggests that, following network extension, multiplet earthquake behavior could be a useful way to investigate the cause of off-axis seismicity at the Endeavour

segment. Krauss et al. (2023) proposed that off-axis seismicity is driven by the propagating ridge segments that are encroaching on the central Endeavour axis and suggested that both crustal fracturing and degassing from underlying mantle melt could generate seismicity. Observed varied multiplet activity off-axis at the Endeavour segment, showing both periodic and burst-like clusters, suggests that multiple mechanisms of deformation are at work in those areas (Figure 3a). Multiplet earthquake analysis in these off-axis regions could help distinguish between tectonic, volcanic, and hydrologic mechanisms of deformation.

Chapter 5: Potential shallow tectonic tremor signals near the deformation front in central Cascadia

Zoe Krauss[1], William Wilcock[1], Ken Creager[1]

[1]School of Oceanography, University of Washington, Seattle, Washington, USA
[2]Ocean Networks Canada, University of Victoria, British Columbia, Canada

5.0 Abstract

To better constrain the locking state of the shallow Cascadia megathrust, we investigate whether shallow tectonic tremor occurs near the deformation front at ~44.5°N during 2015-2024. We focus on two cabled buried ocean bottom seismometers (OBSs) on the portion of Cascadia that has evidence of partial locking extending offshore: one at Slope Base on the incoming plate ~5 km from the deformation front, and another ~20 km east on the overriding plate at Southern Hydrate Ridge. We first use in situ measured bottom currents to show that shallow burial successfully prevents current-generated noise on OBSs. We then develop a single-station approach to isolate tectonic tremor-like signals based on waveform and spectral characteristics. This technique allows the use of isolated stations and small networks and accounts for emergent signals specific to the marine environment, namely T-phases and ship noise. Application of this approach to the buried OBSs in central Cascadia detects tectonic tremor-like signals at the Slope Base site that cannot easily be attributed to instrumental or environmental noise. These signals are not recorded at the Hydrate Ridge site, suggesting they may be associated with highly localized slip near the deformation front. However, additional observations are required to verify this hypothesis.

5.1 Introduction

Subduction zones host the largest faults on the planet and the potential to generate devastating M9 megathrust earthquakes and tsunamis. Geophysical observations over the past several decades have shown that slip on these faults can occur not only as earthquakes, but also as slow

slip events, where stable slip can last from hours to weeks (Beroza & Ide, 2011; Bürgmann, 2018; Peng & Gomberg, 2010; Rubinstein et al., 2010). Stable slow slip can accommodate a significant portion of overall plate motion and reduce the amount of slip in megathrust events (e.g., Ramos et al., 2021). Slow slip events have also been identified as potential precursors to large megathrust earthquakes (e.g., Kato et al., 2012; Meng et al., 2015). Constraints on whether a subduction zone is completely locked, or undergoes interseismic slow slip, has great bearing on anticipated coseismic and tsunamigenic hazard (Borghi et al., 2016; Carvajal et al., 2022). However, for subduction zones, much of the region of potential stable slow slip lies offshore, where geophysical observations are limited. Improving the ability to make seafloor observations of slow slip is therefore important for constraining subduction zone locking and megathrust hazard.

Tectonic tremor, a non-impulsive seismic signal at 1-10 Hz, is an indicator of slow slip and its presence can inform plate locking state (Ide et al., 2007). Across the global subduction zone network, tectonic tremor has been shown to accompany slow slip at shallow depths above the locked zone, in Japan (Annoura et al., 2017; Obana & Kodaira, 2009; Yamashita et al., 2015), Chile (Saez et al., 2019), New Zealand (Todd et al., 2018), Costa Rica (Walter et al., 2011, 2013) and Central America (Plata-Martinez et al., 2021). However, in contrast to tectonic tremor observed at deeper depths below the locked zone, which displays a broad distribution over hundreds of kilometers (e.g., Ide, 2012; Wech, 2021), shallow tectonic tremor tends to be patchy and more limited along-strike (Takemura et al., 2023). Shallow tectonic tremor also tends to be concentrated around subducting features including seamounts and ridges (Ogiso & Tamaribuchi, 2022; Plata-Martinez et al., 2021; Saez et al., 2019; Todd et al., 2018).

Tectonic tremor is traditionally detected using the network-based method of envelope cross-correlation, which identifies a coherent emergent signal across several seismometers and

localizes the signal source in space (Obara, 2002; Wech & Creager, 2008). This technique has been successful in identifying shallow tectonic tremor in offshore areas where station spacing is small (< ~25 km) and the instruments are relatively close to the tremor source (< ~40 km) (Annoura et al., 2017; Obana & Kodaira, 2009; Plata-Martinez et al., 2021; Saez et al., 2019; Todd et al., 2018). However, autonomous ocean bottom seismometer (OBS) experiments that prioritize covering large areas, such as the Cascadia Initiative and Alaska Amphibious Community Seismic Experiment (Barcheck et al., 2020; Toomey et al., 2014), are not well suited for envelope cross-correlation because their station spacing often exceeds ~50 km. Alternatively, single-station methods have been explored to identify periods of tectonic tremor based on long-duration dominance of the tremor frequency band (~1-10 Hz) over earthquake- or anthropogenic noise-dominated frequency bands (Brudzinski & Allen, 2007; Sit et al., 2012). These single-station methods have proven effective in detecting deep tremor on land-based stations, where tremor tends to last for days at a time, but may not work as well for detecting offshore shallow tremor, which tends to be patchier and shorter in duration (e.g., Takemura et al., 2023).

The identification of tectonic tremor on OBSs is further complicated by marine-specific emergent signals in the same 1-10 Hz frequency band (Wilcock et al., 2014). These include noise from passing ships (e.g., Ross & Kuperman, 1989) and T-phases (e.g., De Caro et al., 2020), which are tertiary earthquake arrivals that travel in the water column. T-phases are typically spindle-shaped (Talandier & Okal, 2001) and can be attenuated at higher frequencies, such that they can be picked in the same 1-10 Hz band as tectonic tremor (Hanson & Bowman, 2006; Lawrence, 2004). T-phases can be distinguished from tectonic tremor because they are better recorded on hydrophones, but they can cause tectonic tremor misdetections on OBSs when using the envelope cross-correlation method (Tréhu et al., 2019). Bottom currents can also generate gliding harmonic tremor signals at frequencies below 10 Hz, as currents above 5 cm/s interact

with the OBS and cause resonance of protruding structures (e.g., Corela et al., 2023; Essing et al., 2021).

Various oceanic noise sources can also impact background noise levels on OBSs. This suggests that if clear relationships can be drawn between OBS noise and environmental factors, they could be used in a similar way to the frequency scanning method of Sit et al. (2012); potential tremor periods could be identified as times when ground velocities exceed that expected from environmental noise. Wind speeds, for one, have been shown to increase microseismic noise from very short period ocean waves and can saturate frequencies of 4-30 Hz. Above a given wind speed, noise levels are thought to rise without limit, potentially due to spray off whitecaps as wind waves break at the surface (McCreery et al., 1993). Bottom current speeds must also be considered; Trehu (1985) showed that, at frequencies below 10 Hz, seismic noise levels increase proportionally with the square of bottom current speeds. However, there are also seasonal patterns in background noise due to marine mammal calls, which affect the ~14-30 Hz band in the wintertime in the northeast Pacific (Andrew et al., 2011; Curtis et al., 1999). This could disrupt environmental noise relationships and complicate frequency scanning methods.

In Cascadia, there is extensive tectonic tremor in the deep downdip portion of the subduction zone (Wech, 2021), but it has not been observed offshore in the shallow subduction zone. Full shallow locking along the majority of the margin is suggested by a lack of offshore seismicity on the plate interface (Morton et al., 2023; Stone et al., 2018) and initial GNSS-acoustic observations near the deformation front (DeSanto et al., 2022). Offshore resolution of geodetic models near the deformation front is poor, but there is some evidence of only partial locking offshore Oregon (Burgette et al., 2009; Li et al., 2018; Schmalzle et al., 2014). In this same region, near ~44.5°N, some of the only offshore seismicity located on the plate interface has been attributed to subducted seamounts (Carbotte et al., 2024; Morton et al., 2018; Trehu et

al., 2015; Figure 1a) and very low frequency earthquakes have been reported (Chaudhuri & Ghosh, 2022). Serendipitously, this is the site of one of the longest continuous deployments of seismometers in offshore Cascadia: two broadband OBSs have been in operation since 2015 on the Ocean Observatories Initiative (OOI) Regional Cabled Array (Figure 1). The OOI OBSs are at an ideal station spacing for joint detection of tremor (~20 km), and are buried, which may reduce noise levels (Duennebier & Sutton, 2007). Given the evidence that this portion of the margin may only be partially locked, we focus on these two stations to search for evidence of shallow tectonic tremor.

In this paper, we first take advantage of the OOI cabled instrumentation, which includes in situ bottom current measurements, to investigate the relationship between buried OBS noise and environmental noise in Cascadia. We demonstrate the advantages of OBS burial and explore whether relationships between OBS noise and wind/bottom current speeds could be used to help identify tremor periods. Then, motivated by the global need for a flexible seafloor tectonic tremor detection method, we develop a single-station approach to identify individual tectonic tremor signals on a single OBS amidst the presence of T-phases and ship noise. This is particularly important offshore Cascadia, which is a major shipping corridor (Dahl et al., 2021) close to multiple transform faults and mid-ocean ridges, which generate many T-phases (e.g., Dziak et al., 2011; Shen & Wu, 2023). We validate this technique using an existing offshore tectonic tremor dataset from a network of OBSs in the Hikurangi subduction zone. We then we apply our approach to the OOI dataset for 2015-2024 to explore whether shallow tectonic tremor occurs offshore Cascadia near ~44.5°N.

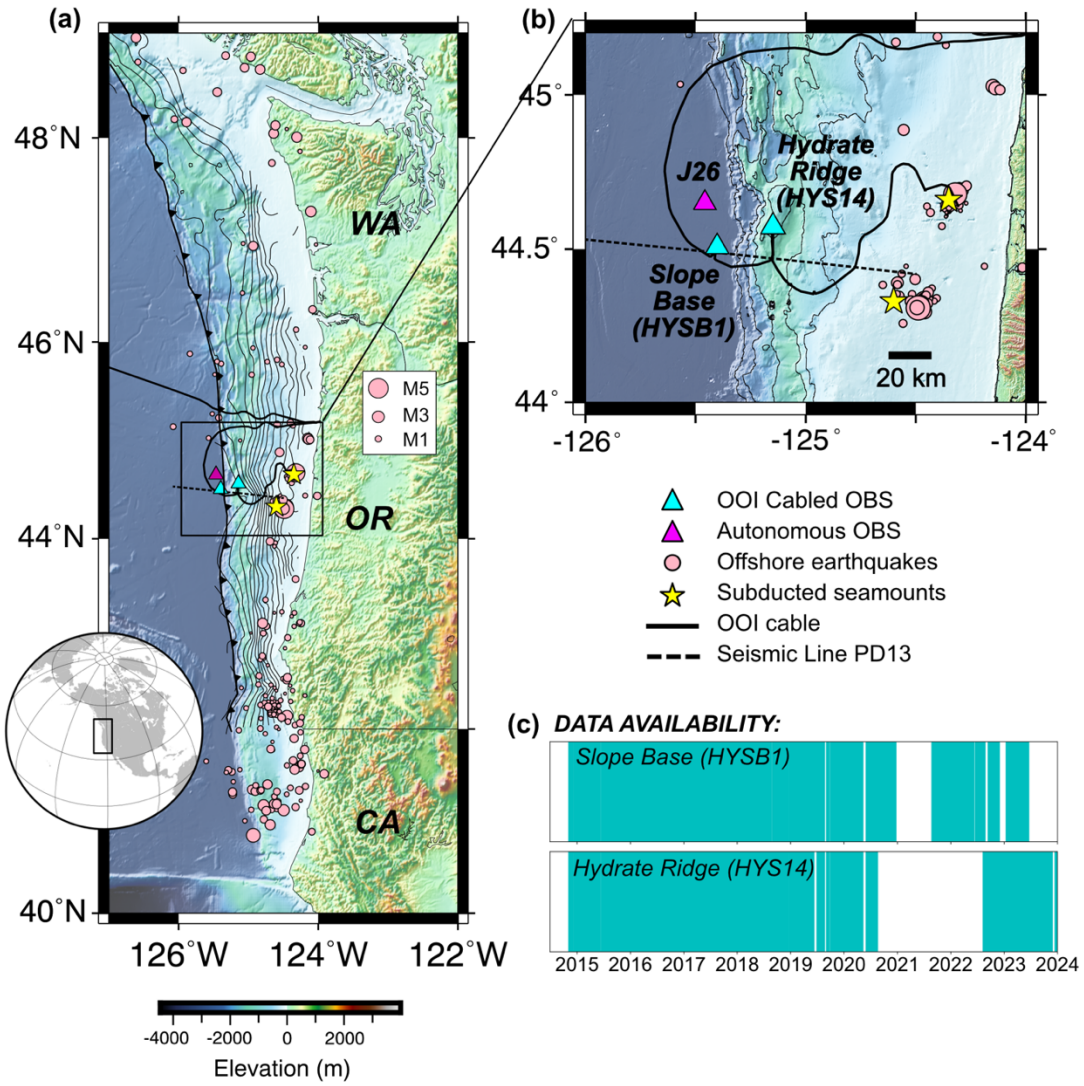

Figure 1. (**a)** Map of the Cascadia subduction zone with deformation front and subducting plate interface contours from Carbotte et al. (2024), shown at 1 km intervals. Earthquakes from Stone et al. (2018) and Tréhu et al. (2012) are shown as pink circles scaled by magnitude, with the largest earthquake shown M4.9. The inferred locations of subducted seamounts, which mark the two main seismicity clusters on the plate interface, are shown with yellow stars. The OOI cable is shown with a thick black line and the cabled OBSs are shown as cyan triangles. The autonomous OBS from the Cascadia Initiative nearest to Slope Base, station code J26D, is shown with a magenta triangle. Seismic line PD13 from the CASIE21 survey is shown with a dashed line (Canales et al., 2022). **(b)** Zoomed map near focused on the deformation front near ~44.5°N. Contours show bathymetry at 500 m intervals. All other symbols follow (a). (c) Data availability of the two stations we focus on in this study, with times of available data marked by cyan bars.

5.2 Data

5.2.1 Cabled OOI seismometer and hydrophone data

Beginning in late 2014, the Ocean Observatories Initiative (OOI) Regional Cabled Array came online with five cabled three-component ocean bottom seismometers (OBSs) at two sites near the deformation front of the Cascadia subduction zone at ~44.5°N (Figure 1) (Kelley et al., 2016; Smith et al., 2018; Trowbridge et al., 2019). At 2920 m depth, the Slope Base site lies 5 kilometers west of the deformation front and is instrumented with one broadband seismometer (station code HYSB1). Just ~20 km east, at 790 m depth, the Southern Hydrate Ridge site hosts a second broadband seismometer (HYS14). Both broadband seismometers are Guralp CMG-1T sensors co-sited with a High Tech HTI-90-U hydrophone. The seismometers and hydrophones all sample at 200 Hz, and the seismometers are buried at < 1 m depth. The seismometers were deployed with a remotely operated vehicle that created a shallow hole by inserting a caisson into the sediments, removing sediment from within the caisson, placing the seismometer within while ensuring that it was not touching the caisson, and then burying the instrument in glass beads (following Romanowicz et al., 2006). At the Southern Hydrate Ridge site, there are also three Guralp CMG-6TF short period seismometers located ~0.5 km to the northwest, northeast and southeast of station HYS14, with station codes HYS11, HYS12, and HYS13, respectively. Because these are essentially co-sited with HYS14, we only use these instruments for manual checks of signal occurrence. We focus on the two broadband stations, HYSB1 and HYS14.

Both HYSB1 and HYS14 have good quality data beginning in February 2015 (Figure 1c). The instruments record nearly continuously, with occasional short outages mainly due to network outages, maintenance, and Navy diversions, until August 2020. HYSB1 resumes recording in August 2021 and continues, amidst several outages, until January 2024, when

communications were lost with the junction box. HYS14 resumes recording in August 2022 and continues into 2024. We analyze all data up to January 2024.

5.2.2 Autonomous Hikurangi seismometer data

To validate our approach, we use data from autonomous OBSs deployed offshore New Zealand in the Hikurangi subduction zone. The HOBITSS experiment deployed 15 OBSs around a subducting seamount to capture a shallow slow slip event that occurred during September and October 2014 (Wallace et al., 2016). Todd et al. (2018) used nine of these OBSs to create a catalog of shallow tectonic tremor associated with the slow slip event. The instruments are not buried. The instruments with station codes starting with "LOBS" are broadband Nanometrics Trillium Compact seismometers that sample at 100 Hz, while the instruments with "EBS" station codes are short period Lennartz LE-3Dlite seismometers that sample at 200 Hz.

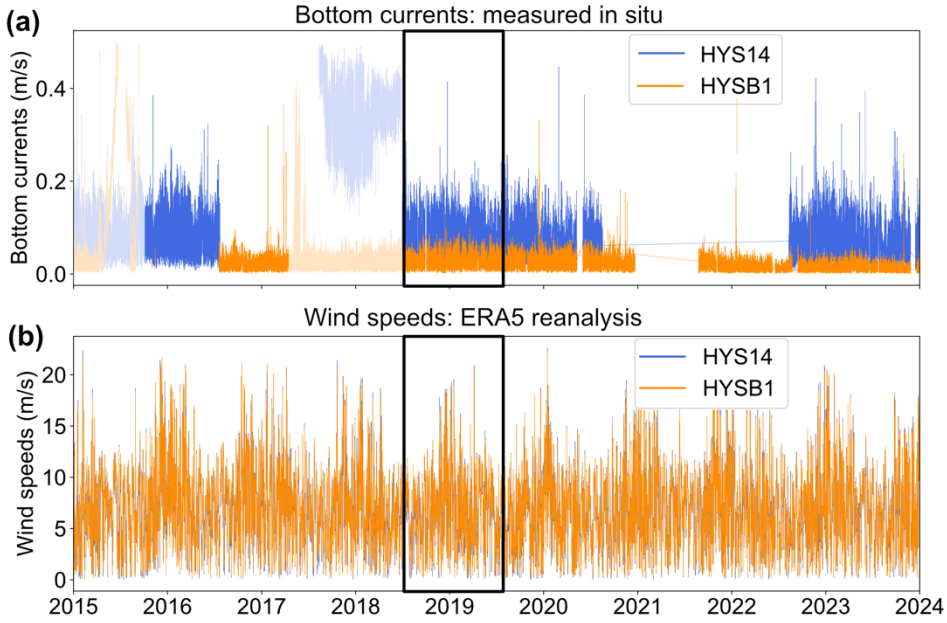

Figure 2. Environmental data used to compare to seismic time series. **(a)** Hourly bottom currents measured in situ by cabled instruments at the Hydrate Ridge (HYS14) and Slope Base (HYSB1) sites. Data is shown as hourly medians. Periods of bad data quality are shown with paler colors. **(b)** Hourly wind speeds from ERA5 climate reanalysis for the two sites. The period we use for our analysis is outlined with a black rectangle in both subplots.

5.2.3 Bottom current data

At both the HYSB1 and HYS14 sites, bottom currents are measured using a cabled 3-D Nobska MAVS-4 single point velocity meter. Water velocity (both speed and direction) is measured at a height of ~1 m from the seafloor and reported once per minute. We take the vector sum of the north and east components of water velocity to yield horizontal bottom current speeds at each site. The bottom current data is prone to clipping, so we remove any measurements greater than 0.5 m/s and calculate an hourly median value (Figure 2a). Bottom current data is available continuously at both sites at the same times as the seismometers, but data quality is compromised for significant time periods and not all available data has been verified (see Figure 2a). Here, we focus on one year of data from July 2018-July 2019, during the longest period that both sites have good quality data.

5.2.4 Wind speed data

We retrieve wind speeds from the ERA5 global reanalysis, which combines observations with models to create a hindcast of atmospheric, land surface, and oceanic parameters from 1950 onwards (Hersbach et al., 2020). We use the two horizontal components of wind, which are calculated at 10 m above earth's surface at hourly time steps and a horizontal resolution of 0.25° latitude by 0.25° longitude. We linearly interpolate the gridded data to the HYSB1 and HYS14 sites and take the vector sum of the two horizontal components to yield hourly horizontal wind speeds for each site (Figure 2b).

5.3 Methods

5.3.1 Environmental modeling to define background noise sources

We attempt to model smoothed amplitudes of the HYSB1 and HYS14 seismic time series using wind speeds from ERA5 reanalysis and bottom current speeds recorded at each site. We do

this separately for two frequency bands of interest. We assume amplitudes in the 3-10 Hz band are representative of tectonic tremor, while amplitudes from 10-25 Hz are representative of other signals, including whale calls (e.g., Wilcock et al., 2014). The minimum frequency of 3 Hz is chosen to minimize the impact of microseismic noise. We calculate hourly median amplitudes of absolute ground velocities with a 50% overlap. For both the HYSB1 and HYS14 stations, we retrieve one hour of data for all three components at a time, padded by 5 minutes on either end. We demean the raw time series, apply a Butterworth bandpass filter, scale the data by the average instrument response in the frequency band, trim the padding on either end, and then take the absolute value of the data. We take a vector sum of the two horizontal channels and then record the median amplitude of the vertical and horizontal data for that hour. Due to occasional network outages, there are some periods of missing seismic data; we infill these times by linearly interpolating between data points. We then smooth the median seismic amplitudes, wind speeds, and median bottom currents, all of which are hourly time series, using a Gaussian filter with a standard deviation of 8 hours. After smoothing, we mask periods of data outages; these data points are ignored in modeling.

We create separate models for wind speeds and bottom currents, using an approach that is intended to be robust against outliers. Seismic noise levels are expected to saturate at a threshold wind speed and then rise without limit (McCreery et al., 1993). Therefore, following Hilmo & Wilcock (2020), we use wind speeds to model smoothed seismic amplitudes as:

$$m_t = b_1 + c_1 w_t \; for \; w_t < B \qquad Eq.\ 1$$

$$m_t = b_2 + c_2 w_t \; for \; w_t \geq B$$

where m is the modeled ground velocity, t is an index of discretized time, w is wind speed, B is the threshold wind speed that acts as a breakpoint for a piecewise linear function with two segments, and b_1, b_2, c_1 and c_2 are constants. For a given hinge point (w_{test}, $B_{test,}$), we fit both portions of the data, $wt < B_{test}$ and $w_t >= B_{test}$, with a line that intersects the hinge point. On either side of the hinge point, we vary the slope of the line and choose that which gives the center of the narrowest band enclosing half the points in the y-direction. We do not allow negative slopes. We perform a grid search over the hinge point and choose the hinge point B that minimizes the weighted average of the two band widths. If no hinge point is visually apparent, we fit the data with only one line.

Trehu (1985) showed that, at frequencies below 10 Hz, seismic noise levels appear to increase proportionally with the square of bottom current speeds. Therefore, using bottom currents, we model smoothed seismic amplitudes as:

$$m_t = b + cs_t^2 \qquad \textit{Eq. 2}$$

where m is the modeled ground velocity, t is an index of discretized time, s is horizontal bottom current speed, and b and c are constants; we do not allow c to be negative. To fit the model, we solve for the line that is the center of the narrowest band enclosing half the points in the y-direction. For both wind speed and bottom current models, we do not report R values as in previous studies, which estimate how well a model can explain observed variation in the data (Hilmo & Wilcock, 2020). This value is only meaningful when model misfits are normally distributed after a least squares minimization, which is not our case.

5.3.2 Detection and classification of emergent signals

5.3.2.1 Envelope cross-correlation

To test the performance of envelope cross-correlation between the two broadband seismometers at the HYSB1 and HYS14 sites, we follow the method of Wech et al. (2013), who focused on OBSs. We process 24 hours of data at a time with 5 s of padding on either end. Using a horizontal channel from each instrument, we first taper the 5 s on both ends of the data using a Hann window, and then apply a 4-corner minimum phase 3-10 Hz Butterworth bandpass filter to minimize the impact of microseismic noise and to isolate the expected frequency of tremor. We take an envelope of the filtered data and apply a 5-s low-pass filter. The enveloped data is decimated to 1 Hz and the padding on either end is trimmed to avoid edge effects. We cross-correlate 300-s windows with 50% overlap. We allow a maximum shift of 10 s, which conservatively accounts for the maximum lag we would expect if S-waves are travelling horizontally 20 km between stations. We save the maximum cross-correlation value of each window to determine windows that likely include tremor.

5.3.2.2 Single-station emergent signal detection and classification

To detect tremor-like signals on a single station, we perform short-term average long-term average (STA/LTA) triggering on one channel at a time. We use the horizontal components and process 24 hours of data at a time with an extra 1000 s at the start to account for the long-term window. Prior to triggering, we pad the data by 5 s on either end, taper the padded data using a Hann window, apply a 4-corner minimum phase 3-10 Hz Butterworth bandpass filter, and trim the padding. We found that a short-term window of 10 s and a long-term window of 1000 s, with triggering on/off thresholds of 2/1, captures emergent signals of varying duration and excludes impulsive signals such as local earthquakes. Any detections with a duration less than 30 s are discarded.

To identify T-phases, we determine the number of waveform peaks in each detection. Regional T-phases typically have one clear prominent peak in their smoothed waveform, whereas tectonic tremor signals more typically exhibit multiple peaks. To smooth the waveform, we take the square of the 3-10 Hz filtered data, apply a 1-dimensional Gaussian filter with a standard deviation of 1.875 seconds, and normalize the data using its maximum. We then calculate the number of peaks in the waveform, between the trigger on/off times, with a prominence exceeding 0.1. If the smoothed waveform only has one peak, we categorize it a T-phase (Figure 3a).

To assess whether the detection likely includes ship noise, we analyze the spectral characteristics of each detected signal. Ship noise is typically identified by monochromatic bands of energy (Ross & Kuperman, 1989). We identify whether strong monochromatic bands are present by first estimating the power spectrum of the unfiltered signal using Welch's method with a 1-s segment length, Hann taper, and 50% overlap (Welch, 1967). To avoid misidentifying peaks related to microseismic noise, we discard the portion of the power spectrum related to the microseism, which we conservatively take as all frequencies below 4 Hz, consistent with microseism levels seen in Cascadia (Hilmo & Wilcock, 2020). We convert the spectrum to decibels and then identify any peaks in the power spectrum, above 4 Hz, that are greater than the median power between 20-80 Hz and have a prominence greater than 10 dB. If there are any peaks that meet these requirements within the power spectrum, we determine that the detection likely includes ship noise (Figure 3b).

To determine whether the detection exhibits a significant decrease in spectral power above 10 Hz, as expected for tectonic tremor, we calculate a ratio between low and high frequency amplitudes (hereafter referred to as F_{LH}). We first pad the detected signal by 30 s on either side of the trigger on and off times, which accounts for times that our detector occasionally

captures only the start of a long-duration T-phase arrival or noise signal. The 30 s padding ensures that the complete spectral characteristics of the signal are captured. We then estimate the power spectrum using Welch's method with a 5-s segment length, Hann taper, and 50% overlap. We compute F_{LH} as the ratio between the median of power between 5-10 Hz and the median of power between 10-15 Hz. For tectonic tremor signals, we expect that F_{LH} will be relatively higher than for non-tectonic tremor signals (i.e., Figure 3c). The F_{LH} threshold used to identify potential tectonic tremor detections is described in Section 4.

We tuned these three analyses on subsets of 200 STA/LTA detections from each OOI station that we visually identified as T-phases, ship noise, or consistent with tectonic tremor (no clear single peak and diminished power above 10 Hz). We used existing detections from Hikurangi to inform expected waveform characteristics of tectonic tremor (Figure 3c). An illustration of these three analyses, applied to representative examples of T-phase, ship noise, and tectonic tremor detections, is shown in Figure 3. We classify a detection as a T-phase if it has only one waveform peak (Figure 3a). We classify a detection as potential tectonic tremor if it has more than one waveform peak and has an F_{LH} higher than a threshold chosen from inspection of the detection subset (Figure 3c). If we identify that a detection contains ship noise (Figure 3b), it may also be classified as a T-phase or potential tectonic tremor, or neither; ship noise, particularly in the region of the OOI, often overlaps other signals.

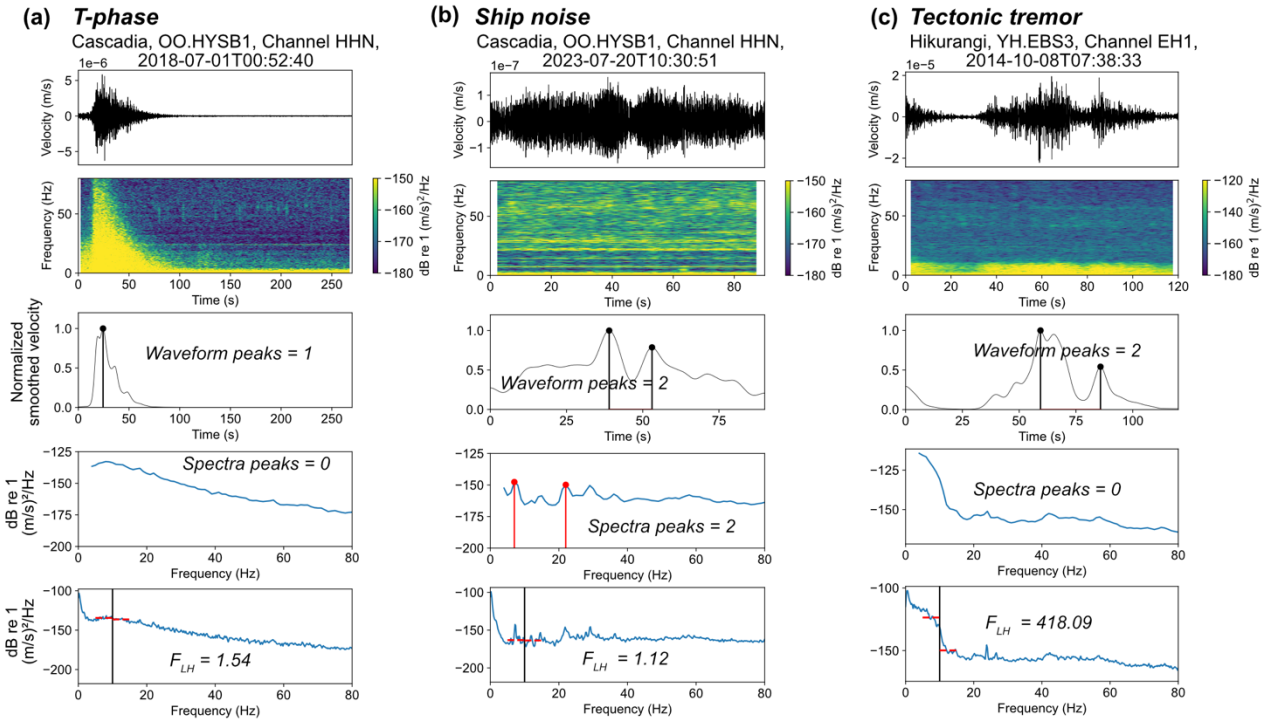

Figure 3. Single-station emergent signal classification analyses shown for three different example signals detected using our STA/LTA approach: **(a)** T-phase in Cascadia, **(b)** ship noise in Cascadia, and **(c)** tectonic tremor in Hikurangi. The title of each subplot lists the station code, channel, and the start time of the window. The first row of each subplot shows the waveform of the signal bandpass filtered from 3-10 Hz and the second row shows a spectrogram of the same waveform. The third row shows results of peak picking on the smoothed waveform: 1 peak indicates a T-phase (a), while > 1 peak indicates a potential tremor-like signal (b and c). The fourth row shows the results of peak picking in the spectra: the presence of peaks indicates ship noise (b). The final row demonstrates the calculation of F_{LH}, or the ratio between power in the 10-15 Hz band and the 5-10 Hz band. Signals consistent with tectonic tremor are expected to have a larger F_{LH} (c).

5.4 Results

5.4.1 Environmental modeling

We find an overall weak and variable relationship between environmental factors and background noise on the OOI OBSs, which prevents us from using them as a proxy to identify periods of potential tremor. For wind speeds, we observe a relationship to seismic ground velocities at both sites, but we do not consistently observe saturation of noise at a threshold wind speed as expected (Equation 1). At Slope Base, the strongest relationship between wind speeds and seismic ground velocities is observed at 3-10 Hz, with a stronger relationship in the

horizontal component (Figure 4a, 4b). The best fit model gives a saturation wind speed of 7.5 m/s and 6.6 m/s for the horizontal and vertical components, respectively. There is no relationship between wind speeds and seismic ground velocities at Slope Base in the 10-25 Hz band (Figure 4c and 4d). Both the horizontal and vertical components do not display an obvious saturation wind speed and our robust model fitting gives a line with zero slope. We note that in all the plots for 10-25 Hz, there are outliers which are due to seasonal fin whale calls in the fall and winter centered at 18-22 Hz.

The relationship between wind speeds and seismic ground velocities is overall weaker at Hydrate Ridge. Only the vertical component in the 3-10 Hz band appears to display a weak break at a saturation wind speed of 6.0 m/s (Figure 4j). The horizontal component in the 3-10 Hz band shows no clear saturation point and is fit using a single line (Figure 4i), while both components in the 10-25 Hz band show no dependence on wind (Figure 4k, 4l).

We observe very little to no relationship between seismic ground velocity amplitudes and in-situ measured bottom currents at either the Hydrate Ridge or Slope Base sites. At Slope Base, there is no relationship in either component in the 3-10 Hz band and only a very weak apparent dependence at 10-25 Hz (Figure 4e-h). At Hydrate Ridge, the only apparent weak dependence is observed on the horizontal components (Figure 4m-p).

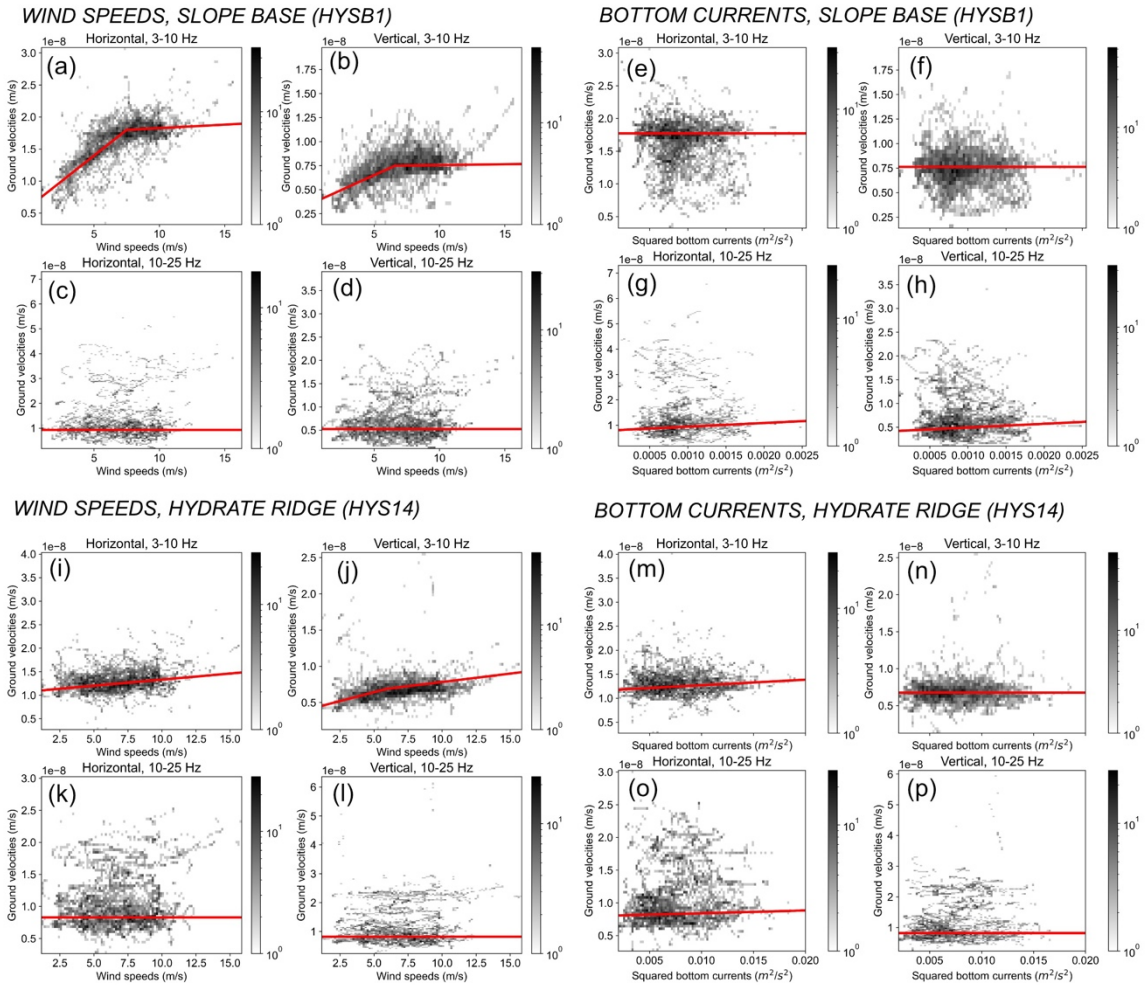

Figure 4. Results of environmental modeling of seismic ground velocity amplitudes. Density plots, shown as 2-D histograms, show the relationship between smoothed hourly environmental time series (x-axis) and smoothed hourly median seismic ground velocities (y-axis) for different frequency bands and seismometer components. The gray scale shows the number of points, one per hour, per 2-D bin on a logarithmic scale. **(a-d)** Modeling of seismic ground velocities using wind speeds at the Slope Base (HYSB1) station. The robust piecewise model (Equation 1) is shown as a red line. Bin dimensions are 0.15 m/s by $0.04e^{-8}$ m/s. Here and in the remaining subplots, results are shown for horizontal and vertical components in the 3-10 Hz and 10-25 Hz frequency bands. **(i-l)** Same as (a-d) but for the Hydrate Ridge (HYS14) station. **(e-h)** Modeling of seismic ground velocities using squared bottom currents at the Slope Base (HYSB1) station. The best-fit model (Equation 2) is shown by a red line. Bin dimensions are 0.0003 m^2/s^2 by $0.04e^{-8}$ m/s. **(m-p)** Same as (e-h) but for the Hydrate Ridge (HYS14) station, with bin dimensions of 0.0002 m^2/s^2 by $0.04e^{-8}$ m/s .

5.4.2 Comparison of envelope cross-correlation and single-station STA/LTA triggering

We compare the performance of envelope cross-correlation and single-station STA/LTA triggering methods for the HYS14 and HYSB1 stations from July 2018-July 2019 (Figure 5), in

order to identify which method is more appropriate to search for small tectonic tremor signals. We use both horizontal channels, HHN (North) and HHE (East), for these comparisons and we also compare each method between channels. For envelope cross-correlation between the two sites, we consider detections as windows with cross-correlation values greater than 0.7.

The temporal pattern of emergent signal detections is similar between envelope cross-correlation and individual STA/LTA detection, and the results are also very similar between channels (Figure 5). On the HHN channels, envelope cross-correlation yields 4,581 detections, while single-station STA/LTA triggering yields 4,098 and 12,348 detections on HYSB1 and HYS14, respectively. On the HHE channels, envelope cross-correlation yields 4,889 detections, while single-station STA/LTA triggering yields 4,380 and 12,246 detections on HYSB1 and HYS14, respectively. We only use the HHN channels going forward (Figure 5).

There is significant overlap between envelope cross-correlation and single-station STA/LTA triggering results. On the HHN channels, 94% and 85% of the envelope cross-correlation detections overlap with an STA/LTA detection on HYS14 and HYSB1, respectively. Visual inspection of a subset of 100 envelope cross-correlation detections reveals that > 65% are clear T-phases, showing that the method does not effectively filter out non-tremor signals. Although the single station method also detects many T-phases, it is simpler to identify T-phases within STA/LTA detections because detections are centered on the signal. Further, STA/LTA detection also allows for the case where only one station records a signal, which is important given the difference in number of emergent signals across stations (Figure 5). We therefore proceed with single-station STA/LTA triggering to detect small tremor signals.

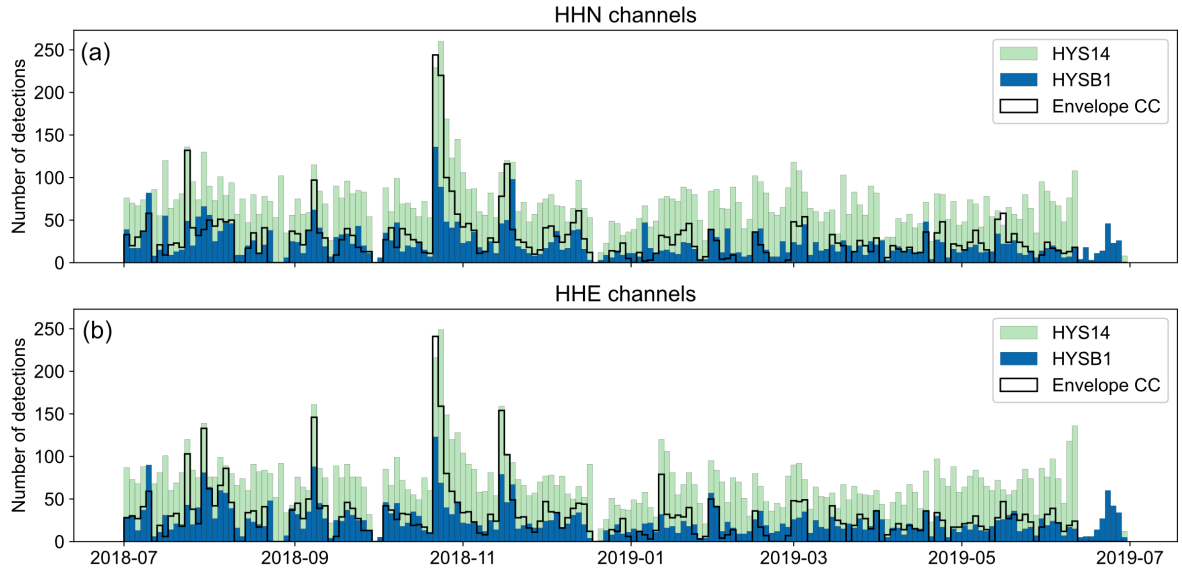

Figure 5. Comparison of emergent signal detection methods for July 2018-July 2019 for **(a)** the HHN and **(b)** HHE channels. On each plot, colored histogram bars show the number of emergent detections, with bin sizes of 2 days, detected on the Hydrate Ridge (HYS14) and Slope Base (HYSB1) OOI stations using STA/LTA on the HHN channels. The unfilled black histogram overlain shows the number of detections from envelope cross-correlation between the two stations. The highest peak in detections corresponds to regional T-phase arrivals from a swarm of earthquakes on the Nootka fault zone in October 2018.

5.4.3 Single-station method validation offshore Hikurangi

To demonstrate that our approach of individual station STA/LTA triggering and subsequent detection classification (Figure 3) effectively identifies tectonic tremor on OBSs, we apply the method to data from the Hikurangi subduction zone for which there is a published catalog of tectonic tremor (Todd et al., 2018) (Figure 6). The tectonic tremor catalog was constructed using envelope cross-correlation with a requirement for correlation coefficients > 0.6 across at least 7 stations. We cannot expect our tremor detections to correlate perfectly with the Todd et al. (2018) catalog because our method uses only a single station; instead, if our method is successful, we may expect many more detections on an individual station but an overall temporal trend that mimics the Todd et al. (2018) catalog. We used data from six of the OBSs used by Todd et al. (2018), selected for their varying distance from the locus of tremor: stations EBS2, EBS3, EBS4, EBS5, LOBS2, and LOBS6 (Figure 6a).

We present results for three OBSs that are representative of overall patterns (Figure 6). Station EBS3 is essentially atop the main tremor patch, while stations EBS5 and LOBS2 are both ~30-40 km away (Figure 6a). Station EBS5 is on the overriding plate at a similar depth to station EBS3 (~1000 m) while LOBS2 is located on the incoming plate at > 3000 m depth (Figure 6a). For September-October 2014, STA/LTA triggering identifies 12,314, 10,539, and 2,716 emergent signals on the EBS3, EBS5, and LOBS2 stations, respectively (Figure 6c). The number of overall STA/LTA detections increases markedly on the EBS3 and EBS5 stations in early October, but this trend is not seen on station LOBS2 (Figure 6c). Manual inspection of the LOBS2 data shows that, even for periods of tremor identified by Todd et al. (2018), tectonic tremor is not recorded at this station; instead, most of the STA/LTA detections appear to be T-phases.

To identify detections that are consistent with tectonic tremor, we first require that a detection have more than one peak in its smoothed waveform (Figure 3a). This removes 62%, 63%, and 61% of detections on EBS3, EBS5, and LOBS2, respectively. Because we are solely interested in the presence of tectonic tremor in this dataset, we do not check for ship noise (Figure 3b); the presence of ship noise does not preclude the presence of tremor. We then calculate the F_{LH} of all detections (Figure 3). We find that the two stations that record tectonic tremor, EBS3 and EBS5, have a much wider distribution of F_{LH} than the station that does not record tectonic tremor, LOBS2 (Figure 6b). LOBS2 has no detections with F_{LH} greater than 100. Visual checks show that almost all detections on EBS3 and EBS5 with $F_{LH} > 100$ appear to be tectonic tremor.

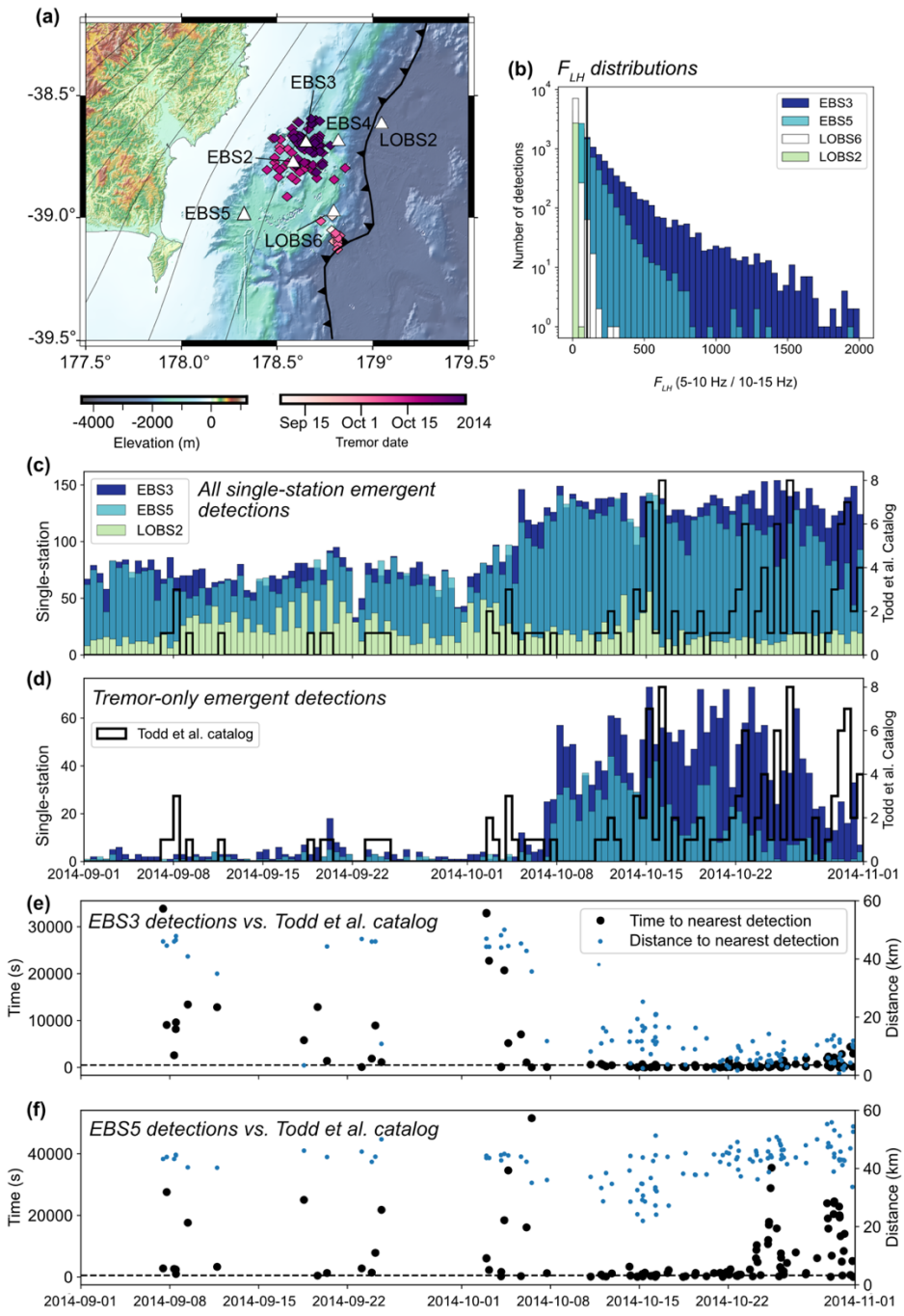

Figure 6. Performance of our single-station STA/LTA detection and classification method on OBSs with cataloged tectonic tremor in the Hikurangi subduction zone. **(a)** Map showing the OBSs we used from the HOBITSS network as white triangles with station names annotated. Tectonic tremor localizations from Todd et al. (2018) are shown as diamonds colored by time. The deformation front and subduction slab depth contours at 3 km intervals (Hayes et al., 2018) are shown as black lines. **(b)** Histogram showing distribution of F_{LH} values for all single-station detections for a subset of HOBITSS OBSs. The black vertical line at F_{LH} = 100 denotes the cut-off we use to classify detections as tremor. Note the y-axis log scale. **(c)** Histogram showing time distributions of single-station emergent detections for stations EBS3, EBS5, and LOBS2 for September-October 2014 as colored bars, overlain by the time distribution of tectonic tremor

localizations from the Todd et al. (2018) as thick black lines. Note the two different y-axes. **(d)** Same as (c), but only showing single-station detections we classify as tremor (more than one peak in the smoothed waveform and $F_{LH} > 100$). Note that there are no tremor detections for station LOBS2. **(e)** Tremor detections from Todd et al. (2018) and STA/LTA for the EBS3 station. Black circles show the minimum time between each detection of Todd et al. (2018) and an STA/LTA detection, plotted on the left axis. Blue dots show the spatial distance between each detection of Todd et al. (2018) and station EBS3, plotted on the right axis. There is one blue circle and one black dot per detection of Todd et al. (2018). The horizontal dashed line corresponds to a timing difference of 500 s. **(f)** same as (e) but for station EBS5.

By requiring more than one peak in the smoothed waveform and a $F_{LH} > 100$, we find 2,403 tectonic tremor detections on EBS3, 966 on EBS5, and zero on LOBS2 (Figure 6d). Todd et al. (2018) observe several bursts of tremor in September 2014 and then more consistent and frequent tremor beginning in October 2014 (Figure 6d). The temporal trends of our tremor detections on EBS3 and EBS5 are in excellent agreement with these patterns (Figure 6d), suggesting that this approach effectively approximates the presence of tremor on a single OBS. Our approach finds approximately one order of magnitude more detections than Todd et al. (2018) (Figure 6d), almost certainly due to their requirement that the tremor signals be coherent across a minimum of 7 stations.

We find that there is much better timing agreement between individual tremor detections from Todd et al. (2018) and our single-station STA/LTA detections when the tremor source from Todd et al. (2018) is < 40 km from the recording station (Figure 6e-f). Prior to October 8, there are typically several hours between each tremor detection from Todd et al. (2018) and a STA/LTA tremor detection, suggesting that the STA/LTA method is detecting either a different tremor source or a different signal altogether when the tremor source is distant. Once tremor reaches closer to the instruments (< ~40 km) around October 8, however, the typical timing difference between a tremor detection from Todd et al. (2018) and an STA/LTA detection drops to several minutes or less, suggesting the STA/LTA approach is detecting signals within the same tremor wave trains. In late October, the tremor source continues to migrate further from

station EBS5 (> 40 km) but closer to station EBS3; correspondingly, the temporal agreement between the detections from Todd et al. (2018) and STA/LTA remains strong at station EBS3, but worsens at station EBS5 (Figure 6e-f).

We found one station, LOBS6 (Figure 6a), dominated by bottom-current induced tremor (Figure 7). This signal is characterized by gliding harmonic frequencies and is not inferred to be related to tectonics, but instead results from the interaction of strong bottom currents and protruding structures on the OBS (Corela et al., 2023a; Essing et al., 2021). Our STA/LTA method produced 7,444 detections on LOBS6 in the two months of investigation and frequently triggered on these signals. These detections have multiple peaks in their smoothed waveform and F_{LH} values that at times are above 100 (Figure 6b, Figure 7a), which precludes them from being discarded by our method. Our check for ship noise, designed to identify spectral banding, does appear to identify the harmonic character of the current induced tremors (Figure 7), suggesting that this approach could be explored to handle instruments that are prone to bottom current-induced tremors.

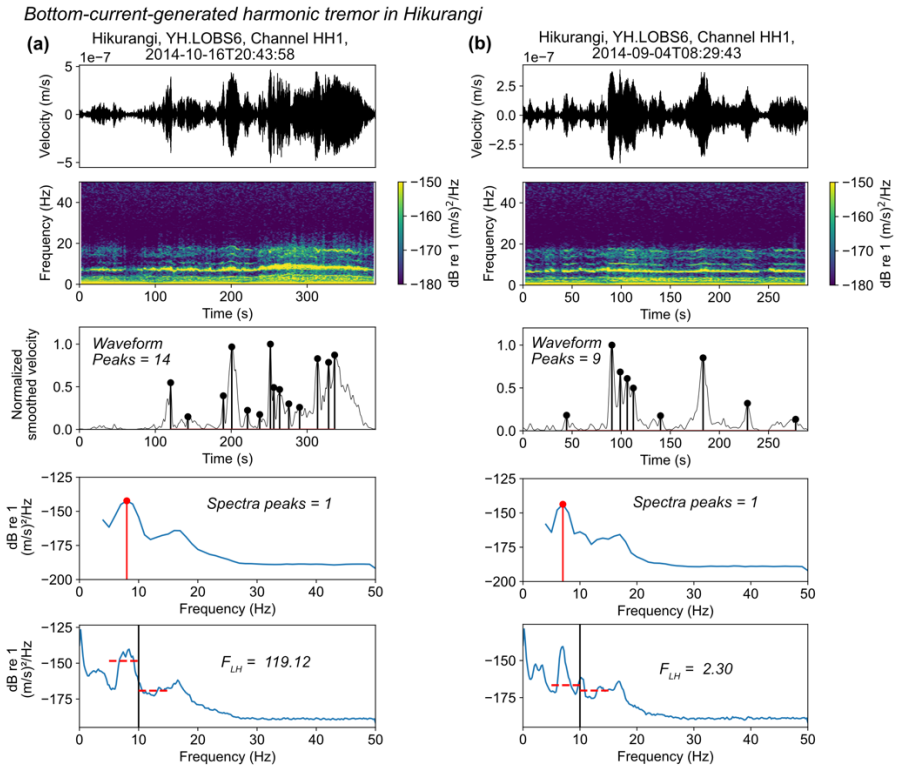

Figure 7. Examples of bottom current-induced tremor detected by STA/LTA triggering on Hikurangi station LOBS6 using the same format as Figure 3.

5.4.4 Detection and classification of emergent signals at Slope Base and Hydrate Ridge

Based on the success of our single-station method at Hikurangi, we apply the same approach to stations HYSB1 (Slope Base) and HYS14 (Hydrate Ridge) on the OOI for February 2015-January 2024. STA/LTA triggering detects 85,166 signals on HYS14 and 30,055 signals on HYSB1 (Figure 8a). Of these detections, 30% on HYS14 and 65% on HYSB1 likely include ship noise in the form of spectral banding (see Figure 3 for method). We then classify 40% of detections at HYS14 and 32% of detections at HYSB1 as T-phases (Figure 8b), which have only one peak in their smoothed waveform (Figure 3a). The largest peak in number of T-phases is coincident with a swarm of earthquakes near the Nootka fault zone (Figure 8b).

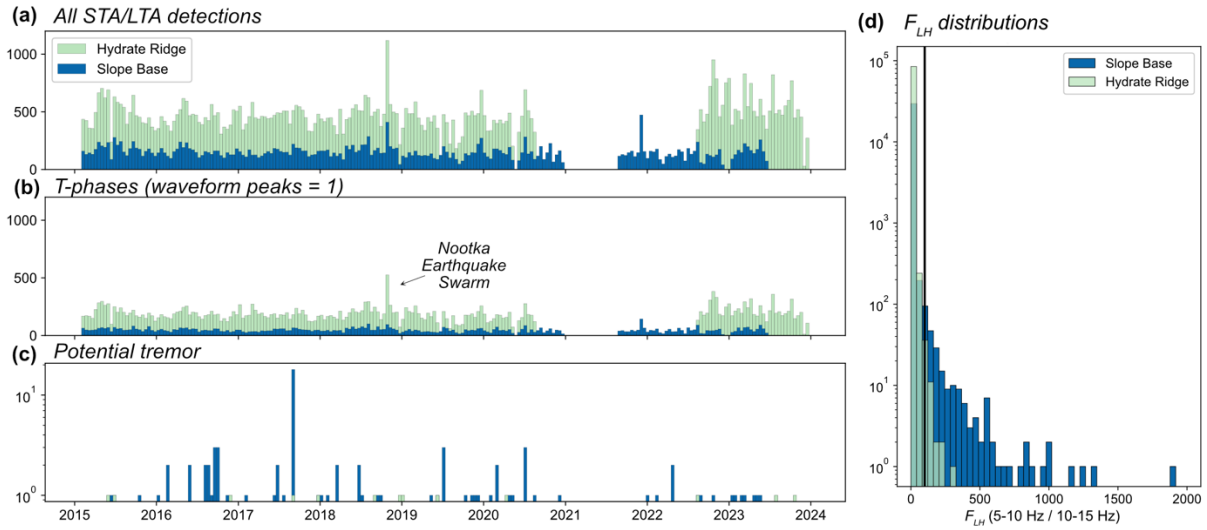

Figure 8. Results of single-station STA/LTA detection and classification on OOI stations HYSB1 (Slope Base) and Hydrate Ridge (HYS14). **(a)** Histogram showing number of detections at Hydrate Ridge and Slope Base over time with bin sizes of 2 weeks. **(b)** Same as (a) but only showing detections that have one peak in their smoothed waveform, indicating they are T-phases. The largest peak can be attributed to a swarm of earthquakes near the Nootka fault zone which generated many regional T-phases. **(c)** Same as (a) but only showing detections which have more than one waveform peak and $F_{LH} > 100$, indicating they are consistent with tectonic tremor. Note the log scale. **(d)** Histogram showing distributions of F_{LH} for all detections for both Slope Base and Hydrate Ridge. The black vertical line indicates the minimum value required for potential tremor, $F_{LH} = 100$. Note the log scale.

To understand the overall spread of spectral characteristics, we calculate F_{LH} for all detections (Figure 8d). We find that detections at HYSB1 have a broader distribution of F_{LH} values in comparison to HYS14, with many more detections with $F_{LH} > 100$. As for our analysis at Hikurangi, we then classify detections as potential tectonic tremor only if they have more than one peak in the smoothed waveform and $F_{LH} > 100$. We do not use the presence of ship noise to filter out detections because we found that ship noise was often present amidst other emergent signals. This leaves 86 potential tectonic tremor detections for HYSB1 and 13 for HYS14 (Figure 8c).

5.4.5 Visual investigation of potential tremor signals

We visually inspected all potential tectonic tremor detections on both HYSB1 and HYS14 to determine whether any show all characteristics expected for tectonic tremor (Figure 9a). We consider a detection to be consistent with tectonic tremor if it lacks energy above 10 Hz, shows multiple emergent peaks in the waveform, is not strongly recorded on the hydrophone as expected for T-phases (Figure 10a), and is not dominated by impulsive energy. Notably, no signals consistent with harmonic bottom current-generated tremor (e.g., Figure 7) were found on either instrument.

At station HYS14, we found that all potential tectonic tremor detections are consistent with regional T-phases: an overall spindle-like shape, evidence for some energy at frequencies > 10 Hz on the vertical channel, and a strong recording by the hydrophone (Figure 10a). We therefore conclude that no signals consistent with tectonic tremor are detected by our method on station HYS14 during 2015-2024 (Figure 9a).

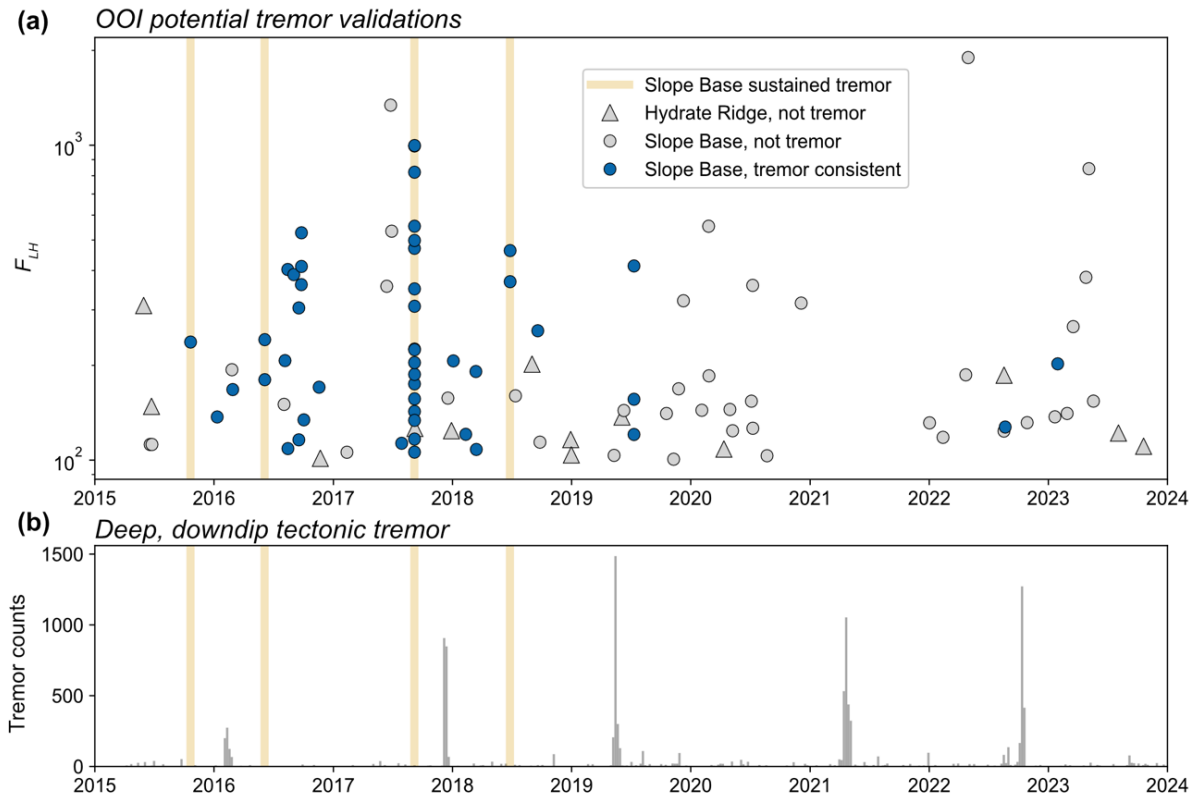

Figure 9. Results of visual inspection of all potential tremor signals at Slope Base and Hydrate Ridge. **(a)** Scatter plot showing the F_{LH} of all potential tremor detections over time for both stations (Figure 8c). Manually validated detections which are consistent with tectonic tremor are shown in blue, and detections that are clearly not tremor shown in gray. The times when a tremor-like signal is observed at Slope Base for more than an hour are marked with yellow vertical lines (see Table 1 for exact times). **(b)** Histogram showing the number of downdip tremor detections over time in deep Cascadia, detected by the Pacific Northwest Seismic Network (Wech, 2010), between 44°N and 45°N . Bin sizes are 1 week. Times of sustained tremor at Slope Base again shown using yellow vertical lines.

In contrast, the potential tectonic tremor detections on HYSB1 do not include any T-phases. However, many detections consist of multiple impulsive peaks that primarily have energy < 10 Hz, abruptly appear and disappear and are not recorded on the hydrophone (Figure 10b). These characteristics are consistent with “short duration events” (SDEs), which are stereotypical noise signals that have long been observed on OBSs throughout the world’s oceans at varying depths and settings (Tary, 2024), including offshore Oregon (MacLeod & Wilcock, 2024; Hilmo & Wilcock, 2020). SDEs are inferred to be unrelated to earthquakes or other tectonic signals and instead have varyingly been attributed to biological activity (Buskirk et al.,

1981) or the movement of gas bubbles through sediments underlying the instrument (Batsi et al., 2019; Tary et al., 2012). They are characterized by their short duration of < 5 s, a single phase arrival and dominance of a narrow frequency band, and are typically recorded on only one OBS at a time and not on the hydrophone (Tary, 2024). We find that 28 of the HYSB1 detections show this behavior (e.g., Figure 10b) and we classify them as non-tremor (Figure 9a).

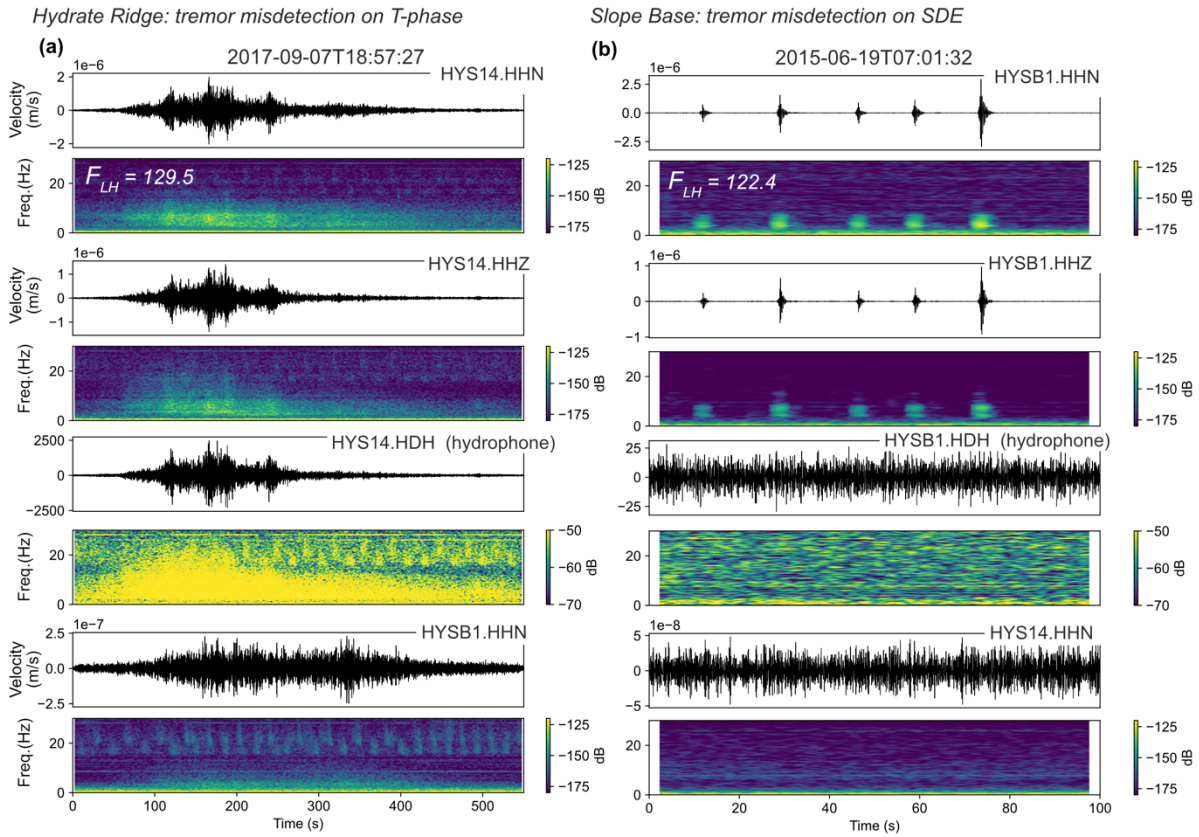

Figure 10. Examples of potential tremor detections (Figure 9a) that were found by visual detection to be inconsistent with tectonic tremor. **(a)** Misdetection on a T-phase at Hydrate Ridge. From top to bottom, each waveform-spectrogram pair set shows the record from the Hydrate Ridge horizontal channel, the Hydrate Ridge vertical channel, the Hydrate Ridge hydrophone, and the Slope Base horizontal channel. All waveforms are filtered from 3-10 Hz. The F_{LH} value of the detection, 129.5, is annotated on the HHN spectrogram. The window start time is the title of the first subplot. **(b)** Misdetection on a sequence of short duration events (SDEs) at Slope Base. The subplot format follows (a) except the plots are for the opposite stations.

We identify 47 detections from HYSB1 that do not appear to be SDEs, T-phases, or instrument noise and are instead consistent with the characteristics expected for tectonic tremor

(Figure 9a). In contrast to T-phases, detections have no clear energy above 10 Hz, the signal is not strongly recorded by the hydrophone, and lacks a spindle-like shape (Figures 11-13). In contrast to short-duration events, energy at frequencies < 10 Hz is present continuously. The signals are also not dominated by spectral banding. For each of these tectonic tremor-like detections, we verified that the signal is not also recorded at HYS14 (Figures 11 and 13) or any of the collocated short-period stations HYS11-13.

Inspection of the time periods surrounding these tectonic tremor-like detections identifies four times when tremor appears to be sustained for at least one hour (Table 1; Figure 9a). During these periods, STA/LTA detections occur on individual emergent signals within the apparent sustained tremor (Figures 11 and 12). The four periods of sustained tremor are shown in their entirety in Figure 12 and contain 23 of the 47 tectonic tremor-like STA/LTA detections. The sustained tremor periods vary in duration from 1 hour to 7 hours. For all four periods, the signal is recorded strongly on all channels (HHN and HHZ are shown in Figure 11). The signal appears to be partially recorded on the hydrophone, though not strongly, and only during times when the frequency content "spikes" above 10 Hz; this may indicate the presence of microearthquakes overlaying the tremor-like background (Figure 11). The sustained periods of tremor typically start with a strong emergent signal on the seismometer, and then fade into what appears to be a background saturation at frequencies < 10 Hz, interspersed with additional strong emergent signals and, occasionally, impulsive signals that are also recorded on the hydrophone (Figure 12). During the longest period of sustained tremor, in September 2017, there are gliding harmonics during the period of strongest tremor (Figure 12c).

The remaining 24 of the visually validated tremor-like STA/LTA detections occur as isolated tremor bursts (Figure 13). These signals are generally quieter than those observed during the four sustained periods. They generally do not contain impulsive signals and are not recorded

on the hydrophone. The highest concentration of isolated tremor signals is observed in late 2016 (Figure 9a), but otherwise, they display no clear temporal pattern.

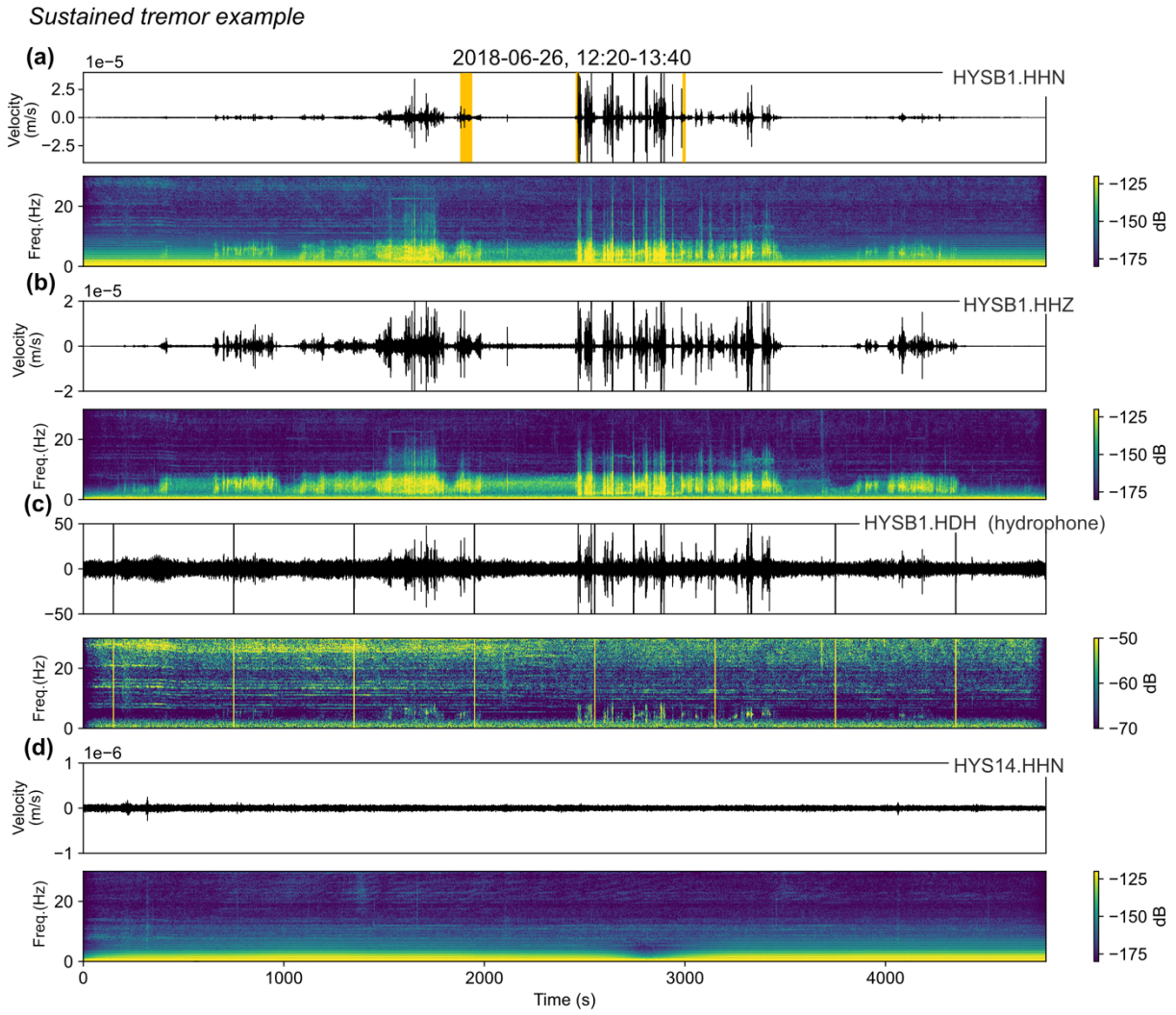

Figure 11. Full 70-minute period for one example of sustained tremor at Slope Base shown for multiple channels and at Hydrate Ridge. All waveforms are filtered from 3-10 Hz. Waveforms in a-c are clipped to focus on the tremor-like signal. Start and end time of the window is noted atop (a). **(a)** Waveform and spectrogram of the Slope Base horizontal channel. On the waveform plot, yellow rectangles denote time windows of our STA/LTA detections (Figure 9a). **(b)** Same as (a) but for the vertical channel. **(c)** Same as (a) but for the hydrophone channel. Note that impulsive broadband signals that recur every 15 minutes are instrument glitches. **(d)** Same as (a) but for the Hydrate Ridge horizontal channel.

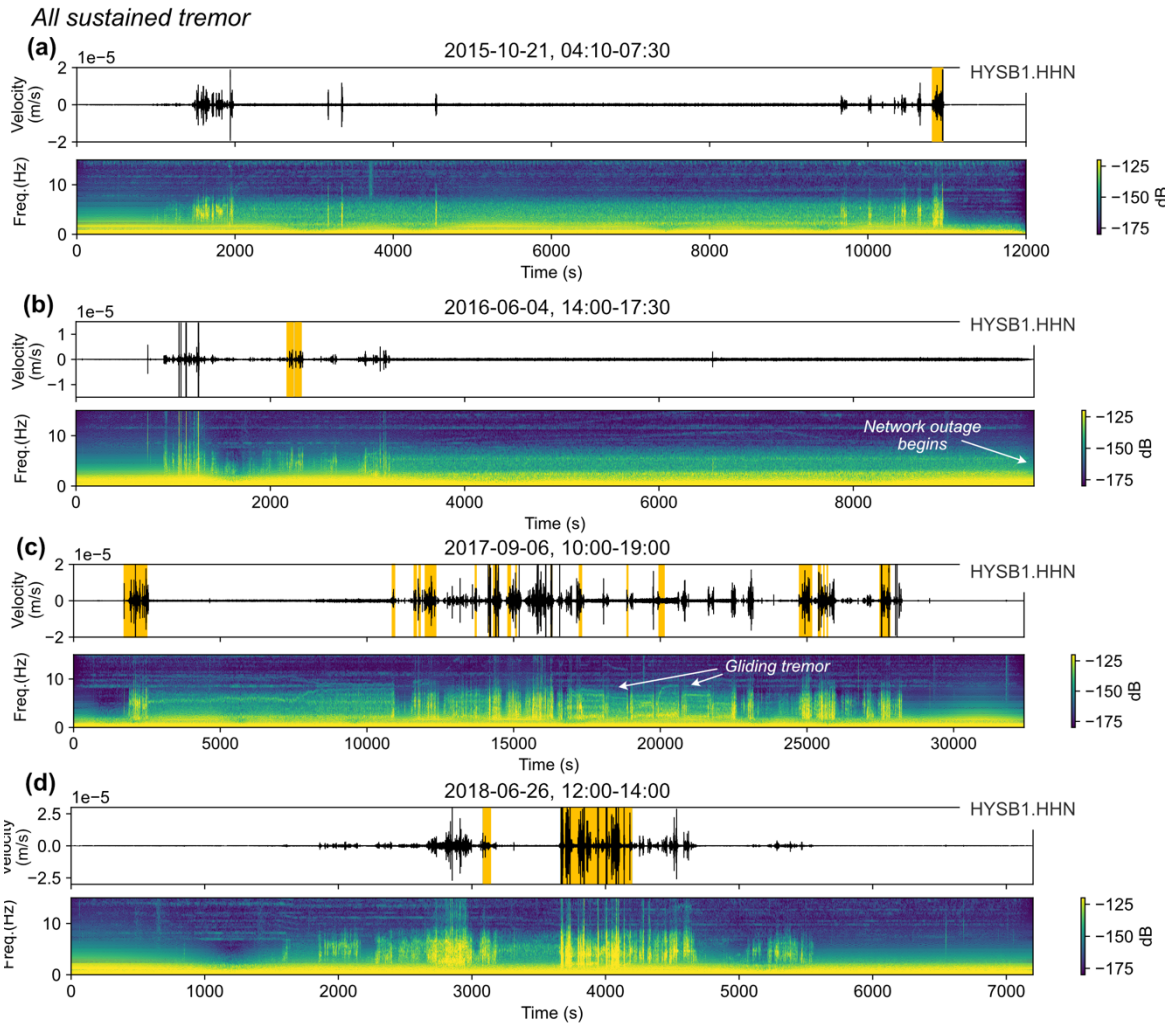

Figure 12. Full intervals for all periods of sustained tremor, shown only for the Slope Base horizontal channel. Note differing time axes. All waveforms are clipped to emphasize the tremor-like signal. **(a-d)** Start and end time of each window is noted in the subplot titles. All waveforms are filtered from 3-10 Hz and overlain by yellow rectangles during the times of our detections (Figure 9a). Gliding tremor seen during the 2017 period, as discussed in the text, is marked in (c).

Date	Time
2015-10-21	04:25 – 07:25
2016-06-04	14:15 - 16:45*
2017-09-06	10:30 – 17:50
2018-06-26	12:25 – 13:35

Table 1. Time periods of observed long-duration tremor on the Slope Base station (HYSB1). *A data outage begins starting at 16:45 that persists until 18:45. When the data comes back online at 18:45, tremor has subsided.

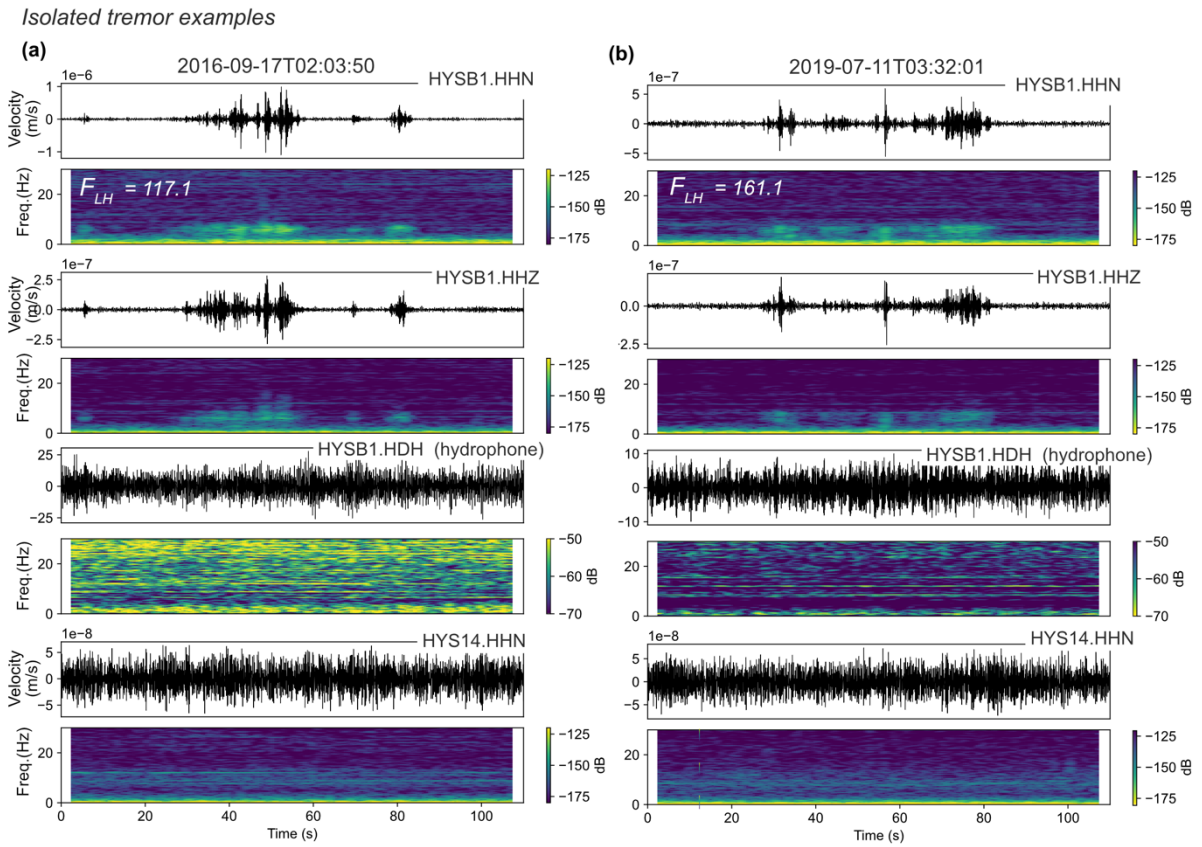

Figure 13. Examples of isolated tremor signals detected at Slope Base. Figure format follows Figure 10b, with all waveforms filtered from 3-10 Hz.

5.5 Discussion

5.5.1 The significance of instrument burial

We do not observe harmonic bottom current-induced tremor signals on the buried OOI instruments, despite high bottom current speeds (up to 0.3 m/s, Figure 2). This is in stark contrast to a similarly situated but unburied OBS very near HYSB1, where we found that bottom current-induced tremors dominate records (station J26D, see Section 5.2 for more details). We did not explore a solution for classifying harmonic bottom current-induced tremor, but it would be necessary for working with unburied OBS in Cascadia or elsewhere. As we have shown for OBSs in Hikurangi, bottom current-induced tremor can be particularly disruptive in the detection of tectonic tremor (Figure 7). Similarly to our identification of ship noise, peaks in spectra could potentially be used to identify the harmonic nature of bottom current-induced tremor (Figure 7).

For both HYSB1 and HYS14, the relationship between background noise levels and in situ measured bottom currents is either weak or nonexistent (Figure 4). The relationship is not clearly stronger on the horizontal channels, as expected for unburied instruments (e.g., Trehu, 1985). Past studies proposed that OBS burial only a short distance beneath the ocean floor could strongly reduce noise (Collins et al., 2001; Duennebier & Sutton, 2007), and this appears to be true for the OOI OBSs, which are buried within soft sediments at less than a meter. These studies directly compared measured bottom currents and OBS noise and reported that burial of instruments reduced current-related noise below 1 Hz, for currents up to 0.1 m/s. We show that burial also reduces current-related noise at higher frequencies relevant to tectonic tremor and body waves from regional and local earthquakes, and we also show that this relationship stands up to bottom current speeds of 0.3 m/s (Figures 2 and 4).

OBS burial does not remove the influence of wind speeds on overall OBS noise, although the relationships we observe are variable (Figure 4). Interestingly, the deeper HYSB1 station shows a much stronger relationship to wind than HYS14 (Figure 4), despite similar wind speeds (Figure 2). One potential reason for this is that Slope Base site is located 20 km further from the coastline and therefore, experiences a greater fetch, which is the distance over which waves propagate under the sustained influence of wind without interruption (Massel, 1996). Longer fetch can increase wave energy at lower frequencies (Webb, 1998); however, prevailing winds are not from the east, such that increased fetch at HYSB1 likely doesn't fully account for the observed difference. The Hydrate Ridge site (790 m) is also situated much closer in depth to the SOFAR channel (~650 m in the Northeast Pacific; Wagstaff, 2005), which acts as a waveguide for sound in the ocean and allows signals to travel over long distances; this leads to higher background noise levels at Hydrate Ridge in comparison to Slope Base (Ragland et al., 2022).

This influence of distant noise sources at Hydrate Ridge could diminish the observed relationship between seismic noise and other factors.

5.5.2 Non-tectonic explanations for Slope Base tremor

The tectonic tremor-like signals recorded at Slope Base (station HYSB1), which occur several times as hour-long episodes and other times as isolated bursts (Figure 9), are the first reported offshore Cascadia. However, it is not possible to conclusively validate these detections as tectonic tremor without them being recorded on multiple instruments and localized to a tectonically feasible source. In this section, we explore several potential non-tectonic sources for our observed signals, and conclude that none seem very likely.

We can rule out the possibility that these signals are related to bottom currents because the instrument is buried, the timing does not correlate with increased in situ measured bottom currents (Figure 2), and the signals do not display the gliding spectral banding expected for bottom current-induced tremor (Corela et al., 2023b; Essing et al., 2021). During one of the sustained periods of tremor-like signals, there are some gliding spectral characteristics, but these occur only during the strongest signals and are not observed during the other sustained tremor periods (Figure 12) or during isolated bursts of tremor (Figure 13). The gliding spectra could be a resonant response of the instrument to ground shaking.

Because they are only seen on station HYSB1, it is possible that the tremor-like signals are related to instrument noise. To investigate whether the tremor-like signals are recorded by a different similarly-situated instrument, and therefore not instrument-specific noise, we applied our approach to a nearby OBS from the autonomous Cascadia Initiative experiment that overlapped with the beginning of the HYSB1 recording period (January 2015-July 2015). The autonomous instrument (network code 7D, station code J26D) is located on the incoming plate, ~15 km north of HYSB1 and, similarly, 6 km west of the deformation front (Figure 1b). We do

not present full findings for the J26D station because the instrument is unburied and therefore plagued by bottom current-generated tremor (Section 5.1), but we do report at least one sustained tremor-like signal in January 2015 (Figure 14c). This signal is similar in both waveform and spectral characteristics to the tremor-like signals on HYSB1, apart from a slightly higher maximum frequency (Figure 14). That these signals are recorded on both HYSB1 (buried Guralp CMG-1T sensor) and J26D (unburied Nanometrics Trillium sensor in Lamont housing) suggests that it is unlikely that they are internally generated instrument noise. However, this signal is not contemporaneously recorded on the HYSB1 station. This suggests that the signals are localized.

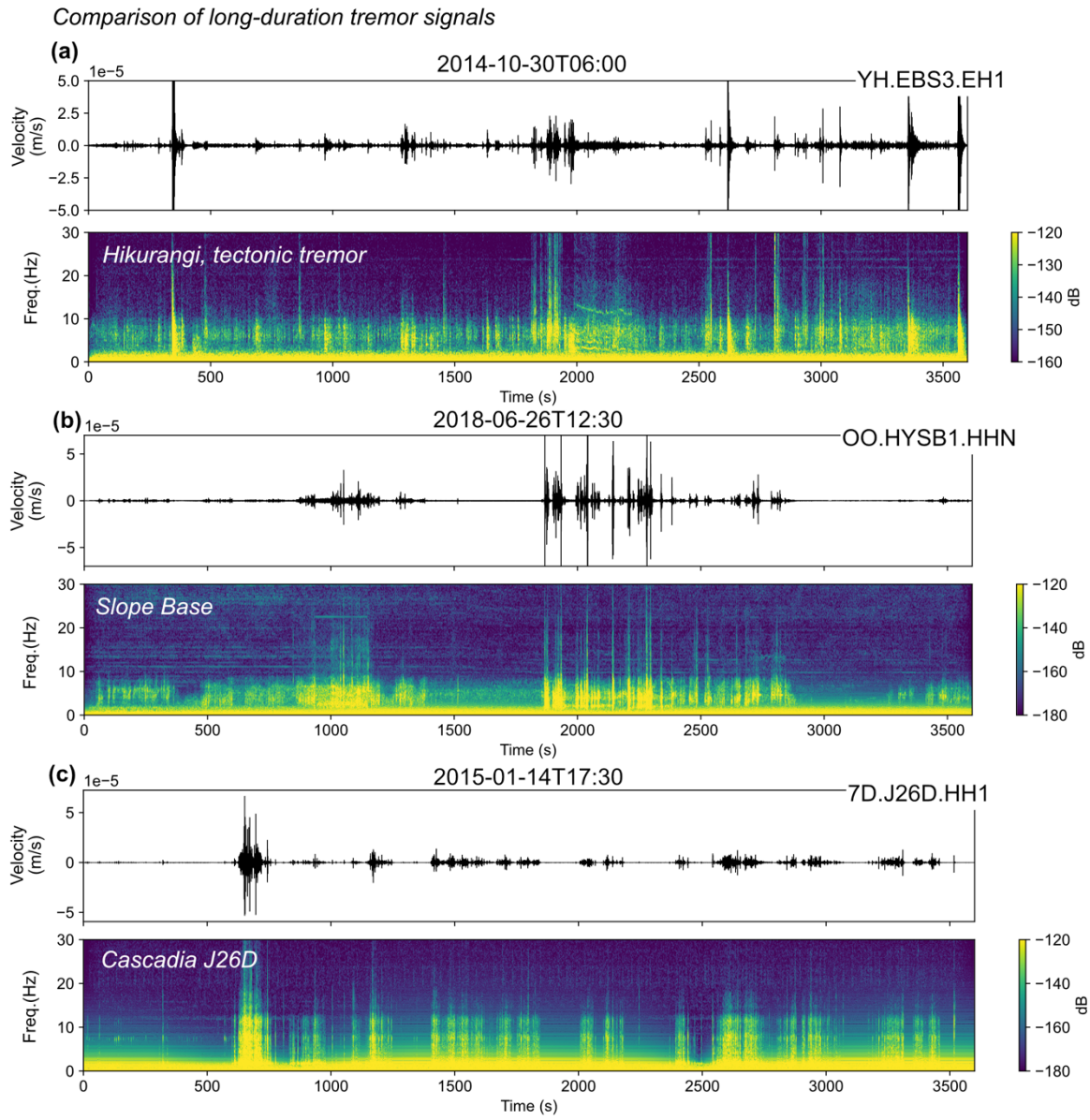

Figure 14. Comparison of 1 hour of tremor-like signals measured on three different instruments: **(a)** Confirmed, located tectonic tremor recorded at Hikurangi by instrument EBS3 (Figure 6a), **(b)** sustained tremor-like signal from our detections at Slope Base, **(c)** similar sustained tremor-like signal at autonomous Cascadia Initiative instrument J26D (Figure 1), found via preliminary application of our approach. In all subplots, the 3-10 Hz waveform and spectrogram are shown for the horizontal channels. The full instrument code, comprising network, station, and channel, and the start time of the window, are labelled atop each subplot.

Our tremor-like signals are distinct from SDEs (Figure 15), but at several other seafloor locations, gas- or fluid-induced SDEs have been shown to occur alongside tremor-like signals (Díaz et al., 2007; Hsu et al., 2013; Tsang-Hin-Sun et al., 2019). Similarly to our case, these reported tremor-like signals are only recorded at one station at a time and not at all on

hydrophones. These signals display similar waveform characteristics to those recorded by HYSB1 at Slope Base, but differing frequency contents. In Galicia, tidally modulated tremors are attributed to resonance of fluid-filled cracks (Díaz et al., 2007), but the tremors are highly monochromatic and each station displays a different dominant frequency. Offshore Taiwan, single-station tidally modulated tremors are attributed to gas expulsions from an active mud volcano, but the tremors begin as broadband signals with power up to 60 Hz and then decay to a harmonic signal at 7 Hz (Hsu et al., 2013). The single-station tremors seen in the Sea of Marmara, which are also attributed to gas emissions, show the highest similarity in waveform envelopes to the tremors we see at Slope Base (Tsang-Hin-Sun et al., 2019; see their Figures 4 and 5), but the tremors are much more broadband, with power up to 60 Hz.

We think it is unlikely that our tremor-like signals are gas-induced tremor. We cannot rule out this mechanism based on frequency characteristics because these are known to vary from site to site (Díaz et al., 2007; Hsu et al., 2013; Tsang-Hin-Sun et al., 2019), and it is not unreasonable that gas or fluid migration, or some form of resonance of fluid-filled cracks (Chouet, 1988) could occur near Slope Base. However, there have been extensive observations of gas seeps offshore Cascadia (Merle et al., 2021; Rudebusch et al., 2023), and only several occur near the deformation front, with most concentrated at ~500 m depth. It would also be surprising to see gas-induced tremor at two sites outboard of the deformation front and not at Hydrate Ridge, a known seep site.

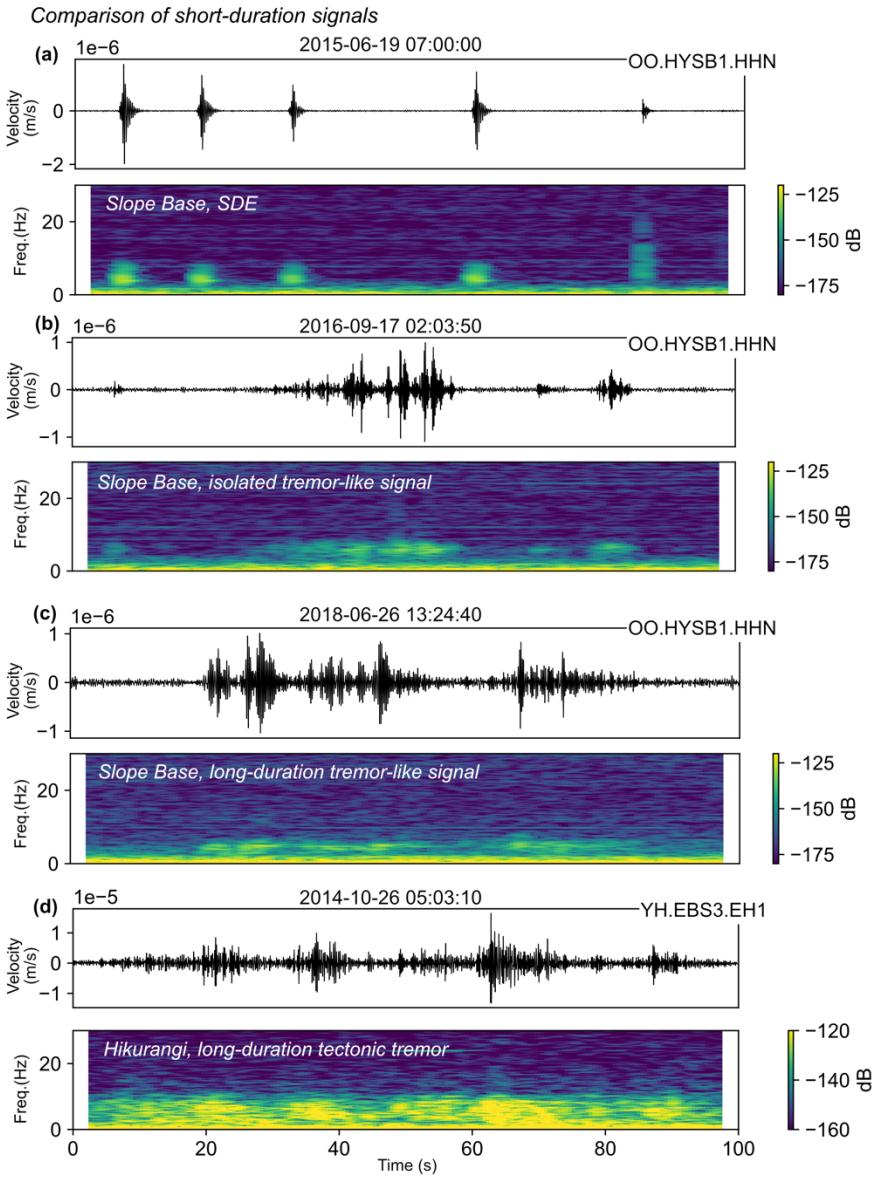

Figure 15. Zoomed-in comparison of 100 seconds of signals: **(a)** short duration events (SDEs) detected at Slope Base, **(b)** an isolated tremor-like signal recorded at Slope Base, **(c)** a snippet of a longer sustained tremor-like signal at Slope Base, **(d)** a snippet from a longer sustained confirmed tectonic tremor period at Hikurangi. Figure format follows Figure 14, with all waveforms filtered from 3-10 Hz.

5.5.3 Tectonic explanations for Slope Base tremor

Our reported tremor-like signals at Slope Base, in both waveform envelope and frequency, are consistent with the tectonic tremor signals observed at Hikurangi (see Figures 14 and 15), so we consider potential nearby tectonic sources. At similar latitudes, subducting seamounts have been linked to two clusters of seismicity underneath the continental shelf

(Carbotte et al., 2024; Morton et al., 2018, 2023; Tréhu et al., 2012; Williams et al., 2011; Figure 1). Subducted seamounts at other subduction zones have been shown to locally create complicated fracturing patterns (Mochizuki et al., 2008; Yamaya et al., 2022) and generate tectonic tremor on the plate interface (Shaddox & Schwartz, 2019; Todd et al., 2018). However, the seamounts and associated seismicity clusters at ~44.5°N have not exhibited significant activity since 2005 (maximum earthquake magnitude of 4.9). They are also ~75 km from Slope Base, and closer to Hydrate Ridge. Because we only see tectonic tremor-like signals on the Slope Base station, seamount-associated deformation is an unlikely tectonic tremor source.

Structures closer to Slope Base that may generate tectonic tremor include protothrusts, wedge faults, and the shallow decollement (Figure 16b). Protothrusts, which appear as small-displacement structures in active seismic imaging and are inferred to be incipient deformation of the incoming plate, have been observed at ~44.5°N (Han et al., 2017; Moore et al., 1995). Protothrusts appear on the oceanic plate along much of the margin (Canales et al., 2022). Tectonic tremor recorded only outboard of the deformation front could also be related to deformation within the outermost accretionary wedge. There are significant wedge faults near the OOI stations that extend to the decollement (Figure 16b). Brittle structures within folds on the accretionary wedge could generate microearthquakes and potentially tremor-like signals within larger stable slip (e.g., Remitti et al., 2024). Indeed, tectonic tremor has recently been shown to extend all the way up to the toe of the accretionary wedge and beyond the trench at the Nankai margin (Ogiso & Tamaribuchi, 2022; Tamaribuchi et al., 2022); high-resolution active seismic imaging supports that this could potentially be generated by a mix of deformational structures, including an incipient decollement and a frontal thrust within the outer accretionary wedge above a near-trench seamount (Kimura et al., 2024).

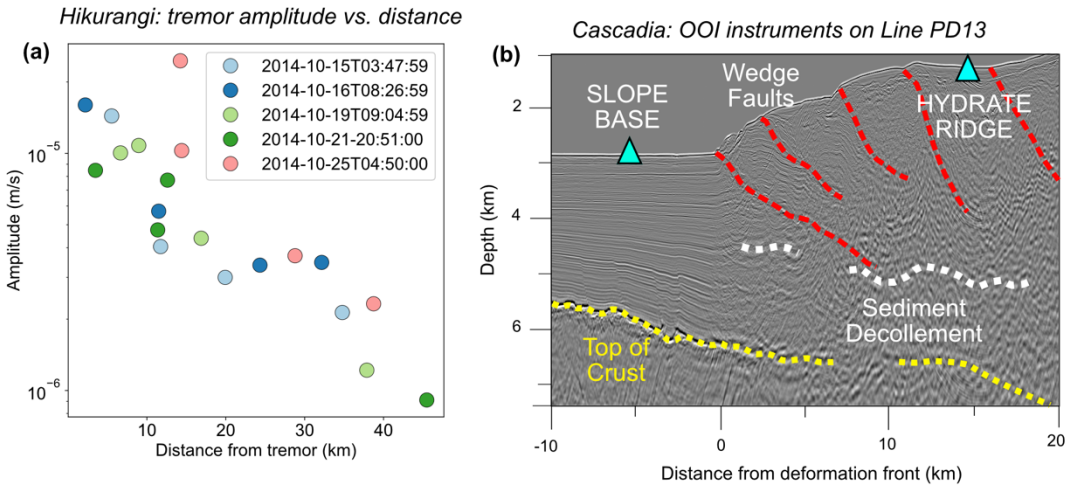

Figure 16. (a) Scatter plot showing maximum amplitudes associated the 3-10 Hz filtered waveform at 4 different stations at varying distances from tremor (EBS2, EBS3, EBS4, and EBS5; see Figure 6a). Points are colored by the tremor time they pertain to; 5 different tremor examples are shown. We visually checked each of the seismometers to confirm that they were recording tectonic tremor and not a different signal. We do not show amplitudes for stations whose codes begin with LOBS because the reported station response yielded unreasonable velocity values. **(b)** Subsurface structure along-strike near the OOI instruments, shown by processed pre-stack depth-migrated seismic reflection data from Line PD13 of the CASIE21 survey (Carbotte et al., 2023). Top of crust, sediment decollement, and wedge faults overlain from Carbotte et al. (2024). Note the ~3x vertical exaggeration. The location of the Slope Base and Hydrate Ridge OBSs are shown using cyan triangles, demonstrating that if tectonic tremor occurs near the deformation front, it is ~15 km from Hydrate Ridge and only ~5 km from Slope Base.

It is also possible that slow slip occurs across a larger portion of the plate interface that includes Hydrate Ridge, but tremor is only generated nearer to the deformation front; a similar scenario has been seen in the Nankai subduction zone. Araki et al. (2017) report small slow slip transients observed using borehole pressure sensors ~30-40 km landward of the trench. Tectonic tremor is also reported in association with these transients, but it is not collocated with the boreholes and is instead located 20-30 km closer to the trench. Araki et al. (2017) reported that tectonic tremor had a delayed onset in relation to slow slip and was only generated once slow slip migrated closer to the trench. They also noted that not all slow slip events generated tectonic tremor. Similarly, Nakano et al. (2018) found that low frequency earthquakes were not generated

by all slow slip events in the area, but only when slow slip occurred < ~24 km from the trench and had a slip of at least 2-4 cm.

If our detected tremor-like signals recorded on HYSB1 at Slope Base are tectonic tremor related to localized slip on the plate interface, this would suggest that there is not full locking right at the toe of the wedge. Although existing models for Cascadia suggest shallow locking (Li et al., 2018), on-land data can be fit with or without slip right at the trench. Initial seafloor geodetic measurements from Cascadia GNSS-A surveys are consistent with full locking (DeSanto et al., 2022) but do not preclude some level of unlocking at the toe. Furthermore, in Nankai, long-term seafloor GNSS-A measurements (Yokota et al., 2016) suggest full locking even in the same regions slow slip transients are observed (Araki et al. 2017).

Based on timing, it is unlikely that the tectonic tremor-like signals observed at Slope Base are triggered either by large earthquakes or downdip slow slip. Tectonic tremor occurring within the passing wave trains of large earthquakes has been extensively observed in deep Cascadia (e.g., Gomberg, 2010; Rubinstein et al., 2007). However, the shortest time between a preceding global M7+ earthquake and an HYSB1 tremor detection is ~9 hours. There is also no clear timing relationship between the HYSB1 tremor detections and episodes of deep tectonic tremor at similar latitudes (Wech, 2010; Figure 9b). Observed triggering relationships between deep downdip and shallow updip slow slip at subduction zones are few, but have been noted at Nankai and Costa Rica at time scales from instantaneous to several weeks (Davis et al., 2015; Hirose et al., 2010). In 2016 and 2017, sustained tremor episodes at HYSB1 occur ~6 months after downdip tremor at similar latitudes, but in 2015 and 2018, no downdip tremor precedes sustained tremor periods (Figure 9b).

5.5.4 Impacts of site location on tremor detection sensitivity

The Hydrate Ridge station does not record the same tectonic tremor-like signals we see at Slope Base (Figures 11 and 13), although it is only 20 km further landward (Figure 1). Although this is likely because the tremor source is localized and much closer to Slope Base, here we also explore how site location may play a role tectonic tremor the recording sensitivity.

The Hydrate Ridge station records many more emergent signals overall in comparison to Slope Base (Figure 8). However, this is likely only due to the closer proximity of Hydrate Ridge to the SOFAR channel, which allows many more T-phases to be recorded (Hamada, 1985; Okal, 2008). Indeed, visual inspection of the Hydrate Ridge detections shows that there are many more T-phases recorded than we discard with our method (e.g., Figure 10a). These can be identified as "slope" type T-phases, which have multiple peaks and frequencies primarily < 10 Hz (de Groot-Hedlin & Orcutt, 2001; Johnson et al., 1967; Walker et al., 1992). Although SOFAR channel proximity clearly increases the overall number of emergent signals recorded on the Hydrate Ridge station, we would not expect it to improve sensitivity to tectonic tremor signals, which do not travel in the water column.

To consider how sensitive tectonic tremor measurement can be to distance, we can consider the Hikurangi OBS tectonic tremor dataset (Figure 6). Figure 16a shows the relationship between station-to-tremor distance and maximum ground velocity amplitudes in 300 s windows reported for five different tremors located by Todd et al. (2018). Although there is some variability, overall, it appears that the amplitude of tectonic tremor signals diminishes by one order of magnitude between recordings made at ~5 km from the source versus those made at ~40 km. Our single-station detection method also shows much better timing agreement with the Todd et al. tremor catalog when the tremor source is < 40 km from the station, with the best agreement observed at distances of < 20 km (Figure 6e-f).

There is also evidence from some other subduction zones of channeling of tremor signals that varies based on relative location of the source to the plate interface. At Hikurangi, the tectonic tremor source is inferred to be at 5-10 km depth on the plate interface (Todd et al., 2018). While tectonic tremor is recorded at two sites on the overriding plate, both directly atop it (EBS3) and at a site ~30-40 km away (EBS5), it is not simultaneously recorded at a site also ~30-40 km away on the incoming plate (LOBS2) (Figure 6). We note that the LOBS2 seismometer type differs from the EBS3 and EBS5 stations. However, we visually checked recordings from the same seismometer type (LOBS5) on the overriding plate and found that it recorded tectonic tremor while LOBS2, on the incoming plate, did not.

Contrastingly, in Nankai, the tectonic tremor source is inferred to be at < 5 km depth on the plate interface, and the signal appears more clearly on stations near the deformation front. Araki et al. (2017) show that tremor occurring near the trench has the highest amplitudes on buried OBSs < 5-10 km landward of the trench; ~20-30 km landward, the tremor is still recorded by some buried OBSs, but is quieter overall is nearly indiscernible on some stations (see their Figure S2). Although the signal type is different, Nakano et al. (2018) also report nearby very low frequency earthquakes that are also most strongly recorded near the trench, with diminished amplitudes on stations 20-30 km landward (see their Figure 2). Taken alongside the contrasting deeper example from Hikurangi, these observations support the idea that a localized tectonic tremor signal occurring at < 5 km depths could be recorded at one station on the incoming plate and not at another station ~20 km away on the overriding plate, as is our case (Figure 16b).

5.6 Conclusions

We have developed a technique to isolate tectonic tremor-like signals on a single OBS amidst the presence of T-phases and ship noise. We demonstrate the efficacy of this technique through comparison to a multi-station tectonic tremor catalog for OBSs in the offshore Hikurangi

subduction zone. This approach could be readily adapted elsewhere to identify tectonic tremor in OBS datasets where station spacing is large and/or T-phases are dominant. However, using unburied instruments would require further work to identify and discard signals of harmonic bottom current-generated tremor. To handle these additional noise signals or process larger datasets, machine learning techniques (e.g., Holtzman et al., 2018; Seydoux et al., 2020) could first identify and cluster similar emergent signals, and then our straightforward waveform and spectra analyses could be applied to help identify tectonic tremor-like signals within clustering results.

We apply our single-station tectonic tremor detection to two long-term cabled OBSs deployed in the Cascadia subduction zone at ~44.5°N. We show that the burial of these instruments prevents harmonic bottom current-generated tremor and likely weakens the overall relationship between bottom currents and seismic noise. We identify tectonic tremor-like signals at the Slope Base HYSB1 station on the incoming plate, ~5 km seaward of the deformation front, that recur throughout the ~8-year observation period. These same signals are not recorded at the Hydrate Ridge HYS14 station, ~15 km landward of the deformation front. We cannot easily attribute the Slope Base tremor-like signals to instrumental, bottom current, or gas-induced noise, and we show that they are largely consistent with the characteristics expected for tectonic tremor. Tectonic tremor sources near Slope Base could include protothrusts on the incoming plate, deformation in the outermost wedge, or localized slow slip on the shallow portion of the plate interface. Observations from other subduction zones suggest it is reasonable that localized slow slip on the plate interface very near the deformation front could generate tectonic tremor that is only recordable at < ~5 km distance (Araki et al., 2017; Todd et al., 2018). However, with observation on only one station, we cannot conclude whether the signals are tectonic tremor from a localized source very near Slope Base, or another signal altogether.

Additional observations are needed to rule out potential signal sources and explore whether slow slip near the deformation front occurs elsewhere in Cascadia. Application of our single-station tectonic tremor detection technique to more sites from the autonomous Cascadia Initiative experiment could explore whether the tremor-like signals we observe at Slope Base are widespread or spatially concentrated. The planned deployment of four additional cabled OBSs to the OOI observatory through the COSZO project will also provide further opportunity to expand observations of potential tectonic tremor-like signals (Wilcock et al., 2024). Seafloor geodetic techniques that can measure small fault slip transients, including fiber optic strainmeters (e.g., Jackson & Zumberge, 2024), borehole strainmeters (Johnston & Linde, 2002), and seafloor pressure sensing (e.g., Woods et al., 2024) would also be useful to determine whether tremor-like signals are tectonic in origin.

5.7 Acknowledgements

We thank Anna Ledeczi, Harold Tobin, Aaron Wech, and Marine Denolle for insightful conversations that improved this manuscript.

Chapter 6: Summary and Future Work

The majority of plate boundary processes occur in the oceans, where mid-ocean ridges and subduction zones are responsible for the creation and destruction of Earth's crust. Due to limitations in seafloor monitoring, much of our knowledge of these plate boundaries is restricted to episodic large events, when mid-ocean ridges undergo extension via dike emplacement and subduction zones fail in very large earthquakes. This dissertation works to understand what types of deformation occur at submarine plate boundaries between episodic large events using novel cabled ocean bottom seismometer datasets. By providing a more complete picture of the deformational cycle, we can better understand the range of fault slip modes possible at different conditions and the relationship between seismic signals and forcings such as slow slip, fluid transients, and overall accumulated strain levels. This enhances fundamental constraints on earth processes and helps us to anticipate large plate boundary events, which in turn informs scientific experiment planning and hazard assessment.

This dissertation demonstrates that cabled ocean bottom seismometer (OBS) networks, despite their sparsity, can provide valuable constraints on submarine plate boundary deformation. In Chapter 2, I use a cabled OBS network to create an earthquake catalog that tracks the increase of strain over an entire seafloor spreading cycle at the Endeavour segment of the Juan de Fuca mid-ocean ridge. Long-term observation of earthquake trends allows us to forecast dike emplacement events and illuminates the interaction between regional tectonics, magmatism and hydrothermal venting. In Chapter 3, I show that a single OBS can approximate earthquake rates at the Endeavour segment. I use this to extend the available earthquake time series from Chapter 2, but I also show that the complicated ridge structure prevents single-station earthquake location. In Chapter 4, I show that multiplet earthquakes occurring between rupture events at the Endeavour segment, as captured by OBS, can illuminate deformation styles including slow slip

and fluid-induced earthquake swarms. In Chapter 5, I move to the Cascadia subduction zone and develop a novel approach to isolate tectonic tremor, a signal of slow slip, using individual cabled OBS. I show potential evidence for shallow tectonic tremor signals in a limited area near the deformation front. This suggests that localized slow slip events may occur at shallow plate depths or in the outermost accretionary wedge in Cascadia, which is a phenomenon that has been speculated but never observed.

The constraints on plate boundary deformation provided by this work have already proven valuable in planning for future seafloor observations. At the Endeavour segment, the improved understanding of the seafloor spreading cycle from Chapters 2 and 3 has allowed us to forecast, based on ongoing near-real-time cabled earthquake observations, that a dike emplacement will take place within the next 5 years. This has allowed the community to plan an interdisciplinary response, including a funded Canadian-U.S. collaborative deployment of additional OBSs and preparation for a rapid response cruise. Further, the potential identification of shallow tectonic tremor in Chapter 4 provides further motivation for the deployment of additional cabled OBS in the offshore Cascadia subduction zone, which will occur over the next several years through the funded COSZO project. The developed single-station tectonic tremor detection technique will provide a useful foundation for analyzing data from this planned extension of the cabled OBS network.

As with any scientific investigation, the findings of this dissertation have identified further areas of inquiry. For example, at the Endeavour segment, our discovery of repeating earthquakes represents the first direct recording of aseismic slip at the mid-ocean ridge environment. This finding represents a novel way to constrain mid-ocean ridge deformation, but future work is required to track aseismic slip rates through the spreading cycle and infer fault coupling characteristics across the ridge setting. At the Cascadia subduction zone, our discovery of

potential shallow tectonic tremor begins to suggest that smaller-scale slow slip events may occur along a broad portion of the margin. Capturing this type of deformation, if it occurs, will require focused, seafloor-specific observations and analysis techniques. Application of our new seafloor tremor detection approach to existing past seafloor datasets and planned upcoming deployments will help to confirm this behavior as slow slip, associate it with a source, and constrain its distribution along the greater subduction zone.

Bibliography

Abercrombie, R. E. (1995). Earthquake source scaling relationships from −1 to 5 M using seismograms recorded at 2.5-km depth. *Journal of Geophysical Research: Solid Earth*, *100*(B12), 24015–24036. https://doi.org/10.1029/95JB02397

Abercrombie, R. E., Bannister, S., Ristau, J., & Doser, D. (2017). Variability of earthquake stress drop in a subduction setting, the Hikurangi Margin, New Zealand. *Geophysical Journal International*, *208*(1), 306–320. https://doi.org/10.1093/gji/ggw393

Agius, M. R., & Galea, P. (2011). A Single-Station Automated Earthquake Location System at Wied Dalam Station, Malta. *Seismological Research Letters*, *82*(4), 545–559. https://doi.org/10.1785/gssrl.82.4.545

Aki, K., & Richards, P. G. (2002). *Quantitative seismology*.

Alessandrini, B., Cattaneo, M., Demartin, M., Gasperini, M., & Lanza, V. (1994). A simple P-wave polarization analysis: its application to earthquake location. *Annali Di Geofisica*, *XXXVII*. Retrieved from https://www.earth-prints.org/handle/2122/1847

Allen, R. V. (1978). Automatic earthquake recognition and timing from single traces. *Bulletin of the Seismological Society of America*, *68*(5), 1521–1532. https://doi.org/10.1785/BSSA0680051521

Andrew, R. K., Howe, B. M., & Mercer, J. A. (2011). Long-time trends in ship traffic noise for four sites off the North American West Coast. *The Journal of the Acoustical Society of America*, *129*(2), 642–651. https://doi.org/10.1121/1.3518770

Annoura, S., Hashimoto, T., Kamaya, N., & Katsumata, A. (2017). Shallow episodic tremor near the Nankai Trough axis off southeast Mie prefecture, Japan. *Geophysical Research Letters*, *44*(8), 3564–3571. https://doi.org/10.1002/2017GL073006

Araki, E., Saffer, D. M., Kopf, A. J., Wallace, L. M., Kimura, T., Machida, Y., et al. (2017). Recurring and triggered slow-slip events near the trench at the Nankai Trough subduction megathrust. *Science*, *356*(6343), 1157–1160. https://doi.org/10.1126/science.aan3120

Arnoux, G. M., Toomey, D. R., Hooft, E. E. E., Wilcock, W. S. D., Morgan, J., Warner, M., & VanderBeek, B. P. (2017). Seismic evidence that black smoker heat flux is influenced by localized magma replenishment and associated increases in crustal permeability: Magma Recharge Governs Heat Flux. *Geophysical Research Letters*, *44*(4), 1687–1695. https://doi.org/10.1002/2016GL071990

Arnoux, G. M., Toomey, D. R., Hooft, E. E. E., & Wilcock, W. S. D. (2019). Seismic Imaging and Physical Properties of the Endeavour Segment: Evidence that Skew Between Mantle and Crustal Magmatic Systems Governs Spreading Center Processes. *Geochemistry, Geophysics, Geosystems*, *20*(3), 1319–1339. https://doi.org/10.1029/2018GC007978

Baillard, C., Crawford, W. C., Ballu, V., Hibert, C., & Mangeney, A. (2014). An automatic kurtosis-based P-and S-phase picker designed for local seismic networks. *Bulletin of the Seismological Society of America*, *104*(1), 394–409.

Barcheck, G., Abers, G. A., Adams, A. N., Bécel, A., Collins, J., Gaherty, J. B., et al. (2020). The Alaska amphibious community seismic experiment. *Seismological Society of America*, *91*(6), 3054–3063.

Barker, D. H. N., Henrys, S., Caratori Tontini, F., Barnes, P. M., Bassett, D., Todd, E., & Wallace, L. (2018). Geophysical Constraints on the Relationship Between Seamount Subduction, Slow Slip, and Tremor at the North Hikurangi Subduction Zone, New Zealand. *Geophysical Research Letters*, *45*(23), 12,804-12,813. https://doi.org/10.1029/2018GL080259

Barnes, C. R., Best, M. M., & Zielinski, A. (2008). The NEPTUNE Canada regional cabled ocean observatory. *Technology (Crayford, England)*, *50*(3).

Batsi, E., Tsang-Hin-Sun, E., Klingelhoefer, F., Bayrakci, G., Chang, E. T. Y., Lin, J.-Y., et al. (2019). Nonseismic Signals in the Ocean: Indicators of Deep Sea and Seafloor Processes on Ocean-Bottom Seismometer Data. *Geochemistry, Geophysics, Geosystems*, *20*(8), 3882–3900. https://doi.org/10.1029/2019GC008349

Battaglia, J., Got, J.-L., & Okubo, P. (2003). Location of long-period events below Kilauea Volcano using seismic amplitudes and accurate relative relocation. *Journal of Geophysical Research: Solid Earth*, *108*(B12). https://doi.org/10.1029/2003JB002517

Bayer, B., Kind, R., Hoffmann, M., Yuan, X., & Meier, T. (2012). Tracking unilateral earthquake rupture by P-wave polarization analysis: Tracking unilateral earthquake. *Geophysical Journal International*, *188*(3), 1141–1153. https://doi.org/10.1111/j.1365-246X.2011.05304.x

Becker, J. A., Bickle, M. J., Galy, A., & Holland, T. J. (2008). Himalayan metamorphic CO2 fluxes: Quantitative constraints from hydrothermal springs. *Earth and Planetary Science Letters*, *265*(3–4), 616–629.

Behn, M. D., & Ito, G. (2008). Magmatic and tectonic extension at mid-ocean ridges: 1. Controls on fault characteristics: extension at mid-ocean ridges. *Geochemistry, Geophysics, Geosystems*, *9*(8), n/a-n/a. https://doi.org/10.1029/2008GC001965

Beroza, G. C., & Ide, S. (2011). Slow Earthquakes and Nonvolcanic Tremor. *Annual Review of Earth and Planetary Sciences*, *39*(1), 271–296. https://doi.org/10.1146/annurev-earth-040809-152531

Bohnenstiehl, D. R., Dziak, R. P., Tolstoy, M., Fox, C. G., & Fowler, M. (2004). Temporal and spatial history of the 1999–2000 Endeavour Segment seismic series, Juan de Fuca Ridge. *Geochemistry, Geophysics, Geosystems*, *5*(9).

Bonamassa, O., & Vidale, J. E. (1991). Directional site resonances observed from aftershocks of the 18 October 1989 Loma Prieta earthquake. *Bulletin of the Seismological Society of America*, *81*(5), 1945–1957. https://doi.org/10.1785/BSSA0810051945

Bonamassa, O., Vidale, J. E., Houston, H., & Schwartz, S. Y. (1991). Directional site resonances and the influence of near-surface geology on ground motion. *Geophysical Research Letters*, *18*(5), 901–904. https://doi.org/10.1029/91GL01063

Borghi, A., Aoudia, A., Javed, F., & Barzaghi, R. (2016). Precursory slow-slip loaded the 2009 L'Aquila earthquake sequence. *Geophysical Journal International*, *205*(2), 776–784. https://doi.org/10.1093/gji/ggw046

Brudzinski, M. R., & Allen, R. M. (2007). Segmentation in episodic tremor and slip all along Cascadia. *Geology*, *35*(10), 907. https://doi.org/10.1130/G23740A.1

Brune, J. N. (1970). Tectonic stress and the spectra of seismic shear waves from earthquakes. *Journal of Geophysical Research*, *75*(26), 4997–5009.

Buck, R., Einarsson, P., & Brandsdóttir, B. (2006). Tectonic stress and magma chamber size as controls on dike propagation: Constraints from the 1975–1984 Krafla rifting episode. *J. Geophys. Res*, *111*. https://doi.org/10.1029/2005JB003879

Buck, W. R., Carbotte, S. M., & Mutter, C. (1997). Controls on extrusion at mid-ocean ridges. *Geology*, *25*(10), 935–938.

Buck, W. R., Lavier, L. L., & Poliakov, A. N. B. (2005). Modes of faulting at mid-ocean ridges. *Nature*, *434*(7034), 719–723. https://doi.org/10.1038/nature03358

Burger, W., & Burge, M. J. (2009). *Principles of Digital Image Processing: Core Algorithms*. London: Springer. https://doi.org/10.1007/978-1-84800-195-4

Burgette, R. J., Weldon II, R. J., & Schmidt, D. A. (2009). Interseismic uplift rates for western Oregon and along-strike variation in locking on the Cascadia subduction zone. *Journal of Geophysical Research: Solid Earth*, *114*(B1). https://doi.org/10.1029/2008JB005679

Bürgmann, R. (2018). The geophysics, geology and mechanics of slow fault slip. *Earth and Planetary Science Letters*, *495*, 112–134.

Buskirk, R. E., Frohlich, C., Latham, G. V., Chen, A. T., & Lawton, J. (1981). Evidence that biological activity affects Ocean Bottom Seismograph recordings. *Marine Geophysical Researches*, *5*(2), 189–205. https://doi.org/10.1007/BF00163479

Butterfield, D. A., McDuff, R. E., Mottl, M. J., Lilley, M. D., Lupton, J. E., & Massoth, G. J. (1994). Gradients in the composition of hydrothermal fluids from the Endeavour segment vent field: Phase separation and brine loss. *Journal of Geophysical Research: Solid Earth*, *99*(B5), 9561–9583.

Cabaniss, H. E., Gregg, P. M., Nooner, S. L., & Chadwick, W. W. (2020). Triggering of eruptions at Axial Seamount, Juan de Fuca Ridge. *Scientific Reports*, *10*(1), 10219. https://doi.org/10.1038/s41598-020-67043-0

Canales, J. P., Sohn, R. A., & deMartin, B. J. (2007). Crustal structure of the Trans-Atlantic Geotraverse (TAG) segment (Mid-Atlantic Ridge, 26°10′N): Implications for the nature of hydrothermal circulation and detachment faulting at slow spreading ridges. *Geochemistry, Geophysics, Geosystems*, *8*(8). https://doi.org/10.1029/2007GC001629

Canales, J. P., Miller, N. C., Baldwin, W. E., Carbotte, S. M., Han, S., Boston, B., & Lizarralde, D. (2022). CASIE21-OBS: Acquisition of a Controlled-Source Marine Wide-Angle

Seismic Refraction/Reflection Dataset Across the Cascadia Margin, *2022*, S55D-0136. Presented at the AGU Fall Meeting Abstracts.

Carbotte, S. M., Nedimović, M. R., Canales, J. P., Kent, G. M., Harding, A. J., & Marjanović, M. (2008). Variable crustal structure along the Juan de Fuca Ridge: Influence of on-axis hot spots and absolute plate motions: variable crustal structure. *Geochemistry, Geophysics, Geosystems*, *9*(8), n/a-n/a. https://doi.org/10.1029/2007GC001922

Carbotte, S. M., Marjanović, M., Arnulf, A. F., Nedimović, M. R., Canales, J. P., & Arnoux, G. M. (2021). Stacked magma lenses beneath mid-ocean ridges: insights from new seismic observations and synthesis with prior geophysical and geologic findings. *Journal of Geophysical Research: Solid Earth*, *126*(4), e2020JB021434.

Carbotte, S. M., Boston, B., Han, S., Shuck, B., Beeson, J., Canales, J. P., et al. (2024). Subducting plate structure and megathrust morphology from deep seismic imaging linked to earthquake rupture segmentation at Cascadia. *Science Advances*, *10*(23), eadl3198. https://doi.org/10.1126/sciadv.adl3198

Carvajal, M., Sun, T., Wang, K., Luo, H., & Zhu, Y. (2022). Evaluating the Tsunamigenic Potential of Buried Versus Trench-Breaching Megathrust Slip. *Journal of Geophysical Research: Solid Earth*, *127*(8), e2021JB023722. https://doi.org/10.1029/2021JB023722

Chadwick Jr, W. W., Wilcock, W. S., Nooner, S. L., Beeson, J. W., Sawyer, A. M., & Lau, T.-K. (2022). Geodetic monitoring at Axial Seamount since its 2015 eruption reveals a waning magma supply and tightly linked rates of deformation and seismicity. *Geochemistry, Geophysics, Geosystems*, *23*(1), e2021GC010153.

Chamberlain, C. J., Hopp, C. J., Boese, C. M., Warren-Smith, E., Chambers, D., Chu, S. X., et al. (2017). EQcorrscan: Repeating and Near-Repeating Earthquake Detection and Analysis

in Python. *Seismological Research Letters*, *89*(1), 173–181. https://doi.org/10.1785/0220170151

Chaudhuri, K., & Ghosh, A. (2022). Widespread Very Low Frequency Earthquakes (VLFEs) Activity Offshore Cascadia. *Geophysical Research Letters*, *49*(13), e2022GL097962. https://doi.org/10.1029/2022GL097962

Chen, K. H., Nadeau, R. M., & Rau, R.-J. (2007). Towards a universal rule on the recurrence interval scaling of repeating earthquakes? *Geophysical Research Letters*, *34*(16). https://doi.org/10.1029/2007GL030554

Chen, X., Shearer, P. M., & Abercrombie, R. E. (2012). Spatial migration of earthquakes within seismic clusters in Southern California: Evidence for fluid diffusion. *Journal of Geophysical Research: Solid Earth*, *117*(B4). https://doi.org/10.1029/2011JB008973

Chen, Y., & Morgan, W. J. (1990). A nonlinear rheology model for mid-ocean ridge axis topography. *Journal of Geophysical Research: Solid Earth*, *95*(B11), 17583–17604. https://doi.org/10.1029/JB095iB11p17583

Chiodini, G., Cardellini, C., Amato, A., Boschi, E., Caliro, S., Frondini, F., & Ventura, G. (2004). Carbon dioxide Earth degassing and seismogenesis in central and southern Italy. *Geophysical Research Letters*, *31*(7).

Chiodini, G., Cardellini, C., Di Luccio, F., Selva, J., Frondini, F., Caliro, S., et al. (2020). Correlation between tectonic CO2 Earth degassing and seismicity is revealed by a 10-year record in the Apennines, Italy. *Science Advances*, *6*(35), eabc2938.

Chouet, B. (1988). Resonance of a fluid-driven crack: Radiation properties and implications for the source of long-period events and harmonic tremor. *Journal of Geophysical Research: Solid Earth*, *93*(B5), 4375–4400. https://doi.org/10.1029/JB093iB05p04375

Clague, D. A., Paduan, J. B., & Davis, A. S. (2009). Widespread strombolian eruptions of mid-ocean ridge basalt. *Journal of Volcanology and Geothermal Research*, *180*(2–4), 171–188.

Clague, D. A., Dreyer, B. M., Paduan, J. B., Martin, J. F., Caress, D. W., Gill, J. B., et al. (2014). Eruptive and tectonic history of the Endeavour Segment, Juan de Fuca Ridge, based on AUV mapping data and lava flow ages. *Geochemistry, Geophysics, Geosystems*, *15*(8), 3364–3391.

Clague, D. A., Martin, J. F., Paduan, J. B., Butterfield, D. A., Jamieson, J. W., Le Saout, M., et al. (2020). Hydrothermal chimney distribution on the Endeavour segment, Juan de Fuca Ridge. *Geochemistry, Geophysics, Geosystems*, *21*(6), e2020GC008917.

Collins, J. A., Vernon, F. L., Orcutt, J. A., Stephen, R. A., Peal, K. R., Wooding, F. B., et al. (2001). Broadband seismology in the oceans: Lessons from the Ocean Seismic Network Pilot Experiment. *Geophysical Research Letters*, *28*(1), 49–52. https://doi.org/10.1029/2000GL011638

Corela, C., Loureiro, A., Duarte, J. L., Matias, L., Rebelo, T., & Bartolomeu, T. (2023a). The effect of deep ocean currents on ocean- bottom seismometers records. *Natural Hazards and Earth System Sciences*, *23*(4), 1433–1451. https://doi.org/10.5194/nhess-23-1433-2023

Cowen, J. P., Baker, E. T., & Embley, R. W. (2004). Detection of and Response to Mid-Ocean Ridge Magmatic Events: Implications for the Subsurface Biosphere. In *The Subseafloor Biosphere at Mid-Ocean Ridges* (pp. 227–243). American Geophysical Union (AGU). https://doi.org/10.1029/144GM15

Cowen, J. P., Fornari, D. J., Shank, T. M., Love, B., Glazer, B., Treusch, A., et al. (2007). Volcanic Eruptions at East Pacific Rise Near 9°50′N. *Eos, Transactions American Geophysical Union*, *88*(7), 81. https://doi.org/10.1029/2007EO070001

Cowie, P. A., Scholz, C. H., Edwards, M., & Malinverno, A. (1993). Fault strain and seismic coupling on mid-ocean ridges. *Journal of Geophysical Research: Solid Earth*, *98*(B10), 17911–17920. https://doi.org/10.1029/93JB01567

Crawford, W. C., Rai, A., Singh, S. C., Cannat, M., Escartin, J., Wang, H., et al. (2013). Hydrothermal seismicity beneath the summit of Lucky Strike volcano, Mid-Atlantic Ridge. *Earth and Planetary Science Letters*, *373*, 118–128. https://doi.org/10.1016/j.epsl.2013.04.028

Crone, T. J., Wilcock, W. S. D., & McDuff, R. E. (2010). Flow rate perturbations in a black smoker hydrothermal vent in response to a mid-ocean ridge earthquake swarm. *Geochemistry, Geophysics, Geosystems*, *11*(3). https://doi.org/10.1029/2009GC002926

Cudrak, C. F., & Clowes, R. M. (1993). Crustal structure of Endeavour Ridge Segment, Juan de Fuca Ridge, from a detailed seismic refraction survey. *Journal of Geophysical Research: Solid Earth*, *98*(B4), 6329–6349.

Curewitz, D., & Karson, J. A. (1997). Structural settings of hydrothermal outflow: Fracture permeability maintained by fault propagation and interaction. *Journal of Volcanology and Geothermal Research*, *79*(3–4), 149–168.

Curtis, K. R., Howe, B. M., & Mercer, J. A. (1999). Low-frequency ambient sound in the North Pacific: Long time series observations. *The Journal of the Acoustical Society of America*, *106*(6), 3189–3200. https://doi.org/10.1121/1.428173

Dahl, P. H., Dall'Osto, D. R., & Harrington, M. J. (2021). Trends in low-frequency underwater noise off the Oregon coast and impacts of COVID-19 pandemic. *The Journal of the Acoustical Society of America*, *149*(6), 4073–4077. https://doi.org/10.1121/10.0005192

D'Alessandro, A., Mangano, G., D'Anna, G., & Luzio, D. (2013). Waveforms clustering and single-station location of microearthquake multiplets recorded in the northern Sicilian offshore region. *Geophysical Journal International*, *194*(3), 1789–1809. https://doi.org/10.1093/gji/ggt192

Danré, P., De Barros, L., Cappa, F., & Ampuero, J.-P. (2022). Prevalence of Aseismic Slip Linking Fluid Injection to Natural and Anthropogenic Seismic Swarms. *Journal of Geophysical Research: Solid Earth*, *127*(12), e2022JB025571. https://doi.org/10.1029/2022JB025571

Davis, E. E., Wang, K., Thomson, R. E., Becker, K., & Cassidy, J. F. (2001). An episode of seafloor spreading and associated plate deformation inferred from crustal fluid pressure transients. *Journal of Geophysical Research: Solid Earth*, *106*(B10), 21953–21963. https://doi.org/10.1029/2000JB000040

Davis, E. E., Villinger, H., & Sun, T. (2015). Slow and delayed deformation and uplift of the outermost subduction prism following ETS and seismogenic slip events beneath Nicoya Peninsula, Costa Rica. *Earth and Planetary Science Letters*, *410*, 117–127. https://doi.org/10.1016/j.epsl.2014.11.015

De Barros, L., Cappa, F., Deschamps, A., & Dublanchet, P. (2020). Imbricated Aseismic Slip and Fluid Diffusion Drive a Seismic Swarm in the Corinth Gulf, Greece. *Geophysical Research Letters*, *47*(9), e2020GL087142. https://doi.org/10.1029/2020GL087142

De Caro, M., Montuori, C., Frugoni, F., Monna, S., Cammarano, F., & Beranzoli, L. (2020). T-Phases Observed at the Ionian Seafloor: Seismic Source and Bathymetric Effects. *Seismological Research Letters*, *92*(1), 481–493. https://doi.org/10.1785/0220200096

Delaney, J. R., Robigou, V., McDuff, R. E., & Tivey, M. K. (1992). Geology of a vigorous hydrothermal system on the Endeavour Segment, Juan de Fuca Ridge. *Journal of Geophysical Research: Solid Earth*, *97*(B13), 19663–19682. https://doi.org/10.1029/92JB00174

Delaney, J. R., Kelley, D. S., Lilley, M. D., Butterfield, D. A., Baross, J. A., Wilcock, W. S. D., et al. (1998). The quantum event of oceanic crustal accretion: Impacts of diking at mid-ocean ridges. *Science*, *281*(5374), 222–230.

deMartin, B. J., Sohn, R. A., Pablo Canales, J., & Humphris, S. E. (2007). Kinematics and geometry of active detachment faulting beneath the Trans-Atlantic Geotraverse (TAG) hydrothermal field on the Mid-Atlantic Ridge. *Geology*, *35*(8), 711. https://doi.org/10.1130/G23718A.1

DeMets, C., Gordon, R. G., & Argus, D. F. (2010). Geologically current plate motions. *Geophysical Journal International*, *181*(1), 1–80.

DeSanto, J. B., Schmidt, D. A., Chadwell, C. D., Zumberge, M. A., & Sasagawa, G. S. (2022). Horizontal deformation rates near the Cascadia subduction zone trench revealed by offshore GNSS-Acoustic time series. In *AGU Fall Meeting Abstracts* (Vol. 2022, pp. T56A-05). Retrieved from https://ui.adsabs.harvard.edu/abs/2022AGUFM.T56A..05D/abstract

Di Giulio, G., Cara, F., Rovelli, A., Lombardo, G., & Rigano, R. (2009). Evidences for strong directional resonances in intensely deformed zones of the Pernicana fault, Mount Etna,

Italy. *Journal of Geophysical Research: Solid Earth*, *114*(B10). https://doi.org/10.1029/2009JB006393

Díaz, J., Gallart, J., & Gaspà, O. (2007). Atypical seismic signals at the Galicia Margin, North Atlantic Ocean, related to the resonance of subsurface fluid-filled cracks. *Tectonophysics*, *433*(1), 1–13. https://doi.org/10.1016/j.tecto.2007.01.004

Dixon, T. H., Jiang, Y., Malservisi, R., McCaffrey, R., Voss, N., Protti, M., & Gonzalez, V. (2014). Earthquake and tsunami forecasts: Relation of slow slip events to subsequent earthquake rupture. *Proceedings of the National Academy of Sciences*, *111*(48), 17039–17044. https://doi.org/10.1073/pnas.1412299111

Duennebier, F. K., & Sutton, G. H. (2007). Why bury ocean bottom seismometers? *Geochemistry, Geophysics, Geosystems*, *8*(2). https://doi.org/10.1029/2006GC001428

Duverger, C., Lambotte, S., Bernard, P., Lyon-Caen, H., Deschamps, A., & Nercessian, A. (2018). Dynamics of microseismicity and its relationship with the active structures in the western Corinth Rift (Greece). *Geophysical Journal International*, *215*(1), 196–221. https://doi.org/10.1093/gji/ggy264

Dziak, R., Chadwick, B., Cowen, J., Baker, E., Embley, R., Bohnenstiehl, D., & Resing, J. (2006). Detecting volcanic events in the northeast Pacific. *Eos, Transactions American Geophysical Union*, *87*(4), 37–42. https://doi.org/10.1029/2006EO040001

Dziak, R., Hammond, S., & Fox, C. (2011). A 20-Year Hydroacoustic Time Series of Seismic and Volcanic Events in the Northeast Pacific Ocean. *Oceanography*, *24*(3), 280–293. https://doi.org/10.5670/oceanog.2011.79

Dziak, R., Bohnenstiehl, D., & Smith, D. (2012a). Hydroacoustic Monitoring of Oceanic Spreading Centers: Past, Present, and Future. *Oceanography*, *25*(1), 116–127. https://doi.org/10.5670/oceanog.2012.10

Dziak, R. P. (2006). Explorer deformation zone: Evidence of a large shear zone and reorganization of the Pacific–Juan de Fuca–North American triple junction. *Geology*, *34*(3), 213–216.

Dziak, R. P., & Fox, C. G. (1999a). Long-term seismicity and ground deformation at Axial Volcano, Juan de Fuca Ridge. *Geophysical Research Letters*, *26*(24), 3641–3644.

Dziak, R. P., & Fox, C. G. (1999b). The January 1998 earthquake swarm at Axial Volcano, Juan de Fuca Ridge: Hydroacoustic evidence of seafloor volcanic activity. *Geophysical Research Letters*, *26*(23), 3429–3432.

Dziak, R. P., Fox, C. G., & Schreiner, A. E. (1995). The June-July 1993 seismo-acoustic event at CoAxial segment, Juan de Fuca Ridge: Evidence for a lateral dike injection. *Geophysical Research Letters*, *22*(2), 135–138.

Dziak, R. P., Smith, D. K., Bohnenstiehl, D. R., Fox, C. G., Desbruyeres, D., Matsumoto, H., et al. (2004). Evidence of a recent magma dike intrusion at the slow spreading Lucky Strike segment, Mid-Atlantic Ridge. *Journal of Geophysical Research: Solid Earth*, *109*(B12).

Dziak, R. P., Bohnenstiehl, D. R., Matsumoto, H., Fowler, M. J., Haxel, J. H., Tolstoy, M., & Waldhauser, F. (2009). January 2006 seafloor-spreading event at 9°50′N, East Pacific Rise: Ridge dike intrusion and transform fault interactions from regional hydroacoustic data. *Geochemistry, Geophysics, Geosystems*, *10*(6). https://doi.org/10.1029/2009GC002388

Dziak, R. P., Haxel, J. H., Bohnenstiehl, D. R., Chadwick, W. W., Nooner, S. L., Fowler, M. J., et al. (2012b). Seismic precursors and magma ascent before the April 2011 eruption at Axial Seamount. *Nature Geoscience*, *5*(7), 478–482. https://doi.org/10.1038/ngeo1490

Efron, B., & Tibshirani, R. J. (1994). *An Introduction to the Bootstrap*. New York: Chapman and Hall/CRC. https://doi.org/10.1201/9780429246593

Einarsson, P., & Brandsdóttir, B. (1980). Seismological evidence for lateral magma intrusion during the July 1978 deflation of the Krafla volcano in NE-Iceland. *Journal of Geophysics*, *47*(1), 160–165.

Escartín, J., Smith, D. K., Cann, J., Schouten, H., Langmuir, C. H., & Escrig, S. (2008). Central role of detachment faults in accretion of slow-spreading oceanic lithosphere. *Nature*, *455*(7214), 790–794. https://doi.org/10.1038/nature07333

Eshelby, J. D., & Peierls, R. E. (1997). The determination of the elastic field of an ellipsoidal inclusion, and related problems. *Proceedings of the Royal Society of London. Series A. Mathematical and Physical Sciences*, *241*(1226), 376–396. https://doi.org/10.1098/rspa.1957.0133

Essing, D., Schlindwein, V., Schmidt-Aursch, M. C., Hadziioannou, C., & Stähler, S. C. (2021). Characteristics of Current-Induced Harmonic Tremor Signals in Ocean-Bottom Seismometer Records. *Seismological Research Letters*, *92*(5), 3100–3112. https://doi.org/10.1785/0220200397

Eyre, T. S., Eaton, D. W., Garagash, D. I., Zecevic, M., Venieri, M., Weir, R., & Lawton, D. C. (2019). The role of aseismic slip in hydraulic fracturing–induced seismicity. *Science Advances*, *5*(8), eaav7172. https://doi.org/10.1126/sciadv.aav7172

Fischer, T., Hainzl, S., & Vlček, J. (2023). Fast migration episodes within earthquake swarms. *Geophysical Journal International*, *235*(1), 312–325. https://doi.org/10.1093/gji/ggad221

Font, Y., Kao, H., Lallemand, S., Liu, C.-S., & Chiao, L.-Y. (2004). Hypocentre determination offshore of eastern Taiwan using the Maximum Intersection method. *Geophysical Journal International*, *158*(2), 655–675.

Fouquet, Y. (1997). Where are the large hydrothermal sulphide deposits in the oceans? *Philosophical Transactions of the Royal Society of London. Series A: Mathematical, Physical and Engineering Sciences*, *355*(1723), 427–441.

Fox, C. G., & Dziak, R. P. (1998). Hydroacoustic detection of volcanic activity on the Gorda Ridge, February–March 1996. *Deep Sea Research Part II: Topical Studies in Oceanography*, *45*(12), 2513–2530.

Frohlich, C., & Pulliam, J. (1999). Single-station location of seismic events: a review and a plea for more research. *Physics of the Earth and Planetary Interiors*, *113*(1), 277–291. https://doi.org/10.1016/S0031-9201(99)00055-2

Frontera, T., Ugalde, A., Olivera, C., Jara, J. A., & Goula, X. (2010). Seismic Ambient Noise Characterization of a New Permanent Broadband Ocean Bottom Seismometer Site offshore Catalonia (Northeastern Iberian Peninsula). *Seismological Research Letters*, *81*(5), 740–749. https://doi.org/10.1785/gssrl.81.5.740

Gao, D., Kao, H., & Wang, B. (2021). Misconception of Waveform Similarity in the Identification of Repeating Earthquakes. *Geophysical Research Letters*, *48*(13), e2021GL092815. https://doi.org/10.1029/2021GL092815

Gilbert, L. A., & Johnson, H. P. (1999). Direct measurements of oceanic crustal density at the northern Juan de Fuca Ridge. *Geophysical Research Letters*, *26*(24), 3633–3636.

Golden, C. E., Webb, S. C., & Sohn, R. A. (2003). Hydrothermal microearthquake swarms beneath active vents at Middle Valley, northern Juan de Fuca Ridge: microearthquake swarms. *Journal of Geophysical Research: Solid Earth*, *108*(B1). https://doi.org/10.1029/2001JB000226

Gomberg, J. (2010). Lessons from (triggered) tremor. *Journal of Geophysical Research: Solid Earth*, *115*(B10). https://doi.org/10.1029/2009JB007011

Gómez-Arredondo, C. M., Montalvo-Arrieta, J. C., Iglesias-Mendoza, A., & Espíndola-Castro, V. H. (2016). Relocation and seismotectonic interpretation of the seismic swarm of August - December of 2012 in the Linares area, northeastern Mexico. *Geofísica Internacional*, *55*(2). https://doi.org/10.22201/igeof.00167169p.2016.55.2.1714

de Groot-Hedlin, C. D., & Orcutt, J. A. (2001). Excitation of T-phases by seafloor scattering. *The Journal of the Acoustical Society of America*, *109*(5), 1944–1954. https://doi.org/10.1121/1.1361057

Hamada, N. (1985). T Waves Recorded by Ocean Bottom Seismographs Off the South Coast of Tokai Area, Central Honshu, Japan. *Journal of Physics of the Earth*, *33*(5), 391–410. https://doi.org/10.4294/jpe1952.33.391

Han, S., Bangs, N. L., Carbotte, S. M., Saffer, D. M., & Gibson, J. C. (2017). Links between sediment consolidation and Cascadia megathrust slip behaviour. *Nature Geoscience*, *10*(12), 954–959. https://doi.org/10.1038/s41561-017-0007-2

Hanks, T. C., & Kanamori, H. (1979). A moment magnitude scale. *Journal of Geophysical Research: Solid Earth*, *84*(B5), 2348–2350.

Hannington, M., Jamieson, J., Monecke, T., Petersen, S., & Beaulieu, S. (2011). The abundance of seafloor massive sulfide deposits. *Geology*, *39*(12), 1155–1158. https://doi.org/10.1130/G32468.1

Hanson, J. A., & Bowman, J. R. (2006). Methods for monitoring hydroacoustic events using direct and reflected T waves in the Indian Ocean. *Journal of Geophysical Research: Solid Earth*, *111*(B2). https://doi.org/10.1029/2004JB003609

Hatch, R. L., Abercrombie, R. E., Ruhl, C. J., & Smith, K. D. (2020). Evidence of Aseismic and Fluid-Driven Processes in a Small Complex Seismic Swarm Near Virginia City, Nevada.

Geophysical Research Letters, *47*(4), e2019GL085477. https://doi.org/10.1029/2019GL085477

Hayes, G. P., Moore, G. L., Portner, D. E., Hearne, M., Flamme, H., Furtney, M., & Smoczyk, G. M. (2018). Slab2, a comprehensive subduction zone geometry model. *Science*, *362*(6410), 58–61. https://doi.org/10.1126/science.aat4723

Hayward, T. W., & Bostock, M. G. (2017). Slip Behavior of the Queen Charlotte Plate Boundary Before and After the 2012, M 7.8 Haida Gwaii Earthquake: Evidence From Repeating Earthquakes. *Journal of Geophysical Research: Solid Earth*, *122*(11), 8990–9011. https://doi.org/10.1002/2017JB014248

Heesemann, M., Insua, T. L., Scherwath, M., Juniper, K. S., & Moran, K. (2014). Ocean Networks Canada: from geohazards research laboratories to smart ocean systems. *Oceanography*, *27*(2), 151–153. https://doi.org/10.5670/oceanog.2014.50

Hersbach, H., Bell, B., Berrisford, P., Hirahara, S., Horányi, A., Muñoz-Sabater, J., et al. (2020). The ERA5 global reanalysis. *Quarterly Journal of the Royal Meteorological Society*, *146*(730), 1999–2049. https://doi.org/10.1002/qj.3803

Hilmo, R., & Wilcock, W. S. D. (2020). Physical Sources of High-Frequency Seismic Noise on Cascadia Initiative Ocean Bottom Seismometers. *Geochemistry, Geophysics, Geosystems*, *21*(10), e2020GC009085. https://doi.org/10.1029/2020GC009085

Hirose, H., Asano, Y., Obara, K., Kimura, T., Matsuzawa, T., Tanaka, S., & Maeda, T. (2010). Slow Earthquakes Linked Along Dip in the Nankai Subduction Zone. *Science*, *330*(6010), 1502–1502. https://doi.org/10.1126/science.1197102

Holloway, J. R. (1998). Graphite-melt equilibria during mantle melting: constraints on CO2 in MORB magmas and the carbon content of the mantle. *Chemical Geology*, *147*(1–2), 89–97.

Holtzman, B. K., Paté, A., Paisley, J., Waldhauser, F., & Repetto, D. (2018). Machine learning reveals cyclic changes in seismic source spectra in Geysers geothermal field. *Science Advances*, *4*(5), eaao2929. https://doi.org/10.1126/sciadv.aao2929

Hooft, E. E., Patel, H., Wilcock, W., Becker, K., Butterfield, D., Davis, E., et al. (2010). A seismic swarm and regional hydrothermal and hydrologic perturbations: The northern Endeavour segment, February 2005. *Geochemistry, Geophysics, Geosystems*, *11*(12).

Hotovec-Ellis, A. J., Vidale, J. E., Gomberg, J., Thelen, W., & Moran, S. C. (2015). Changes in seismic velocity during the first 14 months of the 2004–2008 eruption of Mount St. Helens, Washington. *Journal of Geophysical Research: Solid Earth*, *120*(9), 6226–6240. https://doi.org/10.1002/2015JB012101

Hsu, S.-K., Wang, S.-Y., Liao, Y.-C., Yang, T. F., Jan, S., Lin, J.-Y., & Chen, S.-C. (2013). Tide-modulated gas emissions and tremors off SW Taiwan. *Earth and Planetary Science Letters*, *369–370*, 98–107. https://doi.org/10.1016/j.epsl.2013.03.013

Humphris, S. E., & Cann, J. R. (2000). Constraints on the energy and chemical balances of the modern TAG and ancient Cyprus seafloor sulfide deposits. *Journal of Geophysical Research: Solid Earth*, *105*(B12), 28477–28488. https://doi.org/10.1029/2000JB900289

Hunt, J. A., Zafu, A., Mather, T. A., Pyle, D. M., & Barry, P. H. (2017). Spatially Variable CO2 Degassing in the Main Ethiopian Rift: Implications for Magma Storage, Volatile Transport, and Rift-Related Emissions. *Geochemistry, Geophysics, Geosystems*, *18*(10), 3714–3737. https://doi.org/10.1002/2017GC006975

Ide, S. (2012). Variety and spatial heterogeneity of tectonic tremor worldwide. *Journal of Geophysical Research: Solid Earth*, *117*(B3). https://doi.org/10.1029/2011JB008840

Ide, S., Shelly, D. R., & Beroza, G. C. (2007). Mechanism of deep low frequency earthquakes: Further evidence that deep non-volcanic tremor is generated by shear slip on the plate interface. *Geophysical Research Letters*, *34*(3).

Igarashi, T., Matsuzawa, T., & Hasegawa, A. (2003). Repeating earthquakes and interplate aseismic slip in the northeastern Japan subduction zone. *Journal of Geophysical Research: Solid Earth*, *108*(B5). https://doi.org/10.1029/2002JB001920

Ito, G., & Behn, M. D. (2008). Magmatic and tectonic extension at mid-ocean ridges: 2. Origin of axial morphology. *Geochemistry, Geophysics, Geosystems*, *9*(9). https://doi.org/10.1029/2008GC001970

Jackson, N. M., & Zumberge, M. A. (2024). The Hunt for Shallow Slow Slip in Cascadia Using Seafloor Optical Fiber Strain. AGU24.

Jacobson, R. S., & Lewis, B. T. R. (1990). The first direct measurements of upper oceanic crustal compressional wave attenuation. *Journal of Geophysical Research: Solid Earth*, *95*(B11), 17417–17429.

Jamieson, J. W., Hannington, M. D., Clague, D. A., Kelley, D. S., Delaney, J. R., Holden, J. F., et al. (2013). Sulfide geochronology along the Endeavour Segment of the Juan de Fuca Ridge: Sulfide Ages Along the Endeavour Segment. *Geochemistry, Geophysics, Geosystems*, *14*(7), 2084–2099. https://doi.org/10.1002/ggge.20133

Jamieson, J. W., Clague, D. A., & Hannington, M. D. (2014). Hydrothermal sulfide accumulation along the Endeavour Segment, Juan de Fuca Ridge. *Earth and Planetary Science Letters*, *395*, 136–148. https://doi.org/10.1016/j.epsl.2014.03.035

Johnson, H. P., Karsten, J. L., Delaney, J. R., Davis, E. E., Currie, R. G., & Chase, R. L. (1983). A detailed study of the Cobb offset of the Juan de Fuca Ridge: Evolution of a propagating rift. *Journal of Geophysical Research: Solid Earth*, *88*(B3), 2297–2315.

Johnson, H. P., Hutnak, M., Dziak, R. P., Fox, C. G., Urcuyo, I., Cowen, J. P., et al. (2000). Earthquake-induced changes in a hydrothermal system on the Juan de Fuca mid-ocean ridge. *Nature*, *407*(6801), 174–177.

Johnson, R. H., Norris, R. A., & Duennebier, F. K. (1967). *Abyssally Generated T-phases*. Hawaii Institute of Geophysics, University of Hawaii. Retrieved from https://apps.dtic.mil/sti/citations/AD0649315

Johnston, M. J. S., & Linde, A. T. (2002). Implications of Crustal Strain During Conventional, Slow, and Silent Earthquakes. In W. H. K. Lee, H. Kanamori, P. C. Jennings, & C. Kisslinger (Eds.), *International Geophysics* (Vol. 81, pp. 589–605). Academic Press. https://doi.org/10.1016/S0074-6142(02)80239-X

Jurkevics, A. (1988). Polarization analysis of three-component array data. *Bulletin of the Seismological Society of America*, *78*(5), 1725–1743.

Kagan, Y. Y., & Jackson, D. D. (1991). Long-term earthquake clustering. *Geophysical Journal International*, *104*(1), 117–133. https://doi.org/10.1111/j.1365-246X.1991.tb02498.x

Kaneko, Y., & Shearer, P. M. (2015). Variability of seismic source spectra, estimated stress drop, and radiated energy, derived from cohesive-zone models of symmetrical and asymmetrical circular and elliptical ruptures. *Journal of Geophysical Research: Solid Earth*, *120*(2), 1053–1079. https://doi.org/10.1002/2014JB011642

Kappel, E. S., & Ryan, W. B. (1986). Volcanic episodicity and a non-steady state rift valley along northeast Pacific spreading centers: Evidence from Sea MARC I. *Journal of Geophysical Research: Solid Earth*, *91*(B14), 13925–13940.

Karson, J. A., Thompson, G., Humphris, S. E., Edmond, J. M., Bryan, W. B., Brown, J. R., et al. (1987). Along-axis variations in seafloor spreading in the MARK area. *Nature*, *328*(6132), 681–685. https://doi.org/10.1038/328681a0

Karsten, J. L. (1988). *Spatial and temporal variations in the petrology, morphology and tectonics of a migrating spreading center: The Endeavour Segment, Juan de Fuca Ridge* (Ph.D.). University of Washington, United States -- Washington. Retrieved from https://www.proquest.com/docview/303737974/abstract/1520765338C84CC8PQ/1

Karsten, J. L., Hammond, S. R., Davis, E. E., & Currie, R. G. (1986). Detailed geomorphology and neotectonics of the Endeavour Segment, Juan de Fuca Ridge: New results from Seabeam swath mapping. *Geological Society of America Bulletin*, *97*(2), 213–221.

Karsten, J. L., Delaney, J. R., Rhodes, J. M., & Liias, R. A. (1990). Spatial and temporal evolution of magmatic systems beneath the endeavour segment, Juan de Fuca Ridge: Tectonic and petrologic constraints. *Journal of Geophysical Research*, *95*(B12), 19235. https://doi.org/10.1029/JB095iB12p19235

Kato, A., Obara, K., Igarashi, T., Tsuruoka, H., Nakagawa, S., & Hirata, N. (2012). Propagation of Slow Slip Leading Up to the 2011 Mw 9.0 Tohoku-Oki Earthquake. *Science*, *335*(6069), 705–708. https://doi.org/10.1126/science.1215141

Kelley, D. S. (2015). Processed Bathymetry Grids (NetCDF:GMT format) derived from ship-based Multibeam Sonar Data from the Juan de Fuca Spreading Center Endeavour Segment acquired during the Thomas G. Thompson expedition TN146 (2002). IEDA. Retrieved from doi:10.1594/IEDA/314300

Kelley, D. S., Carbotte, S. M., Caress, D. W., Clague, D. A., Delaney, J. R., Gill, J. B., et al. (2012). Endeavour Segment of the Juan de Fuca Ridge: One of the most remarkable places on Earth. *Oceanography*, *25*(1), 44–61.

Kelley, D. S., Delaney, J. R., & Juniper, S. K. (2014). Establishing a new era of submarine volcanic observatories: Cabling Axial Seamount and the Endeavour Segment of the Juan

de Fuca Ridge. *Marine Geology*, *352*, 426–450. https://doi.org/10.1016/j.margeo.2014.03.010

Kelley, D. S., Delaney, J. R., & Team, C. A. (2016). NSF's Cabled Array: A wired tectonic plate and overlying ocean. In *OCEANS 2016 MTS/IEEE Monterey* (pp. 1–10). https://doi.org/10.1109/OCEANS.2016.7761398

Kellogg, J. P. (2011). *Temporal and spatial variability of hydrothermal fluxes within a mid-ocean ridge segment*. University of Washington.

Kilburn, C. (2012). Precursory deformation and fracture before brittle rock failure and potential application to volcanic unrest: precursors to brittle rock failure. *Journal of Geophysical Research: Solid Earth*, *117*(B2), n/a-n/a. https://doi.org/10.1029/2011JB008703

Kim, E., Toomey, D. R., Hooft, E. E., Wilcock, W. S., Weekly, R. T., Lee, S.-M., & Kim, Y. H. (2019). Upper crustal Vp/Vs ratios at the Endeavour Segment, Juan de Fuca Ridge, from joint inversion of P and S traveltimes: implications for hydrothermal circulation. *Geochemistry, Geophysics, Geosystems*, *20*(1), 208–229.

Kim, S. G., & Gao, F. (1997). Study on Some Characteristics of Earthquakes and Explosions Using the Polarization Method. *Journal of Physics of the Earth*, *45*(1), 13–27. https://doi.org/10.4294/jpe1952.45.13

Kimura, G., Shiraishi, K., Nakamura, Y., Kodaira, S., Fujie, G., Arai, R., & Moore, G. F. (2024). Frontal Thrust Ramp-Up and Slow Earthquakes Due To Underthrusting of Basement High in the Nankai Trough. *Geochemistry, Geophysics, Geosystems*, *25*(7), e2024GC011468. https://doi.org/10.1029/2024GC011468

Kimura, H., Kasahara, K., Igarashi, T., & Hirata, N. (2006). Repeating earthquake activities associated with the Philippine Sea plate subduction in the Kanto district, central Japan: A

new plate configuration revealed by interplate aseismic slips. *Tectonophysics*, *417*(1–2), 101–118. https://doi.org/10.1016/j.tecto.2005.06.013

Klein, F. W. (2002). *User's guide to HYPOINVERSE-2000, a Fortran program to solve for earthquake locations and magnitudes*. US Geological Survey.

Koper, K. D., & Hawley, V. L. (2010). Frequency dependent polarization analysis of ambient seismic noise recorded at a broadband seismometer in the central United States. *Earthquake Science*, *23*(5), 439–447. https://doi.org/10.1007/s11589-010-0743-5

Krauss, Z., Wilcock, W. S. D., Heesemann, M., Schlesinger, A., Kukovica, J., & Farrugia, J. J. (2023). A Long-Term Earthquake Catalog for the Endeavour Segment: Constraints on the Extensional Cycle and Evidence for Hydrothermal Venting Supported by Propagating Rifts. *Journal of Geophysical Research: Solid Earth*, *123*, e2022JB025662. https://doi.org/10.1029/2022JB025662

Lalou, C., Brichet, E., & Hekinian, R. (1985). Age dating of sulfide deposits from axial and off-axial structures on the East Pacific Rise near 12° 50′ N. *Earth and Planetary Science Letters*, *75*(1), 59–71.

Latorre, D., Mirabella, F., Chiaraluce, L., Trippetta, F., & Lomax, A. (2016). Assessment of earthquake locations in 3-D deterministic velocity models: A case study from the Altotiberina Near Fault Observatory (Italy). *Journal of Geophysical Research: Solid Earth*, *121*(11), 8113–8135. https://doi.org/10.1002/2016JB013170

Lawrence, M. W. (2004). Acoustic Monitoring of the Global Ocean for the CTBT.

Le Saout, M., Clague, D. A., & Paduan, J. B. (2019). Evolution of Fine-Scale Segmentation at Intermediate-Spreading Rate Ridges. *Geochemistry, Geophysics, Geosystems*, *20*(8), 3841–3860. https://doi.org/10.1029/2019GC008218

Le Voyer, M., Hauri, E. H., Cottrell, E., Kelley, K. A., Salters, V. J. M., Langmuir, C. H., et al. (2019). Carbon Fluxes and Primary Magma CO $_2$ Contents Along the Global Mid-Ocean Ridge System. *Geochemistry, Geophysics, Geosystems*, *20*(3), 1387–1424. https://doi.org/10.1029/2018GC007630

Lee, H., Muirhead, J. D., Fischer, T. P., Ebinger, C. J., Kattenhorn, S. A., Sharp, Z. D., & Kianji, G. (2016). Massive and prolonged deep carbon emissions associated with continental rifting. *Nature Geoscience*, *9*(2), 145–149. https://doi.org/10.1038/ngeo2622

Li, S., Wang, K., Wang, Y., Jiang, Y., & Dosso, S. E. (2018). Geodetically inferred locking state of the Cascadia megathrust based on a viscoelastic Earth model. *Journal of Geophysical Research: Solid Earth*, *123*(9), 8056–8072.

Lilley, M. D., Butterfield, D. A., Lupton, J. E., & Olson, E. J. (2003). Magmatic events can produce rapid changes in hydrothermal vent chemistry. *Nature*, *422*(6934), 878–881. https://doi.org/10.1038/nature01569

Lister, C. R. B. (1974). On the penetration of water into hot rock. *Geophysical Journal International*, *39*(3), 465–509.

Liu, L., & Lowell, R. P. (2009). Models of hydrothermal heat output from a convecting, crystallizing, replenished magma chamber beneath an oceanic spreading center. *Journal of Geophysical Research*, *114*(B2), B02102. https://doi.org/10.1029/2008JB005846

Liu, Y., Tao, C., Liu, C., Qiu, L., Schlindwein, V., Zhang, H., et al. (2019). Seismic activity recorded by a single OBS/H near the active Longqi hydrothermal vent at the ultraslow spreading Southwest Indian Ridge (49°39′ E). *Marine Georesources & Geotechnology*, *37*(2), 201–211. https://doi.org/10.1080/1064119X.2017.1420114

Liu, Z., & Buck, W. R. (2020). Global Trends of Axial Relief and Faulting at Plate Spreading Centers Imply Discrete Magmatic Events. *Journal of Geophysical Research: Solid Earth*, *125*(8). https://doi.org/10.1029/2020JB019465

Lomax, A., Virieux, J., Volant, P., & Berge-Thierry, C. (2000). Probabilistic earthquake location in 3D and layered models. In *Advances in seismic event location* (pp. 101–134). Springer.

Lomax, A., Michelini, A., Curtis, A., & Meyers, R. A. (2009). Earthquake location, direct, global-search methods. *Encyclopedia of Complexity and Systems Science*, *5*, 2449–2473.

Love, B., Lilley, M., Butterfield, D., Olson, E., & Larson, B. (2017). Rapid variations in fluid chemistry constrain hydrothermal phase separation at the Main Endeavour Field. *Geochemistry, Geophysics, Geosystems*, *18*(2), 531–543.

Lowell, R. P., & Germanovich, L. N. (1994). On the temporal evolution of high-temperature hydrothermal systems at ocean ridge crests. *Journal of Geophysical Research: Solid Earth*, *99*(B1), 565–575. https://doi.org/10.1029/93JB02568

Magotra, N., Ahmed, N., & Chael, E. (1989). Single-station seismic event detection and location. *IEEE Transactions on Geoscience and Remote Sensing*, *27*(1), 15–23. https://doi.org/10.1109/36.20270

Massel, S. R. (1996). *Ocean Surface Waves: Their Physics and Prediction*. World Scientific.

Massin, F., Farrell, J., & Smith, R. B. (2013). Repeating earthquakes in the Yellowstone volcanic field: Implications for rupture dynamics, ground deformation, and migration in earthquake swarms. *Journal of Volcanology and Geothermal Research*, *257*, 159–173. https://doi.org/10.1016/j.jvolgeores.2013.03.022

Materna, K., Taira, T., & Bürgmann, R. (2018). Aseismic Transform Fault Slip at the Mendocino Triple Junction From Characteristically Repeating Earthquakes. *Geophysical Research Letters*, *45*(2), 699–707. https://doi.org/10.1002/2017GL075899

McCreery, C. S., Duennebier, F. K., & Sutton, G. H. (1993). Correlation of deep ocean noise (0.4–30 Hz) with wind, and the Holu Spectrum—A worldwide constant. *The Journal of the Acoustical Society of America*, *93*(5), 2639–2648. https://doi.org/10.1121/1.405838

Meng, L., Huang, H., Bürgmann, R., Ampuero, J. P., & Strader, A. (2015). Dual megathrust slip behaviors of the 2014 Iquique earthquake sequence. *Earth and Planetary Science Letters*, *411*, 177–187. https://doi.org/10.1016/j.epsl.2014.11.041

Menke, W., Lerner-Lam, A., Dubendorff, B., & Pacheco, J. (1990). Polarization and coherence of 5 to 30 Hz seismic wave fields at a hard-rock site and their relevance to velocity heterogeneities in the crust. *Bulletin - Seismological Society of America*, *80*. https://doi.org/10.1785/BSSA0800020430

Merle, S. G., Embley, R. W., Johnson, H. P., Lau, T.-K., Phrampus, B. J., Raineault, N. A., & Gee, L. J. (2021). Distribution of Methane Plumes on Cascadia Margin and Implications for the Landward Limit of Methane Hydrate Stability. *Frontiers in Earth Science*, *9*. https://doi.org/10.3389/feart.2021.531714

Mesimeri, M., & Karakostas, V. (2018). Repeating earthquakes in western Corinth Gulf (Greece): implications for aseismic slip near locked faults. *Geophysical Journal International*, *215*(1), 659–676. https://doi.org/10.1093/gji/ggy301

Métois, M., Socquet, A., & Vigny, C. (2012). Interseismic coupling, segmentation and mechanical behavior of the central Chile subduction zone. *Journal of Geophysical Research: Solid Earth*, *117*(B3). https://doi.org/10.1029/2011JB008736

Michael, P. J., & Graham, D. W. (2015). The behavior and concentration of CO2 in the suboceanic mantle: Inferences from undegassed ocean ridge and ocean island basalts. *Lithos*, *236–237*, 338–351. https://doi.org/10.1016/j.lithos.2015.08.020

Miller, S. A., Collettini, C., Chiaraluce, L., Cocco, M., Barchi, M., & Kaus, B. J. P. (2004). Aftershocks driven by a high-pressure CO2 source at depth. *Nature*, *427*(6976), 724–727. https://doi.org/10.1038/nature02251

Mochizuki, K., Yamada, T., Shinohara, M., Yamanaka, Y., & Kanazawa, T. (2008). Weak Interplate Coupling by Seamounts and Repeating *M* ~ 7 Earthquakes. *Science*, *321*(5893), 1194–1197. https://doi.org/10.1126/science.1160250

Monna, S., Falcone, G., Beranzoli, L., Chierici, F., Cianchini, G., De Caro, M., et al. (2014). Underwater geophysical monitoring for European Multidisciplinary Seafloor and water column Observatories. *Journal of Marine Systems*, *130*, 12–30. https://doi.org/10.1016/j.jmarsys.2013.09.010

Moore, J. C., Moore, G. F., Cochrane, G. R., & Tobin, H. J. (1995). Negative-polarity seismic reflections along faults of the Oregon accretionary prism: Indicators of overpressuring. *Journal of Geophysical Research: Solid Earth*, *100*(B7), 12895–12906. https://doi.org/10.1029/94JB02049

Morton, E. A., Bilek, S. L., & Rowe, C. A. (2018). Newly detected earthquakes in the Cascadia subduction zone linked to seamount subduction and deformed upper plate. *Geology*, *46*(11), 943–946.

Morton, E. A., Bilek, S. L., & Rowe, C. A. (2023). Cascadia Subduction Zone Fault Heterogeneities From Newly Detected Small Magnitude Earthquakes. *Journal of Geophysical Research: Solid Earth*, *128*(6), e2023JB026607. https://doi.org/10.1029/2023JB026607

Moser, T. J. (1991). Shortest path calculation of seismic rays. *Geophysics*, *56*(1), 59–67.

Nadeau, R., & McEvilly, T. V. (1999). Fault slip rates at depth from recurrence intervals of repeating microearthquakes. *Science*, *285*.

Nadeau, R., Antolik, M., Johnson, P. A., Foxall, W., & McEvilly, T. V. (1994). Seismological studies at Parkfield III: Microearthquake clusters in the study of fault-zone dynamics. *Bulletin of the Seismological Society of America*, *84*(2), 247–263.

Nadeau, R., Foxall, W., & McEvilly, T. (1995). Clustering and Periodic Recurrence of Microearthquakes on the San Andreas Fault at Parkfield, California. *Science (New York, N.Y.)*, *267*, 503–7. https://doi.org/10.1126/science.267.5197.503

Nadeau, R. M., & Johnson, L. R. (1998). Seismological studies at Parkfield VI: Moment release rates and estimates of source parameters for small repeating earthquakes. *Bulletin of the Seismological Society of America*, *88*(3), 790–814. https://doi.org/10.1785/BSSA0880030790

Nadeau, R. M., & McEvilly, T. V. (2004). Periodic Pulsing of Characteristic Microearthquakes on the San Andreas Fault. *Science*, *303*(5655), 220–222. https://doi.org/10.1126/science.1090353

Nakano, M., Hori, T., Araki, E., Kodaira, S., & Ide, S. (2018). Shallow very-low-frequency earthquakes accompany slow slip events in the Nankai subduction zone. *Nature Communications*, *9*(1), 984. https://doi.org/10.1038/s41467-018-03431-5

Nedimović, M. R., Carbotte, S. M., Harding, A. J., Detrick, R. S., Canales, J. P., Diebold, J. B., et al. (2005). Frozen magma lenses below the oceanic crust. *Nature*, *436*(7054), 1149–1152. https://doi.org/10.1038/nature03944

Nooner, S. L., & Chadwick Jr, W. W. (2016). Inflation-predictable behavior and co-eruption deformation at Axial Seamount. *Science*, *354*(6318), 1399–1403.

Obana, K., & Kodaira, S. (2009). Low-frequency tremors associated with reverse faults in a shallow accretionary prism. *Earth and Planetary Science Letters*, *287*(1), 168–174. https://doi.org/10.1016/j.epsl.2009.08.005

Obara, K. (2002). Nonvolcanic deep tremor associated with subduction in southwest Japan. *Science*, *296*(5573), 1679–1681. https://doi.org/10.1126/science.1070378

Ogiso, M., & Tamaribuchi, K. (2022). Spatiotemporal evolution of tremor activity near the Nankai Trough trench axis inferred from the spatial distribution of seismic amplitudes. *Earth, Planets and Space*, *74*(1), 49. https://doi.org/10.1186/s40623-022-01601-w

Okal, E. A. (2008). The generation of *T* waves by earthquakes. In R. Dmowska (Ed.), *Advances in Geophysics* (Vol. 49, pp. 1–65). Elsevier. https://doi.org/10.1016/S0065-2687(07)49001-X

Olive, J.-A., & Crone, T. J. (2018). Smoke Without Fire: How Long Can Thermal Cracking Sustain Hydrothermal Circulation in the Absence of Magmatic Heat? *Journal of Geophysical Research: Solid Earth*, *123*(6), 4561–4581. https://doi.org/10.1029/2017JB014900

Olive, J.-A., & Escartín, J. (2016). Dependence of seismic coupling on normal fault style along the Northern Mid-Atlantic Ridge. *Geochemistry, Geophysics, Geosystems*, *17*(10), 4128–4152. https://doi.org/10.1002/2016GC006460

Park, J., Vernon, F. L., & Lindberg, C. R. (1987). Frequency dependent polarization analysis of high-frequency seismograms. *Journal of Geophysical Research*, *92*(B12), 12664. https://doi.org/10.1029/JB092iB12p12664

Parnell-Turner, R., Sohn, R. A., Peirce, C., Reston, T. J., MacLeod, C. J., Searle, R. C., & Simão, N. M. (2017). Oceanic detachment faults generate compression in extension. *Geology*, *45*(10), 923–926. https://doi.org/10.1130/G39232.1

Parnell-Turner, R., Sohn, R. A., Peirce, C., Reston, T. J., MacLeod, C. J., Searle, R. C., & Simão, N. M. (2020). Seismicity trends and detachment fault structure at 13°N, Mid-Atlantic Ridge. *Geology*, *49*(3), 320–324. https://doi.org/10.1130/G48420.1

Peng, Z., & Gomberg, J. (2010). An integrated perspective of the continuum between earthquakes and slow-slip phenomena. *Nature Geoscience*, *3*(9), 599–607. https://doi.org/10.1038/ngeo940

Pischiutta, M., Salvini, F., Fletcher, J., Rovelli, A., & Ben-Zion, Y. (2012). Horizontal polarization of ground motion in the Hayward fault zone at Fremont, California: dominant fault-high-angle polarization and fault-induced cracks. *Geophysical Journal International*, *188*(3), 1255–1272. https://doi.org/10.1111/j.1365-246X.2011.05319.x

Plata-Martinez, R., Ide, S., Shinohara, M., Garcia, E. S., Mizuno, N., Dominguez, L. A., et al. (2021). Shallow slow earthquakes to decipher future catastrophic earthquakes in the Guerrero seismic gap. *Nature Communications*, *12*(1), 3976. https://doi.org/10.1038/s41467-021-24210-9

Podvin, P., & Lecomte, I. (1991). Finite difference computation of traveltimes in very contrasted velocity models: a massively parallel approach and its associated tools. *Geophysical Journal International*, *105*(1), 271–284. https://doi.org/10.1111/j.1365-246X.1991.tb03461.x

Pollard, D. D., & Aydin, A. (1984). Propagation and linkage of oceanic ridge segments. *Journal of Geophysical Research: Solid Earth*, *89*(B12), 10017–10028. https://doi.org/10.1029/JB089iB12p10017

Proskurowski, G., Lilley, M. D., & Brown, T. A. (2004). Isotopic evidence of magmatism and seawater bicarbonate removal at the Endeavour hydrothermal system. *Earth and Planetary Science Letters*, *225*(1–2), 53–61.

Qin, R., & Buck, W. R. (2008). Why meter-wide dikes at oceanic spreading centers? *Earth and Planetary Science Letters*, *265*(3–4), 466–474.

Radiguet, M., Cotton, F., Vergnolle, M., Campillo, M., Walpersdorf, A., Cotte, N., & Kostoglodov, V. (2012). Slow slip events and strain accumulation in the Guerrero gap, Mexico. *Journal of Geophysical Research: Solid Earth*, *117*(B4). https://doi.org/10.1029/2011JB008801

Ragland, J., Schwock, F., Munson, M., & Abadi, S. (2022). An overview of ambient sound using Ocean Observatories Initiative hydrophones. *The Journal of the Acoustical Society of America*, *151*(3), 2085–2100. https://doi.org/10.1121/10.0009836

Ramos, M. D., Huang, Y., Ulrich, T., Li, D., Gabriel, A.-A., & Thomas, A. M. (2021). Assessing Margin-Wide Rupture Behaviors Along the Cascadia Megathrust With 3-D Dynamic Rupture Simulations. *Journal of Geophysical Research: Solid Earth*, *126*(7), e2021JB022005. https://doi.org/10.1029/2021JB022005

Remitti, F., Festa, A., Nirta, G., Barbero, E., & Mittempergher, S. (2024). Role of folding-related deformation in the seismicity of shallow accretionary prisms. *Nature Geoscience*, *17*(7), 600–607. https://doi.org/10.1038/s41561-024-01474-6

Rigano, R., Cara, F., Lombardo, G., & Rovelli, A. (2008). Evidence for ground motion polarization on fault zones of Mount Etna volcano. *Journal of Geophysical Research: Solid Earth*, *113*(B10). https://doi.org/10.1029/2007JB005574

Roberts, R. G., Christoffersson, A., & Cassidy, F. (1989). Real-Time Event Detection, Phase Identification and Source Location Estimation Using Single Station Three-Component Seismic Data. *Geophysical Journal International*, *97*(3), 471–480. https://doi.org/10.1111/j.1365-246X.1989.tb00517.x

Roland, E., & McGuire, J. J. (2009). Earthquake swarms on transform faults. *Geophysical Journal International*, *178*(3), 1677–1690. https://doi.org/10.1111/j.1365-246X.2009.04214.x

Romanowicz, B., Stakes, D., Dolenc, D., Neuhauser, D., McGill, P., Uhrhammer, R., & Ramirez, T. (2006). The Monterey Bay broadband ocean bottom seismic observatory. *Annals of Geophysics*, *49*(2–3).

Ross, D., & Kuperman, W. A. (1989). Mechanics of Underwater Noise. *The Journal of the Acoustical Society of America*, *86*(4), 1626. https://doi.org/10.1121/1.398685

Rubin, A. M., Gillard, D., & Got, J.-L. (1999). Streaks of microearthquakes along creeping faults. *Nature*, *400*(6745), 635–641. https://doi.org/10.1038/23196

Rubinstein, J. L., Vidale, J. E., Gomberg, J., Bodin, P., Creager, K. C., & Malone, S. D. (2007). Non-volcanic tremor driven by large transient shear stresses. *Nature*, *448*(7153), 579–582. https://doi.org/10.1038/nature06017

Rubinstein, J. L., Shelly, D. R., & Ellsworth, W. L. (2010). Non-volcanic tremor: A window into the roots of fault zones. *New Frontiers in Integrated Solid Earth Sciences*, 287–314.

Rudebusch, J. A., Prouty, N. G., Conrad, J. E., Watt, J. T., Kluesner, J. W., Hill, J. C., et al. (2023). Diving deeper into seep distribution along the Cascadia convergent margin, United States. *Frontiers in Earth Science*, *11*. https://doi.org/10.3389/feart.2023.1205211

Ruud, B. O., Husebye, E. S., Ingate, S. F., & Christoffersson, A. (1988). Event location at any distance using seismic data from a single, three-component station. *Bulletin of the Seismological Society of America*, *78*(1), 308–325. https://doi.org/10.1785/BSSA0780010308

Saez, M., Ruiz, S., Ide, S., & Sugioka, H. (2019). Shallow non-volcanic tremor activity and potential repeating earthquakes in the Chile triple joint: Seismic evidence of the subduction of the active Nazca-Antartic spreading Center. *Seismological Research Letters*. https://doi.org/10.1785/0220180394

Satake, K., & Atwater, B. (2007). Long-Term Perspectives on Giant Earthquakes and Tsunamis at Subduction Zones*. *Annual Review of Earth and Planetary Sciences*, *35*, 349–374. https://doi.org/10.1146/annurev.earth.35.031306.140302

Schaff, D. P., Beroza, G. C., & Shaw, B. E. (1998). Postseismic response of repeating aftershocks. *Geophysical Research Letters*, *25*(24), 4549–4552. https://doi.org/10.1029/1998GL900192

Schlindwein, V., & Schmid, F. (2016). Mid-ocean-ridge seismicity reveals extreme types of ocean lithosphere. *Nature*, *535*(7611), 276–279. https://doi.org/10.1038/nature18277

Schmalzle, G. M., McCaffrey, R., & Creager, K. C. (2014). Central Cascadia subduction zone creep. *Geochemistry, Geophysics, Geosystems*, *15*(4), 1515–1532.

Schmid, F., & Schlindwein, V. (2016). Microearthquake activity, lithospheric structure, and deformation modes at an amagmatic ultraslow spreading Southwest Indian Ridge segment. *Geochemistry, Geophysics, Geosystems*, *17*(7), 2905–2921. https://doi.org/10.1002/2016GC006271

Scholz, C. H., Dawers, N. H., Yu, J.-Z., Anders, M. H., & Cowie, P. A. (1993). Fault growth and fault scaling laws: Preliminary results. *Journal of Geophysical Research: Solid Earth*, *98*(B12), 21951–21961.

Seewald, J., Cruse, A., & Saccocia, P. (2003). Aqueous volatiles in hydrothermal fluids from the Main Endeavour Field, northern Juan de Fuca Ridge: temporal variability following earthquake activity. *Earth and Planetary Science Letters*, *216*(4), 575–590.

Seydoux, L., Balestriero, R., Poli, P., Hoop, M. de, Campillo, M., & Baraniuk, R. (2020). Clustering earthquake signals and background noises in continuous seismic data with unsupervised deep learning. *Nature Communications*, *11*(1), 3972. https://doi.org/10.1038/s41467-020-17841-x

Seyfried Jr, W. E., Seewald, J. S., Berndt, M. E., Ding, K., & Foustoukos, D. I. (2003a). Chemistry of hydrothermal vent fluids from the Main Endeavour Field, northern Juan de Fuca Ridge: Geochemical controls in the aftermath of June 1999 seismic events. *Journal of Geophysical Research: Solid Earth*, *108*(B9).

Seyfried Jr, W. E., Seewald, J. S., Berndt, M. E., Ding, K., & Foustoukos, D. I. (2003b). Chemistry of hydrothermal vent fluids from the Main Endeavour Field, northern Juan de Fuca Ridge: Geochemical controls in the aftermath of June 1999 seismic events. *Journal of Geophysical Research: Solid Earth*, *108*(B9).

Sgroi, T., Beranzoli, L., Di Grazia, G., Ursino, A., & Favali, P. (2007). New observations of local seismicity by the SN-1 seafloor observatory in the Ionian Sea, off-shore Eastern Sicily (Italy). *Geophysical Journal International*, *169*(2), 490–501. https://doi.org/10.1111/j.1365-246X.2007.03348.x

Sgroi, T., Barberi, G., & Marchetti, A. (2021). The contribution of the NEMO-SN1 seafloor observatory to improve the seismic locations in the Ionian Sea (Italy). *Annals of Geophysics*, *64*(6), SE655. https://doi.org/10.4401/ag-8575

Shaddox, H. R., & Schwartz, S. Y. (2019). Subducted seamount diverts shallow slow slip to the forearc of the northern Hikurangi subduction zone, New Zealand. *Geology*, *47*(5), 415–418. https://doi.org/10.1130/G45810.1

Shapiro, S. A. (2015). *Fluid-Induced Seismicity*. Cambridge University Press.

Shapiro, S. A., & Dinske, C. (2009). Fluid-induced seismicity: Pressure diffusion and hydraulic fracturing. *Geophysical Prospecting*, *57*(2), 301–310. https://doi.org/10.1111/j.1365-2478.2008.00770.x

Shapiro, S. A., Huenges, E., & Borm, G. (1997). Estimating the crust permeability from fluid-injection-induced seismic emission at the KTB site. *Geophysical Journal International*, *131*(2), F15–F18. https://doi.org/10.1111/j.1365-246X.1997.tb01215.x

Shearer, P., Hauksson, E., & Lin, G. (2005). Southern California Hypocenter Relocation with Waveform Cross-Correlation, Part 2: Results Using Source-Specific Station Terms and Cluster Analysis. *Bulletin of the Seismological Society of America*, *95*(3), 904–915. https://doi.org/10.1785/0120040168

Shen, Z., & Wu, W. (2023). *Ocean bottom distributed acoustic sensing for T-wave detection and seismic ocean thermometry* (preprint). Preprints. https://doi.org/10.22541/essoar.169186309.95288597/v1

Shi, Y., & Bolt, B. A. (1982). The standard error of the magnitude-frequency b value. *Bulletin of the Seismological Society of America*, *72*(5), 1677–1687.

Shillington, D. J., Bécel, A., Nedimović, M. R., Kuehn, H., Webb, S. C., Abers, G. A., et al. (2015). Link between plate fabric, hydration and subduction zone seismicity in Alaska. *Nature Geoscience*, *8*(12), 961–964. https://doi.org/10.1038/ngeo2586

Shoberg, T., Stein, S., & Karsten, J. (1991). Constraints on rift propagation history at the Cobb Offset, Juan de Fuca Ridge, from numerical modeling of tectonic fabric. *Tectonophysics*, *197*(2–4), 295–308.

Sit, S., Brudzinski, M., & Kao, H. (2012). Detecting tectonic tremor through frequency scanning at a single station: Application to the Cascadia margin. *Earth and Planetary Science Letters*, *353*, 134–144.

Smith, D. K., Tolstoy, M., Fox, C. G., Bohnenstiehl, D. R., Matsumoto, H., & J. Fowler, M. (2002). Hydroacoustic monitoring of seismicity at the slow-spreading Mid-Atlantic

Ridge. *Geophysical Research Letters*, *29*(11), 13-1-13–4. https://doi.org/10.1029/2001GL013912

Smith, L., Barth, J., Kelley, D., Plueddemann, A., Rodero, I., Ulses, G., et al. (2018). The Ocean Observatories Initiative. *Oceanography*, *31*(1), 16–35. https://doi.org/10.5670/oceanog.2018.105

Sohn, R. A., Hildebrand, J. A., & Webb, S. C. (1998a). Postrifting seismicity and a model for the 1993 diking event on the CoAxial segment, Juan de Fuca Ridge. *Journal of Geophysical Research: Solid Earth*, *103*(B5), 9867–9877.

Sohn, R. A., Fornari, D. J., Von Damm, K. L., Hildebrand, J. A., & Webb, S. C. (1998b). Seismic and hydrothermal evidence for a cracking event on the East Pacific Rise crest at 9 50′ N. *Nature*, *396*(6707), 159–161.

Sohn, R. A., Barclay, A. H., & Webb, S. C. (2004). Microearthquake patterns following the 1998 eruption of Axial Volcano, Juan de Fuca Ridge: Mechanical relaxation and thermal strain: AXIAL VOLCANO MICROEARTHQUAKES. *Journal of Geophysical Research: Solid Earth*, *109*(B1). https://doi.org/10.1029/2003JB002499

Soule, D., Wilcock, W. S., Toomey, D. R., Hooft, E. E., & Weekly, R. T. (2016). Near-axis crustal structure and thickness of the Endeavour Segment, Juan de Fuca Ridge. *Geophysical Research Letters*, *43*(11), 5688–5695.

Stakes, D., McClain, J., VanZandt, T., McGill, P., & Begnaud, M. (1998). Corehole seismometer development for low-noise seismic data in a long-term seafloor observatory. *Geophysical Research Letters*, *25*(14), 2745–2748.

Stakes, D., Romanowicz, B., Begnaud, M. L., McNally, K. C., Montagner, J. P., Stutzmann, E., et al. (2002). The MBARI margin seismology experiment: A prototype seafloor

observatory. *Science-Technology Synergy for Research in the Marine Environment: Challenges for the XXI Century*, 93–110.

Stone, I., Vidale, J. E., Han, S., & Roland, E. (2018). Catalog of offshore seismicity in Cascadia: Insights into the regional distribution of microseismicity and its relation to subduction processes. *Journal of Geophysical Research: Solid Earth*, *123*(1), 641–652.

Sun, C. T., & Jin, Z. H. (2012). The Elastic Stress Field Around a Crack Tip. In *Fracture Mechanics* (pp. 25–73). Elsevier.

Takemura, S., Hamada, Y., Okuda, H., Okada, Y., Okubo, K., Akuhara, T., et al. (2023). A review of shallow slow earthquakes along the Nankai Trough. *Earth, Planets and Space*, *75*(1), 164. https://doi.org/10.1186/s40623-023-01920-6

Talandier, J., & Okal, E. A. (2001). Identification Criteria for Sources of T Waves Recorded in French Polynesia. *Pure and Applied Geophysics*, *158*(3), 567–603. https://doi.org/10.1007/PL00001195

Talwani, P., Chen, L., & Gahalaut, K. (2007). Seismogenic permeability, ks. *Journal of Geophysical Research: Solid Earth*, *112*(B7). https://doi.org/10.1029/2006JB004665

Tamaribuchi, K., Ogiso, M., & Noda, A. (2022). Spatiotemporal Distribution of Shallow Tremors Along the Nankai Trough, Southwest Japan, as Determined From Waveform Amplitudes and Cross-Correlations. *Journal of Geophysical Research: Solid Earth*, *127*(8), e2022JB024403. https://doi.org/10.1029/2022JB024403

Tamburello, G., Pondrelli, S., Chiodini, G., & Rouwet, D. (2018). Global-scale control of extensional tectonics on CO2 earth degassing. *Nature Communications*, *9*(1), 4608. https://doi.org/10.1038/s41467-018-07087-z

Tan, Y. J., Tolstoy, M., Waldhauser, F., & Wilcock, W. (2016). Dynamics of a seafloor-spreading episode at the East Pacific Rise. *Nature*, *540*. https://doi.org/10.1038/nature20116

Tarantola, A., & Valette, B. (1982). Generalized nonlinear inverse problems solved using the least squares criterion. *Reviews of Geophysics*, *20*(2), 219–232.

Tary, J. B. (2024). Atypical Signals. In *Noisy Oceans* (pp. 119–141). American Geophysical Union (AGU). https://doi.org/10.1002/9781119750925.ch8

Tary, J. B., Géli, L., Guennou, C., Henry, P., Sultan, N., Çağatay, N., & Vidal, V. (2012). Microevents produced by gas migration and expulsion at the seabed: a study based on sea bottom recordings from the Sea of Marmara: Microevents produced by gas migration. *Geophysical Journal International*, *190*(2), 993–1007. https://doi.org/10.1111/j.1365-246X.2012.05533.x

Templeton, D. C., Nadeau, R. M., & Burgmann, R. (2008). Behavior of Repeating Earthquake Sequences in Central California and the Implications for Subsurface Fault Creep. *Bulletin of the Seismological Society of America*, *98*(1), 52–65. https://doi.org/10.1785/0120070026

Thelen, W., Malone, S., & West, M. (2011). Multiplets: Their behavior and utility at dacitic and andesitic volcanic centers. *Journal of Geophysical Research: Solid Earth*, *116*(B8). https://doi.org/10.1029/2010JB007924

Thyng, K. M., Greene, C. A., Hetland, R. D., Zimmerle, H. M., & DiMarco, S. F. (2016). True colors of oceanography: Guidelines for effective and accurate colormap selection. *Oceanography*, *29*(3), 9–13.

Todd, E. K., Schwartz, S. Y., Mochizuki, K., Wallace, L. M., Sheehan, A. F., Webb, S. C., et al. (2018). Earthquakes and tremor linked to seamount subduction during shallow slow slip

at the Hikurangi margin, New Zealand. *Journal of Geophysical Research: Solid Earth*, *123*(8), 6769–6783.

Tolstoy, M., Bohnenstiehl, D. R., & Edwards, M. H. (2001). Seismic character of volcanic activity at the ultraslow-spreading Gakkel Ridge, 4.

Tolstoy, M., Cowen, J. P., Baker, E. T., Fornari, D. J., Rubin, K. H., Shank, T. M., et al. (2006). A sea-floor spreading event captured by seismometers. *Science*, *314*(5807), 1920–1922.

Tolstoy, M., Waldhauser, F., Bohnenstiehl, D. R., Weekly, R. T., & Kim, W.-Y. (2008). Seismic identification of along-axis hydrothermal flow on the East Pacific Rise. *Nature*, *451*(7175), 181–184. https://doi.org/10.1038/nature06424

Toomey, D. R., Solomon, S. C., Purdy, G. M., & Murray, M. H. (1985). Microearthquakes beneath the Median Valley of the Mid-Atlantic Ridge near 23°N: Hypocenters and focal mechanisms. *Journal of Geophysical Research: Solid Earth*, *90*(B7), 5443–5458. https://doi.org/10.1029/JB090iB07p05443

Toomey, D. R., Solomon, S. C., & Purdy, G. M. (1988). Microearthquakes beneath median valley of Mid-Atlantic Ridge near 23° N: Tomography and tectonics. *Journal of Geophysical Research: Solid Earth*, *93*(B8), 9093–9112.

Toomey, D. R., Solomon, S. C., & Purdy, G. M. (1994). Tomographic imaging of the shallow crustal structure of the East Pacific Rise at 9° 30′ N. *Journal of Geophysical Research: Solid Earth*, *99*(B12), 24135–24157.

Toomey, D. R., Jousselin, D., Dunn, R. A., Wilcock, W. S. D., & Detrick, R. S. (2007). Skew of mantle upwelling beneath the East Pacific Rise governs segmentation. *Nature*, *446*(7134), 409–414. https://doi.org/10.1038/nature05679

Toomey, D. R., Allen, R. M., Barclay, A. H., Bell, S. W., Bromirski, P. D., Carlson, R. L., et al. (2014). The Cascadia Initiative: A sea change in seismological studies of subduction zones. *Oceanography*, *27*(2), 138–150.

Trehu, A. (1985). A note on the effect of bottom currents on an ocean bottom seismometer. *Bulletin of the Seismological Society of America*, *75*(4), 1195–1204. https://doi.org/10.1785/BSSA0750041195

Tréhu, A. M., & Solomon, S. C. (1983). Earthquakes in the Orozco transform zone: Seismicity, source mechanisms, and tectonics. *Journal of Geophysical Research: Solid Earth*, *88*(B10), 8203–8225.

Tréhu, A. M., Blakely, R. J., & Williams, M. C. (2012). Subducted seamounts and recent earthquakes beneath the central Cascadia forearc. *Geology*, *40*(2), 103–106.

Trehu, A. M., Braunmiller, J., & Davis, E. (2015). Seismicity of the Central Cascadia Continental Margin near 44.5 N: A Decadal View. *Seismological Research Letters*, *86*(3), 819–829. https://doi.org/10.1785/0220140207

Tréhu, A. M., Wilcock, W. S. D., Hilmo, R., Bodin, P., Connolly, J., Roland, E. C., & Braunmiller, J. (2018). The Role of the Ocean Observatories Initiative in Monitoring the Offshore Earthquake Activity of the Cascadia Subduction Zone. *Oceanography*, *31*(1), 104–113.

Tréhu, A. M., de Moor, A., Madrid, J. M., Sáez, M., Chadwell, C. D., Ortega-Culaciati, F., et al. (2019). Post-seismic response of the outer accretionary prism after the 2010 Maule earthquake, Chile. *Geosphere*, *16*(1), 13–32. https://doi.org/10.1130/GES02102.1

Trowbridge, J., Weller, R., Kelley, D., Dever, E., Plueddemann, A., Barth, J. A., & Kawka, O. (2019). The Ocean Observatories Initiative. *Frontiers in Marine Science*, *6*, 74. https://doi.org/10.3389/fmars.2019.00074

Trugman, D. T., & Shearer, P. M. (2017). GrowClust: A Hierarchical Clustering Algorithm for Relative Earthquake Relocation, with Application to the Spanish Springs and Sheldon, Nevada, Earthquake Sequences. *Seismological Research Letters*, *88*(2A), 379–391. https://doi.org/10.1785/0220160188

Trugman, D. T., Chamberlain, C. J., Savvaidis, A., & Lomax, A. (2022). GrowClust3D. jl: A Julia Package for the Relative Relocation of Earthquake Hypocenters Using 3D Velocity Models. *Seismological Research Letters*.

Tsang-Hin-Sun, E., Batsi, E., Klingelhoefer, F., & Géli, L. (2019). Spatial and temporal dynamics of gas-related processes in the Sea of Marmara monitored with ocean bottom seismometers. *Geophysical Journal International*, *216*(3), 1989–2003. https://doi.org/10.1093/gji/ggy535

Uchida, N. (2019). Detection of repeating earthquakes and their application in characterizing slow fault slip. *Progress in Earth and Planetary Science*, *6*(1), 40. https://doi.org/10.1186/s40645-019-0284-z

Uchida, N., & Bürgmann, R. (2019). Repeating earthquakes. *Annual Review of Earth and Planetary Sciences*, *47*(1), 305–332.

Uchida, N., Matsuzawa, T., Hasegawa, A., & Igarashi, T. (2003). Interplate quasi-static slip off Sanriku, NE Japan, estimated from repeating earthquakes. *Geophysical Research Letters*, *30*(15). https://doi.org/10.1029/2003GL017452

Uchida, N., Iinuma, T., Nadeau, R. M., Bürgmann, R., & Hino, R. (2016). Periodic slow slip triggers megathrust zone earthquakes in northeastern Japan. *Science*, *351*(6272), 488–492. https://doi.org/10.1126/science.aad3108

Van Ark, E. M., Detrick, R. S., Canales, J. P., Carbotte, S. M., Harding, A. J., Kent, G. M., et al. (2007). Seismic structure of the Endeavour Segment, Juan de Fuca Ridge: Correlations

with seismicity and hydrothermal activity. *Journal of Geophysical Research*, *112*(B2), B02401. https://doi.org/10.1029/2005JB004210

VanderBeek, B. P., Toomey, D. R., Hooft, E. E. E., & Wilcock, W. S. D. (2016). Segmentation of mid-ocean ridges attributed to oblique mantle divergence. *Nature Geoscience*, *9*(8), 636–642. https://doi.org/10.1038/ngeo2745

Vidale, J. E., Bonamassa, O., & Houston, H. (1991). Directional site resonances observed from the 1 October 1987 Whittier Narrows, California, earthquake and the 4 October aftershock. *Earthquake Spectra*, *7*(1), 107–125.

Vidale, J. E., ElIsworth, W. L., Cole, A., & Marone, C. (1994). Variations in rupture process with recurrence interval in a repeated small earthquake. *Nature*, *368*(6472), 624–626.

Wagstaff, R. A. (2005). An ambient noise model for the northeast Pacific Ocean basin. *IEEE Journal of Oceanic Engineering*, *30*(2), 286–294. https://doi.org/10.1109/JOE.2004.836993

Waldhauser, F., & Ellsworth, W. L. (2002). Fault structure and mechanics of the Hayward Fault, California, from double-difference earthquake locations. *Journal of Geophysical Research: Solid Earth*, *107*(B3), ESE 3-1-ESE 3-15. https://doi.org/10.1029/2000JB000084

Waldhauser, F., & Tolstoy, M. (2011). Seismogenic structure and processes associated with magma inflation and hydrothermal circulation beneath the East Pacific Rise at 9°50′N. *Geochemistry, Geophysics, Geosystems*, *12*(8). https://doi.org/10.1029/2011GC003568

Walker, D. A., McCreery, C. S., & Hiyoshi, Y. (1992). T-phase spectra, seismic moments, and tsunamigenesis. *Bulletin of the Seismological Society of America*, *82*(3), 1275–1305. https://doi.org/10.1785/BSSA0820031275

Wallace, L. M., Webb, S. C., Ito, Y., Mochizuki, K., Hino, R., Henrys, S., et al. (2016). Slow slip near the trench at the Hikurangi subduction zone, New Zealand. *Science*, *352*(6286), 701–704. https://doi.org/10.1126/science.aaf2349

Wallace, P., & Anderson Jr, A. T. (2000). Volatiles in Magmas. Encyclopedia of Volcanoes, Sigurdsson H. Academic Press.

Walter, J. I., Schwartz, S. Y., Protti, J. M., & Gonzalez, V. (2011). Persistent tremor within the northern Costa Rica seismogenic zone. *Geophysical Research Letters*, *38*(1). https://doi.org/10.1029/2010GL045586

Walter, J. I., Schwartz, S. Y., Protti, M., & Gonzalez, V. (2013). The synchronous occurrence of shallow tremor and very low frequency earthquakes offshore of the Nicoya Peninsula, Costa Rica: VLFEs during slow slip in Costa Rica. *Geophysical Research Letters*, *40*(8), 1517–1522. https://doi.org/10.1002/grl.50213

Webb, S. C. (1998). Broadband seismology and noise under the ocean. *Reviews of Geophysics*, *36*(1), 105–142. https://doi.org/10.1029/97RG02287

Wech, A. G. (2010). Interactive tremor monitoring. *Seismological Research Letters*, *81*(4), 664–669.

Wech, A. G. (2021). Cataloging Tectonic Tremor Energy Radiation in the Cascadia Subduction Zone. *Journal of Geophysical Research: Solid Earth*, *126*(10), e2021JB022523. https://doi.org/10.1029/2021JB022523

Wech, A. G., & Creager, K. C. (2008). Automated detection and location of Cascadia tremor. *Geophysical Research Letters*, *35*(20).

Wech, A. G., Sheehan, A. F., Boese, C. M., Townend, J., Stern, T. A., & Collins, J. A. (2013). Tectonic Tremor Recorded by Ocean Bottom Seismometers. *Seismological Research Letters*, *84*(5), 752–758. https://doi.org/10.1785/0220120184

Weekly, R. T., Wilcock, W. S. D., Hooft, E. E. E., Toomey, D. R., McGill, P. R., & Stakes, D. S. (2013). Termination of a 6 year ridge-spreading event observed using a seafloor seismic network on the Endeavour Segment, Juan de Fuca Ridge: Spreading Event On The Endeavour Segment. *Geochemistry, Geophysics, Geosystems*, *14*(5), 1375–1398. https://doi.org/10.1002/ggge.20105

Weekly, R. T., Wilcock, W. S., Toomey, D. R., Hooft, E. E., & Kim, E. (2014). Upper crustal seismic structure of the Endeavour segment, Juan de Fuca Ridge from traveltime tomography: Implications for oceanic crustal accretion. *Geochemistry, Geophysics, Geosystems*, *15*(4), 1296–1315.

Welch, P. (1967). The use of fast Fourier transform for the estimation of power spectra: A method based on time averaging over short, modified periodograms. *IEEE Transactions on Audio and Electroacoustics*, *15*(2), 70–73. https://doi.org/10.1109/TAU.1967.1161901

White, S. M., Haymon, R. M., Fornari, D. J., Perfit, M. R., & Macdonald, K. C. (2002). Correlation between volcanic and tectonic segmentation of fast-spreading ridges: Evidence from volcanic structures and lava flow morphology on the East Pacific Rise at 9–10 N. *Journal of Geophysical Research: Solid Earth*, *107*(B8), EPM-7.

Wiemer, S., & Wyss, M. (2002). Mapping spatial variability of the frequency-magnitude distribution of earthquakes. In *Advances in geophysics* (Vol. 45, pp. 259–V). Elsevier.

Wilcock, W. S., Archer, S. D., & Purdy, G. M. (2002). Microearthquakes on the Endeavour segment of the Juan de Fuca Ridge. *Journal of Geophysical Research: Solid Earth*, *107*(B12), EPM-4.

Wilcock, W. S., Hooft, E. E., Toomey, D. R., McGill, P. R., Barclay, A. H., Stakes, D. S., & Ramirez, T. M. (2009). The role of magma injection in localizing black-smoker activity. *Nature Geoscience*, *2*(7), 509–513.

Wilcock, W. S., Tolstoy, M., Waldhauser, F., Garcia, C., Tan, Y. J., Bohnenstiehl, D. R., et al. (2016). Seismic constraints on caldera dynamics from the 2015 Axial Seamount eruption. *Science*, *354*(6318), 1395–1399.

Wilcock, W. S., Harrington, M., Schmidt, D. A., Kelley, D., Tobin, H. J., Denolle, M., et al. (2024). Seafloor Cabled Observations off the US Coast of the Pacific Northwest: The Cascadia Offshore Subduction Zone Observatory (COSZO) and Beyond. In *AGU24*. AGU.

Wilcock, W. S. D., & Delaney, J. R. (1996). Mid-ocean ridge sulfide deposits: Evidence for heat extraction from magma chambers or cracking fronts? *Earth and Planetary Science Letters*, *145*(1–4), 49–64. https://doi.org/10.1016/S0012-821X(96)00195-1

Wilcock, W. S. D., & McNabb, A. (1996). Estimates of crustal permeability on the endeavour segment of the Juan de Fuca mid-ocean ridge. *Earth and Planetary Science Letters*, *138*(1–4), 83–91. https://doi.org/10.1016/0012-821X(95)00225-2

Wilcock, W. S. D., Solomon, S. C., Purdy, G. M., & Toomey, D. R. (1992). The Seismic Attenuation Structure of a Fast-Spreading Mid-Ocean Ridge. *Science*, *258*(5087), 1470–1474. https://doi.org/10.1126/science.258.5087.1470

Wilcock, W. S. D., Stafford, K. M., Andrew, R. K., & Odom, R. I. (2014). Sounds in the Ocean at 1–100 Hz. *Annual Review of Marine Science*, *6*(1), 117–140. https://doi.org/10.1146/annurev-marine-121211-172423

Williams, M. C., Tréhu, A. M., & Braunmiller, J. (2011). Seismicity at the Cascadia Plate Boundary beneath the Oregon Continental Shelf. *Bulletin of the Seismological Society of America*, *101*(3), 940–950. https://doi.org/10.1785/0120100198

Woods, K., Wallace, L. M., Williams, C. A., Hamling, I. J., Webb, S. C., Ito, Y., et al. (2024). Spatiotemporal Evolution of Slow Slip Events at the Offshore Hikurangi Subduction

Zone in 2019 Using GNSS, InSAR, and Seafloor Geodetic Data. *Journal of Geophysical Research: Solid Earth*, *129*(8), e2024JB029068. https://doi.org/10.1029/2024JB029068

Xu, Z., Schwartz, S. Y., & Lay, T. (1996). Seismic wave-field observations at a dense, small-aperture array located on a landslide in the Santa Cruz Mountains, California. *Bulletin of the Seismological Society of America*, *86*(3), 655–669. https://doi.org/10.1785/BSSA0860030655

Yamashita, T. (1999). Pore Creation due to Fault Slip in a Fluid-permeated Fault Zone and its Effect on Seismicity: Generation Mechanism of Earthquake Swarm. In M. Wyss, K. Shimazaki, & A. Ito (Eds.), *Seismicity Patterns, their Statistical Significance and Physical Meaning* (pp. 625–647). Basel: Birkhäuser. https://doi.org/10.1007/978-3-0348-8677-2_19

Yamashita, Y., Yakiwara, H., Asano, Y., Shimizu, H., Uchida, K., Hirano, S., et al. (2015). Migrating tremor off southern Kyushu as evidence for slow slip of a shallow subduction interface. *Science*, *348*(6235), 676–679. https://doi.org/10.1126/science.aaa4242

Yamaya, L., Mochizuki, K., Akuhara, T., Takemura, S., Shinohara, M., & Yamada, T. (2022). CMT inversion for small-to-moderate earthquakes applying to dense short-period OBS array at off Ibaraki region. *Earth, Planets and Space*, *74*(1), 164. https://doi.org/10.1186/s40623-022-01721-3

Yokota, Y., Ishikawa, T., Watanabe, S., Tashiro, T., & Asada, A. (2016). Seafloor geodetic constraints on interplate coupling of the Nankai Trough megathrust zone. *Nature*, *534*(7607), 374–377. https://doi.org/10.1038/nature17632

Yu, Z., Li, J., Niu, X., Rawlinson, N., Ruan, A., Wang, W., et al. (2018). Lithospheric Structure and Tectonic Processes Constrained by Microearthquake Activity at the Central

Ultraslow-Spreading Southwest Indian Ridge (49.2° to 50.8°E). *Journal of Geophysical Research: Solid Earth*. https://doi.org/10.1029/2017JB015367

Zhao, M., Canales, J. P., & Sohn, R. A. (2012). Three-dimensional seismic structure of a Mid-Atlantic Ridge segment characterized by active detachment faulting (Trans-Atlantic Geotraverse, 25°55′N-26°20′N). *Geochemistry, Geophysics, Geosystems*, *13*(11). https://doi.org/10.1029/2012GC004454

Appendix 1: Supplementary Materials for Chapter 2

Text S1. Details of the 1995 and 2003-2006 OBS Experiments

1995 OBS Experiment. Because of limited storage capacity, the OBSs recorded discontinuously in event triggering mode for the majority of the experiment with the same triggering parameters applied to identify earthquakes in periods of continuous recording (Wilcock et al., 2002). Phase arrival times were first picked manually. For earthquakes in swarms, waveforms were cross-correlated to improve the consistency of arrival times. Within the location scheme, both S-wave arrival time picks and picks not refined using cross-correlation were successively downweighted by 0.5, such that manually-picked S-waves were weighted by a factor of 0.25 relative to a cross-correlated P-wave pick. Earthquake locations required ≥ 5 picks including at least one S-wave. To account for shallow structure beneath stations, station corrections were iteratively calculated for the best recorded events and applied to the travel-time picks to reduce the mean residual to zero for each phase on each station. Since most off-axis earthquakes within the network are located at mid-crustal depths, earthquakes further than 3 km from the network have fixed depths of 3 km. The moment of each earthquake was taken as the mean of all P- and S-waves identified in good quality waveform records (Wilcock et al., 2002).

2003-2006 OBS Experiment. An ROV was used for instrument deployments to ensure good seafloor coupling (Wilcock et al., 2009). Due to instrument failures, there were periods during the second and third year when only four and five stations were operational, respectively (Weekly et al., 2013). For the automatically picked catalog, phase arrivals were initially picked using a short-term to long-term root mean squared (RMS) amplitude ratio method

and then refined using an autoregressive method. Pick weights were assigned for Hypoinverse (Klein, 2002) based on signal-to-noise ratios and S-wave picks were downweighted by a factor of 0.5. A fully-weighted P-wave pick was given an uncertainty of 0.05 s. To account for shallow structure beneath stations, station corrections were calculated using the same approach as the 1995 experiment. The final catalog (Weekly et al., 2013) contains earthquakes with a minimum of six picks, including at least two P-wave and two S-wave arrivals. Using the same approach as Wilcock et al. (2002), events that did not have recorded arrivals on an OBS within 3 km were given a 3 km fixed depth.

Text S2. Investigating similarity of velocity models

To validate concurrent use of the Arnoux et. al (2019) model, which constrained only P-wave structure, and the S-wave model from Kim et al. (2019), which constrained both P- and S-wave structure, we compared several parameters of the two models with depth. There are two concerns when using P- and S-wave velocity models from two different inversions: that the combination may create unrealistic V_P/V_S ratios, and that the V_P/V_S ratio depth profiles resulting from the combination of V_P and V_S from different inversions is significantly different than the V_P/V_S ratio depth profile from one inversion. We first visually inspected average depth profiles of the V_P/V_S ratio to ensure that the ratios maintained realistic values with depth. No discontinuities appear in the depth profile up to the depth at which the Kim et al. (2019) S-wave model is constrained, 4.4 km (Figure S1), and the ratio remains consistently between 1.6 and 3.4 at all depths for both models, with reasonable values of ~1.8 at 1-4 km depth.

We then compared the V_P:V_P/V_S and V_P/V_S ratios between the two different combinations of the Arnoux et. al (2019) and Kim et al. (2019) models (Kim P and Kim S versus Arnoux P and Kim S) at 1 km depth increments. We found that across all grid nodes for a given depth, the ratio values between the two combinations at > 1 km depth were within 10%.

Text S3. Three-dimensional model extrapolation

In order to extrapolate the 3-dimensional (3-D) velocity models to a 180 x 120 x 9 km^3 volume while avoiding sharp spatial discontinuities in velocity values, we used a weighted algorithm that smoothly transitioned the extrapolated model to a 2-D depth-averaged background model. Working at a constant depth and starting with nodes adjacent to the starting model, for each added extrapolated grid node (x_0, y_0) we first calculate a velocity value $v^*(x_0,y_0)$ using all existing model nodes within a given range, r_{max}, such that closer nodes received a higher weight:

$$v^*(x_0, y_0) = \frac{\sum_{r_i<r_{max}} \frac{v(x_i, y_i)}{r_i^2}}{\sum \frac{1}{r_i^2}} \qquad \text{(S1)}$$

Where r_i gives the distance between the extrapolated point and other existing nodes (either from the starting model or created through extrapolation):

$$r_i = \sqrt{(x_i - x_0)^2 + (y_i - y_0)^2}\,. \qquad \text{(S2)}$$

We then took a weighted average of the velocity of the background model at the associated depth, v_{ref}, and the velocity extrapolated from the existing nodes $v^*(x_0,y_0)$, such that the weight of the extrapolated value decreases with distance from the starting model:

$$v^*(x_0, y_0) = \frac{bv_{ref} + av^*(x_0, y_0)}{a + b} \qquad \text{(S3)}$$

Where b is a constant value, and a downweights the extrapolated value with increasing distance from the starting model:

$$a = \frac{1}{r^* / R_{ref}} \tag{S4}$$

Where r^* is the distance to the nearest starting model node. The variables r_{max}, b, and R_{ref} were chosen based on visual inspection to produce a reasonable balance of smoothing and the extension of features near the edge of the unextrapolated model. To create the extrapolated models for the earthquake locations seen in Figure 4, we chose r_{max}, = 1 km, b = 0.01, and R_{ref} = 5 km.

Text S4. Automated algorithm to create the ONC catalog

To find events, we bandpass filter the data from 4 to 30 Hz and identify impulsive signals on each channel when the ratio of short term (0.3 s) and long term (3.0 s) root mean square (RMS) average exceeds 3. Triggers are associated into events when at least 3 stations and 4 channels trigger within 1.5 s.

The algorithm then searches for the S-wave on each station, by calculating a single RMS amplitude time series for the two horizontal channels on each station in a 20-s long window centered on the first trigger time and smoothed with a 0.2 s running average. We then use a least squares approach to fit this smoothed time series with the combination of a constant amplitude and a Hann (cosine) window of variable half width h, amplitude, and center time position. Some of the stations are commonly triggered when the apparent amplitude of the noise decreases markedly for up to a few seconds. This appears to be an instrumental problem and is identified by our approach when the best fitting Hann window has a negative amplitude. Probable fin whale calls are flagged on each channel when the power of signals averaged over the three channels within the Hann window, bandpass filtered between 17-25 Hz, is at least 20% of those in the 5-13 Hz band. Electronic glitches are also present on some stations and are flagged when the waveforms on the three channels within the time limits of the Hann window do not have the spectral characteristics of fin whales but are strongly correlated on all three channels (median cross-correlation coefficient for the three combinations of channels of 0.85). For the remaining events, if the half width of the Hann window $h < 4$ s, it is flagged as a local earthquake with an S-wave detection time that corresponds to the onset of the Hann window.

If the half width of the Hann window h is ≥ 4 s, it is initially assigned as a regional distant earthquake that is considered too far away to be located. There are a significant number of instances where an event flagged as a distant earthquake results from the S-waves of two or

more closely spaced local earthquake multiplets being fit by a wide Hann window. For each event flagged as distant earthquake, we check for this by cross-correlating the 20-s window of each horizontal channel with a 1-s template that corresponds to the time interval with the highest RMS amplitude of the horizontal channel. If we find a correlation coefficient elsewhere in the 20-s window for both horizontal channels that exceeds 0.7, we identify this as a multiplet and subdivide the detection into two or more events that are flagged as local earthquakes that are assigned a center time based on the cross correlation, and set h = 0.5 s.

At this point we have flagged the detection on each station as a local earthquake, a distant earthquake, a fin whale, a glitch, or as noise. If most reporting stations have flagged an event as a local earthquake, we categorize it as a local earthquake and attempt to pick S and P arrival times and locate it.

For S-waves, we assume that the S-wave pick will occur within a time interval that extends from -0.5 d before the S -ave detection time to 1.0 d after it, where d is defined in seconds as $d = \min(1, \max(0.5, h))$. To make the S-wave pick, we filter the horizontal channels from 5-15 Hz and 5-30 Hz and create time series of "signal to noise" by considering a ratio of the RMS amplitude in moving signal and noise windows that extend both 0.25 s and 0.5 s after and before the time being considered. This leads to four time series of signal to noise for the two choices of filter and moving window durations. They have large values when the amplitudes increase sharply. We then make a preliminary pick of the S-wave that corresponds to the highest signal to noise in any of the time series that (1) occurs within the time interval identified for the S wave pick and (2) has a polarization that is consistent with an S wave (Baillard et al., 2014). If the pick has a signal to noise of < 6 dB we discard it. Otherwise, the pick is refined using the Kurtosis method of Baillard et al. (2014) with the constraint that the pick time changes by no more than 0.5 s.

To pick a P-wave on a station, we first define a time window in which it might occur. This starts no earlier than 10 s before the S-wave pick for that station (or the earliest S-wave pick for all stations if there is no S-wave for a particular station) and no earlier than 1 s after any P-wave pick for the previous event. It ends 0.75h before the S-wave pick on the station, a time that was determined empirically based on the observation of minimum S-P times that increase for more distant events with longer duration S-waves. If the event is the first in a set of multiplets, the P-wave window is defined to start no earlier than 4 s before the S-wave pick (multiplets are found to be quite near the network). If the event is a multiplet but not the first of the set, the P-wave window is defined to be within ±0.2 s of the predicted pick time based on the pick for the first multiplet.

To make the P-wave pick, we filter the vertical channel from 5-30 Hz and 15-45 Hz and again create a time series of "signal to noise" by considering a ratio of the RMS amplitude in moving noise windows that extend 0.4 s before and signal windows that extend 0.1 s, 0.2 s and 0.4 s after the time being considered. This combination of filters and windows leads to six time series of signal to noise. Possible picks are identified as peaks in the signal to noise time series that (1) exceed 6 dB, (2) occur within the P-wave pick time window, (3) have a polarization consistent with a P-wave (Baillard et al., 2014), and (4) do not occur at a time when the signal to noise surrounding a higher amplitude possible pick exceeds 6 dB. Once possible P-wave picks have been obtained for all stations, we select the set with the highest cumulative signal to noise in dB that occurs with a 1.2 s time window (the largest time difference for P-wave arrivals for the network geometry). We refine the pick times using the Kurtosis method of Baillard et al. (2014) with the constraint that the pick time changes by no more than 0.25 s.

If there are at least 5 pick times, the earthquake is located using Hypoinverse (Klein, 2002) with the relative phase weights set based on pick signal to noise (1.0 for > 15 dB, 0.75 for

> 10 dB and 0.5 for > 6 dB) and S-picks downweighted by 0.5. If there are any residuals that exceed 0.15 s for P-waves and 0.45 s for S-waves, the picks are eliminated. The earthquake is relocated if there are still at least 5 picked arrivals and otherwise discarded.

Text S5. Details of earthquake moment calculation

To calculate earthquake moments we follow the approach of Toomey et al. (1988) and Tréhu & Solomon (1983). The spectral amplitude of each waveform is calculated from a window containing the arrival, the size of which varies based on distance of the earthquake from the network and is selected based on the inspection of representative waveforms. Earthquakes within 10 km of the network have P- and S-moment windows of 0.3 s and 1 s to avoid capturing the S-wave in the P-wave window for close earthquakes with short S-P times. Earthquakes further than 10 km but closer than 30 km have moment windows of 0.5 and 1 s, and earthquakes further than 30 km have windows of 1 and 2 s for P- and S-waves respectively.

Displacement spectral amplitudes of P- and S-wave arrivals are first corrected for waveform attenuation using a quality factor, Q:

$$\Omega = \Omega_0 e^{\pi f t Q^{-1}}, \qquad \text{(S5)}$$

where Ω is the attenuation-corrected spectral amplitude, Ω_0 the uncorrected amplitude, f the reference frequency, and t the travel time of the wave from source to receiver. We take the travel time t directly from the predicted travel time of the NonLinLoc earthquake location, which is calculated using the 3-D travel time grids. We take $Q_S = Q_P$, with Q_P=40 for the first 0.16 s of the path, equivalent to the travel time through 0.4 km of the highly attenuating layer 2A (Van Ark et al., 2007), and 500 elsewhere. Similarly, Q_S=40 for the first 0.28 s of the path and 500 elsewhere.

Our Q_P values follow direct measurement of attenuation of the southern Juan de Fuca Ridge, which gives a Q_P value of 20-50 in the uppermost 0.6 km of the crust (Jacobson & Lewis,

1990), and an attenuation inversion study on the East Pacific Rise, which shows similar Q_P values at shallow depths near-axis but increases to a Q_P of 500 below 2 km depth (Wilcock et al., 1992).

To ensure that the effect of attenuation in earthquake moment calculation is properly corrected, we choose a S-wave quality factor Q_S such that the ratio between P- and S-wave moments is not dependent on distance from the network. To do so, we calculated moments for a subset of the catalog with Q_P = 500 and several different Q_S values used in previous studies. We fitted the resulting distributions of the log of the P/S moment ratio versus range with a line (Figure S2) and choose the Q_S that yields a slope closest to 1. We performed this test for six months of the ONC dataset, from July-December 2016, for all earthquakes on all stations.

Previous earthquake studies on mid-ocean ridges either assumed that $Q_P = Q_S$ (Toomey et al., 1988; Tréhu & Solomon, 1983), or assumed $Q_P > Q_S$ (Weekly et al., 2013). We show the relationship between log of the P/S moment ratio and range in Figure S2 for two examples, $Q_P = Q_S$ = 500 (Toomey et al., 1988; Trehu & Solomon, 1983) (Figure S2a), and Q_P = 500 and Q_S = 395 (similar to Weekly et al., 2013) (Figure S2b). We find that although the range dependence is not very sensitive to relative changes in Q_P and Q_S, $Q_P = Q_S$ = 500 gives a linear fit to the log of the P/S moment ratio versus s. range closest to 1 (Figure S2), and thus we use Q_S = 500 when calculating moments for the ONC catalog.

The attenuation-corrected displacement spectral amplitudes are then averaged within a frequency band of 5-15 Hz and used to estimate seismic moment, M_0, following the method of Brune (1970):

$$M_0 = \frac{4\pi\rho x V^3 \overline{\Omega}}{KR}\ , \qquad \text{(S6)}$$

where ρ and V are the density and seismic velocity of the earth at the source, x the length of the path from source to receiver, R the correction for radiation pattern, and K the free surface correction for the interaction of the seismometer with the seafloor. Values for all parameters used in ONC catalog moment calculations can be found in Table S3.

Velocity V is taken as the depth-averaged value at 3 km from our 3-D velocity grids, and R values follow Weekly et al. (2013). We calculated an appropriate K for both P- and S-waves using plane wave theory (Aki & Richards, 2002). Assuming an upper crustal density of 2240 kg m^{-3} (Gilbert & Johnson, 1999), seawater density of 1030 kg/m^3, incidence angles of 20º and 15º degrees for P- and S-waves, respectively, P-wave upper-crustal velocities of 2.5 km/s (Van Ark et al., 2007), P-wave seawater velocities of 1.5 km s^{-1}, and S-wave upper-crustal velocities of 1 km s^{-1} (Wilcock et al., 2002), we find a corrective K_P of 1.5 and K_S of 2.

The parameters we define and use to calculate moments for the ONC catalog differ from those applied in previous experiments. To improve cross-network comparison, we recalculate moments from the 1995 experiment using our values for Q_P, Q_S, ρ, V, K, and R. For the Keck experiment, we adjust for the differences in the physical parameters of Equation 3 by calculating a corrective factor of 0.87 for P moments and 0.73 for S moments. We take the average of these corrections and multiply all Keck moments by 0.8. The moments for the Keck experiment were calculated with somewhat different Q_p and Q_s models than used for the ONC network, which will lead to slightly higher moments for the Keck experiment, but the maximum discrepancy is only ~15% for earthquakes at 50 km range so we do not correct for this.

Moment magnitudes, M_W, are then calculated using the relation of Hanks & Kanamori (1979).

$$M_w = {}^{2}/_{3} \log_{10} M_0 - 10.7 \qquad \text{(S7)}$$

Text S6. Calculation of station- and phase-based corrections for earthquake moments

To obtain corrections for site effects in moment calculations, we first calculate moments for all arrivals recorded during Period 1. For each station-phase combination (8 in total for Period 1, for 4 stations each having a P- and S-wave moment calculation), we calculate the median moment ratio, p, between arrivals with that station-phase combination and all 7 other combinations :

$$p_{i,j} = median\left(\frac{moment_{i,k}}{moment_{j,k}}\right) \quad \text{(S8)}$$

Where both i and j are indices that iterate through all possible station-phase combinations, in our case {KEMF-P, KEMF-S, KEMO-P, KEMO-S, NCHR-P, NCHR-S, ENWF-P, ENWF-S}, and k is an index that iterates over all earthquakes that have arrivals for both the i-th and j-th station-phase pair.

Plots showing median moment ratios between different station-phase combinations, for example station-phase combination KEMF-P, can be found in Figure S3. As can be seen in the example plots, the ratios between moments calculated using different stations and phases is not 1 for all combinations, showing that there are site effects and conceivably instrument response scaling and sensitivity errors causing systematic offsets in the waveform amplitudes.

We calculate a correction coefficient factor, G, for each station-phase combination such that when the moments for that station-phase pair are multiplied by the coefficient, the logarithmic mean of the ratios between it and all other combinations is 1:

$$G_i = 10^{-\left(\frac{\sum_j log_{10}(p_{i,j})}{N}\right)} \quad \text{(S9)}$$

where *N* is the total number of station-phase combinations, which for Period 1 is 8. Correction coefficient factors *G* for stations only in operation during Period 2, ENHR and KEMF-W3, are calculated in reference to the Period 1 stations by keeping the correction coefficients *G* for the instruments from Period 1 fixed, such that the average ratio in Period 2 considering all instruments is not 1 and N = 12. The value of *G* for all station-phase combinations can be found in Table S4.

Multiplying all arrivals by their corresponding correction coefficient *G* ensures that they are consistent across earthquakes regardless of which stations recorded which phases. This allows us to simply take the median of all corrected moments for the *k*-th earthquake as the final moment for the *k*-th earthquake:

$$M_k = median\left(\frac{M_{k,i}}{G_i}\right) \quad \text{(S10)}$$

Text S7. Three-dimensional uncertainties visualized using NonLinLoc

The OctTree method employed by the NonLinLoc software (Lomax et al., 2000) calculates earthquake locations by approximating a full grid search. As OctTree converges on a location, it records the locations and relative likelihoods of all points it searches, producing a scatter cloud that approximates the probability density function of a location. By plotting samples of this scatter cloud, we can understand the spatial characteristics of our uncertainties in more detail.

Figure S12 shows four representative examples of the NonLinLoc scatter cloud for free-depth earthquakes located with the Keck network. Many of the free-depth location clouds have small ellipsoidal shapes, reflected in their relatively small horizontal and vertical uncertainties (Figure S12a and S12b). Earthquakes that have small, symmetric scatter clouds such as these tend to show less movement between original locations obtained with a linearized inversion using Hypoinverse (Klein, 2002) (green stars in Figure S12) and our relocations made using NonLinLoc (red stars in Figure S12). In contrast, some locations show broad asymmetric location clouds (Figure S12c), at times resulting in similar locations between the linear and nonlinear methods, but producing greater uncertainty estimates. Large movement between linear and nonlinear location estimates is at times explained by bimodal location clouds, as seen in Figure S12d. These location clouds show that although the original location does fit the arrival times acceptably, the nonlinear method coupled with the more complex 3-dimensional velocity model is able to find a location that fits slightly better.

Similar location cloud characteristics are observed for locations with fixed depths, as seen in four representative examples from the Keck network in Figure S13. The majority of locations display small, symmetric, ellipsoidal clouds with relatively small horizontal

uncertainties (Figures S13a and S13b). These typical clouds show that uncertainties tend to be larger in the tangential direction with respect to the network, reflected in the typical ellipses for distal earthquakes. Interestingly, Figure S13b shows that the original location lies completely outside of the tight and symmetrical relocation cloud, highlighting the effect of the large changes in the velocity model at the segment ends. Figures S13c and S13d illuminate the location structure of earthquakes that were moved to more geologically sensible locations; both relocations are close to the main Endeavour axis, whereas the original locations were not coincident with any significant feature. Figure S13c is an example of a broad location cloud that produces large horizontal uncertainties, and Figure S13d is an example of a multimodal location cloud that leads to a location movement. These location clouds and the overall striking improvement of alignment to geologic features in the relocations (Figure 8) emphasize the value of a 3-dimensional velocity model and a nonlinear location method that, together, more fully account for the effects of complexity of in the velocity structure.

Text S8. Vertical location uncertainties and picking errors

The vertical uncertainties observed for vent field earthquakes located with a free depth highlight how nonlinear location can amplify uncertainties relative to a linear method. In particular, the large median vertical uncertainty of 1.6 km for the Keck catalog is surprising, given that Weekly et al. (2013) reported a much lower vertical uncertainty of 0.8 km and our relocations yield a large improvement in the picking error, from 0.095 s to 0.068 s. Similar to epicentral uncertainties, examination of the NonLinLoc probability distributions shows that many earthquakes have bimodal probabilities with both a shallow tight cluster and a more diffuse deeper cluster or have very long-tailed probability distributions in the depth direction (Figure S12). This long-tailed effect appears more frequently for the Keck catalog free-depth earthquakes than the other experiments because the arrival times used to calculate locations have higher uncertainties; 58% of picks in the Keck catalog have weights < 0.2, compared to only 37% in the ONC catalog. This effect is not as prevalent for the other experiments due to better picks. For example, the depth scatter from Swarm V1 of 0.43 km (Figure S15c) is consistent with the mean vertical uncertainty of 0.39 km calculated from NonLinLoc.

In the ONC network catalog, there is a higher proportion of outlier residuals in locations with fewer arrivals: the picking error calculated using Equation 1 increases from 0.030 s for earthquakes with eight arrivals to 0.041 s for all located earthquakes. It is clear that refinement of picks using kurtosis (Baillard et al., 2014) significantly improves their quality; the ONC picking error of 0.030 s is less than half of the 0.068 s error for the Keck catalog which does not pick using kurtosis. However, our picking algorithm is still fully automatic, and inspection of the data shows that phase arrivals are occasionally mispicked on noise or fin whale calls. For earthquakes far from the network the picked P-wave may be *Pn* or *PmP*, whereas we model times as *Pg*. Our location method first locates earthquakes using Hypoinverse, which includes an algorithm to

downweight and eliminate arrivals with very large residuals, but the final location with NonLinLoc lacks a mechanism to remove minor mispicks. This problem is amplified by the small size of the ONC network; distinguishing an outlier is much more difficult when there are only a few observations.

The picking error of 0.030 s for the best-recorded earthquakes in the ONC catalog is a combined error from two sources: the phase identification error and velocity model error. Despite the marked improvement in pick quality for the ONC catalog compared to the Keck catalog, we infer that phase identification uncertainties dominate location errors. The velocity model errors can be approximated by the RMS residuals for the tomographic inversions although these will likely be an underestimate in regions where the velocity models are extrapolated. For P-waves, the RMS residual of the inversion of 0.011 s (Arnoux et al., 2019) can only account for ~10% of the picking error variance. Likewise for S-waves, the RMS residual of 0.038 s for *Sg* arrivals only accounts for 10% of the travel time variance given that S-waves are weighted by 0.25 in the earthquake locations.

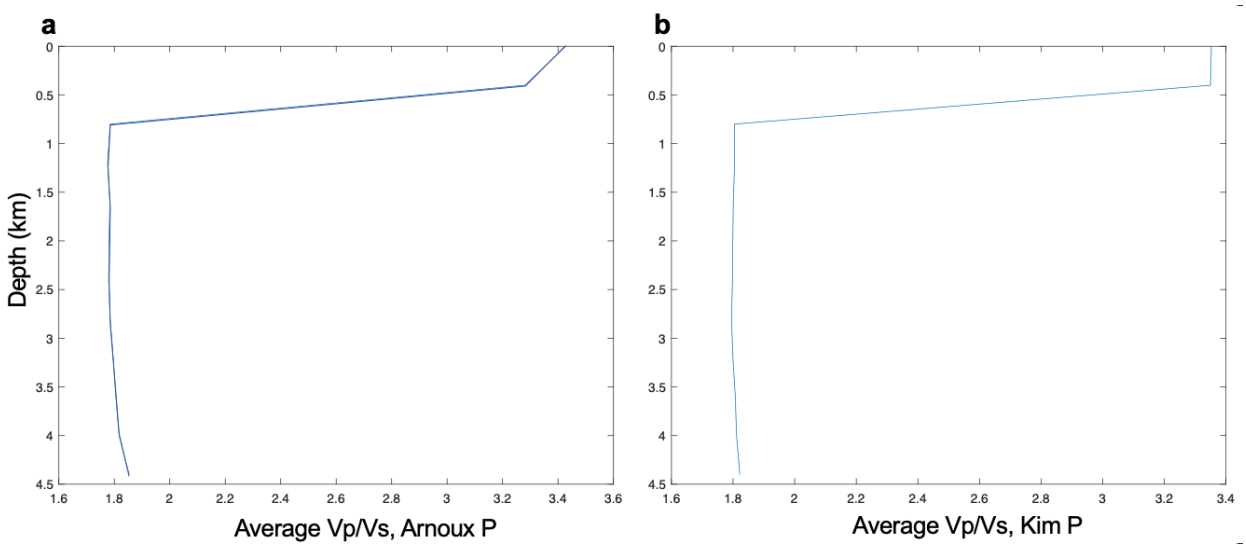

Figure S1. Depth profiles of average V_P/V_S ratio at 0.4 km increments for the 3-dimensional velocity models. V_S values in both (a) and (b) are from the Kim et al. (2019) model. V_P values in (a) are from the Arnoux et al. (2019) model and in (b) are from the Kim et a. (2019) model.

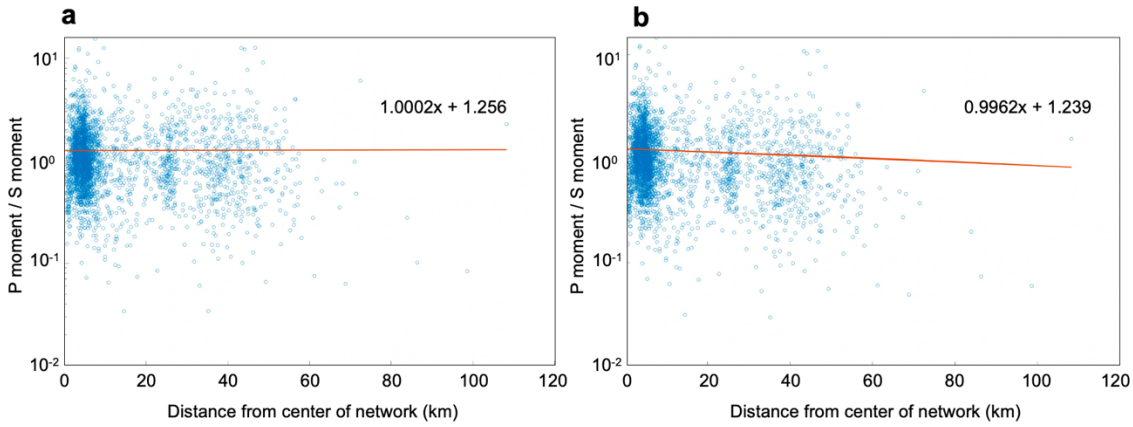

Figure S2. Scatter plots of the log of P moment to S moment ratio versus distance from network for all earthquakes on all stations for the ONC network from July-December 2016, overlain with the best linear fit in red. Both plots are annotated with the equation of the best linear fit, with the relationship between the ratio and distance given by log(slope). Subplot (a) shows the results of moments calculated with $Q_P = Q_S = 500$ and (b) $Q_P = 500$ and $Q_S = 395$. The comparison shows that the ratio is not very sensitive to relative changes in Q_P and Q_S, but that $Q_P = Q_S$ produces a better result.

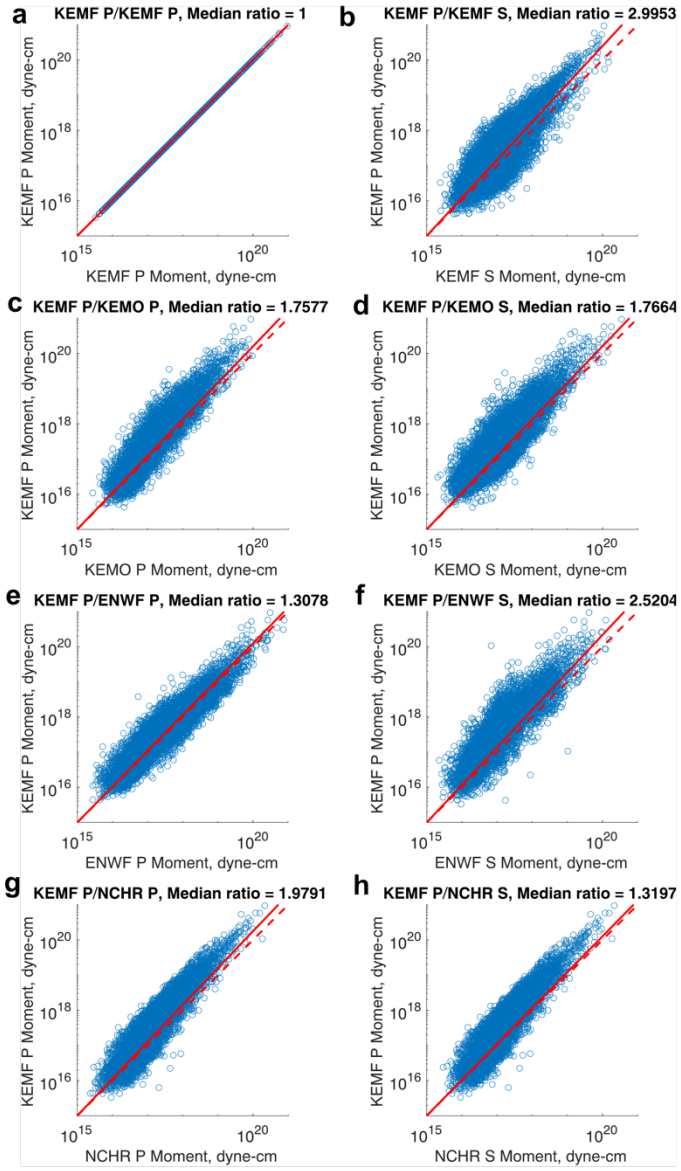

Figure S3. Scatter plots showing the ratios of moment calculations between example station-phase combination KEMF-P and all other station-phase combinations from Period 1. Each point on each scatter plot represents an earthquake that had a recorded arrival for both station-phase combinations, such that the number of points varies between each subplot. The median ratios listed in the subplot titles make up the p_j list from Equation S8, and are used to calculate a correction coefficient for all KEMF-P moment calculations using Equation S9. Each subplot is overlain with a 1:1 line in dashed red and a 1:1 median line in solid red.

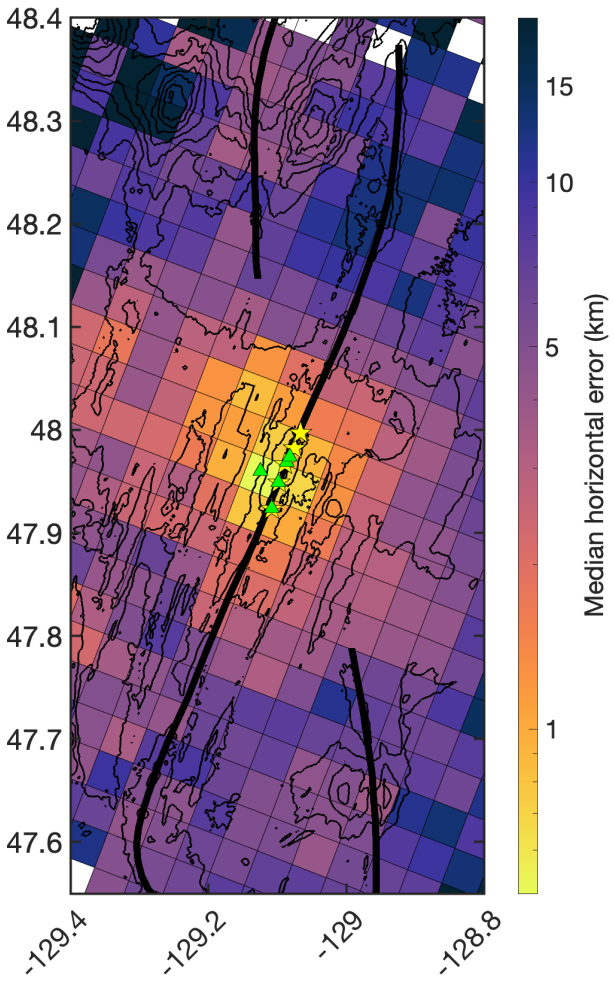

Figure S4. Median maximum horizontal uncertainties for earthquakes in the 2016-2021 ONC catalog, shown as a spatial histogram of the median maximum horizontal value for all earthquakes within each bin. Bin sizes are 4 km x 4 km and are shaded using a logarithmic scale. Symbols follow Figure 1.

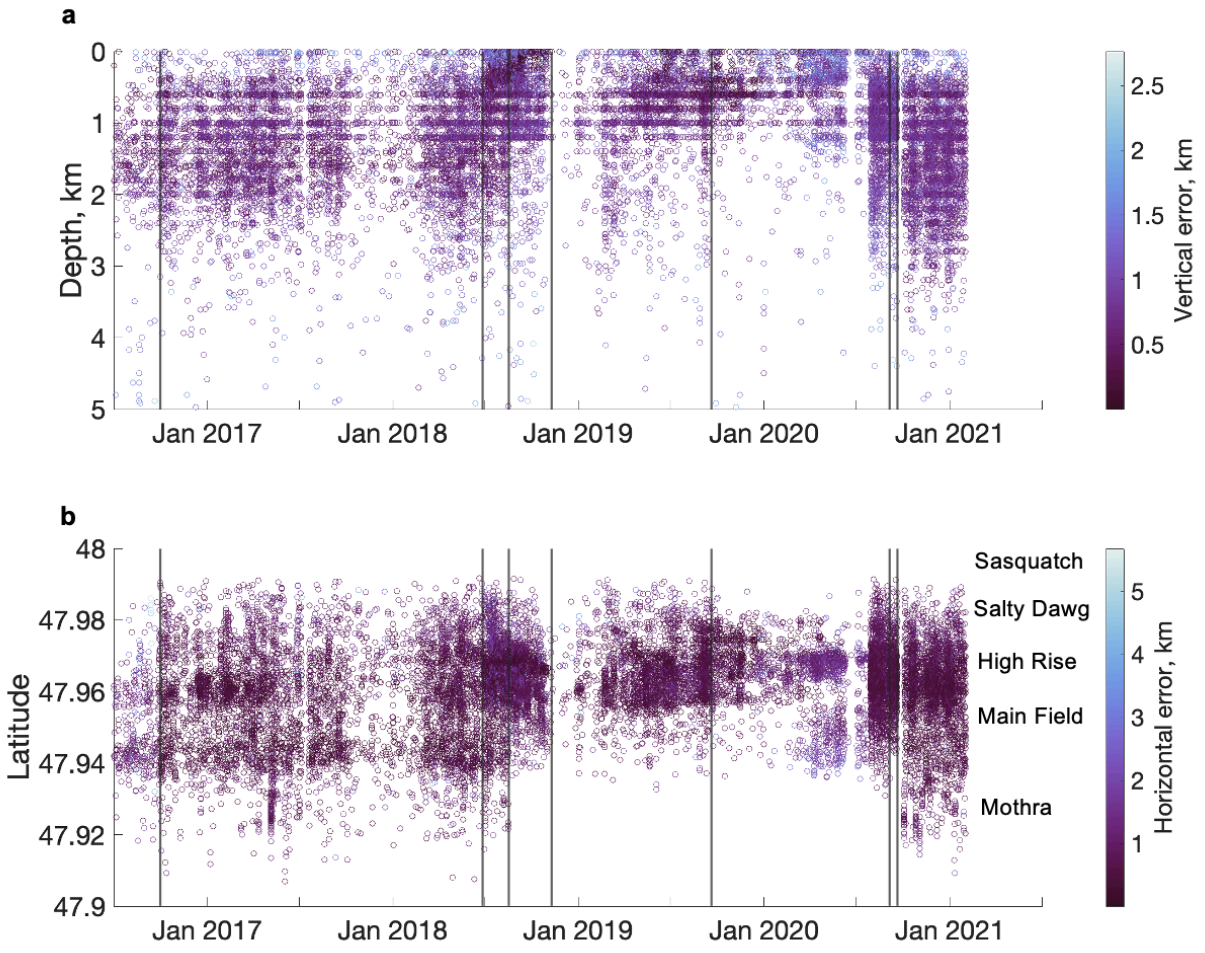

Figure S5. Scatter plots of all earthquakes with constrained depths within the vent fields for the ONC network, showing (a) earthquake depth versus time, colored by vertical error, and (b) earthquake latitude versus time, colored by horizontal error. Black vertical lines represent all times the network underwent an instrument change (see Figure 3 and Table S1). The names of the hydrothermal vent fields are annotated at the latitude at which they are located in (b). The banding of locations at certain depths seen in (a) corresponds to the vertical grid of our travel time model. Note that the changes in moment release rates observed in September 2018 and August 2020 and the deepening of earthquakes seen in August 2020 do not coincide with network changes.

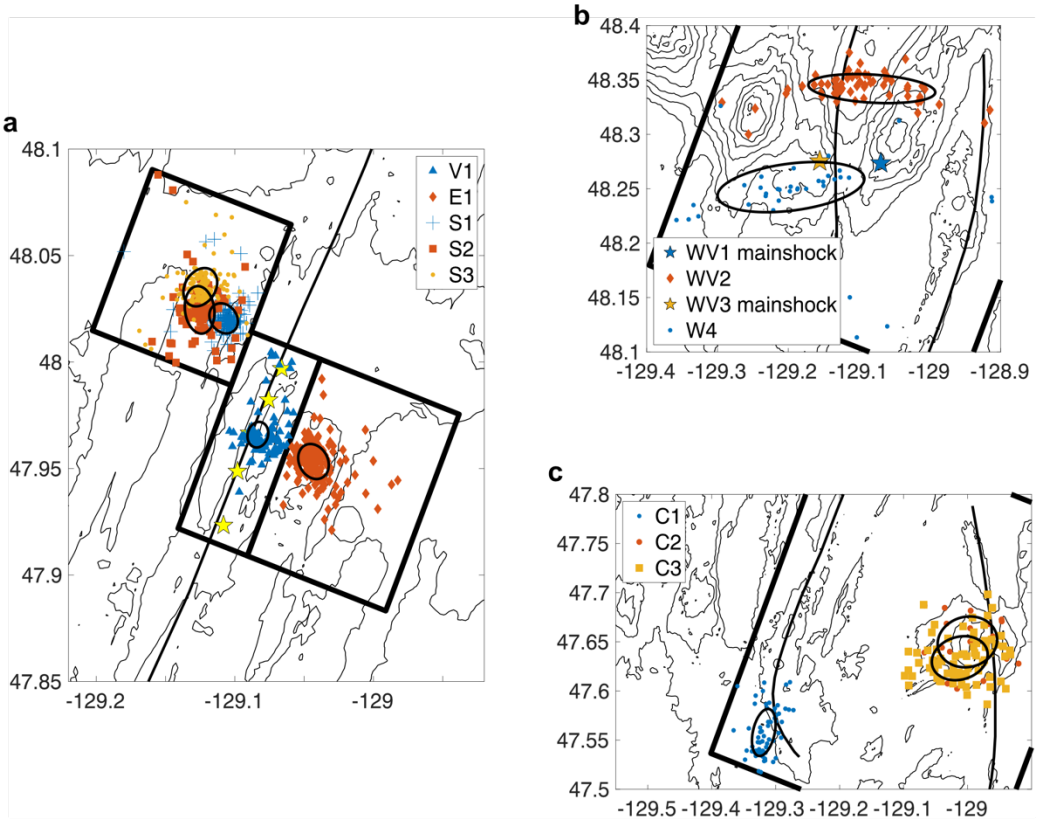

Figure S6. Locations of swarms of interest for the 2016-2021 ONC catalog, overlain by their corresponding 1-σ covariance ellipses (see Table S5 for lengths of major ellipse axes). (a) Swarm locations for the central regions of the segment. Locations of vent fields shown with yellow stars. (b) Swarm locations for the West Valley OSC. Only locations of the mainshock are shown for swarms WV1 and WV3. (c) Swarm locations for the Cobb OSC.

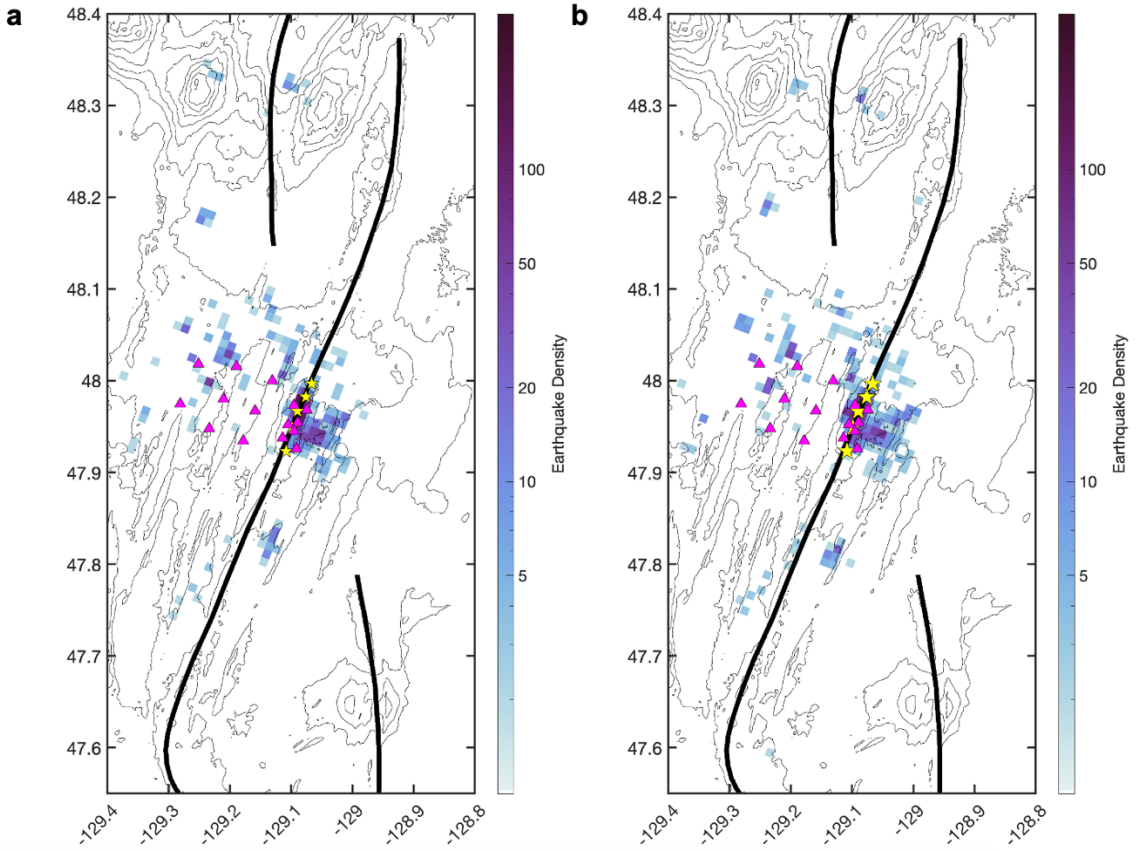

Figure S7. Maps showing spatial density of earthquake locations in 1 km^2 bins, shaded on a logarithmic scale, for (a) original 1995 locations (Wilcock et al., 2002) and (b) relocations of the same earthquakes as presented in this study. Station locations are shown with magenta triangles, vent field locations with yellow stars, and main tectonic boundaries with black lines. Bathymetric contour lines are at 200 m intervals.

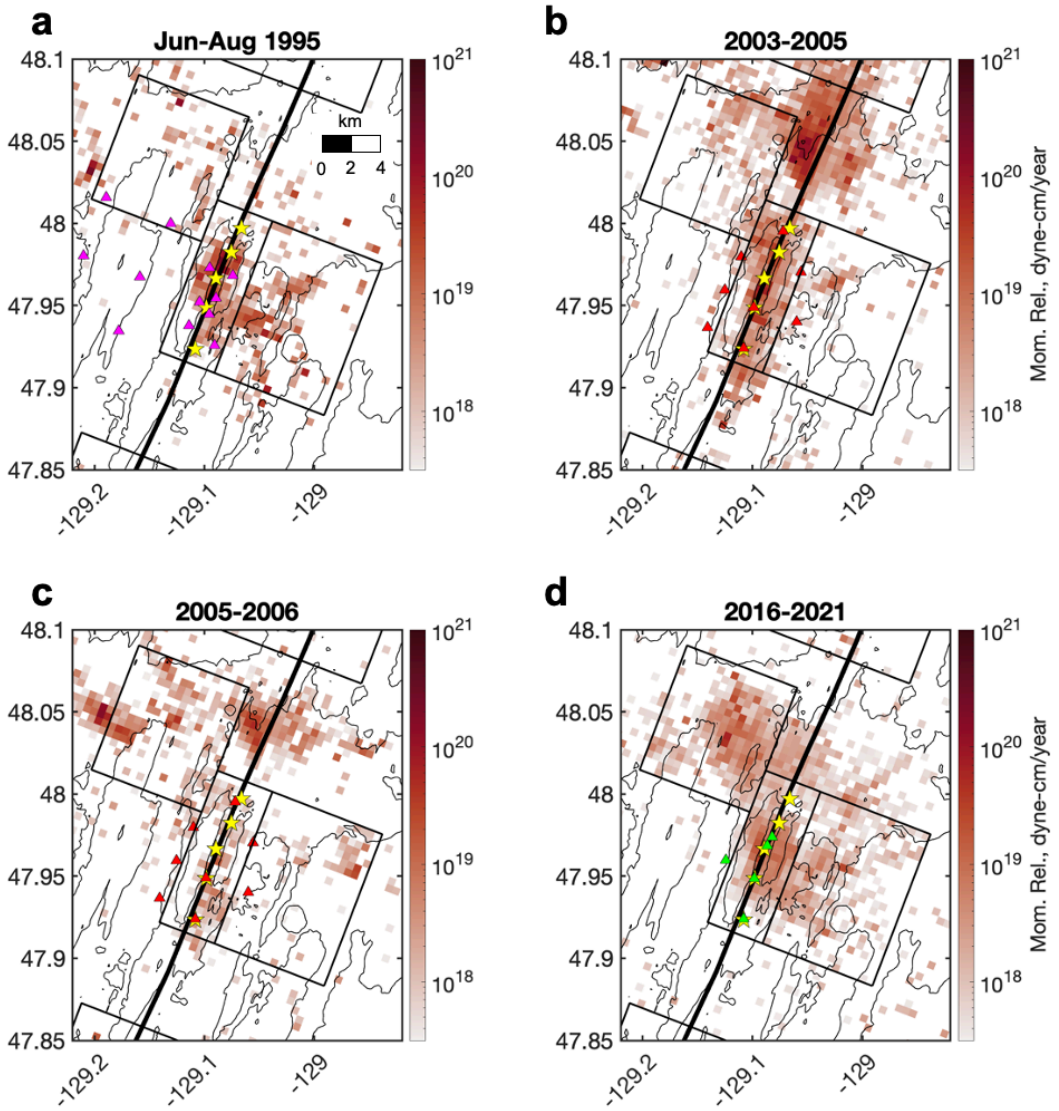

Figure S8. Vent-scale seismicity patterns for different time periods, scaled to represent 1 year of moment release not corrected for magnitude of completeness, shown as spatial histograms with bin sizes of 0.5 km x 0.5 km. Symbols follow Figure 5.

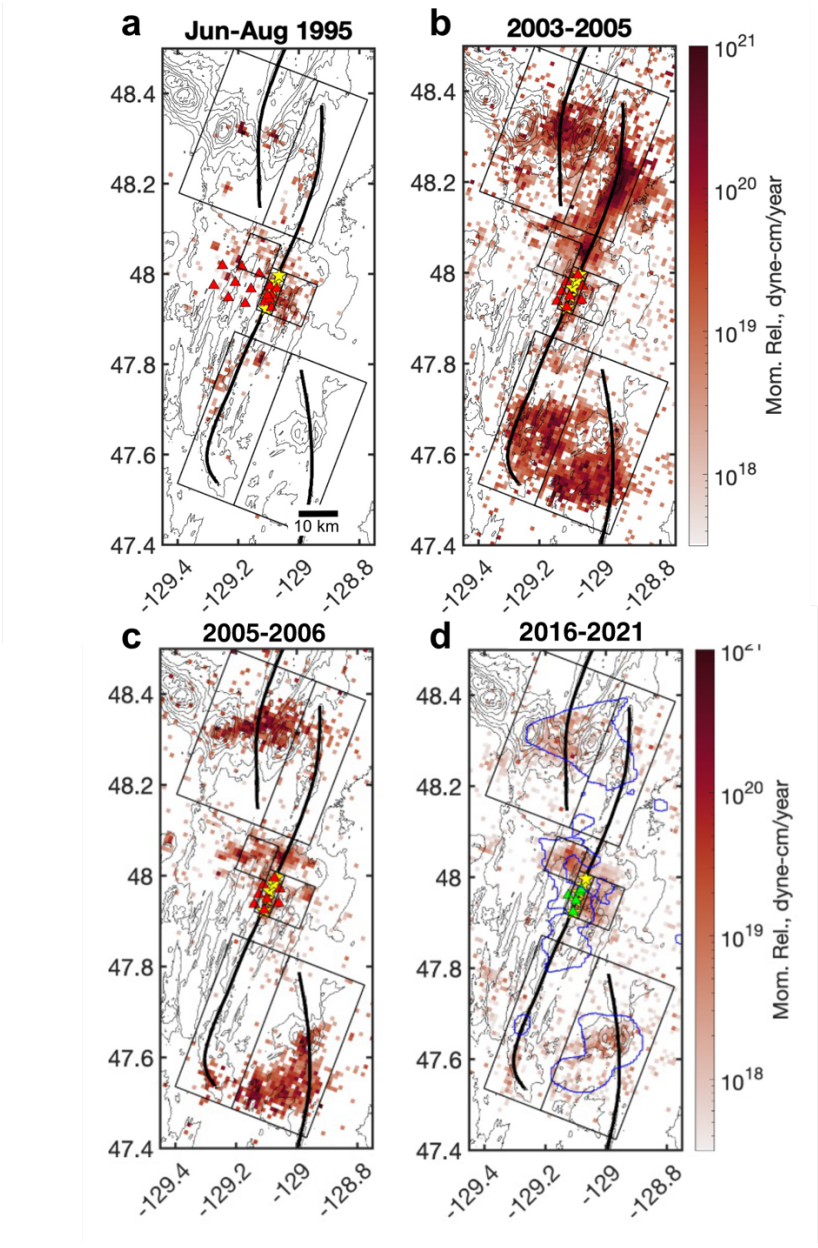

Figure S9. Segment-scale seismicity patterns for different time periods, scaled to represent 1 year of moment release not corrected for magnitude of completeness, shown as spatial histograms with bin sizes of 1 x 1 km^2. Symbols follow Figure 5, except for the mantle melt contour in (d) which is shown here in blue.

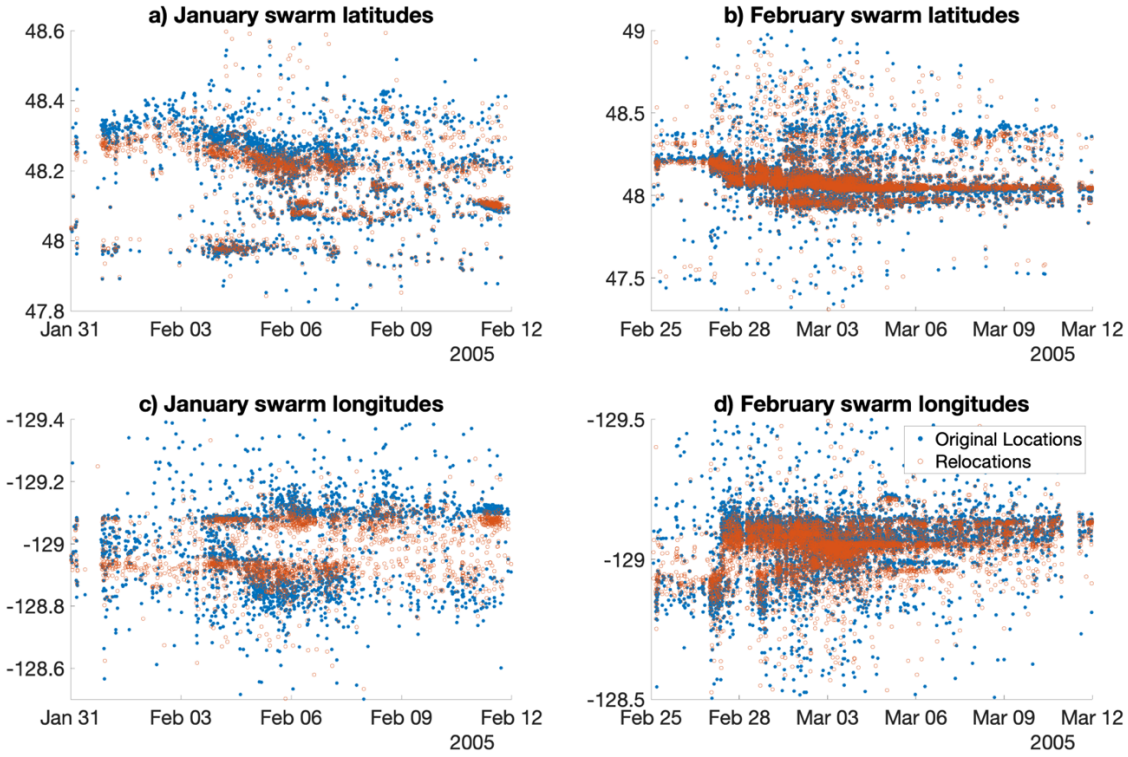

Figure S10. Scatter plots illustrating earthquake location migration throughout time for the January and February 2005 swarms, comparing original Weekly et al. (2013) locations (blue) to the relocations made in this study (orange). Scatter plots show (a) latitude versus time for the January swarm, (b) latitude versus time for the February swarm, (c) longitude versus time for the January swarm, and (d) longitude versus time for the February swarm.

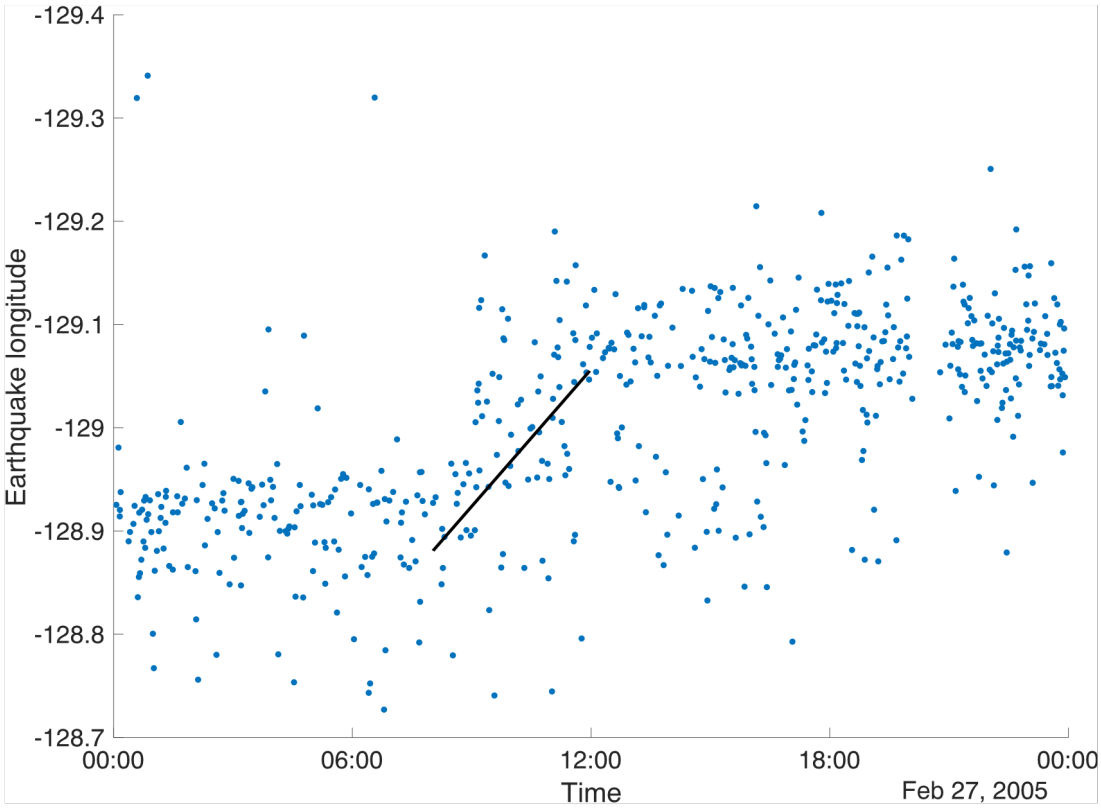

Figure S11. Scatter plot of earthquake longitude versus time showing the migration of earthquakes across the WV OSC during the February 2005 swarm, fit with a least squares line consistent with earthquakes migrating ~20 km southwestward at 3.3 km hr^{-1} on February 27, 2005.

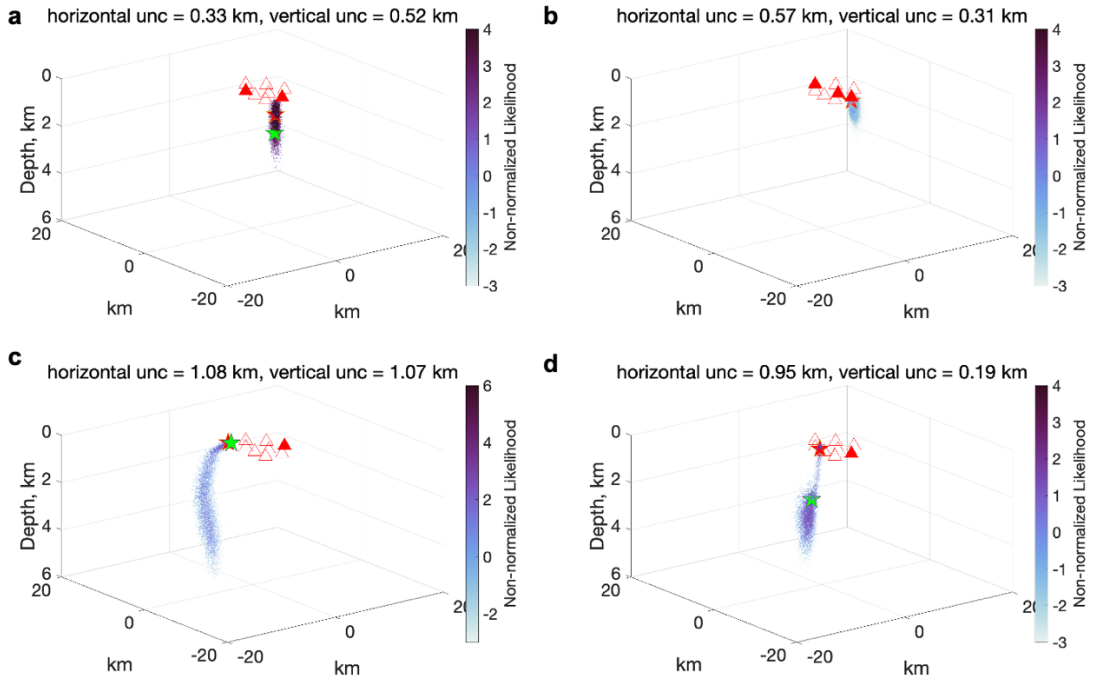

Figure S12. Examples of location scatter clouds from NonLinLoc for free-depth earthquakes recorded by the Keck network, shown in 3 dimensions with all axes in kilometers, centered on the network with the left-hand axis running roughly N-S and the right-hand axis E-W. Red triangles are the locations of the seismic stations, sitting on the seafloor at 0 km depth. Filled red triangles are stations that did not record arrivals for the earthquake and open red triangles are stations that did. Scatter plots are 5,000 scatter samples from the NonLinLoc probability density function, colored by non-normalized likelihood. Green stars are original locations made with Hypoinverse and a 1-D velocity model. Red stars are the relocations presented in this study, which NonLinLoc calculates to be the scatter point with the highest likelihood. Note the green star is hidden in (b) because the location has barely changed.

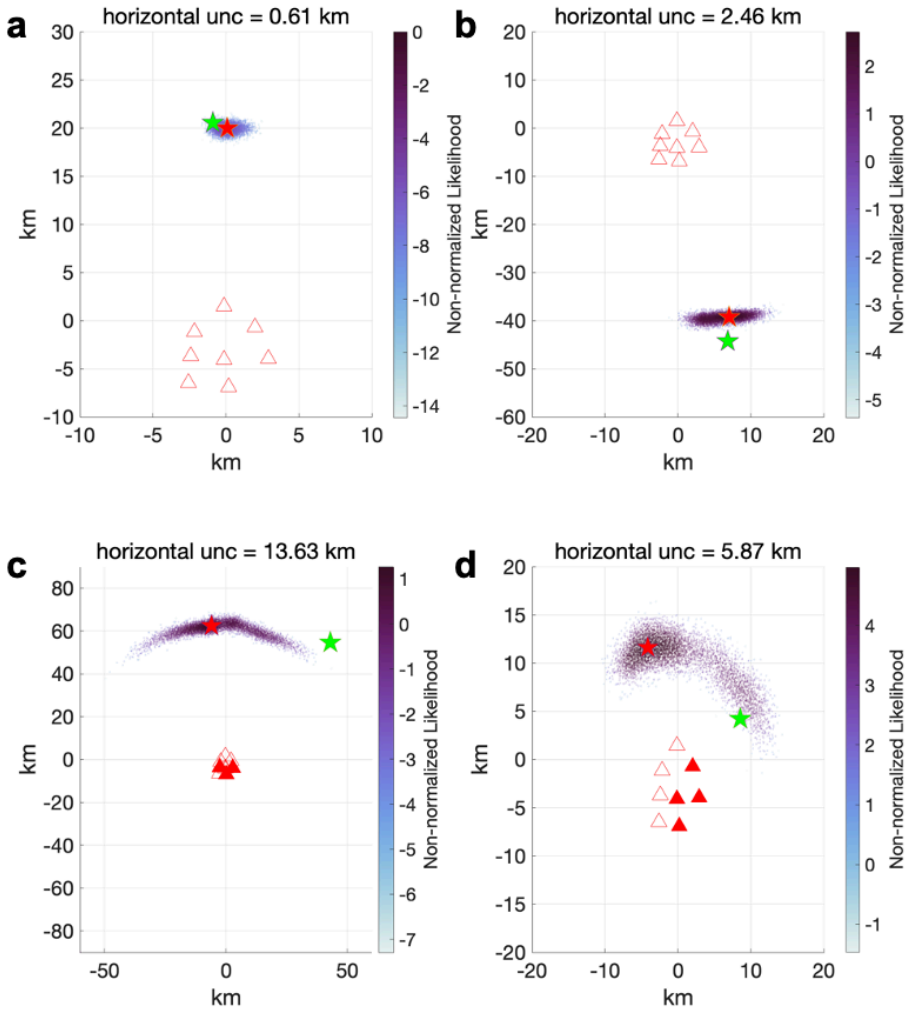

Figure S13. Examples of location scatter clouds from NonLinLoc for fixed-depth earthquakes recorded by the Keck network, following Figure S12 but shown in map plan. Symbols are as in Figure S12.

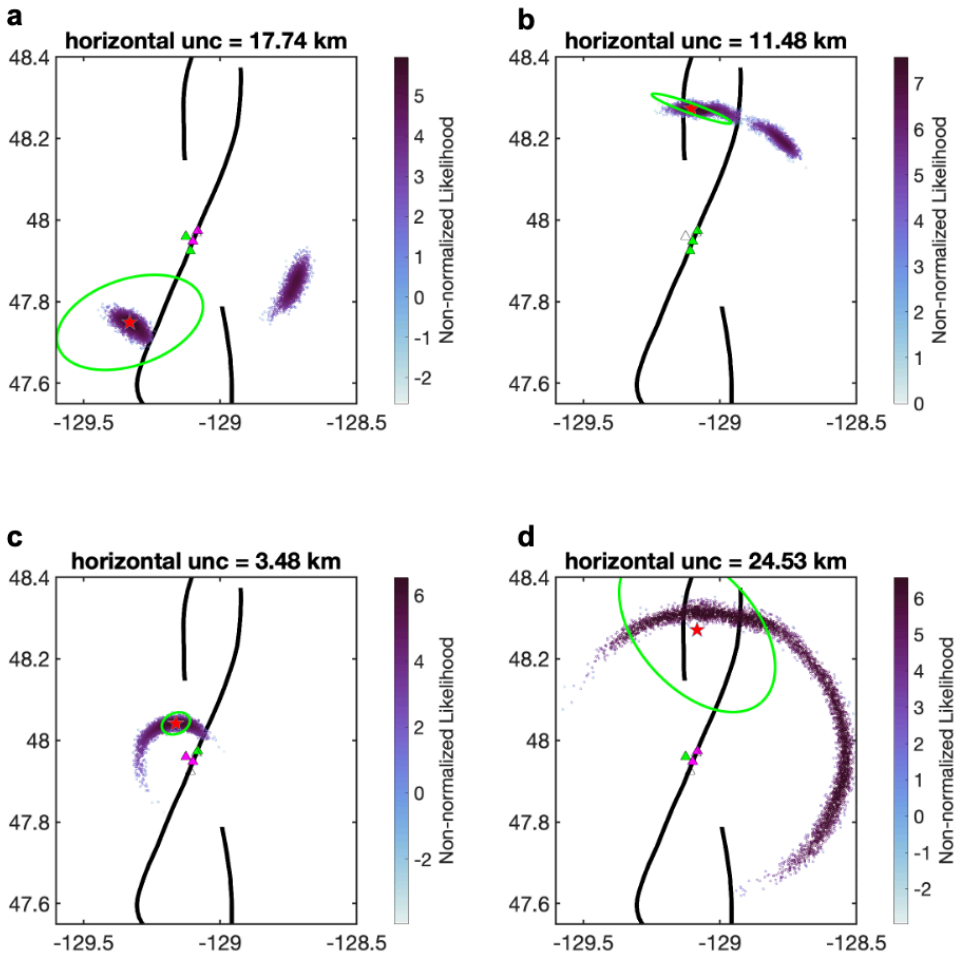

Figure S14. Examples of location probability scatter clouds from NonLinLoc for fixed-depth earthquakes from the ONC network with large and complex distributions. Red stars are the best fit earthquake location, and triangles represent ONC stations colored as green for stations recording two picks, magenta for stations recording one pick, and empty for stations without arrivals. Scatter plots are 5,000 scatter samples from the NonLinLoc probability density function, colored by non-normalized likelihood. The best fit locations are overlain by the 1-σ uncertainty ellipse calculated using the singular value decomposition of the probability density function, with the corresponding maximum horizontal uncertainty noted in the title of each subplot. All other symbols follow Figure 1. Station combinations that resulted in a near-linear network geometry which yielded bimodal probability distributions are shown in (a) and (b), where the corresponding ellipses can be seen to be much larger and skewed in orientation than they would be if the location was resolved to one of the probability clusters. Poorly recorded earthquakes resulting in large arc-like probability distributions are shown in (c) and (d), where the ellipses can also be seen to be skewed in orientation and size due to the arced shape of the probability.

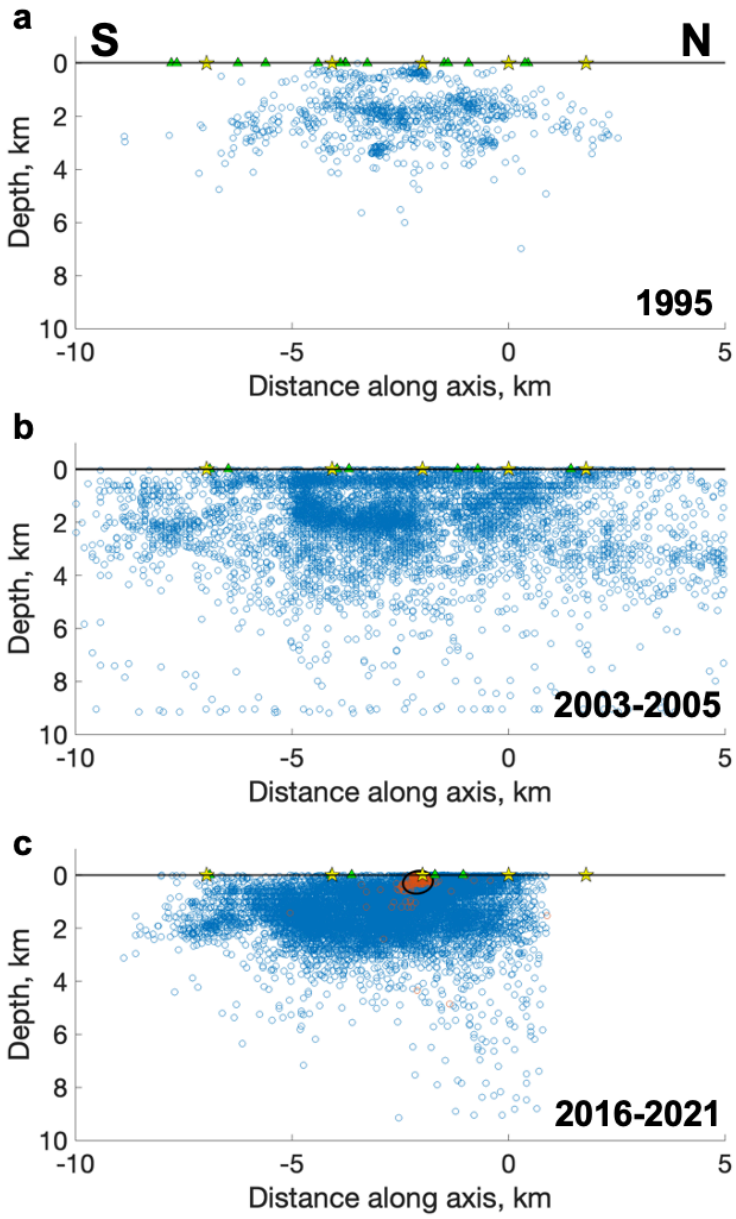

Figure S15. Along-axis cross-sectional scatter plots of all earthquake locations with constrained depths for all 3 networks. The vertical spread of earthquake depths can be seen to scale with the median maximum vertical uncertainty calculated for each network, of (a) 0.53 km for the 1995 network, (b) 1.64 km for the Keck network, and (c) 0.74 km for the ONC network. The depths and locations of Swarm V1 (Figure S6a) are plotted in orange in (c) and overlain by the 1-σ covariance ellipse for the swarm, whose major axis length of 0.43 km is consistent with the mean vertical uncertainty of earthquakes in the swarm, 0.39 km.

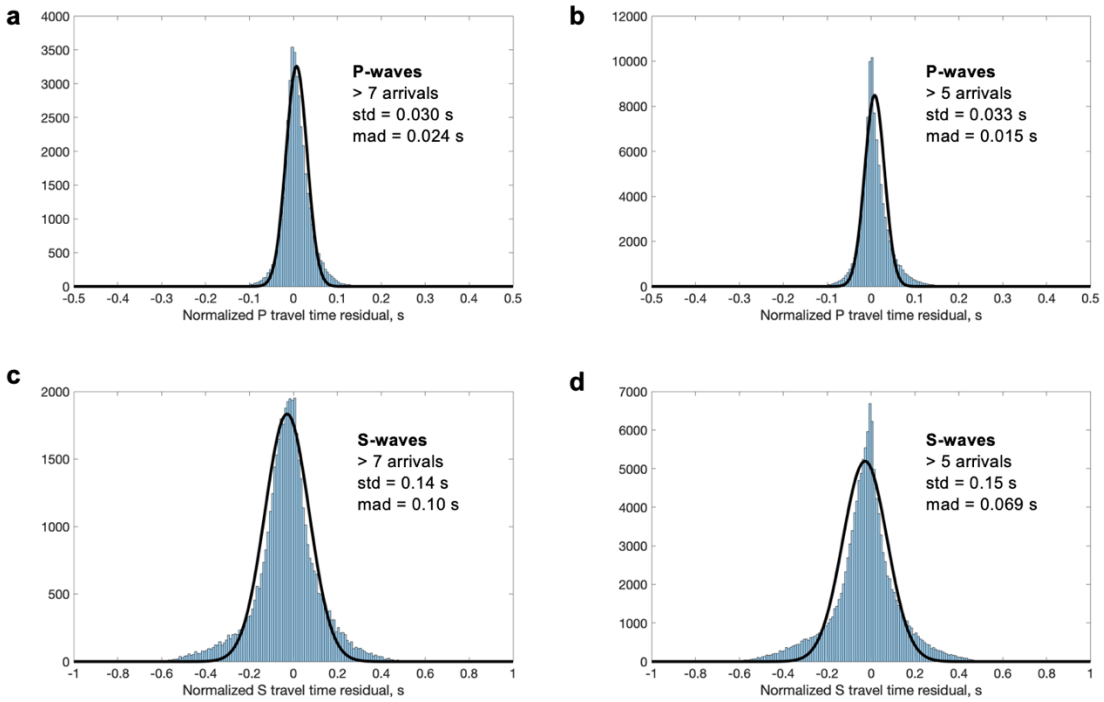

Figure S16. Distributions of travel time residuals, normalized by pick weight, for the ONC network locations, shown as histograms for (a) P travel time residuals for earthquakes with > 7 arrivals, (b) P travel time residuals for earthquakes with > 5 arrivals, (c) S travel time residuals for earthquakes with 8 arrivals, (d) S travel time residuals for earthquakes with > 5 arrivals. (a) and (b) have a bin size of 5 ms and (c) and (d) have a bin size of 10 ms. All distributions are overlain with a Gaussian distribution constructed using the median absolute deviation and normalized to match the area under the curve of the histogram, emphasizing that the residuals are non-normally distributed with an increased proportion of outliers. Each distribution is annotated with its standard deviation (std) and median absolute deviation (mad).

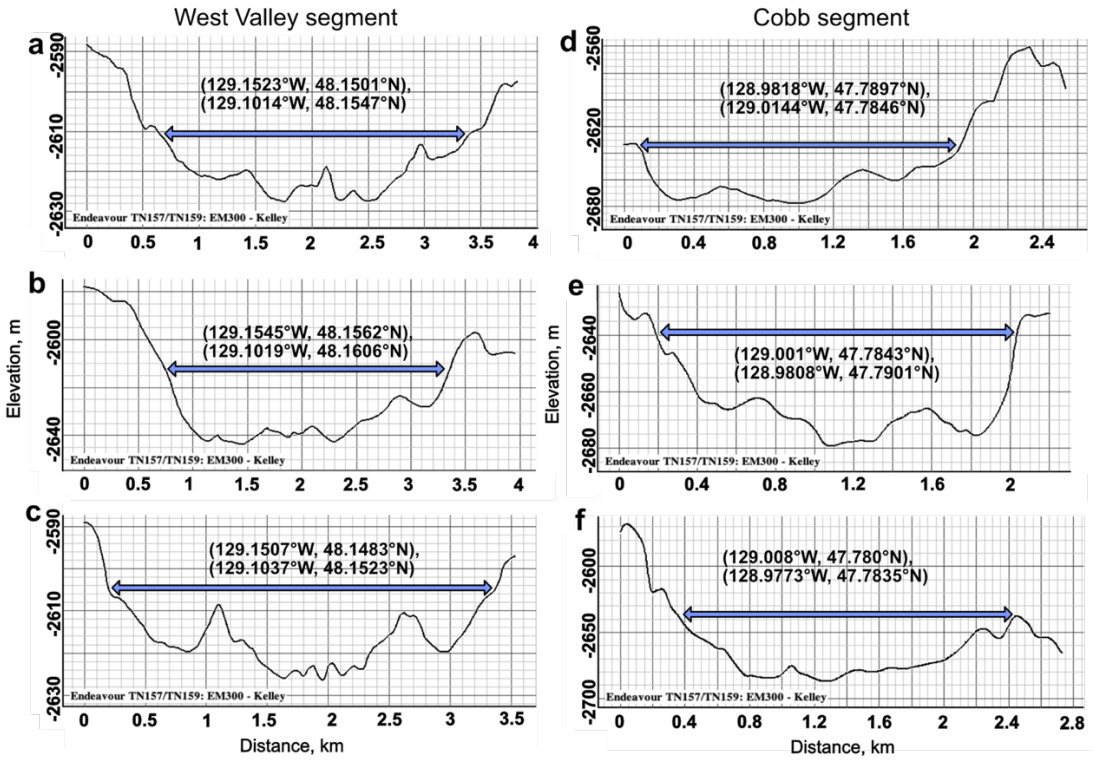

Figure S17. Examples of bathymetric cross-sections taken perpendicular to the strike of propagator tips near the apparent end of the features, plotted from the bathymetry of Kelley (2015) using GeoMapApp (geomapapp.org), for (a-c) the West Valley segment and (d-f) the Cobb segment. End points of the cross sections are noted on each subplot. Blue horizontal arrows on each subplot denote the region we define as subsided.

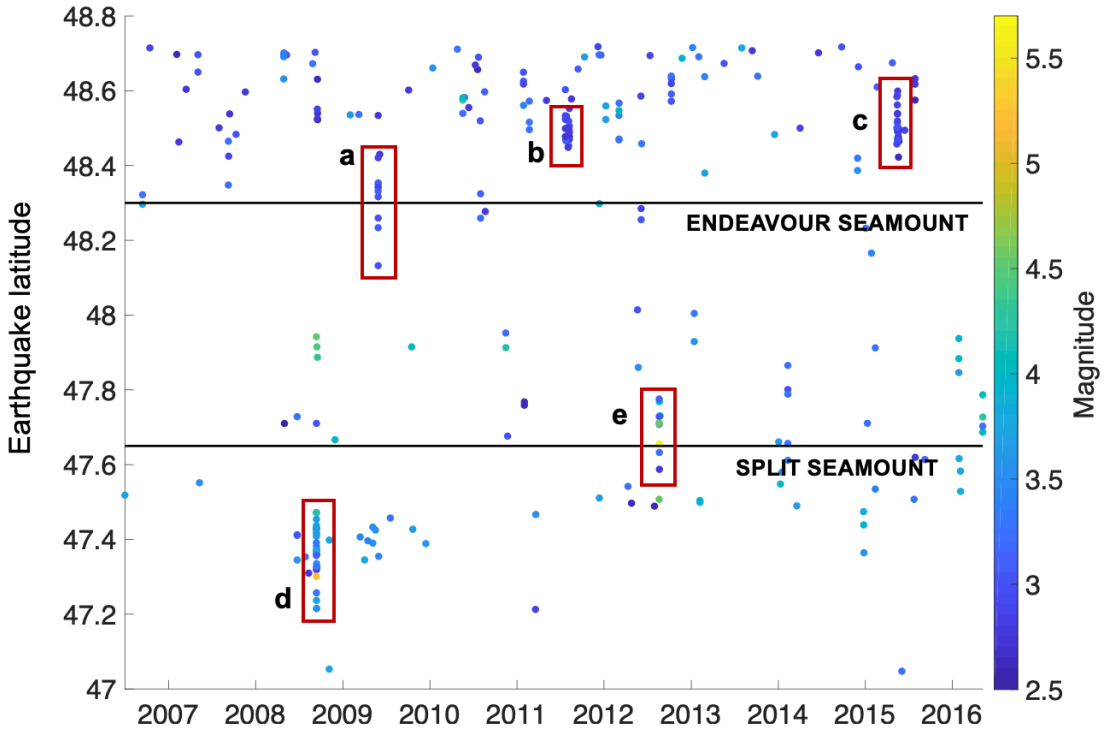

Figure S18. Scatter plot of earthquake latitudes over time for all earthquakes available through the IRIS FDSN from the IDC, ISC, NEIC, PGC and USGS catalogs for July 2006-June 2016 between 46.78-48.72° N and 129.72-128.5° W, colored by earthquake magnitude. Horizontal lines indicate the latitude of the Endeavour seamount and Split seamount. Clustered earthquake groups that display a latitudinal migration of earthquakes that could potentially be related to extensional events on the WV and Cobb segments are delineated with red boxes. Possible events on the WV segment include (a) one migration from 48.15-48.4° N during the first 6 hours of May 29 2009, (b) two successive southward migrations from 48.54-48.44 °N on July 23 and August 8 2011, and (c) one migration from 48.54-48.44° N during May 13-22 2015. Possible events on the Cobb segment include (d) one migration from 47.45-47.2° N during September 12-13 2008, and (e) activity without a clear migration from 47.8-47.55° N during August 19-20 2012.

Table S1. ONC Network Instrumentation Metadata

Instrument code and time period[1]	Sensor type	Sampling rate	Deployment style
ENHR 06/27/2018 – 09/20/2019	Guralp Maris Radian broadband seismometer	200 Hz	3 point of contact plate
NCHR 06/20/2016 – 02/28/2021	Geosense BH1 short period seismometer	200 Hz	Corehole
KEMF 06/20/2016 - 11/10/2018; 06/10/2020 – 03/01/2021	Geosense BH1 short period seismometer	200 Hz	Corehole
KEMF-W3 11/10/2018 – 06/10/2020	Guralp Maris Radian accerelerometer	500 Hz	3 point of contact plate
KEMO 06/20/2016 – 08/17/2018	Geosense BH1 short period seismometer	200 Hz	Corehole
KEMO 09/20/2020 – 03/01/2021	Guralp CMG-1T broadband seismometer	200 Hz	Plate with glass bag weights
ENWF 09/30/2016 – 03/01/2021	Guralp CMG-1T broadband seismometer	200 Hz	Buried

[1]The time period reflects that analyzed in this catalog, not the entire operation of the instrument.

Table S2. *NonLinLoc Grid Search Parameters*

Location type	Number of starting grid nodes			Minimum final node size	Maximum number of nodes	# of travel time grid nodes			Travel time grid node spacing (km)		
	x	y	z			x	y	z	x	y	z
Free depth	40	60	50	1 m	100000	601	901	46	0.2	0.2	0.2
Fixed depth	40	60	1	1 m	100000	601	901	2[1]	0.2	0.2	0.01

[1]Centered on fixed depth.

Table S3. Physical Parameters for Earthquake Moment Calculation

Parameter	P-waves	S-waves
Q (x < 0.4 km)	40	40
Q (x > 0.4 km)	500	500
V (km/s)	6.35	3.60
f (Hz)	5-15	5-15
K	1.5	2
R	0.42	0.59
ρ (kg/m^3)	2800	

Table S4. Moment Correction Factors

Station	Phase	Moment correction
NCHR	P	1.12
	S	0.81
ENHR	P	0.87
	S	0.58
KEMF	P	0.57
	S	1.47
KEMF-W3 (accelerometer)	P	1.20
	S	0.72
ENWF	P	0.72
	S	1.56
KEMO	P	1.05
	S	1.09

Table S5. NonLinLoc versus Swarm Uncertainties

Swarm	Maximum 1-σ horizontal uncertainty from swarm (km)	Median maximum 1-σ horizontal uncertainty from NonLinLoc for corresponding region (km)
V1	0.68	0.64
E1	0.96	1.6
S1	0.85	0.95
S2	1.25	0.95
S3	1.08	0.95
WV2	6.66	6
WV4	7.75	6
C1	2.72	5.4
C2	3.52	5.4
C3	3.34	5.4

Note. Comparison is between the maximum 1-σ horizontal uncertainties derived from the covariance of swarm locations and the median of those calculated by NonLinLoc in the ONC network for each region. Swarm locations and ellipses can be found in Figure S6.

Table S6. Magnitudes of completeness (M_c) for subregions for all 3 experiments

	VF	EF	SWEV	WV OSC	Cobb OSC
1995	0.9	1	1	-	-
Keck	1	1	1.6	2	2
ONC	0.52	0.63	0.55	1.16	1.15

Note. Magnitudes of completeness could not be estimated for the segment-end regions for the 1995 experiment due to limited sensitivity of the network to earthquakes at segment ends.

Appendix 2: Supplementary Materials for Chapter 3

Text S1: Theoretical single-station earthquake location approach using P_W

Here we discuss a method for determining earthquake hypocenters at the Endeavour from measurements of *P*, *S* and P_W arrival times that we planned to implement but could not because it requires that the azimuth to the earthquake is well-determined so that the bathymetry is known along the source-receiver path.

Three-dimensional *P* and *S* wave travel time grids that include the effects of bathymetry could be obtained by applying the shortest-path ray tracing algorithm of Toomey et al. (1994) to the *P* and *S* wave velocity models previously obtained by refraction tomography with the same ray tracer (Arnoux et al., 2019b; Kim et al., 2019b). A 3-D P_W grid could then be calculated by seeding each seafloor node with the water path time for a source located two water depths above the receiver, and then using the shortest-path ray tracing algorithm to calculate *P* wave travel times from the station to each grid point. Three-dimensional differenced *S* - *P* and $P_W - P$ grids could then be calculated.

With the back azimuth to the earthquake determined, 2-D slices of the *S* - *P* and $P_W - P$ grids could be taken in the direction of the calculated earthquake azimuth, with the station as the origin, by linearly interpolating between the original cartesian travel time grid and a 2-D vertical grid along the calculated azimuth (Figure 2c).

As detailed in section 3.1, *P* and *S* wave arrival times are picked using an iterative approach (Krauss et al., 2023) and then refined using Kurtosis (Baillard et al., 2014). To aid in the picking of P_W arrival times, a preliminary location could be calculated by fixing the depth to 2 km and finding the horizontal position in the grid that matches the observed *S*-*P* times.

The preliminary epicenter could then be used to guide the picking of the P_W arrival. A preliminary P_W pick could be made by first calculating a predicted $P_W - P$ time. The method of Baillard et al. (2014), which uses kurtosis to define the onset of a body wave, could then be applied to a window around the predicted arrival time (P_W wave) using the vertical channel and then used to calculate a P_W - P time. The P_W - P time could be further refined by cross-correlating the two waveforms and picking the most negative value to account for the change in polarity from the sea surface reflection. Except when the P_W arrival is obscured by the S wave, it can be picked accurately (Figure S4).

A hypocenter could then be calculated from the azimuth and two differential travel-time grids: the S-P grid and P_W-P grid (Figure 1c). Grids of residuals could then be calculated by differencing all the nodes of the differential travel time grid slices and the observed S-P and P_W-P times. The two residual grids could then be combined as follows:

$$G_{RMS,ij} = \sqrt{\frac{\left(w_{SP} * G_{SP,ij}^2\right) + \left(w_{PWP} * G_{PWP,ij}^2\right)}{w_{SP} + w_{PWP}}},$$

where G_{SP} and G_{PWP} are the S-P and P_W-P residual grids, respectively, w_{SP} and w_{PWP} are weights assigned to each grid, and i and j are the grid indices. The final location would be chosen as the grid location with the smallest value of G_{RMS}.

Uncertainties in the range and depth of earthquakes could then be calculated through a bootstrapping approach. Synthetic S-P and P_W-P travel time differences could be created by adding normally distributed random errors based on chosen differential time uncertainties. The covariance matrix of the resulting point cloud could then be calculated and χ–squared statistics

could be used to define errors in the range and depth using the corresponding covariance matrix element.

The challenge of using the *S*-*P* and P_W-*P* differential times to determine range and depth is illustrated by looking at the contours of differential times (Figure S1). The contours of *S*-*P* and P_W-*P* times intersect at high angles (Figure S1c), suggesting that the locations can be well resolved, but this requires P_W-*P* that are picked and modeled to an uncertainty of ~0.01 s. Cross-correlation picking can yield P_W-*P* times with such accuracies, but the P_W-*P* models will only achieve this accuracy if the seafloor depths used to model the P_W paths propagating upwards across the seafloor are accurate to ~15 m. Given that seafloor depths vary by hundreds of meters around the seismic stations at the Endeavour, such accuracy cannot be achieved when the azimuth to the earthquake is not well constrained. For this reason, at the Endeavour segment, the P_W-*P* times could not be combined with *S*-*P* times used to constrain range and depth.

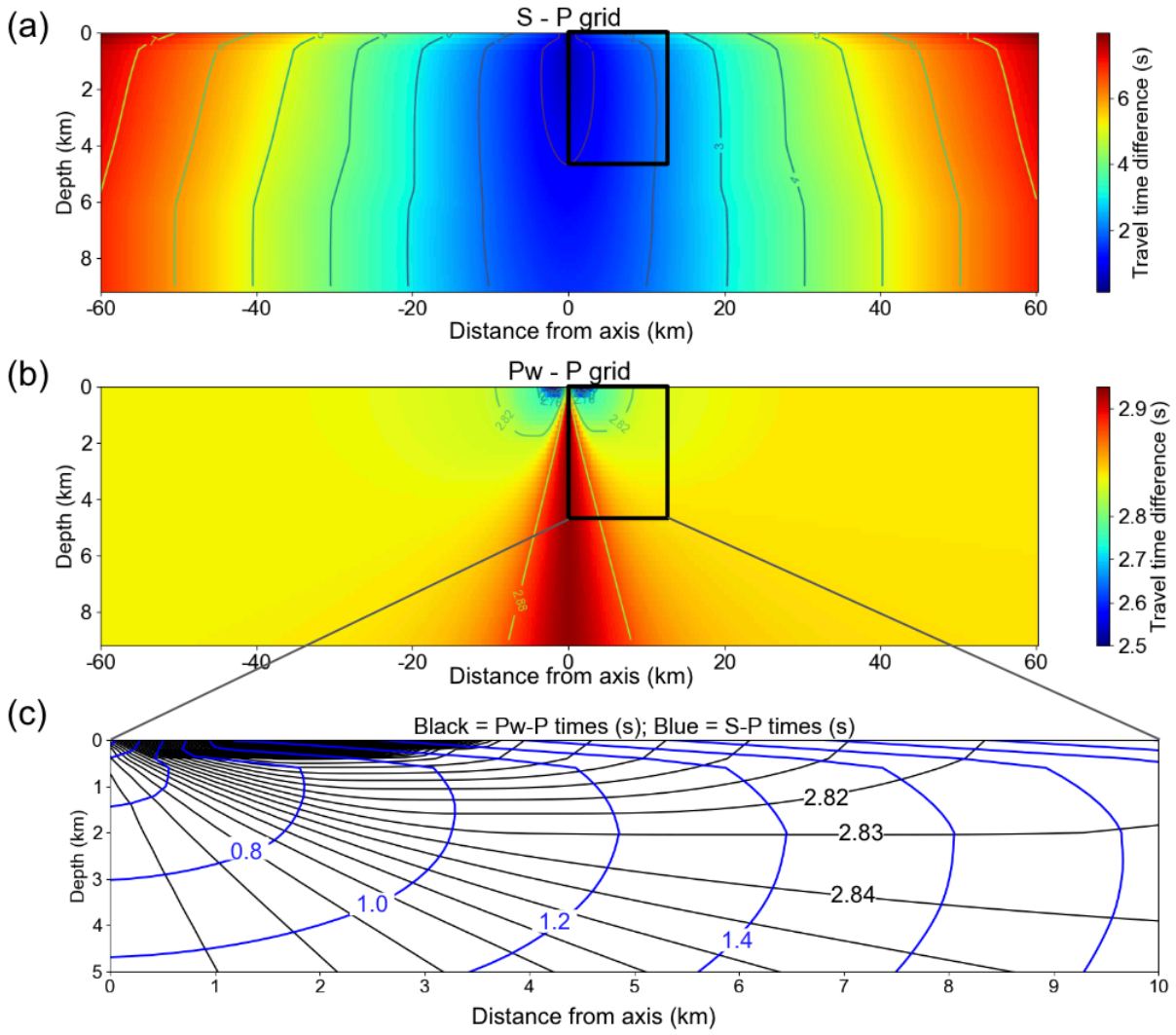

Figure S1. Differenced travel-time grids shown as cross-sections taken across-axis centered on the KEMF station. The 3-D velocity models used to generate these grids are from Arnoux et al. (2019b) and Kim et al. (2019b). The travel-time grids assume flat bathymetry. **(a)** Cross-section showing differential travel times with a color scale overlain by contours of the *S-P* differenced travel time grid. **(b)** Same as (a), but for the *Pw-P* travel time grid. **(c)** *S-P* (blue) and *Pw-P* (black) travel time difference contours for a region marked by a black box in (a) and (b).

Text S2: Iteration on P-wave polarization window and frequency band

Polarization Window

When choosing how many samples before the P-wave arrival and after the arrival to run a polarization analysis on, the goal is to ensure the window captures the entire first peak and sufficient oscillations to measure rectilinear motions before the arrival is shrouded by the coda of scattered energy. To see which window size worked best with our data, we tested 9 different window sizes on 11 high-quality local earthquake seismograms (see table below). For these iterations, each stream was filtered from 8-45 Hz and converted to displacement after the removal of the instrument response. Each test was visually evaluated based on the number of realistic oscillations it appeared to capture, as well as the rectilinearity of the particle motions (see example in Figure S2). A perfectly rectilinear waveform has a rectilinearity of 1.

Polarization Window Test Number	Seconds Before P-wave	Seconds After P-wave
1	0.02	0.48
2	0.02	0.28
3	0.02	0.2
4	0.02	0.12
5	0.02	0.15
6	0.01	0.15
7	0.03	0.15
8	0.02	0.10
9	0.05	0.10

Based on resulting combinations from these tests, we selected a window size of [0.05,0.12]. This size best preserves the rectilinearity of the waveform: it effectively captures the entire first oscillation without capturing pre-arrival noise.

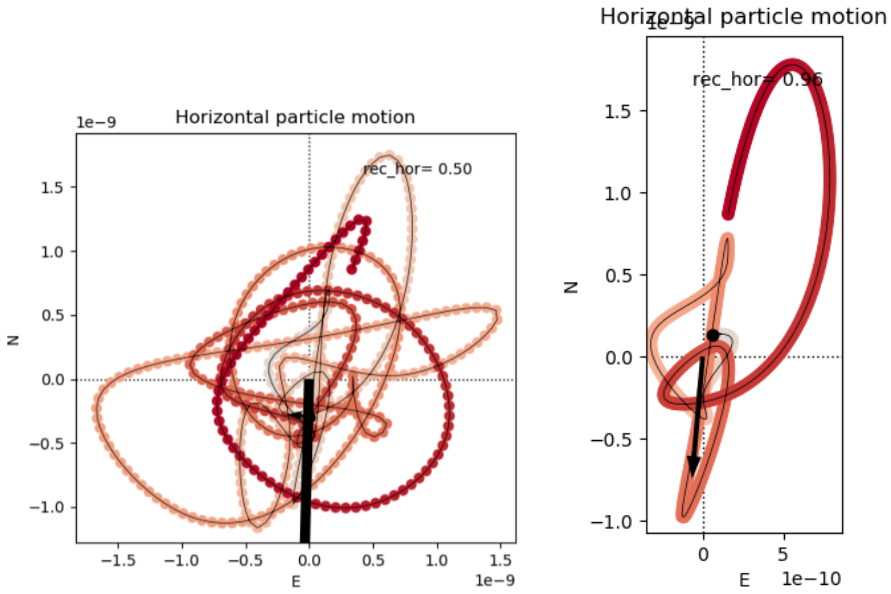

Figure S2. Plots of horizontal displacement components corresponding to a *P* wave for two different window lengths, with the lightest colors representing the earlier samples. The thickest black arrow/line in each subplot represents the azimuth calculated by the polarization analysis; the black dots should be ignored. **(left)** Figure from Test 1, with 4 samples before and 96 samples after. It is clear that far too much of the later waveform is captured with this window, compromising the rectilinearity which is 0.50. **(right)** Figure from Test 9, with 10 samples before and 20 samples after. This window clearly captures enough of the waveform to discern clear particle motion in the direction of the calculated azimuth while not incorporating the scattered part of the waveform, giving a rectilinearity of 0.96.

Frequency Bandwidth

The 100-Hz sample rate sets an upper bound on our frequency band of ~45 Hz. We tested 11 different frequency bands using the [0.05,0.12] polarization window (see table below). In the same way as the polarization window iterations, we visually assessed each test for improved rectilinearity and consistency of azimuth calculation. Based on these tests, we chose a frequency band of 8-35 Hz.

Test Number	Frequency Band (Hz)
Clear	8-45, as used in Polarization Window testing
1	4-45
2	4-15
3	8-15
4	4-25
5	8-25
6	4-8
7	15-45
8	30-45
9	2-25
10	8-35
11	8-35

Text S3: Differences in travel time grids between multi-station and single-station location

We see a systematic difference between earthquake ranges calculated using the multi-station method and the KEMF single-station method, with KEMF single-station ranges on average 1.26 km lower than the corresponding multi-station range. One potential reason for this is the difference in travel-time grids used to calculate earthquake ranges. Although the travel-time grids for both the multi-station and single-station location methods were derived from the same 3-D velocity models (Arnoux et al., 2019b; Kim et al., 2019b), the differing ray-tracing methods used (shortest path with bathymetry for multi-station, finite-difference with flat-bathymetry for single-station) result in slightly different travel-time grids. In this section, we examine how much this could contribute to a difference in the calculated range of earthquakes.

For both multi-station and single-station location, we construct travel-time grids using the same 3-D velocity models. The P-wave model used was obtained from Arnoux et al. (2019b) and includes anisotropy, and the S-wave model was obtained from Kim et al. (2019) and does not include anisotropy. In the multi-station location performed by Krauss et al. (2023), the "Stingray" algorithm of Toomey et al. (1994) was used to compute travel-time grids. Stingray creates travel time grids using ray tracing through the shortest path method of Moser (1991). Stingray uses elevation to accurately represent seafloor bathymetry and can take anisotropy into account. Alternatively, in our single-station approach, where we did not have constrained earthquake azimuths, we assumed a flat-bathymetry model and used the more computationally efficient algorithm available with the NonLinLoc package, Grid2Time (Lomax et al., 2009), which does not take anisotropy into account. Grid2Time uses the eikonal finite difference scheme of Podvin & Lecomte (1991), which approximates a time field from a velocity model.

Raypaths from source to receiver for each grid node are then "backtracked" through the time field approximation to yield a travel time grid.

To determine whether the 1.26 km systematic range difference we observe is consistent with the different travel-time grids, we examine the magnitude of difference between the S-P travel time grids ($\Delta T_{S\text{-}P}$) constructed using the same depth-averaged 3-D velocity models (Figure S3). Specifically, for locations made using the KEMF instrument, we are interested in how much the S-P travel time grids differ along a slice taken along the most common azimuth, which is ~182° for KEMF (160° relative to the ridge-oriented grid). We note that this estimate does not account for all differences between the multi-station and single-station method: in multi-station location, additional differences include variation in earthquake azimuth and the use of anisotropy in travel-time calculation. The estimate we walk through here only isolates the expected differences due to the use of flat bathymetry and finite differences in the travel-time grid calculation.

The range D between source and receiver is equal to the difference in S- and P-wave arrival times ($T_{S\text{-}P}$) divided by the difference in S and P-wave slowness:

$$D = \frac{T_{S-P}}{\frac{1}{V_S} - \frac{1}{V_P}}$$

V_S and V_P are the same between the multi-station and single-station methods because the same velocity model is used, so a difference in range ΔD can be estimated from travel-time differences $\Delta T_{S\text{-}P}$:

$$\Delta D = \frac{\Delta T_{S-P}}{\frac{1}{V_S} - \frac{1}{V_P}}$$

Comparison between the travel time grids for multi-station (Stingray, shortest path with bathymetry) and single-station (Grid2Time, finite difference with flat-bathymetry) show that, within a cross-sectional slice taken along the most used azimuth for KEMF (182°), travel times are consistently larger in the single-station (finite difference flat-earth) grid ($\Delta T_{S\text{-}P}$ is positive; Figure S3a). At depths of 2 km and 3 km, the depths at which we fix earthquakes, the single-station grids have an average $\Delta T_{S\text{-}P}$ of +0.13 s (Figure S3b, S3c). At 2 km depth, where the starting depth-averaged velocity model has a V_P and V_S of 6.14 km s^{-1} and 3.45 km s^{-1}, respectively, this longer travel time corresponds to an average difference in range ΔD of 1.00 km. At 3 km depth, with an average V_P and V_S of 6.48 km s^{-1} and 3.61 km s^{-1}, respectively, this corresponds to an average difference in range ΔD of 1.03 km. So, because the single-station travel-time grids estimate a longer travel time between the source and receiver, it is expected that the same earthquake would have a comparatively shorter range on the order of ~1 km to accommodate arrival times.

In short, we expect that earthquake ranges calculated using shortest path and bathymetry (as in the multi-station approach) will be systematically longer. This is consistent with our observed results. However, we reemphasize that this does not account for all differences between the multi- and single-station methods: namely, varying azimuth in the multi-station locations and anisotropy in the multi-station model can be expected to contribute more discrepancies in calculated ranges. Still, our estimate shows that much of the observed systematic range difference can be attributed to a combination of bathymetry and ray tracing methods. It is

expected that true ray-tracing would yield smaller travel times than can be approximated by either finite difference or shortest path methods.

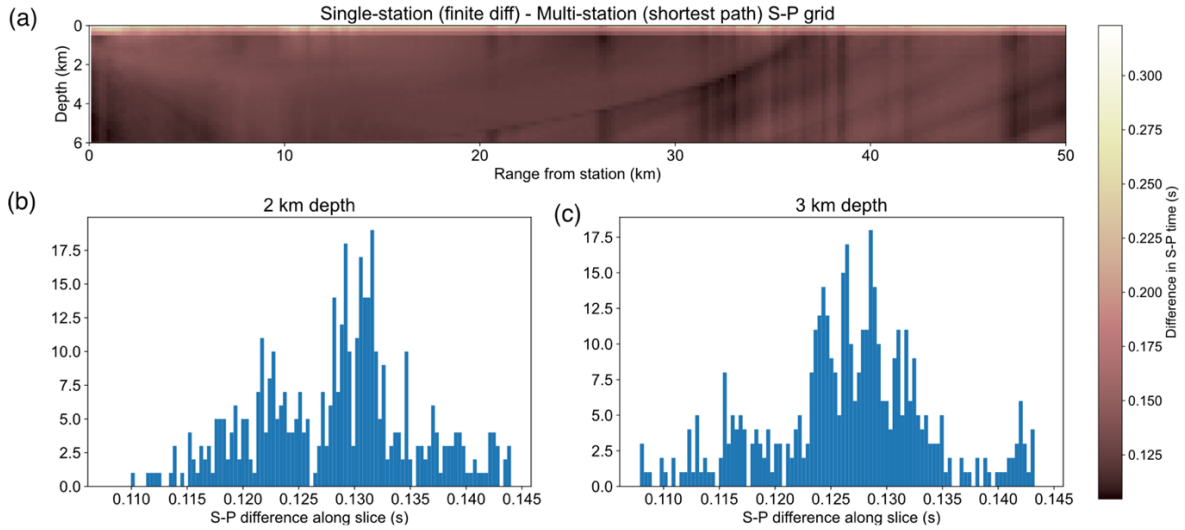

Figure S3. Differences between travel-time grids**,** $\Delta T_{S\text{-}P}$, shown as single-station (finite difference flat-earth) minus the multi-station (shortest path with bathymetry) grid. **(a)** Horizontal cross-sections of $\Delta T_{S\text{-}P}$ for the differenced travel time grids taken along a slice at 182°. Grid nodes have 0.2 km spacing. **(b)** and **(c)** show histograms of $\Delta T_{S\text{-}P}$ values for each grid node along the slice at 2 and 3 km depths, respectively.

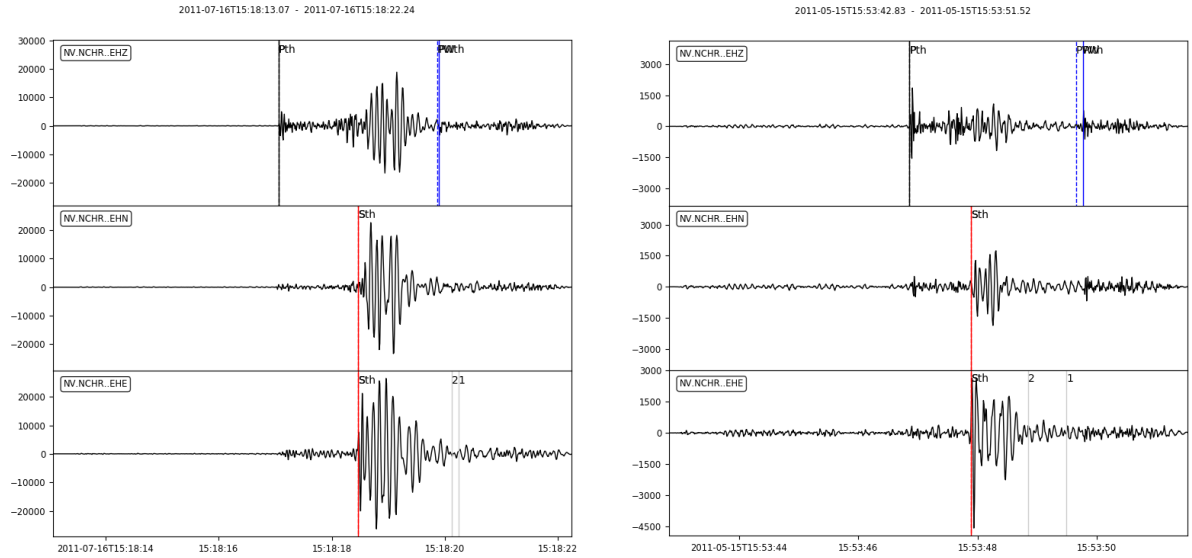

Figure S4. Example P_W picks. Both subplots show three components of motion from station NCHR with P-waves picks as black vertical lines, S-waves as red lines, cross correlation P_W picks as dashed blue lines, and kurtosis P_W picks as blue solid lines.

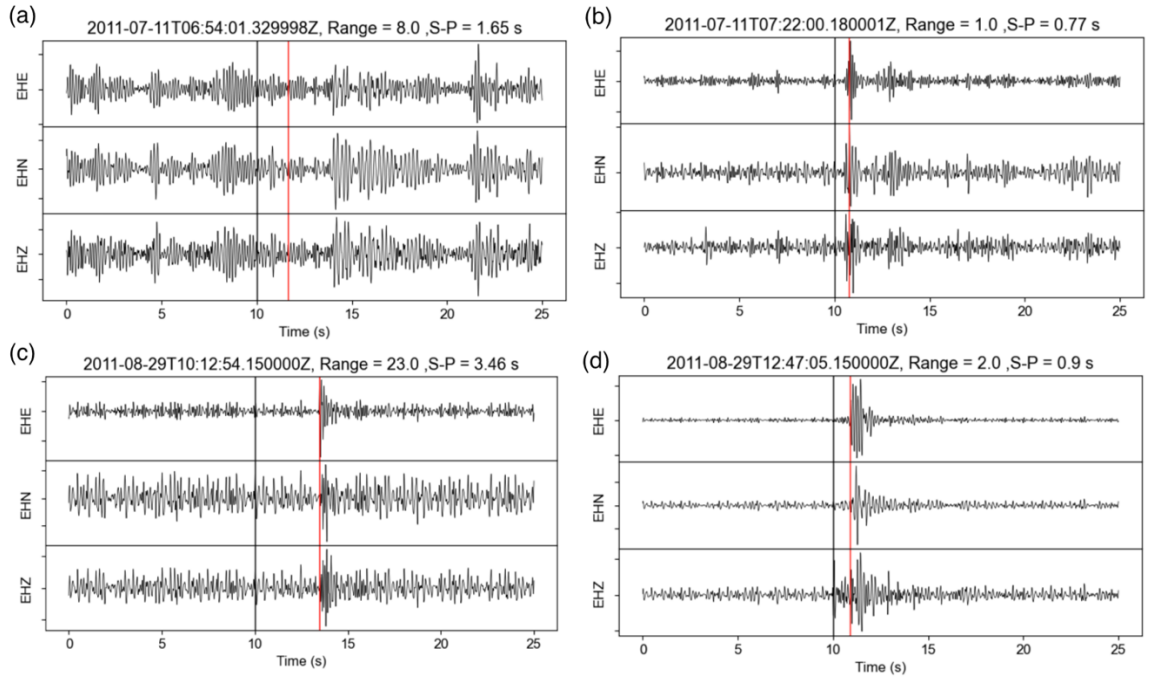

Figure S5. Examples of noisy single-station detection from station NCHR. Three-component waveforms are shown for a 25 s window with P- and S-wave picks marked by black and red vertical lines, respectively. The calculated earthquake origin time, range in km, and S-P differential time is given in the title of each subplot. **(a)** Example of a misdetection on noise. **(b)** Example of a potential misdetection/potential true earthquake, with arrivals indistinguishable from other surrounding signals. **(c)** Example of a likely earthquake with an indistinguishable P-wave due to high frequency noise. **(d)** Example of a correctly picked earthquake.

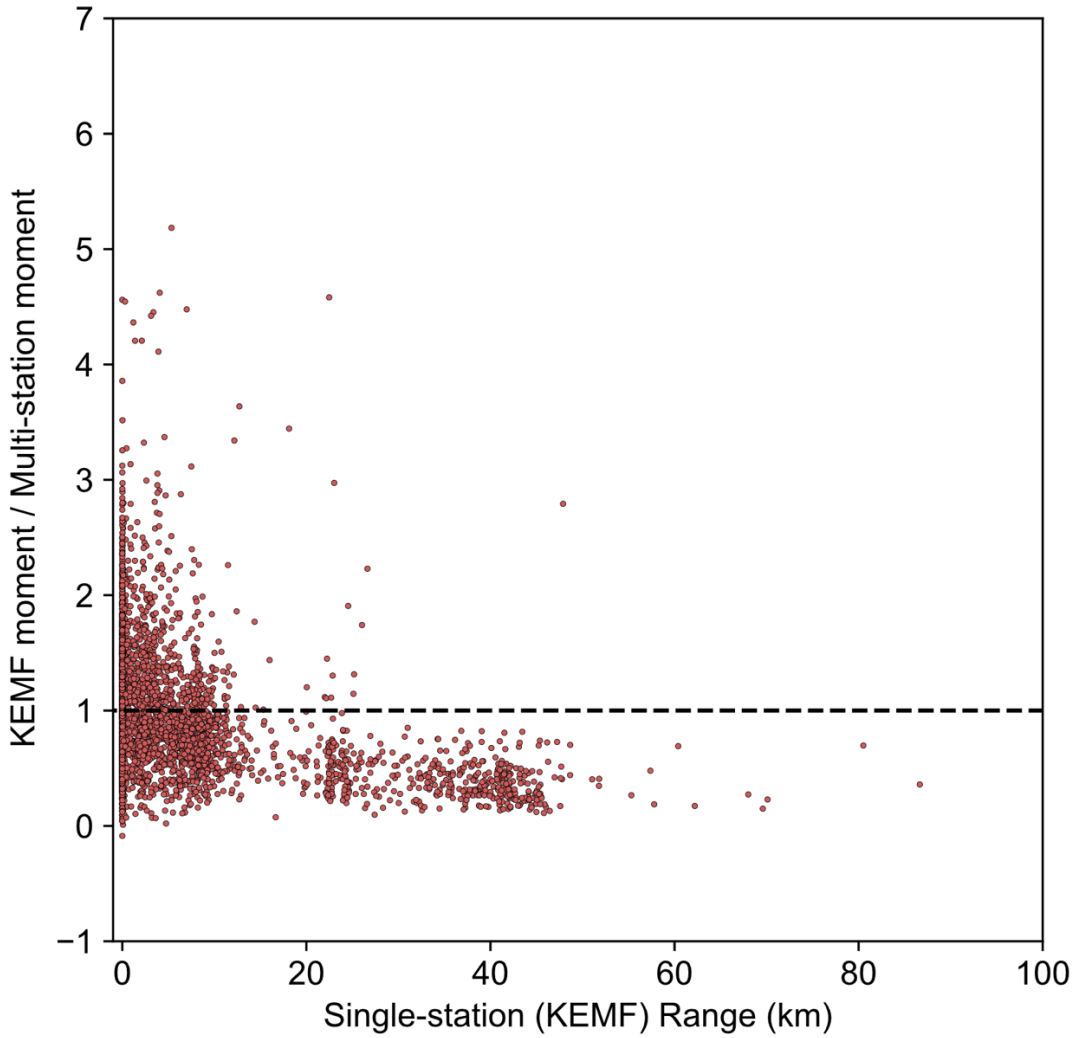

Figure S6. Scatter plot showing ratios of moments calculated for the same earthquake (origin time within 1 s) versus range. The ratio is defined as the single station moment (KEMF) divided by multi-station moment. The horizontal dashed black line shows a ratio of 1.

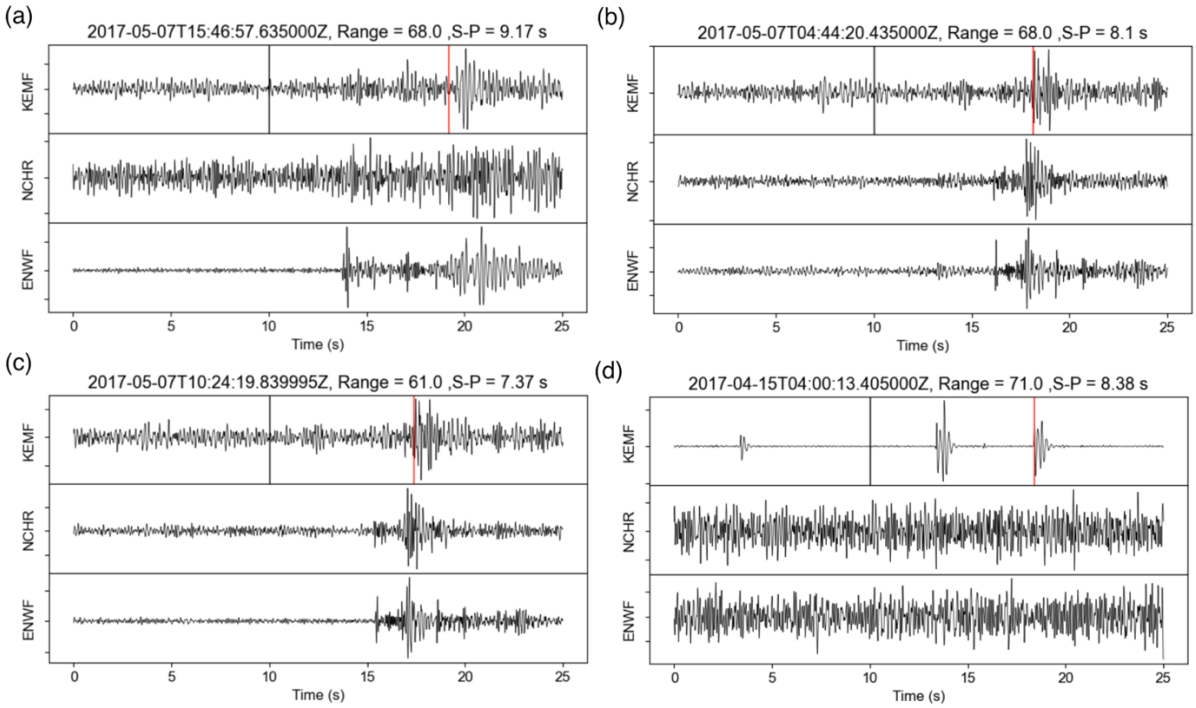

Figure S7. Examples of events detected on station KEMF with very large ranges. In all subplots, waveforms of the vertical channels are shown for KEMF, NCHR and ENWF for a 25 s window. The P- and S-wave picks made by the single-station detection algorithm on the KEMF station are shown with black and red vertical lines, respectively. The calculated earthquake origin time, range in km, and S-P differential time is given in the title of each subplot. **(a-c)** Examples where there is not a clear P-wave arrival on the KEMF station but a clear P-wave arrival on other stations; in single-station detection, the P-wave is incorrectly picked. **(d)** Example where the detection is likely noise and the detection would have been discarded in the multi-station catalog.

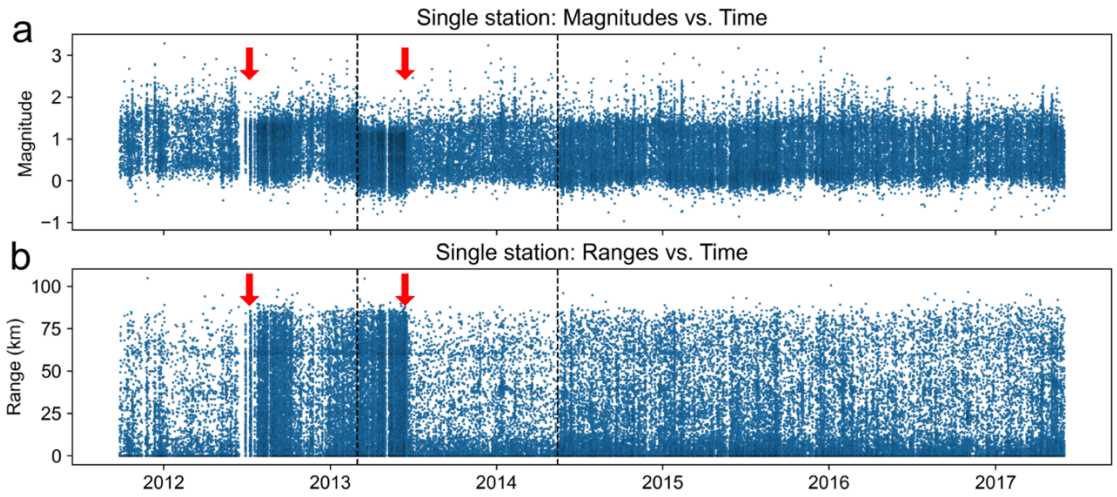

Figure S8. Scatter plots showing overall distributions of **(a)** magnitudes and **(b)** ranges for all earthquakes detected on KEMF by the single-station method versus time. Instrument changes are shown with black dashed vertical lines. The start and end of the time period that the junction box noise was active are marked using red arrows. An example of the noise is shown in Figure S9.

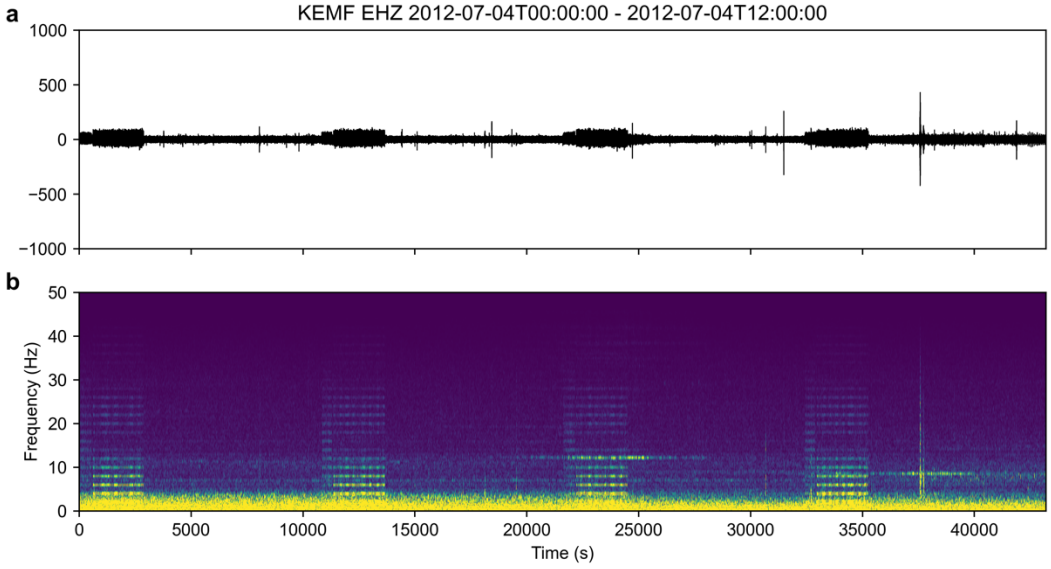

Figure S9. 12-hour time series example of episodic noise, assumed to be caused by a failed junction box, that recurs about every 3 hours for 45 minutes during the period marked in Figure 4. **(a)** shows the unfiltered waveform of the vertical component of station KEMF and **(b)** shows the spectrogram.